Exploring the Precursor-Process-Property Space in Metal Halide Perovskite Thin-Films

Dissertation

zur Erlangung des akademischen Grades
doctor rerum naturalium (Dr. rer. nat.)

im Fach Chemie

eingereicht an der
Mathematisch-Naturwissenschaftlichen Fakultät
der Humboldt-Universität zu Berlin
und durchgeführt am Helmholtz Zentrum Berlin
von

Carolin Rehermann, M.Sc.

Präsidentin der Humboldt-Universität zu Berlin
Prof. Dr.-Ing. Dr. Sabine Kunst

Dekan der Mathematisch-Naturwissenschaftlichen Fakultät
Prof. Dr. Elmar Kulke

Abstract

The material class of metal halide perovskites with the stoichiometry ABX_3 is characterized by its outstanding properties, such as bandgap tunability by ion substitution and the easy fabrication due to solution-based processes. Thus, they present as a promising material for application in various thin-film opto-electronic devices, such as solar cells and LEDs. However, these applications require the deposition of high-quality thin-films, in particular with respect to their morphology, which is defined by a high coverage and a smooth surface, over the entire compositional range. The thin-film quality is strongly dependent on the crystallization behavior predetermined by the precursor composition in solution. Therefore, objective of this thesis is to evaluate the correlations in the wide precursor-process-property space of metal halide perovskite and to rationalize formation processes and their dependence on individual preparation parameters.

The quality of perovskite thin-films is determined through their phase purity, morphology and associated absorption properties. The perovskite preparation process determines the thin-film quality, particularly in terms of morphology. A dependence of the formation processes on both the precursor composition and the preparation parameters is evident. These interdependencies underline the necessity to optimize preparation processes for each individual ion composition in order to obtain high-quality thin-films. Therefore, the structure-property relationship is extended to the triangle precursor-process-property for metal halide perovskites prepared by solution-based techniques. The rationalization of these formation processes proves to be essential to design reliable and reproducible preparation routines.

Due to the characteristic optical properties of metal halide perovskites and potential intermediates, optical in-situ methods are suitable for rationalizing formation processes within this material class. The development of such an optical set-up allows to evaluate the impact of different parameters on the formation process.

The halide ratio, tailoring the bandgap, influences the perovskite formation in the $MAPb(I_xBr_{1-x})_3$ series in terms of film homogeneity. Depending on the halide ratio in the precursor solution, different formation pathways are taken during spin-coating and annealing: while the pure bromide forms directly during spin-coating and iodide-rich perovskites form via the intermediate solvate phase $(MA)_2(DMSO)_2Pb_3I_8$, mixed stoichiometry between $0.1 \leq x \leq 0.6$ form via both pathways. This leads to a heterogeneous formation process via two competing reaction pathways, inducing a heterogeneous mixture of phases, and rationalizes the compositional heterogeneity of mixed bromide/iodide samples.

The individual rationalization of the anti-solvent drop, the solvent system, and the cation composition each reveals a characteristic influence on the direct formation process of bromide-based perovskites. Furthermore, the formation process of $FA_{0.85}MA_{0.10}Cs_{0.05}PbBr_3$ (3CatPbBr$_3$) is dependent on the precursor solution concentration. Lower concentrations lead to accelerated crystallization kinetics and increased evaporation rates of the solvent from the wet-film. Therefore, there is no uniform saturation concentration at the onset of crystallization. Lower colloid interactions and lower coordinated lead-bromide complexes in diluted solutions can explain this trend. Furthermore, a model for rationalizing the change in layer thickness in complex multilayer systems after setting an anti-solvent drop is drawn by means of interference analysis. The strong correlation in the precursor-process-property space rises the preparation of perovskites via spin-coating to a non-trivial process from a chemical point of view. A complete rationalization of the

complex formation processes provides guidelines for or targeted process development to produce high-quality metal halide perovskite thin-films.

Kurzfassung

Die Materialklasse der Metallhalogenid-Perowskite mit der Stöchiometrie ABX_3 wird durch herausragende Eigenschaften, wie die Anpassung der Bandlücke durch Ionenaustausch und die einfache Herstellung aufgrund von lösungsbasierten Prozessen, charakterisiert. Daher stellen sie ein vielversprechendes Material für die Anwendung in verschiedenen opto-elektronischen Dünnschichtbauteilen wie Solarzellen und LEDs dar. Diese Anwendungen erfordern jedoch die Abscheidung qualitativ hochwertiger Dünnschichtfilme über den gesamten Kompositionsbereich, insbesondere im Hinblick auf die Morphologie, welche durch einen hohen Deckungsgrad und eine glatte Oberfläche definiert ist. Die Qualität der Dünnschicht hängt stark von dem Kristallisationsverhalten ab, welches durch die Zusammensetzung der Präkursoren in Lösung vorgegeben ist. Ziel dieser Arbeit ist es, die Korrelationen im breiten Feld „Präkursoren-Prozess-Eigenschaften" von Metallhalogenid-Perowskit zu bewerten, sowie Formierungsprozesse und deren Abhängigkeit von einzelnen Präparationsparametern zu rationalisieren.

Die Qualität von Perowskit-Dünnschichten wird durch ihre Phasenreinheit, Morphologie und die damit verbundenen Absorptionseigenschaften bestimmt. Formierungsprozesse bestimmen die Dünnschichtqualität, insbesondere in Bezug auf die Morphologie. Wiederum zeigt sich eine Abhängigkeit der Formierungsprozesse sowohl von der Perowskit-Komposition als auch von den Präparationsparametern. Diese wechselseitigen Beziehungen unterstreichen die Notwendigkeit, die Präparationsprozesse für jede einzelne Ionenzusammensetzung zu optimieren um qualitativ hochwertige Filme zu erhalten. Daher erweitern sich Struktur-Eigenschafts-Beziehungen für Metallhalogenid-Perowskite, die durch lösungsbasierte Prozesse hergestellt werden, zu dem Dreieck „Präkursoren-Prozess-Eigenschaften". Die Rationalisierung dieser Formierungsprozesse erweist sich als unabdinglich für die Entwicklung zuverlässiger und reproduzierbarer Herstellungsroutinen.

Aufgrund charakteristischer optischer Eigenschaften von Metallhalogenid-Perowskiten und potentieller Zwischenstufen bieten sich optische in-situ-Methoden zur Rationalisierung der Formierung an. Die Entwicklung eines solchen optischen Aufbaus erlaubt es den Einfluss verschiedener Parameter auf den Formierungsprozess zu bewerten.

Das Halogenidverhältnis, das die Bandlücke maßgeblich bestimmt, beeinflusst die Perowskitformierung in der $MAPb(I_xBr_{1-x})_3$-Reihe in Bezug auf die Homogenität. Abhängig vom Halogenidverhältnis in der Präkursorenlösung werden während des Spin-coatings und Annealens unterschiedliche Formierungswege beschritten: Während sich das reine Bromid direkt beim Spin-coating bildet und Iodid-reiche Perowskite über die intermediäre Solvatphase $(MA)_2(DMSO)_2Pb_3I_8$ entstehen, werden bei Mischungen zwischen $0.1 \leq x \leq 0.6$ beide Formierungspfade beschritten. Dies führt zu einem heterogenen Formierungsprozess über zwei konkurrierende Reaktionswege, wodurch ein heterogenes Phasengemisch induziert wird. Dieses Phasengemisch rationalisiert die kompositorische Heterogenität der gemischten Bromid/Iodid Proben auch nach dem Ausheizen.

Die individuelle Rationalisierung des Anti-solvent-drops, des Lösungsmittelsystems und der Kationenzusammensetzung zeigt jeweils einen charakteristischen Einfluss der Parameter auf den direkten Formierungsprozess von reinen Bromid-Perowskiten. Darüber hinaus zeigt sich eine Abhängigkeit des Formierungsprozesses bei $FA_{0.85}MA_{0.10}Cs_{0.05}PbBr_3$ ($3CatPbB_{r3}$) von der Konzentration der Präkursorenlösung. Niedrigere Konzentrationen führen zu beschleunigter Kristallisationskinetik und erhöhten Verdampfungsraten der Lösemittel aus dem Nassfilm. Daher liegt keine einheitliche Sättigungskonzentration beim Einsetzten der Kristallisation vor. Dieser

Trend ist durch geringere Kolloidwechselwirkungen und niedriger koordinierte Blei-Bromid-Komplexe in verdünnten Lösungen erklärbar. Des Weiteren wird ein Modell zur Rationalisierung der Schichtdickenänderung in komplexen mehrschichtigen Systemen nach Setzen eines Anti-solvent-drops mittels Interferenzanalyse aufgezeichnet. Solch eine detaillierte Analyse ermöglicht es, den Einfluss des Anti-solvents und verknüpfte Formierungsmechanismen im Detail zu ergründen. Die starke Korrelation „Präkursoren-Prozess-Eigenschaften" zeichnet die Herstellung von Perowskiten über Spin-coating aus chemischer Sicht als einem nicht-trivialen Prozess aus. Eine vollständige Rationalisierung der komplexen Formationsprozesse liefert einen Leidfaden für zielgerichtete Prozessentwicklung zur Herstellung von Metallhalogenid-Perowskit Dünnschichten.

Table of Contents

1. Introduction

"Each of us must work for his own improvement and at the same time share a general responsibility for all humanity." – Marie Curie

Improving yourself often means taking new paths that no one has taken before. To stay where it can be uncomfortable, to endure the pressure of being different, to have no one to orientate oneself and yet to confidently continue on this path.

This is not only true in life, but also in science, because new knowledge can only be gained where nobody has looked before. Gaining knowledge means exceeding the limits of what has already been explored. This often makes the step of researching, learning and gaining knowledge difficult and grueling.

However, what always builds you up are the other people around you, who keep you company. They cross our path, add color, laughter and sun to this difficult way outside the comfort zone. Then, when we are tempted to lose ourselves in improvement, they guide us back to a possible path. In the end we should not try to improve ourselves for our own ends. Rather see that we humans only function as a community and that we, therefore, have a responsibility not only for ourselves, but also for all humanity, to whatever extent.

With this doctoral thesis, I have found my own path in science, in gaining knowledge, and I have grown along with it as a scientist, but also as a person. It is my wish for myself and for society that the knowledge I have gained from this work will enable me to fulfil my responsibility for humanity, at least to a small extent, by inspiring and supporting others to go their own way, not only through my work but also through my actions.

Objective of this thesis

Metal halide perovskites are a versatile material class with a stoichiometry of ABX_3 and consist of an organic or alkaline monovalent A^+ cation, a divalent metal B^{2+} cation and monovalent halide X^- anions. They are characterized by an all-corner sharing $[BX_6]^-$ octahedron framework with the A^+ cation in the 12-fold cub-octahedral void. Based on the tolerance of the structure, in the case of lead-based ABX_3 materials, the A^+ site can be occupied by caesium (Cs^+), methyl ammonium (MA^+), and formamidinium (FA^+) and the X^- site by chloride (Cl^-), bromide (Br^-), and iodide (I^-).

Metal halide perovskites receive strong attention within the last 10 years due to their preparation by solution-based processes and outstanding applicability in opto-electronic devices, especially in single- and multi-junction solar cells. The fabrication of high-quality perovskite thin-films, in terms of morphology and opto-electronic properties, is required for their application in those devices. The crystallization behavior during processing critically determines the thin-film quality. Thus, the crystallization and fabrication of metal halide perovskites have to be tailored to meet the required film quality. However, the exact formation processes of metal halide perovskites from precursor solutions during the preparation steps of spin-coating and annealing are not clarified. So far, it is only known that the formation depends strongly on the precursor composition in solution and can be influenced by process engineering. However, there is a lack of knowledge about details of formation processes, which are necessary to design the fabrication processes in a targeted way.

The comprehensive rationalization of metal halide perovskite formation processes will enable target-orientated process design for their thin-film deposition on a laboratory and, in the long-term, on an industry scale. Especially the development of higher bandgap perovskites, with up to now little established preparation routines will benefit from such a rationalization, as their fabrication processes can be specifically designed. The rationalization of the formation of metal halide perovskites through targeted process design will drive the fabrication of high-quality thin-films by upscaling techniques, improve the efficiency of all perovskite-based opto-electronic devices, and make an important contribution to their market maturity.

Thus, this work focuses on the fundamental illumination to rationalize formation processes from solution and addresses the questions: How does the precursor-process-property space connect in metal halide perovskites?

Outline of this thesis

Chapter 2 presents the material class of semiconducting metal halide perovskites, which have a stoichiometry of ABX_3 and are characterized by an all-corner sharing $[BX_6]^-$ octahedron framework with the A^+ cation in the 12-fold cub-octahedral void. Their wide compositional space is justified by Goldschmidt´s tolerance factor; their bandgap tunability and electronic structure are presented. By means of big data, challenges in bandgap tuning and the connected identification of suitable preparation parameters are demonstrated. Furthermore, insights into the status of perovskite formation from solution to the final film are given.

Chapter 3 gives an overview of the precursor materials used for metal halide perovskites. Furthermore, it describes the general solution-based fabrication routines and techniques, from solution preparation to thin-film deposition by spin-coating and subsequent annealing, as applied

in this work. All analytical techniques are listed which were exploit to investigate precursor solutions, the formation processes, and the final film properties.

Chapter 4 meets the challenge of fabricating high-quality perovskite thin-films over their broad compositional space of $APbX_3$, with $A^+ = Cs^+$, MA^+, FA^+ and $X^- = Cl^-$, Br^-, I^-, in order to determine reliable optical properties. The final film quality is determined by SEM imaging, structural and optical properties are evaluated by XRD and in-sphere UV-vis measurements. This study shows that the optical properties, such as bandgap and exciton binding energy, correlate with the lattice dimensions and, thus, with the perovskite composition. In addition, it turns out that the process conditions have to be re-optimized for every precursor composition, which caused the scientific questions of the two following chapters.

Chapter 5 deals with the scientific question, how and why the solution composition and the process determine the final perovskite film composition in terms of homogeneity. Within the mixed halide $MAPb(I_xBr_{1-x})_3$ series, the dependency of the growth process on the halide composition in the precursor solution during spin-coating and annealing is followed by in-situ UV-vis measurements. Single spectrum analysis and ex-situ XRD measurements reveal a heterogeneous crystallization process via the direct formation of a bromide-rich perovskite phase and an intermediate iodide-rich solvate phase. Due to this inhomogeneous formation process, heterogeneities in final mixed halide films are rationalized.

Starting from the pure bromide $APbBr_3$ series, with $A^+ = Cs^+$, MA^+, FA^+ and their mixture, **Chapter 6** addresses the question how the precursor solution affects the thin-film formation in terms of concentration, solvent, and what influence the anti-solvent has. During spin-coating the formation process is investigated by in-situ UV-vis, PL, and interference measurements, while solution-based SAXS and UV-vis measurements provide insights into the chemistry of the precursor solution. Due to different colloidal compositions, the solution concentration influences the crystallization kinetics, while the solvent system influences them due to different precursor chemistry. The anti-solvent drop induces crystallization and, thus, must be aligned with the crystallization mechanism.

Figure 2.2 visualizes the respective compositional space studied in each chapter.

Chapter 7 takes up the scientific questions raised in Chapters 4, 5, and 6 and summarizes the main results and the findings on rationalizing the perovskite formation process. Finally, it shows how these initial rationalizations, together with the current development of in-situ metrology, can provide insights into more complex formation process, e.g. quenching by an anti-solvent drop. This rationalization of complex formation processes lays the foundation for process design in solution-based upscaling techniques to achieve high film quality even on a large, industrially relevant scale.

2. Fundamentals

This chapter gives an overview of the relevant properties of metal halide perovskites as an essential basis for understanding this work and the related discussions. First, the material class of metal halide perovskites is introduced with a focus on their crystal structure, their versatile composition in connection with the resulting bandgap tunability, as well as their electronic structure. The second part gives an overview of perovskite research with regard to their bandgap and connected device performance. The relevance of solvent-based fabrication processes, their broad parameter space and the related importance of formation rationalization for reliable process design are discussed. Finally, the fabrication of metal halide perovskite from solution to the final thin-film is described, including the basics regarding their solution chemistry, general formation processes, and possible process engineering.

2.1 Metal Halide Perovskites – A versatile material class

Perovskites, with a stoichiometry of ABX_3, belong to one of the most diverse crystal families in terms of their versatile chemical composition and properties. Today ~2000 different perovskite compositions are known.[1] Their structural template supports a variety of properties, including insulating,[2] semiconducting,[3] and metallic[4] behavior. In 1840, the first oxide-based perovskite, precisely $CaTiO_3$, was found by Rose in the Ural Mountains, today's Russia, and named after the mineralogist Lev Perovski.[5] One of the subclasses in the versatile crystal class of perovskites are the metal halide perovskites, which were first mentioned in literature at the end of the 19th century.[6] In 1978, Weber *et al.*[7] introduced hybrid organic-inorganic metal halide perovskites, with an organic cation on the A^+ site. These hybrid perovskites are an artificially produced material and do not exist in this composition in nature. Chondroudis *et al.*[8] described in 1999 for the first time the semiconducting properties of hybrid organic-inorganic metal halide perovskites, which provide the basis for their current application in a variety of opto-electronic devices. In 2009, Miyasaka *et al.*[9] presented the first solar cell device, based on $MAPbI_3$ and $MAPbBr_3$ as the absorber layer. The application in solar cell devices triggered a real boom in the field of metal halide perovskite research and explains the increased interest in this material class known for ~40 years.

From a crystallographic point, the term *perovskite* is clearly defined. First, a perovskite material must have a stoichiometry of ABX_3. In general, the ionic components can assume different charges, but the sum of the A and B cations must balance the negative charge of the anions X. The class of metal halide perovskites is composed of an organic or inorganic monovalent A^+ site cation, a divalent metal cation B^{2+} and the halide anion X^-. Second, perovskites crystallize in a defined structure. The B^{2+} cation is coordinated by 6 X^- halides, which leads to the formation of $[BX_6]^{4-}$ octahedrons. These octahedrons are connected in an all-corner-sharing 3D network, comparable to the ReO_3-type structure. The A^+ site cation stabilizes this lead-halide framework, sitting in the 12-fold cub-octahedral void.[10] Figure 2.1 illustrates the cubic perovskite structure.
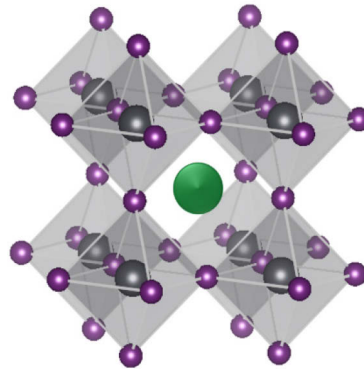
Figure 2.1: Schematic illustration of the cubic perovskite crystal structure. In green the A^+ cation, in black the B^{2+} cations, and in purple the X^- anions are presented.

Whether a particular composition crystallizes in a cubic perovskite structure can be estimated by Goldschmidt's tolerance factor (T_f),[11] which is based on a geometrical concept utilizing ionic radii:

$$T_f = \frac{(r_{A^+} + r_{X^-})}{\sqrt{2}(r_{B^{2+}} + r_{X^-})} \tag{2.1}$$

with r_A^+, r_B^{2+} and r_X^- as the ionic radii of A^+, B^{2+} and X^-. The tolerance factor is a semi-empirical relationship derived from oxide-based perovskites and assumes dense ion packing. Kieslich *et. al.*[12] showed that this geometrical estimation also applies for metal halide perovskites.

In Figure 2.2 the values for the tolerance factor (T_f) for lead-based metal halide perovskites are visualized as a function of X^- halide anions and A^+ cation ion radii. The halide radii are varied from chloride (Cl^-) to bromide (Br^-) and iodide (I^-), while the A^+ cation radii range from caesium (Cs^+) to methyl ammonium (MA^+) and formamidinium (FA^+). Tabulated values from Shannon *et al.*[13] were utilized for the halide radii, while a reduced radius of 1.0 Å is assumed for Pb^{2+}. According to Travis *et al.*[14] the effective cation radius of Pb^{2+} is decreased due to the reduced ionic character of bonds forming with large halides, in contrast to bonds forming with oxides or fluorides.
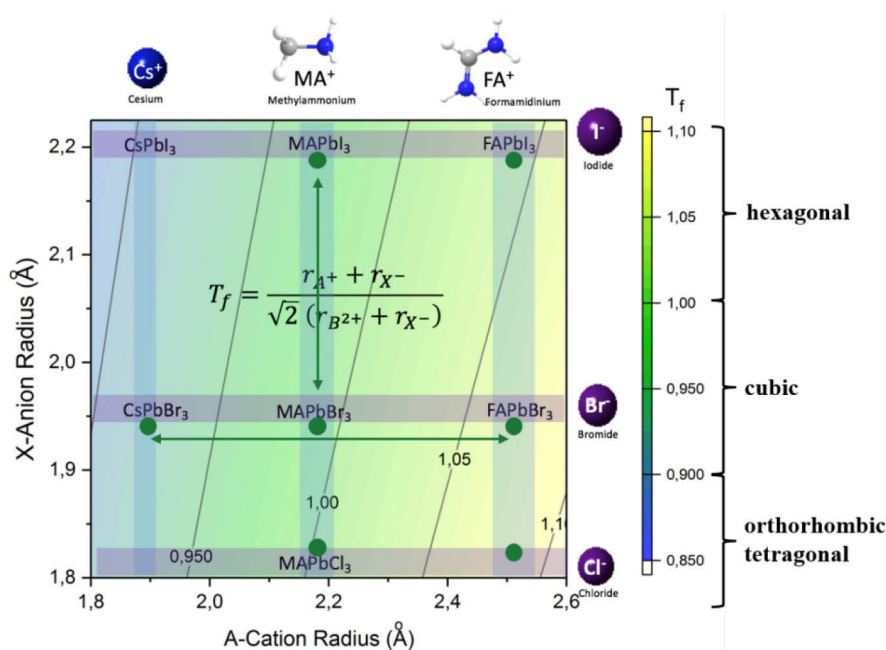
Figure 2.2: Illustration of the compositional space of metal halide perovskites with respect to Goldschmidt´s tolerance factor and preferred crystal symmetries formed. The green dots symbolize the perovskite compositions investigated in Chapter 4, while the vertical arrow visualizes the MAPb(I_xBr_{1-x})$_3$ series and the horizontal arrow the APbBr$_3$ series studied in Chapters 5 and 6, respectively. Adapted from[15].

The perovskite structure can tolerate a certain mismatch in ion radii before another type of structure is form. For a tolerance factor of 0.9 - 1.0 a cubic perovskite crystallizes, which is the ideal structure. At $T_f < 0.9$, the lead-halide octahedral network starts to tilt and distorted perovskite structures in orthorhombic symmetry crystallize. Octahedral tilting can be classified according to Glazer's concept.[16] If the tolerance factor is < 0.7, no perovskite structure is formed anymore. Hexagonal structures with face-sharing octahedrons are preferably formed, when $T_f > 1$.[12,17] In the cubic symmetry all lattice constants are equal (a = b= c) and all angle are 90° ($\alpha = \beta = \gamma = 90°$). Also in the tetragonal and orthorhombic symmetry all three angles are equal to 90°, but the lattice constants change in the tetragonal symmetry to a = b ≠ c and in the orthorhombic one to a ≠ b ≠ c.[10]

The T_f is useful to assume trends in the metal halide perovskite structure. For example, MAPbI$_3$, with a slightly too small radius of MA$^+$, crystallizes at room temperature in the distorted tetragonal

phase. A temperature-dependent phase transition is known for MAPbI$_3$ from the tetragonal, into the cubic phase above 330 K.[18] Additionally, by adding ~15 % of the smaller halide bromide, the crystal structure becomes cubic.[19] In the case of CsPbBr$_3$, the Cs$^+$ is too small, giving a T_f < 0.9. Thus, strong octahedral tilting occurs and CsPbBr$_3$ crystallizes in the orthorhombic phase.[20] On the contrary, the FA$^+$ cation is slightly too large and tolerance values ~1 occur. Thus, the perovskite α-phase of FAPbI$_3$ is meta-stable and transforms in the non-perovskite, yellow δ-phase.[21,22] However, upon mixing, e.g. Cs$^+$ and FA$^+$, stable, cubic perovskites form.[23,24] The possibility of mixing the individual ions, to reduce structural mismatches, opens up a broad compositional space in metal halide perovskites. This is the basis for their bandgap tunability, which opens up a large variety of applications in the field of multi-junction solar cells or lighting emitting devices.

Additional concepts like the octahedral tilting factor have been introduced to postulate stable perovskite structures.[25] A combination of these concepts is applied in machine learning to evaluate possible new compositions for perovskite materials.[1,26]

Although the term perovskite is clearly defined, it is sometimes used misleadingly in the literature, e.g. for Ruddlesden-Popper phases.[27–29] When the word perovskite is utilized in this work, it stands for the metal halide perovskite described here, either in cubic, tetragonal or orthorhombic symmetry.

The bandgap tunability in metal halide perovskites follows Vegard´s law[30] and is based on the variation in the lattice constant. Figure 2.3 presents the bandgap in metal halide perovskites as a function of the pseudo cubic lattice constant a_0. For pure iodide-based perovskites, with a larger pseudo cubic lattice constant ~6.2 Å a bandgap of ~1.5 eV is realized. Exchanging iodide with bromide and chloride decreases the pseudo cubic lattice constant and, thus, the bandgap increases. Chloride-based perovskite materials present a pseudo cubic lattice constant ~5.6 Å and have a bandgap of ~3.0 eV. The bandgap tunability is based on a pure size effect defined by the lead-halide bond distance, represented in the pseudo cubic lattice constant. Alloying iodide and bromide in the MAPb(I$_x$Br$_{1-x}$)$_3$ series tunes the bandgap over the full visible range.[19]
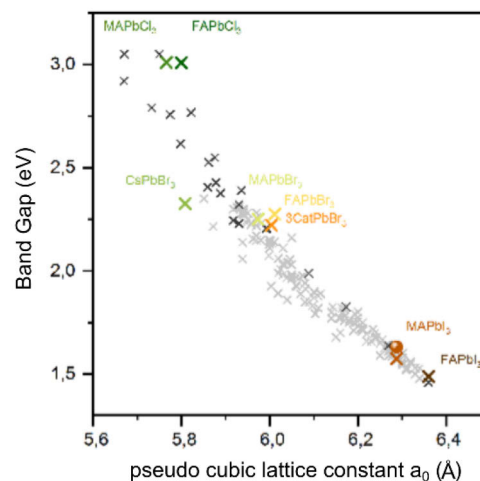

Figure 2.3: Bandgap tuning in metal halide perovskites. The bandgap is plotted as a function of the pseudo cubic lattice constant a_0 from pure chlorides with bandgaps ~3.0 eV to iodides with bandgaps ~1.5 eV.

The lead-halide framework mainly determines the electronic properties in metal halide perovskites. As shown in Figure 2.4 the valance band maximum (VBM) is characterized by an

overlap of the Pb(6s) and I(5p) atomic orbitals. The anti-bonding character of the I(5p) dominates the VBM. In contrast, the minimum of the conduction band (CBM) is dominated by the Pb(6p) orbital. Thus, exchanging halides in terms of bandgap tuning, only slightly affects the position of the CBM. A minor increase in the CBM position is connected to a confinement effect, since the lead-halide distance decreases exchanging iodide with bromide and chloride. For this described halide substitution, the electrons are more confined at the lead atoms and, thus, their energy increases. Contrary, the VBM position is shifted strongly exchanging the halides. Due to the strong increase in the electronegativity going from iodide to chloride, the energy levels of the Br(4p) and Cl(3p) orbitals are positioned at lower energies. Since the halide orbitals dominate the VBM, it shifts downwards accordingly. However, two counter-effects need to be considered. Based on the small contribution of the Pb(6s) orbital to the VBM, the same confinement effect as for the CBM occurs and the hybridization of the lead-halide bond gets stronger exchanging iodide with bromide and chloride. Nevertheless, the strong effect of the electronegativity increase dominates and the VBM is shifted downwards upon ion substitution.[31–33]
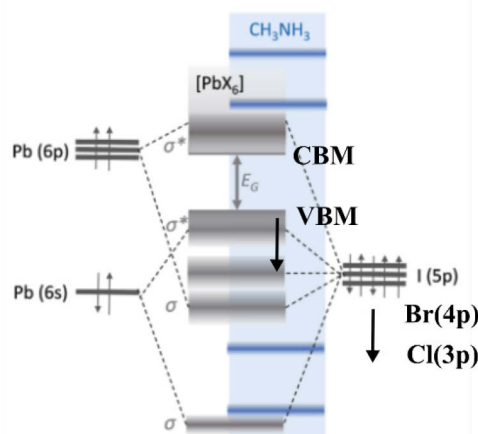
Figure 2.4: Band diagram derived from theoretical calculated band structures adapted from[32,34]. The black arrows indicate the shift of the halide p-orbitals and the related shift in the valence band maximum (VBM) to lower energies. Adapted from[15].

As shown in Figure 2.4, for the case of MA$^+$, the orbitals of the A$^+$ cation are located far away from the CBM and VBM. Thus, they do not take part in the bonding. However, the A$^+$ cation indirectly influences the electronic structure via a structural effect. If the A$^+$ cation is too small, as described in the case of Cs$^+$, the perovskite structure is distorted and the dimensions of the lattice parameters change. This structural deformation results in a lower hybridization between the respective lead-halide orbitals and shifts both, CBM and VBM, downwards. However, the VBM is more affected by the hybridization and, thus, changes stronger due to the A$^+$ cation influence. Increasing the cation radii by substituting Cs$^+$ with MA$^+$ and FA$^+$ the volume of the unit cell increases and the energy levels of the lead atom are lowered, since the confinement effect is reduced. Since the CBM is mostly dominated by the lead states, this effect shifts the CBM mainly upwards. Overall, the effect of de-confinement dominates the shift within the electronic structure, unless the perovskite structure is distorted too much.[31]

Due to the halide substitution from iodide to chloride, the bonding type in the lead-halide framework changes from a covalent to a more ionic character.[35] Based on the shorter lattice distance and resulting higher band curvature in chloride-based perovskites, the effective mass is reduced and electrons are more delocalized. Thus the exciton binding energy increases. Due to the excitonic contribution, the absorption onset does not directly correspond to the optical

bandgap in perovskite materials. Thus, the lattice is more polarizable and electrons are more delocalized. This effect results in an increased exciton binding energy. Due to the strong polarizability, electrons and holes are located in different surroundings in the excited state. The increased exciton binding energy can be identified in high-quality perovskite thin-films as an additional peak at the absorption onset. Exciton binding energies in metal halide perovskites are reported from ~10 - ~100 meV.[36] According to Saha's equation, at "1 sun" excitation density even for exciton binding energies of ~70 meV most charge carriers will be free charges.[37] Thus, the exciton binding energy can be neglected for metal halide perovskites with regard to device performance. However, it can still play a role in e.g. PL dynamics due to a possible concentration change of free charge carriers.

2.2 Performance and Preparation statistics

The following section is based on statistics and trends drained from the Perovskite Database Project.[38] To better utilize the huge amount of research data generated in the perovskite field the Perovskite Database Project was initiated as a communal bottom-up approach where all available device data in the over 17000 perovskite papers published today was extracted. Over 40000 devices have been found and have set up an open database, developed open-sourced protocols, procedures, and a meta-data ontology for reporting perovskite solar cell data. Simple and interactive tools enabling anyone to interactively explore, search, filter, analyze, and visualize the data. The long-term goal of that project is to change how our research data is collectively treated and we hope that all future device data will be shared in this way, which will accelerate future perovskite development. Due to the meta-data ontology, the hereafter-discussed preparation parameters exemplarily demonstrate the versatility beyond device data.

Since the first publication of perovskite solar cells in 2009[9], this research field has developed rapidly within a decade. The data collected and published on perovskite solar cells have been continuously increasing and reached a scientific output of ~10000 data points in 2018 and 2019 (Figure 2.5 (a)). The sudden decline in 2020 is attributed to the fact that at this date only a small percentage of the publications from that year were implemented into the database. Thus, a scientific output comparable to the previous years can be expected. This tremendous increase in perovskite solar cell research can be attributed to its promising potential and at the same time explain the unique increase in power conversion efficiencies, which are now reaching record levels of 25.5 %.[39] Furthermore, the increase in perovskite research is connected to their technically simple and cost-effective, solution-based deposition by spin-coating on a laboratory scale. Thus, perovskite research itself had the advantage to be implemented into existing laboratory facilities and opened directly to a large scientific community.
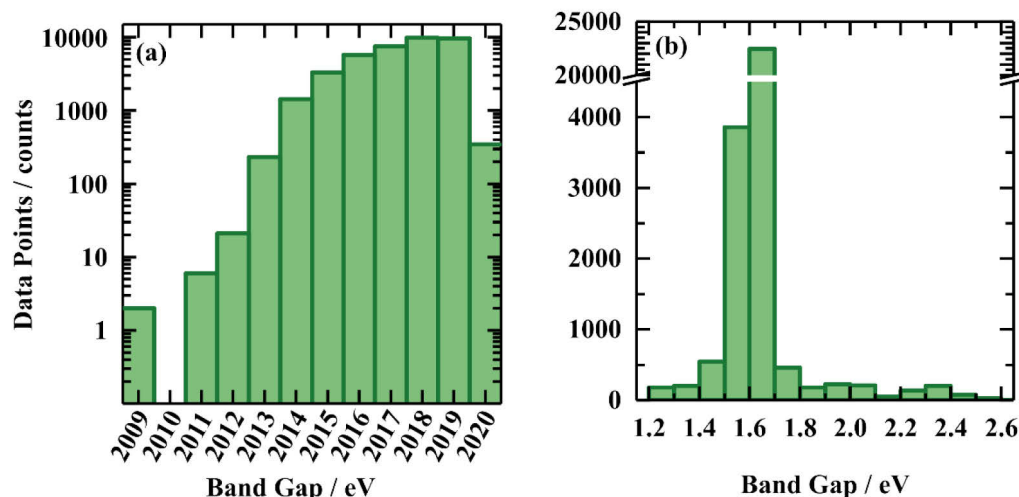
Figure 2.5: Statistics on data points published as a function of publication year (a) and the given bandgap (b).

Comparing the scientific output in terms of the perovskite bandgap (Figure 2.5 (b)), a research focus on metal halide perovskites with a bandgap between 1.5 and 1.7 eV, perfectly fitting for applications in single junction solar cells, is presented. Up to ~30000 data points, corresponding to ~75 %, are published in this sector. For perovskites with a bandgap ≥ 1.7 eV each, only a few hundred data points are available in the literature. However, perovskites with a high bandgap are of interest e.g. for semitransparent tandem applications or LEDs. Overall, this comparison makes clear that research in the field of perovskites is very much driven by their potential application in solar cells and at the same time shows what potential is still available, especially for perovskites with a high bandgap.

When describing the dependencies of the bandgap, it should be kept in mind that it is not straightforward to derive the exact bandgap for perovskites. In the literature, different methods with different quality and reference points are utilized.[40–42] Krückemeier *et al.*[43] recommend deriving the bandgap from the inflection point of the EQE onset. Based on the contribution of the exciton binding energy, the application of a Tauc plot[44] will overestimate the optical bandgap with a growing error for perovskites with high bandgaps. Therefore, a simple Tauc plot should not be utilized for a detailed bandgap analysis in metal halide perovskites.[45] Furthermore, the absorption spectra are highly dependent on the thin-film morphology,[46] which may contribute to an error by flat absorption onsets. Thus, not all bandgap values entered into the database may be precisely defined, but sufficient for these overviews.

Due to the strong focus on perovskite materials with a bandgap ~1.6 eV, preparation routines for materials such $MAPbI_3$ or $Cs_{0.05}(MA_{0.17}FA_{0.83})_{(0.95)}Pb(I_{0.83}Br_{0.17})_3$ are well established in the community and even detailed, reproducible preparation procedures are published.[47] For higher bandgap perovskites such optimized and established recipes are missing, simply because they are less studied. This discrepancy illustrates the main obstacle in this work and for perovskites with high bandgaps in general. First, such reliable recipes for the wide compositional range of perovskites have to be developed and established. The establishment of such recipes for the low bandgap counterparts has taken years and illustrates the amount of work required for such optimizations.
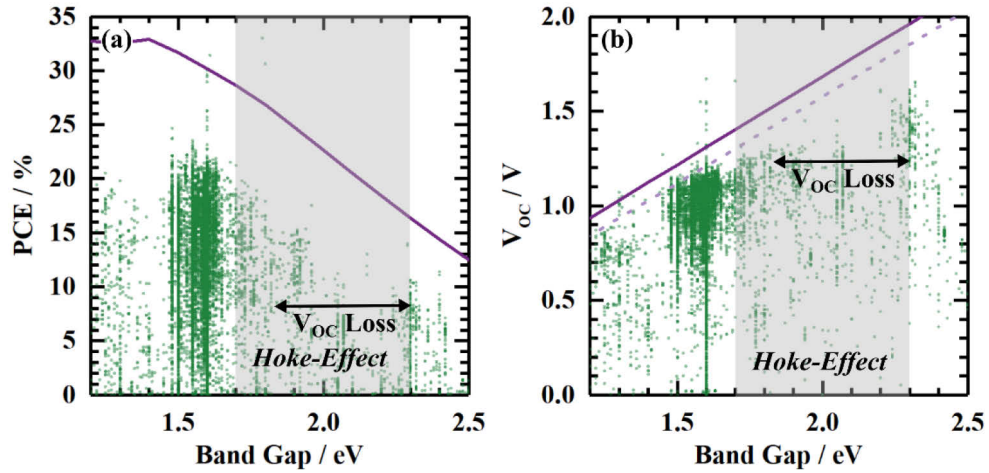
Figure 2.6: Statistics on device characteristics. The PCE (a) and the V_{OC} (b) are given as function of the perovskite bandgap. The purple line represents the theoretical limits in the PCE and the $V_{OC,Max}$, respectively, based on the Shockley-Queisser limits. The dashed purple line in (b) presents the $V_{OC,MPP}$.[48] In both plots, the grey filed region indicates the bandgap region, where the Hoke-Effect might occur and the area of high V_{OC} losses visualized.

A comparison of the device performance versus the bandgap (Figure 2.6 (a)), visualizes the previously discussed trend of focused research on bandgaps ~ 1.6 eV. In this area of the bandgap, a large number of devices achieve an adequate performance ~20 % and the V_{OC}s (Figure 2.6 (b)) approaching to theoretical limits. Record efficiencies ~ 25% stand out, but some data points in this high efficiency range should be considered carefully. They themselves or their V_{OC}s are located above the theoretical limit[49] and indicate errors of some kind. For devices utilizing perovskites with bandgaps from 1.8 to 2.3 eV, there are still significant losses in device performance, defined mainly by losses in the V_{OC} (Figure 2.6 (b)). One reason for this is of course lower research effort that has been discussed for these high bandgap materials.

However, there are a number of factors playing a role in V_{OC} losses in particular. First, contact layers are highly optimized for solar cell devices with bandgaps ~1.6 eV.[50] Due to a shift in the bands, a simple transfer of contact layers into high bandgap devices induces a band offset and reduces the V_{OC}. Since mainly the valance band shifts due to bandgap tuning, especially the hole contact layers need to be adjusted. Second, a poor morphology with pinholes favors losses due to shunts.[51] The morphology can be improved by fabrication optimization. In addition, the pure bromide-based perovskite face the problem of mid-gap defects[52] limiting the V_{OC}. Their nature must be understood in order to eliminate them either by adapted preparation routines or by passivation.[53] For mixed halide perovskites with bandgaps from $1.7 - 2.2$ eV the phenomenon of light-induced phase segregation, also known as the *Hoke-Effect,*[54] plays a role in V_{OC} losses. Under illumination, mixed halide perovskites segregate into iodide- and bromide-rich phases. Various mechanisms are suggested in the literature to explain the phenomenon of light-induced phase segregation.[55–58] The lower bandgap, iodide-rich domains forming are responsible for losses in the V_{OC}.

Figure 2.7 visualizes statistics on selected preparation features. Such meta-data is available in the database and, thus, provides information and connections far beyond device performance. In total 97 % of the data points are assigned to perovskites that were deposited from solution. This underlines the importance of this remarkable characteristic of perovskites for semiconductor preparation. Evaporation represents an alternative preparation route from solids.[59]

From the database, 176 different preparation procedures could be identified used to deposit the perovskite thin-film. These include combinations and sequences of two or more individual deposition techniques, e.g. evaporation and spin-coating[60], 2-step spin-coating[61], and spin- and spray-coating[62] of the perovskite layer. However, spin-coating stands out as the main preparation technique for perovskite thin-films (Figure 2.7 (b)). 68 % of the thin-films are produced by conventional 1-step spin-coating and further 24 % by spin-coating as the main preparation step, only 8 % of perovskite layers are produced e.g. by printing techniques[63], spray-coating[64], or evaporation[65] and do not use spin-coating at all. Thus, solution-based spin-coating is currently the standard technique for the deposition of perovskite layers. However, spin-coating will not serve on a large industrial scale. Efforts should therefore be made to rationalize the preparation of spin-coating to transfer established and new routines to the upscaling techniques.
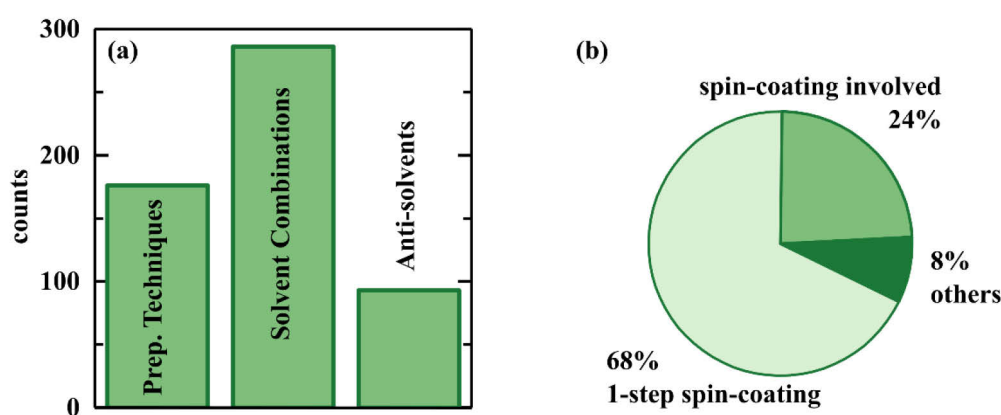
Figure 2.7: Statistics on perovskite preparation techniques and parameters. In (a) the number of different preparation techniques, solvent combinations, and anti-solvents is visualized. (b) presents the shares of spin-coating in perovskite preparation techniques.

The database identifies 40 different characteristics for precursors, solution preparation, and perovskite deposition, including e.g. solvents, anti-solvents, additives, their respective ratios, and annealing parameters. These features do not yet include parameters such as spin speed and time. Each parameter opens up a new space with many possibilities for optimizing perovskite preparation. As an example, 286 solvent and 93 anti-solvent combinations are utilized in literature so far (Figure 2.7 (a)). This brief insight already shows how many possible and optimizable preparation parameters are available. On one hand, this gives the possibility to fabricate high-quality perovskite thin-films over the entire compositional range, but on the other hand, it also represents an obstacle. Even with a structured but still blind trial-and-error optimization of preparation parameters, it is not possible to work through all parameters for every composition. This correlation makes clear how important it is to understand and rationalize formation processes in metal halide perovskites to narrow down process parameters in a meaningful way and to be able to develop a targeted way of process design.

2.3 From the precursor solution to the final thin-film

A unique feature of metal halide perovskites is their solution-based processability, which makes them easily accessible for laboratory research. The possibility to fabricate perovskites via solution-based processes opens unique opportunities for upscaling based on printing techniques such as inkjet printing, slot-die coating, or roll-to-roll processes. Such low-cost fabrication processes distinguish metal halide perovskites from conventional inorganic semiconductors.

In principle, the perovskite preparation on a laboratory scale involves three steps: solution preparation - spin-coating - annealing. However, the microstructure and the opto-electronic quality of the perovskite thin-film highly depends on the crystallization behavior during the process. Complex solution chemistry and process parameters predetermine the crystallization behavior and, thus, present a point of process engineering.

As precursor materials, in the simplest case, the direct organic/inorganic-halide (AX) and lead-halide (BX_2) salts are dissolved in polar, aprotic solvents.[66] The maximal solubility of the precursors is determined by the choice of solvent. The solubility in aqueous solutions is overall low and decreases from $PbCl_2$ to PbI_2.[67,68] Thus, Lewis-base solvents, such as dimethyl formamide (DMF), dimethyl sulfoxide (DMSO), or γ-butyrolactone (GBL) are utilized since the solubility of lead-halide salts is typically high and can reach concentrations over 1 M. In solution, the Lewis-base competes with the halide to coordinate the lead cation.[69] For a stronger Lewis-base, the formation of a solvent adduct is favored in comparison to the lead-halide bond due to its enthalpy advantage. Overall, the caesium-halide salts have low solubility, due to their strong ionic bonding character. The solubility limit of CsBr is ~0.25 M in pure DMSO, for CsBr/$PbBr_2$ mixtures in DMSO the solubility limit is increased to ~0.5 M.[70] Thus, the concentration of Cs^+ cation in perovskite solutions is limited and explains why those films cannot be deposited from commonly high concentrated precursor solutions.

Figure 2.8 gives an overview of the different lead-halide-complexes with an assumed octahedral coordination of $[PbX_x(S)_{6-x}]^{(x-2)-}$ (1 - 7) and colloids that can form in solution. These complexes are in a chemical equilibrium with each other and higher coordinated lead-halide complexes form with an increase in the halide concentration. Stevenson *et. al.*[71] postulate that the real geometry of the lead-halide-solvent would be likely eight- or nine-coordinated due to the stereoactivity of the lone pair (8).

The halidoplumbates, $[PbX_3(S)_3]^-$ and $[PbX_4(S)_2]^{2-}$, are identified in perovskite solutions in DMF and DMSO, and serve as ideal building blocks for the perovskite structure.[72–74] The addition of organic-halide salts to the solution shifts the chemical equilibrium to higher coordinated lead-halide complexes.[72] In general, the equilibrium between those species is determined by the solution concentration, the bonding strength of the specific halide and the solvent utilized. In higher concentrated solutions, colloidal or chain-like poly-nuclear species form (9 - 11), stabilized by hydrogen bonding with the methyl ammonium cations. Those poly-nuclear chains remind of the crystalline solvate phases identified by Cao *et. al.*[75].
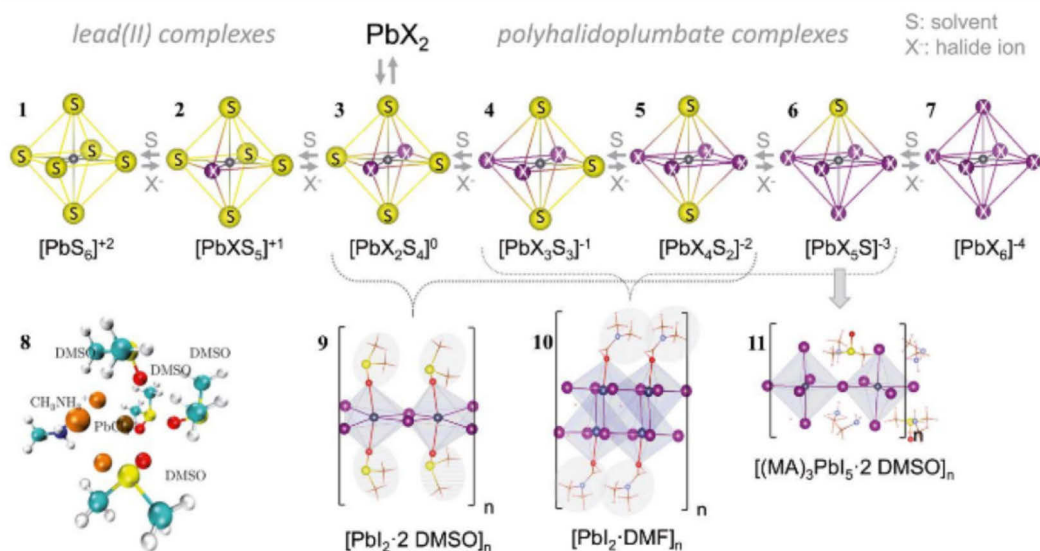
Figure 2.8: Overview of the equilibrium between lead-halide complexes with Lewis-base solvent (S) forming various Pb(II) complexes of $[PbS_{6-x}X_x]^{2-x}$, according to Rahimnejad *et al.*[72] (1-7). Simplified octahedral solvent–lead–halide complexes are presented. This visualization was chosen to relate features in solution complexes with crystalline lead-halide materials. However, steric effects of the stereoactive Pb(II) lone pair are ignored. A more realistic solution complex structure is one calculated by Stevenson *et al.*[71] for the $[MA^+][PbCl_3]^-\cdot 4DMSO$ complex (8). Crystal structures of PbI_2–solvent complexes forming polymeric lead–halide chains, reported by Cao *et. al.*[75], are presented in (9 - 11). Adopted from [15].

Those polymer-like chain structures of $[PbI_2\cdot 2\,DMSO]_n$ (9) and $[PbI_2\cdot DMF]_n$ (10) can be derived from the octahedral building blocks. In solutions, also containing AX salts, corner-sharing pentahalidoplumbates $[(MA)_3PbI_5\cdot 2\,DMSO]_n$ (11) exist. This described complex chemistry of building blocks defines intermediate stages and the crystallization behavior during perovskite formation, thus, influencing the overall final film quality in terms of e.g. composition and morphology. For a more detailed understanding of the solution chemistry of metal halide perovskites, detailed studies are required, but beyond the scope of this work.

Petrov *et al.*[76] identified stable crystalline solvate phases of $[(MA)_2(DMF)_2Pb_2I_6]$, $[(MA)_2(DMF)_2Pb_3I_8]$, and $[(MA)_3(DMF)PbI_5]$ (Figure 2.6), which form as an intermediate step in the formation of $MAPbI_3$ from solution during spin-coating. They are formed preferentially, since they have lower formation enthalpies than $MAPbI_3$.[76,77] Due to their needle-like morphology, those solvate phases have a strong templating effect on the film morphology and prevent the formation of smooth homogeneous films. Only upon annealing, the residual solvent molecules evaporate and the $MAPbI_3$ perovskite forms.
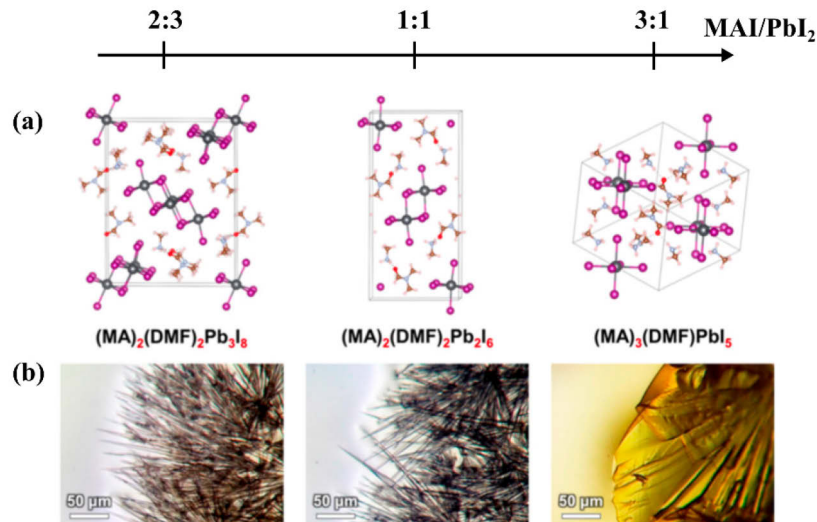
Figure 2.9: Stable MAI-PbI$_2$-DMF solvates phases, with their exact compositions depending on the precursor ratio. (a) visualizes the refined crystal structure, while (b) shows photographs of the needle-like crystals forming. Adapted with permission from[76]. Copyright 2017 American Chemical Society.

Figure 2.10 (a) illustrates the formation of a perovskite film using a weakly coordinating solvent like DMF during coating and annealing. During coating or drying a high amount of intermediate solvate phase, e.g. [(MA)$_2$(DMF)$_2$Pb$_3$I$_8$], crystallizes and co-exists with lead-halide complexes in the wet-film. Due to the templating effect and the intermediate step a disordered, low-quality perovskite film forms during annealing. To prevent such an unfavorable crystallization behavior, process engineering is a suitable way to control and dictate the formation of perovskites and, thus, end up in high-quality films.

Next to solvent engineering,[78] sequential deposition,[79] and the utilization of spectator ions[80] as parameters to engineer the deposition process, quenching by dropping an anti-solvent during spin-coating has emerged as one of the most used strategies. Thus, the nucleation and crystallization is controlled (Figure 2.10 (b)). The anti-solvent induces crystallization since it preferably dissolves the constituent solution solvents but does not dissolve the perovskite. Thus, seed crystals form at the top of the wet-film due to oversaturation by removing a substantial amount of solvent. By induced crystallization of the perovskite, the formation of intermediate phases is suppressed and an ordered, high-quality film grows from the seed crystals during annealing. Besides dropping an anti-solvent the process can also be quenched by gas or heat.[15]

(a) equimolar (weakly coordinating solvent)

coating/drying | annealing

solvate phase, Pb-X complexes | ABX$_3$ (disordered)

(b) solvent-engineering and rapid quenching

coating | *quenching (anti-solvent, gas, heat)* | annealing

solvate | *seed crystals* | ABX$_3$ perovskite
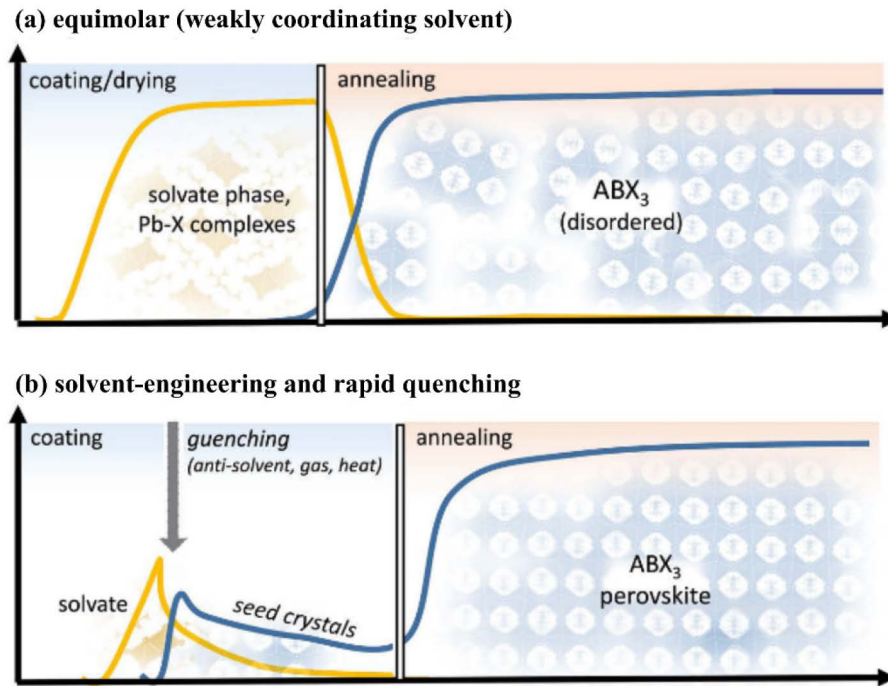
Figure 2.10: Schematic illustration of (a) an equimolar and (b) a solvent-engineered solution-based perovskite thin-film deposition including rapid quenching. The reaction mechanisms are captured from various experimental findings and are deliberately presented in a generic way to allow the categorization of different processing approaches. Adapted from[15].

Although several ways of process engineering are introduced and known to influence the formation process, a detailed understanding on a chemical level from the precursor solution to the final film is missing, especially for compositions beyond pure iodide perovskites. Thus, the herein introduced in-situ spectroscopy will act as an eye on the fabrication of perovskites and allow evaluating and rationalizing characteristic formation steps during the perovskite deposition.

3. Materials and General Sample Preparation

3.1 Materials

Table 3.1 lists the metal halide perovskite precursors and additional chemicals used in this work, with their chemical formula, supplier and purity. For organic solvents, the molecular structure is included. All precursors and other chemicals were stored and used inside N_2 filled gloveboxes.

Table 3.1: Metal halide perovskite precursors and additional chemicals used in this work.

	Substance	Chemical Formula	Molecular Structure	Supplier	Purity
precursor salt	lead(II) iodide	PbI_2	-	TCI (Tokyo Chemical Industry)	>98 %, 99.99 % trace metals basis
	lead(II) bromide	$PbBr_2$	-	TCI	>98 %
	lead(II) chloride	$PbCl_2$	-	TCI	-
	methyl ammonium iodide	$(CH_3NH_3)I$	-	dyenamo	99.99 % trace elements basis, anhydrous
	methyl ammonium bromide	$(CH_3NH_3)Br$	-	dyenamo	99.99 % trace elements basis, anhydrous
	methyl ammonium chloride	$(CH_3NH_3)Cl$	-	dyenamo	99.99 % trace elements basis, anhydrous
	formamidinium iodide	$(CH(NH_2)_2)I$	-	dyenamo	99.99 % trace elements basis, anhydrous
	formamidinium bromide	$(CH(NH_2)_2)Br$	-	GreatCellSolar	>99 %
	formamidinium chloride	$(CH(NH_2)_2)Cl$	-	GreatCellSolar	>99 %
	caesium bromide	$CsBr$	-	abcr	99.999 % metals basis
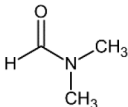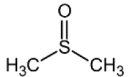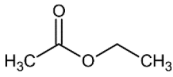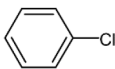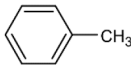
solvent	dimethyl formamide	C$_3$H$_7$NO		Sigma-Aldrich	99.8 %, anhydrous
	dimethyl sulfoxide	C$_2$H$_6$OS		Sigma-Aldrich	≥ 99.9 %, anhydrous
anti-solvent	ethyl acetate	C4H8O2		Sigma-Aldrich	99.8 %, anhydrous
	chlorobenzene	C$_6$H$_5$Cl		Sigma-Aldrich	99.8 %, anhydrous
	toluene	C$_7$H$_8$		Sigma-Aldrich	99.8 %, anhydrous

Table 3.2 lists the substrates employed for perovskite thin-film deposition. All substrates have a size of 2.54 x 2.54 cm^2.

Table 3.2: Substrates used in this work.

Substrate	supplier	specifications
Soda lime glass	VWR	Microscope slides
Corning glass	Corning Incorporated	Corning EAGLE XG
ITO covered substrates	Automatic Research	R = 15 Ω/sq.

The substrate type was chosen depending on the specific measurement carried out. Since corning glass has minimum interaction with light over a wide range of wavelength, this substrate was employed for sensitive optical measurements in Chapter 4. While soda lime glass was used for formation studies in Chapters 5 and 6, ITO substrates were utilized as a conductive substrate for surface photovoltage (SPV) measurements in Chapter 6.

3.2 Sample Preparation

The following section introduces the general sample preparation conditions and steps, including the overall procedure for the metal halide perovskite thin-film deposition used in this work. In contrast, Chapters 4.3, 5.3 and 6.2 precisely describe the particular preparation parameters for the discussed samples and formation processes. This separation shall be made since the detailed preparation parameters have an enormous influence on the formation process and the final sample quality, additionally affected by differences in the perovskite composition.

Substrate Cleaning – All substrates were cleaned consecutively for 10 min with an alkaline detergent, acetone and isopropanol in an ultrasonic bath (GeneralSonic D4). Subsequently, the substrates were dried via a N$_2$ flow and, directly before layer deposition, chemically cleaned by exposing them to O$_3$-plasma (FHR UVOH 150 LAB) for 20 min.

Any other preparation steps were carried out within N_2 filled gloveboxes (H_2O < 0.1 ppm, O_2 < 0.1 ppm, MBraun 200B (Eco)), if not explicitly described otherwise.

Solution Preparation – First, stock solutions of the respective lead-halide (PbX_2) salts were weighed, dissolved and shaken at 60 °C in a thermal shaker (CellMedia TS·basic) overnight. After cooling down to room temperature, the PbX_2 stock solutions were mixed accordingly with the respective organic or inorganic halide salt (AX), shaken again for at least 3 h at 60 °C, and cooled down before thin-film preparation. To realize different halide ratios, appropriate proportions from single halide precursor solutions were mixed at least 30 min before layer deposition. In general, precursor solutions were always prepared fresh, more precisely, at most one day before perovskite preparation.

Metal halide perovskite thin-film preparation – After blowing of possible residual dust particles with a N_2 gun, 60 µL of solution were dropped on the static substrate, followed by starting the spin-coating process, where necessary an anti-solvent was dropped during the spin-coating. The perovskite thin-films were prepared utilizing an MBraun SC-210 spin-coater. Subsequently, the films were annealed on a Präzitherm PZ28-2 hotplate to complete the thin-film preparation process.

Chapters 4.3, 5.3 and 6.2 comprise a detailed, tabulated description of the respective solution compositions and preparation parameters for the spin-coating and annealing steps.

Metal Evaporation – For in-situ formation measurements an Ag mirror was evaporated on the backside of soda lime glass substrates to increase the transflectance signal. About 100 nm of Ag were thermally evaporated at a base pressure of 10^{-6} mbar with an evaporation rate of 1.5 - 2.0 Å/s using an MBraun ProVap T5 or CreaVac Creament 350 MEV.

3.3 Methods

If not stated otherwise, all measurements were carried out under ambient conditions.

Scanning Electron Microscopy (SEM) - SEM images were taken on a Hitachi S4100 with a cold field emitter and an acceleration voltage of 5 kV.

UV-vis Spectroscopy (UV-vis) - UV-vis measurements on perovskite thin-films were realized with a Lambda1050 system from PerkinElmer in a standard transmission mode and within an Ulbricht sphere, hereafter referred to as in-sphere mode. In contrast, UV-vis measurements on the precursor solutions were carried out on a Cary 5000 UV-Vis-NIR from Agilent utilizing demountable cuvettes from Hellma Analytics (type 106-QS) with quartz glass windows permeable from 200 – 2500 nm and a path length of 10 (± 3.0) µm.

In-situ spectroscopy (in-situ UV-vis and in-situ PL) - Optical in-situ characterization during the perovskite formation was carried out with a home-built set-up described in detail in Chapter 5.2.

Photoluminescence Microscopy (PLmic) – PLmic measurements were performed on a home-built inverted set-up (Olympus IX-71 body) with a 415 nm excitation (Thorlabs M415F3) and an objective from Olympus (LUCPlanFL 40, NA 0.6). Emission spectra were collected utilizing a fiber-optic spectrometer (Ocean Optics Flame FLMS12200).

Photoluminescence Quantum Yield (PLQY) - PLQY measurements were carried out in a home-built integrating sphere with 415 nm excitation (Thorlabs M415F3) at 30mW/cm^2, establishing 1 sun equivalent illumination conditions. The measurements consists of two consecutive measurements. First, the excitation without sample is measured (I_0) and second the remainder of the excitation (I_r) and the emission (I_{PL}), now with the sample mounted, is measured with a fiber-coupled spectrometer (OceanOptics, QEPro). By comparing absorbed vs. emitted photons, the PLQY is calculated as:

$$PLQY = \frac{I_{PL}}{(I_0 - I_r)} \tag{3.1}$$

The system is calibrated before measurements with a calibration lamp (Avantes AvaLight-CAL(-Mini)).

Ellipsometry – Ellipsometry measurements were carried out on a Sentech SE850 DUV variable angle spectroscopic ellipsometer with a spectral range from 190 - 2500 nm to determine the dielectric properties (*n, k*) of the perovskite thin-films. With micro spots the measurement area was reduced to ~ 1 mm^2 and measurements were performed at 50°, 60°, and 70° angles.

Surface Photovoltage (SPV) – Modulated SPV spectra were performed on a home-built set-up in the configuration of a parallel plate capacitor, composed of a quartz cylinder partially coated with an FTO electrode and a mica sheet as an insulator. Thin-film samples were mounted under ambient atmosphere; however, measurements were carried out under inert atmosphere. The change in surface potential upon illumination defines the SPV signal. As a light source, a white light halogen lamp, coupled to a quartz prism monochromator (SPM2), is implemented. The excitation light is modulated at a frequency of 8 Hz by an optical chopper. SPV signals were detected with a high-impedance buffer and a double phase lock-in amplifier (EG&G 5210). For defect sensitive measurements a LP filter at 610 nm was mounted behind the monochromator.

X-ray diffraction (XRD): XRD measurements were carried out on a Bruker Advanced D8 in Bragg-Brentano geometry with a CuKα X-ray source (λ = 1.5406 Å).

Small Angle X-ray Scattering (SAXS): SAXS data were measured at the four crystal monochromator beamline in the PTB (Physikalisch-Technische Bundesanstalt) laboratory at BESSYII.[81] The sample to detector distance is variable without breaking the vacuum due to an adjustable about 3 m long support structure with a long edge-welded bellow.[82] A Dectris 1M PILATUS2 in-vacuum hybrid-pixel detector collets the two-dimensional scattering images. The measurements were carried out at energies of 10 keV and 8 keV, and two distances of 0.8 m and 3.7 m, respectively, thus, a *q*-range from 0.02 - 8.5 nm^{-1} was covered. The sample exposure time was set to 600 s with two repetitions for the short and three for the long distance. 0.1 mm thin, rectangular borosilicate cuvettes (CM Scientific, UK) were utilized due to the low transmittance of the lead containing perovskite precursor solutions. The BerSAS software[83] was utilized for data reduction in radial averaging into the 1D pattern.

Rheology - Dynamic viscosity was measured with an Automated Micro Viscometer (AMVn) from Anton Paar. A cleaned capillary (∅ = 1.6 mm) was filled under ambient conditions with the sample solution and a stainless steel ball (ρ = 7.62 g cm^{-3}; ∅ = 1.5 mm). The capillary was set to an angle of 70° with respect to the horizon and each measurement was carried out with four repetitions at 20°C. Refractive indices were measured with an Abbé refractometer from Krüss. To obtain the density of the solutions, the mass of a specific volume (100 µL) was determined by a precision scale.

4. Process optimization for bandgap tuning of metal halide perovskites and consequential structure-property correlations

The combination of bandgap tunabilty by ion substitution and the possibility of solution-based processing is a unique feature of semiconducting metal halide perovskites, which makes them interesting for application in opto-electronic devices. However, these applications require a high thin-film quality, which strongly depends on the perovskite preparation.

This chapter presents a definition of high sample quality in terms of structure, morphology, and optical properties and describes its relevance for reliable property determination. The importance of optimizing the formation process, which enables the deposition of high-quality layers, is emphasized. In the case of perovskites, the ideal preparation parameters strongly depend on their exact composition. Therefore, the preparation parameters in $APbX_3$ perovskites are optimized over the broad compositional space. The structural, optical, and opto-electronic properties of these high-quality bandgap tuned films are described and their dependence on the ion composition is discussed.

Overall, a strong correlation between composition, fabrication process, and the resulting final film properties in bandgap tuned metal halide perovskites is shown. Understanding and rationalizing the detailed film formation processes is highlighted as a key step to achieve target-orientated process design.

4.1 Introduction

A unique advantage of metal halide perovskite semiconductors with the chemical formula $APbX_3$ is the bandgap tunability upon cation (A^+) and anion (X^-) substitution[19,24,84–90], hence, being of interest as an active layer in a multitude of thin-film based opto-electronic devices.[50,91–96] Perovskites with a bandgap of around 1.6 to 1.7 eV are currently being investigated based on their applicability in single and multi-junction solar cells (Chapters 2.1 and 2.2).[97–99] This chapter will cover the precursor-process-property correlation for the full bandgap range from 1.6 to 3.0 eV of metal halide perovskites ranging in their composition from $APbI_3$ to $APbCl_3$.

Since the lead-halide crystal lattice primarily defines the structural dimension of perovskites using bromide or chloride instead of iodide results in a reduction of lattice parameters due to decreasing halide radii. Reduced lattice parameters mean a smaller unit cell and, therefore, the ideal cation radius fitting in the cuboctahedral void shrinks. The A^+ cations, likewise depending on their respective ionic radii, either stabilize, tilt or destabilize the ReO_3-type lead-halide lattice.[11,12,16,100] The lead-halide lattice is the main determining factor of the electronic structure. Thus, halide substitution likewise modifies the electronic structure through different electronegativity, bonding types, and orbital overlap.[31,35,101] For that reason, structural, optical, and opto-electronic properties are interconnected in metal halide perovskites and consequently change with one another during ion substitution. Furthermore, the intrinsic difference in the precursor's chemical nature influences the solution-based preparation process, and thereon fabrication predetermines the overall thin-film quality. Therefore, material characteristics and preparation are closely interwoven.
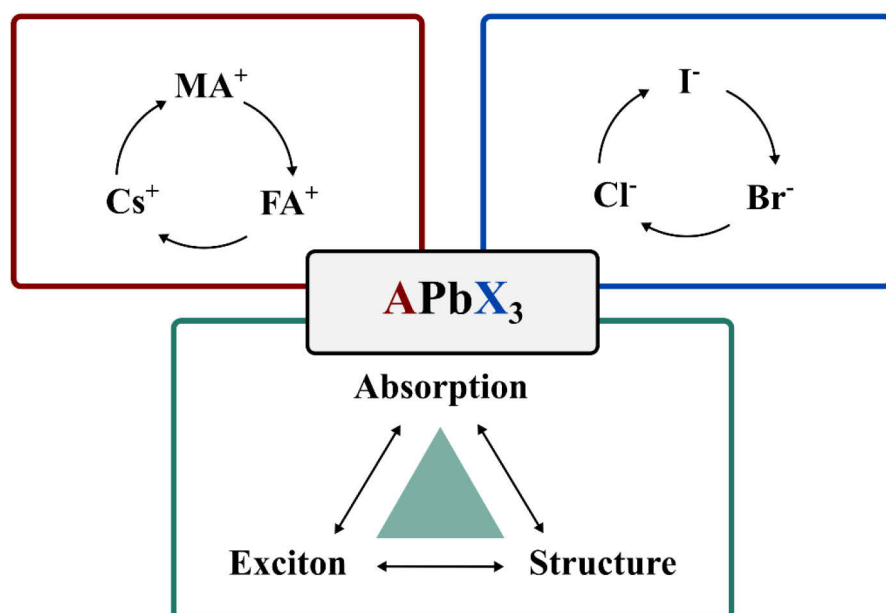
Figure 4.1: Schematic overview of selected cations A^+ (red) and anions X^- (blue) for ion substitution in the $APbX_3$ perovskite structure and the correlation of structural, optical, and opto-electronic properties (green) in metal halide perovskite.

This chapter provides comprehensive insights into the metal halide perovskite semiconductors that can be made through ionic substitution, though limited to single cation and halide combinations (Figure 4.1), combined with the rationalization and importance of material and layer optimization for each individual composition. The first part of this chapter presents the analysis

of structural, morphological, optical, and opto-electronic metal halide perovskite properties allying XRD, SEM, and UV-vis measurements, thereto including and discussing criteria and importance of high sample quality. The second part demonstrates the experimental preparation optimization and related parameters resulting in high-quality films required for detailed material analysis and the correlation of structural, optical, and opto-electronic properties. For each individual perovskite composition, the preparation parameters need to be re-optimized due to the strong correlation between precursors and the fabrication process. Finally, this chapter compares metal halide perovskite properties for different ionic compositions. Individually, both structural, optical, and opto-electronic properties are discussed and trends are reasoned based on the respective ion composition. By applying Elliot´s formula, the exciton binding energy (E_B), as an opto-electronic property, is derived from absorption measurements.[102,103] The absorption onset and the optical bandgap are distinguishable via the determined excitonic contribution. Altogether, the strong interconnection of the triangle precursor-process-property in metal halide perovskites is demonstrated.

4.2 Perovskite thin-film characterization techniques and sample quality standards

The herein studied metal halide perovskites are prepared from precursor solutions by commonly used spin-coating and subsequent annealing. The optical, structural, and electronic analysis of the resulting thin-film are determined by the properties of the sample. The film and sample quality influences the performed measurements and, therefore, the derived material properties. It is important to point out, that optimizing and controlling film preparation is key to high-quality samples and reliable determination of metal halide perovskite properties in thin-films. Optimizing the preparation parameters will be discussed in Chapter 4.3, whereas Chapters 5 and 6 focus on understanding and rationalizing detailed aspects in the perovskite formation process via spin-coating and annealing.

Following, this chapter introduces XRD, SEM, and UV-vis for perovskite sample analysis, combined with a detailed definition of different sample quality levels, and discusses their importance for reliable material property determination in metal halide perovskite thin-films.

For structural analysis, XRD measurements were carried out. Lab-based XRD measurements provide macroscopic information about the crystalline phases in terms of their space group, which constitute the sample. Besides the requested perovskite phase, XRD analysis identifies secondary phases formed during preparation or residual precursor materials, strain, and homogeneity in the thin-film.
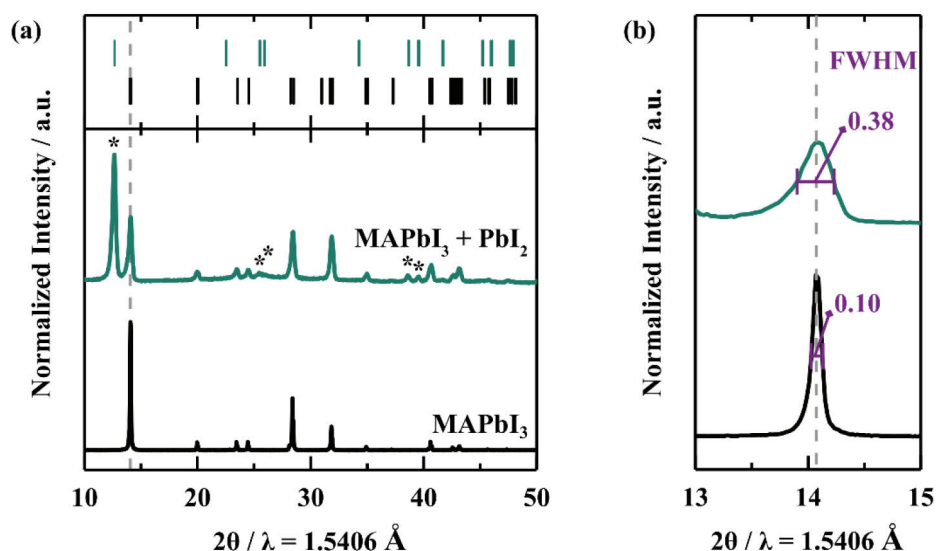
Figure 4.2 Structural differentiation of high- and low-quality perovskite thin-film samples. (a) XRD patterns presenting a phase pure, high-quality MAPbI₃ film (black) and a low-quality MAPbI₃ film (green) with residual phase impurities of PbI₂ labeled with asterisks. In the upper section, MAPbI₃ (black) and PbI₂ (green) reference pattern from[104,105] are present. The grey dashed line marks the position of the 110 MAPbI₃ reflection at 2θ = 14.1. (b) Zoom in on the 110 MAPbI₃ reflection. The grey dashed line indicates the reflection position and the orange horizontal bar the FWHM for both samples, respectively.

In this study, a phase pure perovskite thin-film without additional phases indicates a high sample quality. In contrast, the occurrence of multiple phases in the XRD pattern characterizes a low structural sample quality. Figure 4.2 (a) represents an optimized, phase pure MAPbI₃ (black) thin-film with reflections at 2θ = 14.1, 20.0, 23.5, 24.5, 28.4, and 31.9 assigned to the 110, 112 and 200, 211, 202, 220, and 310 lattice plains. The reflections of the 112 and 200 lattice plain merge in the peak at 2θ = 20.0. Furthermore, reflections with low intensities at higher 2θ angles indicate perovskite lattice symmetries of higher orders. Comparing the high-quality MAPbI₃ film (black) to an non-optimized, low-quality one (green), additional reflections at 2θ = 12.6, 25.6, 38.6, and 39.5, marked with asterisks, are identified and attributed to crystalline PbI₂ as a secondary phase introducing a material impurity.

Figure 4.2 (b) displays the FWHM of the 110 MAPbI₃ reflection at 2θ = 14.1 for both, the low- and high-quality film. Comparing the FWHM, the phase pure MAPbI₃ (black) presents a narrow FWHM of 0.10. In contrast, the phase impure MAPbI₃ (green) exhibits a broadened FWHM of 0.38. This broadened peak width indicates defective MAPbI₃ crystallites in terms of strain and disorder. An instrumental influence on the peak broadening and comparable parameters is negligible since measurements were carried out on the same diffractometer. Therefore, the peak broadening originates from the sample itself.

While characteristics of different crystal structures are distinguishable in XRD, impurities affect the hereafter-discussed results. Therefore, properties derived from structural low-quality thin-films belong rather to the particular sample than the perovskite material itself. Only single-phase perovskite systems enable the determination of specific optical and opto-electronic material properties. Therefore, one objective in this study is the preparation of bandgap tuned, phase pure perovskite thin-films via process optimization.

Morphological changes on the microscopic scale and, thus, film coverage and thickness can be determined by SEM imaging. For reliable absorption measurements, with a high absorption and

a low scattering, pinhole free and low-roughness films are needed, which are also favorable for opto-electronic devices.

In UV-vis measurements, thin-film morphology alongside set-up configurations affects spectra accuracy, as discussed herein. Determining the exciton binding energy (E_B) and the optical bandgap (E_g) requires accurate absorption spectra.

MAPbBr$_3$ thin film sample with low quality

(a) Standard measurement
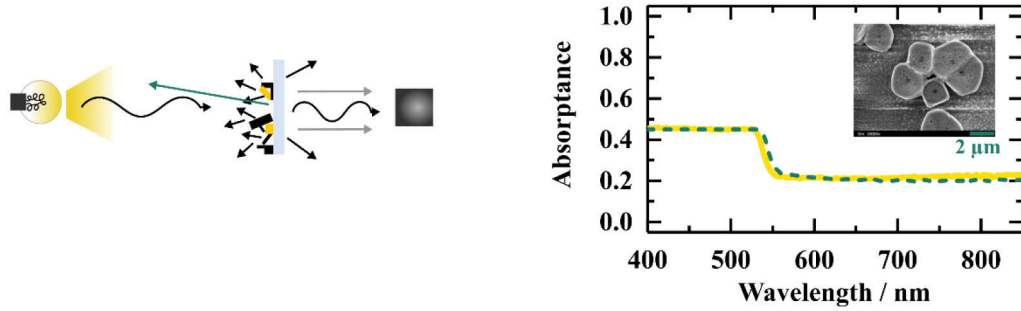
(b) In-sphere measurement

Figure 4.3: Comparison of absorption data of a low-quality MAPbBr$_3$ film concerning the set-up configuration, (a) standard, linear assembly in transmission mode and (b) in-sphere assembly. For (a) and (b), an illustration of the measurement with sample-light interaction is shown on the left and the resulting spectrum on the right. The dashed green line in (a) presents a calculated spectrum from equation 4.3. The SEM picture illustrates well the low morphological quality due to poor coverage caused by individual crystallites.

Figure 4.3 compares the absorption spectra acquired from standard transmission and in-sphere measurements on a low-quality MAPbBr$_3$ sample, characterized by high scattering and poor absorption. The standard transmission mode (Figure 4.3 (a)) relies on the internal transmittance (T); energy loss is described by absorption only and, therefore, is defined as the quotient of the attenuated light intensity after passing a medium (I_t) and the incident light (I_0):

$$T = \frac{I_t}{I_0} \tag{4.1}$$

The spectra are shown in absorptance, defined as:

$$A = 1 - T \tag{4.2}$$

For the standard transmission mode (Figure 4.3 (a)), a step-like, featureless shape above the band edge at 550 nm and a high background characterizes the absorption spectrum. As displayed in Figure 4.3 (a) on the left, the rough film surface causes increased light scattering. Due to the linear geometry, scattered light is not detected, simulating high transmittance and, therefore, resulting in a high background at long wavelengths as a pure measurement artifact. Because of the low substrate coverage, light passing through uncovered sample parts undergoes no absorption by the MAPbBr$_3$ film, artificially lowering the transmittance above the band edge, resulting in a step-like, featureless shape vanishing absorption details. The dashed green line represents an absorption spectrum calculated taking the degree of coverage and scattering into account, details are discussed later in this chapter.

In contrast, the in-sphere mode (Figure 4.3 (b)) determines the total transmittance considering scattering and reflection besides absorption. In the in-sphere mode, the sample is placed within the Ulbricht sphere at a small angle, thus, scattered (I_{sct}) and reflected (I_{R}) light is guided along with the transmitted light and detected, thus, avoiding an artificial increase in the transmittance. For this reason, the in-sphere mode corrects for high scattering and reduces the background. Nevertheless, a very slight increase in the background at longer wavelength is detected as an artifact and might be explained by higher scattering at longer wavelengths. However, the step-like, featureless absorption remains due to an overall low transmittance of the sample. Hence, in-sphere measurements although correcting for scattering, still require high sample coverage in order to measure precise absorption features.

Figure 4.4 presents a standard, linear transmission and an in-sphere measurement on a high-quality MAPbBr$_3$ film, illustrating changed sample-light interaction (left) and the respective resulting absorption spectra (right). Optimizing the MAPbBr$_3$ preparation parameter yields a film of high morphological quality with high coverage and a smooth surface as can be seen in the SEM image inset. The smooth surface decreases light scattering significantly and simultaneously increases the amount of light potentially undergoing absorption, which is additionally increased by the high coverage (Figure 4.4 (a)). Due to increased transmittance, absorption features, like an excitonic peak directly located at the band edge (highlighted in the figure by a green backdrop) and an increase in absorption at shorter wavelength, are detected, revealing a feature-rich absorption spectrum above the band edge. Nevertheless, scattering and reflection still occur and increase the background at long wavelengths. For high-quality samples, reflection dominates the background, resulting in a wave-shaped baseline.

Hence, measurements in in-sphere mode (Figure 4.4 (b)), improve spectra accuracy for optimized films as well by accounting for scattering and reflection, providing a reduced background. In addition, absorption features above the band edge at 550 nm get more pronounced when accounting for scattered light. These accurate absorption spectra enable fitting the exciton binding energy applying Elliot´s formula (Chapter 4.4.2). Thus, the determination of optical and opto-electronic material properties requires optimizing both, perovskite thin-film preparation and optical measurement geometry. In this case, sample properties match with the material properties.

MAPbBr$_3$ thin film sample with high quality
(a) Standard measurement

(b) In-sphere measurement
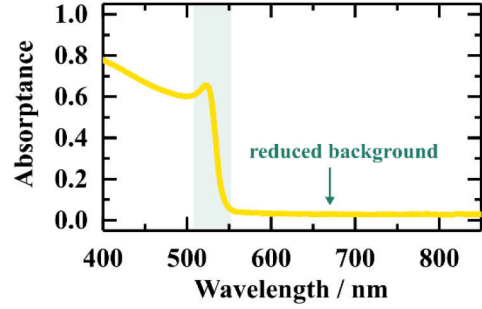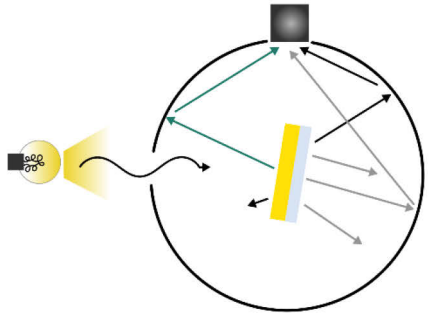
incident light (I_0)   transmitted light (I_t)
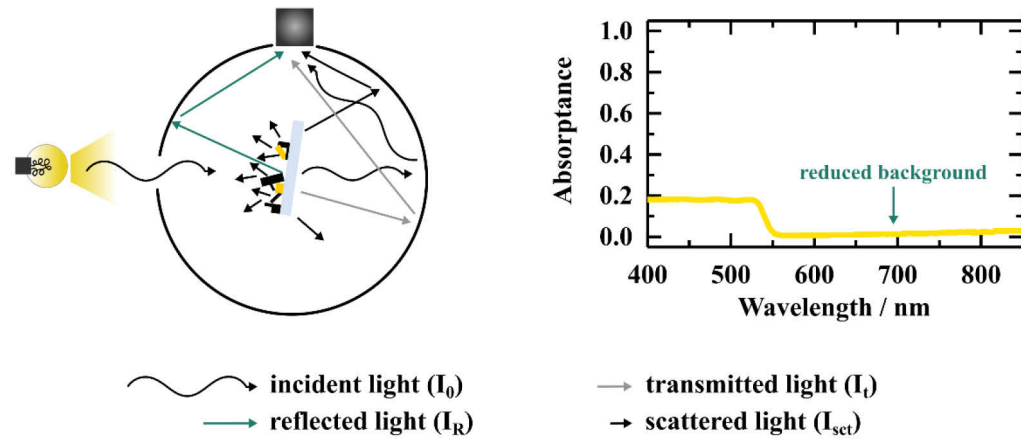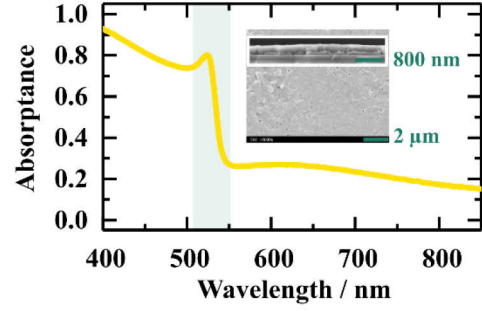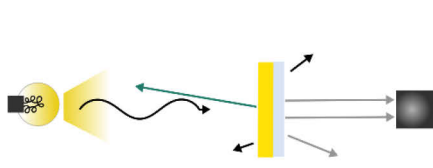reflected light (I_R)   scattered light (I_{sct})

Figure 4.4: Comparison of absorption data of a high-quality MAPbBr$_3$ film with regard to the set-up configuration, (a) standard, linear assembly in transmission mode and (b) an in-sphere assembly. In each case, on the left an illustration of the measurements with sample-light interaction and on the right side the resulting spectrum is shown. The excitonic peak at the absorption onset of both spectra is highlighted in green. The SEM picture indicates the high optical quality due to a high coverage and a smooth surface.

To investigate the respective influence of coverage β and the scattering γ on the shape of the absorption spectra, hypothetical spectra for the standard transmission mode in a linear geometry are calculated by:

$$I_t = I_0\beta\left[\left(1 - \gamma(\lambda)\right)10^{\alpha(\lambda)d} + I_0(1 - \beta)\right] \qquad (4.3)$$

where I_t is the intensity of internal transmitted light, I_0 is the intensity of incident light, $\alpha(\lambda)$ is the wavelength dependent absorption coefficent and d is the film thickness.[46] From the high-quality optical absorption measurement, presented in Figure 4.4, $\alpha(\lambda)$ is estimated by[106]:

$$I_t = I_0 e^{-\alpha(\lambda)d} \qquad (4.4)$$

From the SEM cross section (Figure 4.4) the film thickness is determined, $d = 270$ nm. The thus calculated absorption coefficient is presented in Figure A.1.1.

To simplify the spectra calculation the scattering γ is assumed to be constant over all wavelengths. Figure 4.5 demonstrates calculated absorption spectra via equation 4.3 for a MAPbBr$_3$ thin-film with a thickness of 270 nm assuming different amounts of (a) coverage β and (b) scattering γ due to changing sample quality.
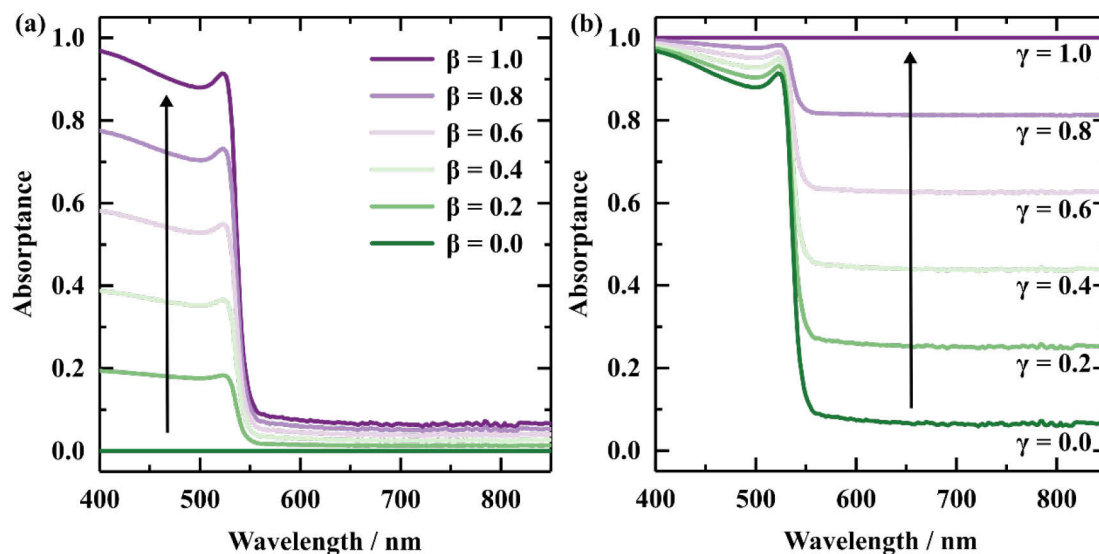
Figure 4.5: Calculated absorption spectra for MAPbBr₃ thin-films with a thickness of 270 nm accounting for different thin-film qualities by applying equation 4.3. (a) Spectra assuming no scattering ($\gamma = 0$) with varying degrees of sample coverage included by changing β and (b) spectra assuming full coverage ($\beta = 1$) with varying degrees of light scattering due to sample roughness included by changing γ.

Assuming no scattering ($\gamma = 0$) and at the same time increasing the coverage β results in an overall higher absorption above the band edge and pronounces simultaneous absorption features, such as the excitonic contribution at the absorption edge at 550 nm and a stronger absorption at shorter wavelength (Figure 4.5 (a)). This illustrates again the importance of high coverage for richly informative absorption spectra. On the other hand, assuming full coverage ($\beta = 1$) and varying the amount of scattered light increases the background at longer wavelength. Although full coverage is assumed to result in a high absorptance, the ratio between absorbed and scattered light decreases and absorption features vanish. Thus, both criteria, reduced scattering and increased absorption, achieved by ensuring a smooth surface and high coverage, must be met to enable the measurement and analysis of detailed absorption features. Additionally, the film thickness influences the characteristics of the absorption spectrum (Figure A.1.2). For thick films with high coverage, absorption features above the band edge vanish due to high absorption. However, the threshold is around 1 μm and samples in this work show a thickness of around several hundred nanometers. Consequently, the film thickness is automatically in an acceptable range for accurate absorption measurements. Once again, this points to the importance of sample optimization by careful preparation control in order to obtain reliable thin-film material properties.

Equation 4.3 allows the estimation of the coverage β and scattering γ of the low-quality film presented in Figure 4.3 (a). The fitting employs the absorption coefficient $\alpha(\lambda)$ derived from the high-quality film and a crystal thickness of 1500 nm, determined from the SEM cross section (Figure A.1.3). In Figure 4.3 (a) the green dashed line presents the calculated spectrum, defining a coverage of $\beta = 0.45$ and a scattering of $\gamma = 0.2$. With a small deviation, this value corresponds well with the 40% coverage calculated from the SEM image in Figure 4.3. Hence, thin-film coverage and scattering can be estimated via equation 4.3 from absorption measurements.

In conclusion, the properties of a perovskite thin-film sample do not necessarily correspond to the perovskite material properties. This is the case solely for thin-film samples with thin-films optimized structural and morphological features. Caution should be used when generalizing and comparing perovskite properties derived from samples varying in quality. Thin-film preparation

has a major influence on sample and material quality. Thus, the first milestone in this study is the elaborate optimization of preparation parameters, before deriving material properties from perovskite thin-film samples.

4.3 Optimizing preparation parameters for solution-based bandgap tuning in metal halide perovskites

As previously discussed, optimizing sample preparation is key to high-quality metal halide perovskite thin-films, necessary for the determination and correlation of the individual material characteristics in account of ion substitution.
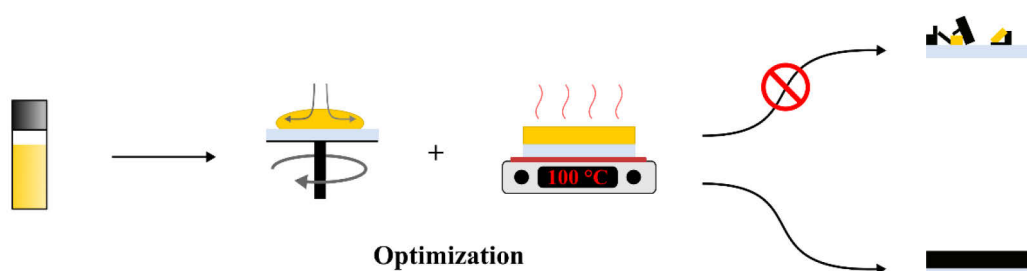

Figure 4.6: Schematic of thin-film preparation process from solution over spin-coating and annealing. Spin-coating and annealing parameters influence the overall film quality, optimizing and controlling these steps avoids the formation of low-quality films (top) and favors high-quality films (bottom).

While Chapter 3 details general fabrication details, hereafter, the experimental and optimization steps for bandgap tuning are described. In general, every preparation step, independently of precursor selection, is optimizable. A wide parameter space for each ABX_3 composition opens up by carefully considering solvent composition, spin-coating, anti-solvent dripping, and annealing. To narrow down possible optimization parameters, precursor salts are limited to the respective AX and PbX_2 variants, while excluding spectator ions or additives. Fixing the solution concentration to 1.2 M and the solvent system to 4:1 DMF:DMSO, justified by their widespread use in the perovskite community, additionally limits the parameter space. For this solution composition, spin-coating parameters, such as spin speed and time, and anti-solvent choice and drop time, were optimized. Based on precursor solubility, solvent evaporation rates and potential intermediates, the perovskite formation pathway and the crystallization kinetics change for each perovskite composition. Therefore, spin-coating parameters must be tailored precisely in each case and cannot be taken over upon bandgap tuning, to obtain high-quality films.

Figure 4.7 describes the influence of the anti-solvent drop time on the final film quality of $MAPbBr_3$ exemplary for all other optimizable process parameters. All thin-films were spin-coated from the same 1.2 M $MAPbBr_3$ stock solution (1:1 $MABr:PbBr_2$) at 4000 rpm for 60 s and annealed at 100 °C for 30 min. Only the anti-solvent drop of 150 µL toluene was varied in time from no anti-solvent drop to drop times at 10 s, 20 s, and 30 s within the spin-coating process.
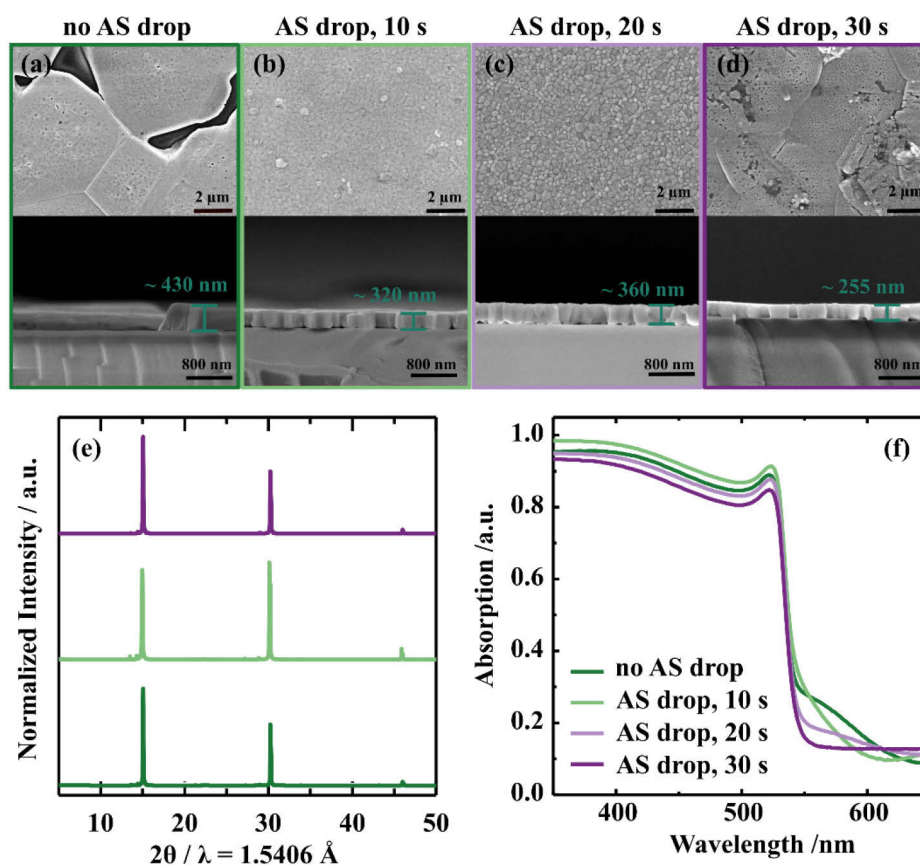
Figure 4.7: Influence of the anti-solvent drop time on the final thin-film quality of MAPbBr₃ exemplary for all optimizable process parameters. Beside the anti-solvent drop time, all process parameters were maintained constant. (a), (b), (c), and (d) present the SEM images (top) and cross section (bottom) with the film thickness for no anti-solvent drop, an anti-solvent drop after 10 s, 20 s, and 30 s, respectively. (e) and (f) display the corresponding XRD patterns and UV-vis spectra.

A difference in the film morphology is clearly identifiable from the SEM images (Figure 4.7 (a) - (d)) in relation to the anti-solvent drop time. While the MAPbBr₃ film prepared setting no anti-solvent drop shows deep holes between individual grains (Figure 4.7 (a)), all three films prepared with an anti-solvent drop are pinhole-free. Additionally, the grain size within the films differs significantly. Grains with a size of several micrometers, in parts bigger than 10 μm, occur in films without an anti-solvent drop and with one set at 30 s. In contrast, films prepared with the anti-solvent dropped at 10 s show no clear boundaries between individual grains. Furthermore, dropping the anti-solvent at 20 s results in a large number of small-sized grains around several 100 nm that are close connected but clearly differentiable by grain boundaries. Beside the morphology, setting an anti-solvent drop influences the film thickness as well, which is evident from the SEM cross sections. Dropping no anti-solvent results in a more floes-like morphology and a film thickness of ~ 430 nm (Figure 4.7 (a), bottom). In general, an anti-solvent drop generates films with continuous grains throughout the film and reduces the film thickness (Figure 4.7 (b)-(d), bottom). Film thicknesses of 320 nm, 360 nm, and 255 nm are measured for anti-solvent drops at 10 s, 20 s, and 30 s respectively. This detailed look into the morphology emphasizes the importance of setting an anti-solvent drop at an appropriate time to achieve pinhole-free, smooth films.

Although the morphology differs with the anti-solvent drop, XRD measurements (Figure 4.7 (e)) for samples with no anti-solvent drop and one after 10 s and after 30 s indicate the formation of

phase pure $MAPbBr_3$ films with similar FWHMs of 0.1. However, the 200 reflection at $2\theta = 30.2$ is more pronounced for the film prepared with an anti-solvent drop at 10 s than in the other two films. This indicates a modified preferred grain orientation in this thin-film. Due to the high film coverage arising from the solvent mixture of 4:1 DMF:DMSO the UV-vis spectra of all sample present detailed absorption features, such as an excitonic peak at the band edge at 550 nm and an increased absorption at shorter wavelengths. However, directly below the bandgap from 550 – 600 nm samples show differences in the background due to reflection and scattering.

This example demonstrates that small changes in the thin-film preparation influence the final film quality drastically and emphasizes the challenge of process optimization for different compositions. Furthermore, it underlines the importance of detailed preparation description for all parameters to ensure reproducibility and to enable the comparison of perovskite thin-film samples.

Table 4.1 lists the optimized spin-coating parameters in addition to details on solution preparation and annealing for all perovskite compositions discussed in Chapter 4.4. While the preparation parameters for all MA^+ and FA^+-based halide compositions were optimized, those for the inorganic Cs^+-based perovskites are limited to $CsPbBr_3$ for two reasons: one is the instability of the $CsPbI_3$ perovskite phase due to the Goldschmidt tolerance factor deviation upon ion radii mismatch (Chapter 2.1); the other, the fact that the comparatively low solubility of Cs-halide salts in organic solvents prevents solution-based preparation of $CsPbCl_3$ and only allows preparing a 0.4 M solution of $CsPbBr_3$ in DMSO.

Optimizing these parameters required preparing hundreds of samples. This motivated a rationalization of perovskite preparation by understanding the thin-film formation process, which is explored in Chapters 5 and 6.

Table 4.1: Solution characteristics, optimized spin-coating and annealing parameters for bandgap tuned metal halide perovskite thin-films analyzed and discussed in Chapter 4.4.

Solution	Precursor ratio	Concentration / mol L^{-1}	Solvent	Spin speed / rpm, Spin time / s	Anti-solvent, drop time / s	Annealing Temp. / °C, time / min
MAPbI$_3$	MAI:PbI$_2$ 1:1	1.2	4:1 DMF:DMSO	4000, 30	500 µL EtAc, 30	100, 30
MAPbBr$_3$	MABr:PbBr$_2$ 1:1	1.2	4:1 DMF:DMSO	2000, 40	150 µL Tol, 15	100, 30
MAPbCl$_3$	MACl:PbCl$_2$ 1:1	1.2	4:1 DMF:DMSO	1000 | 5000, 10 | 60	150 µL CBZ, 30	100, 30
FAPbI$_3$	FAI:PbI$_2$ 1:1	1.2	4:1 DMF:DMSO	1000 | 5000, 10 | 60	150 µL CBZ, 40	100, 30
FAPbBr$_3$	FABr:PbBr$_2$ 1:1	1.2	4:1 DMF:DMSO	1000 | 5000, 10 | 60	150 µL CBZ, 15	100, 30
FAPbCl$_3$	FACl:PbCl$_2$ 1:1	1.2	4:1 DMF:DMSO	1000 | 5000, 10 | 60	150 µL CBZ, 40	100, 30
CsPbBr$_3$	CsBr:PbBr$_2$ 1:1	0.4	DMSO	1000 | 4000, 10 | 30	150 µL Tol, 35	100, 30
3CatPbBr$_3$	(MABr:FABr:CsBr):PbBr$_2$ (0.1:0.85:0.05):1	1.2	7:3 DMF:DMSO	1000 | 4500, 10 | 20	500 µL Tol, 17	50|100, 2|5

4.4 Perovskite thin-film characteristics upon bandgap tuning

Following, structural, optical, and opto-electronic properties of bandgap tuned perovskites thin-film are discussed based on optimized, high-quality samples. Changes and trends herein are set in a precursor-property relationship.

4.4.1 Structural properties

Figure 4.8 (a) presents an overview of the MAPbX$_3$ series XRD pattern and labels occurring peaks with the corresponding lattice plane. All three samples crystallize, based on the optimization of their preparation, in the desired pure perovskite phase.[18] The direct comparison of the MAPbX$_3$ series demonstrates the change from the tetragonal crystal symmetry in MAPbI$_3$, to the higher symmetric cubic one in MAPbBr$_3$ and MAPbCl$_3$, as expected from Goldschmidt´s tolerance factor. In the case of MAPbI$_3$, the MA$^+$ cation is slightly too small to stabilize the ideal cubic perovskite structure and causes the distortion of the lead-iodide framework into the tetragonal symmetry. In the case of MAPbBr$_3$ and MAPbCl$_3$, such a mismatch of ion radii does not occur. Thus, both compositions crystallize in the ideal cubic structure.

Looking at the overview of the FAPbX$_3$ series (Figure 4.8 (b)), additional peaks marked with asterisks indicate the presence of the non-perovskite, hexagonal δ-FAPbI$_3$ phase,[21] beside the cubic perovskite α-FAPbI$_3$ phase[22] in this sample. Due to the mismatch in ion radii based on the FA$^+$ cation being slightly too big, the α-FAPbI$_3$ phase is meta-stable and re-organizes in the stable, yellow δ-FAPbI$_3$ phase over time at room temperature, accelerated by air exposure. Through the use of additives, the black α-FAPbI$_3$ can be stabilized.[107,108] In spite of the mismatch in ionic radii, a cubic perovskite structure is formed for FAPbBr$_3$ and FAPbCl$_3$. In the case of FAPbBr$_3$, additional reflections represent the 110, 210, 211, and 220 lattice plains and indicate a lower orientation of the individual grains within the thin-film.
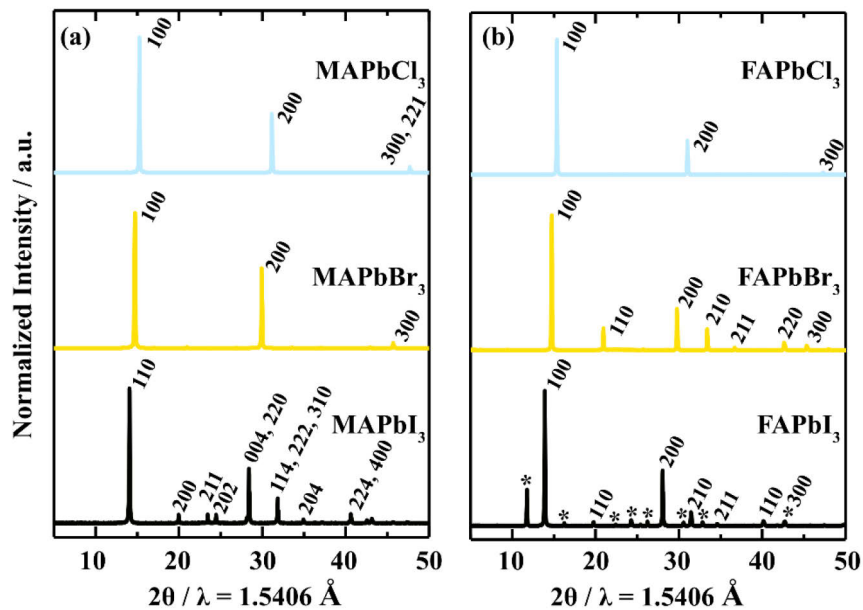

Figure 4.8: XRD pattern of the MAPbX$_3$ (a) and the FAPbX$_3$ (b) thin-film series with substituted halides, X = I, Br, and Cl.

The exact peak position of the main perovskite reflection, corresponding either to the 110 or 100 lattice plain, presents a shift for both, the MAPbX$_3$ and the FAPbX$_3$ series (Figure 4.9 (a) and (b)). By exchanging iodide with bromide and chloride, the peak position moves from $2\theta \sim 14.0°$ to $\sim 15.3°$. The shift in the peak position is based on a size effect. Due to smaller ion radii, the unit cell and connected cell parameters become smaller and result in reflections shifted to higher 2θ.
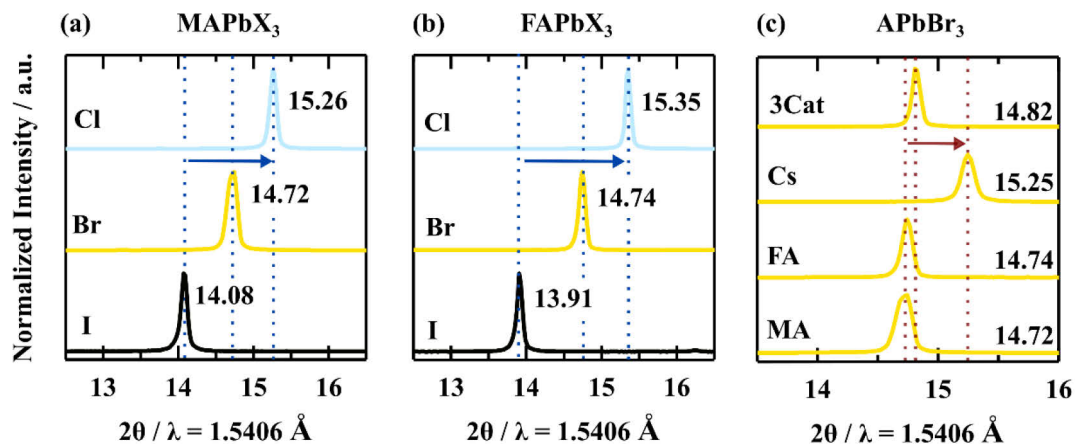

Figure 4.9: Zoom-in on main perovskite peaks (110 resp. 100) presenting shifts due to halide substitution (a) and (b) in the MAPbX$_3$ and the FAPbX$_3$ series, respectively, and cation substitution (c) in the APbBr$_3$ series.

Exchanging the cations in the APbBr$_3$ series (Figure 4.9 (c)), demonstrates no peak shift between the MAPbBr$_3$ and the FAPbBr$_3$ perovskite thin-film, with reflections at $2\theta = 14.72$ and 14.74, respectively. However, for the CsPbBr$_3$ the main reflection shifts to $2\theta = 15.25$. The Cs$^+$ cation is too small to stabilize a cubic perovskite structure for CsPbBr$_3$. The structure is distorted by octahedral tilting and CsPbBr$_3$ crystallizes in the orthorhombic phase with reduced lattice parameters.[20] These reduced lattice parameters explain the shift to higher 2θ in the case of CsPbBr$_3$. Due to the main impact of the organic cations MA$^+$ and FA$^+$, the mixed cation sample, 3Cat, presents only a slight shift to $2\theta = 14.82$.

Based on Bragg´s equation the *d* spacing, corresponding to the distance between two lattice planes (Figure 4.10 (a)) can be estimated in a cubic structure by:[10]

$$d_{hkl} = \frac{a_0}{\sqrt{h^2 + k^2 + l^2}} \tag{4.5}$$

where a_0 is the lattice constant and *hkl* are the Laue indices of the respective lattice plane. Figure 4.10 (b) presents the *d* spacing with regard to the halide composition. As expected, the *d* spacing reduces with a decreased ionic radius of the implemented halide. Thus, the *d* spacing descriptively presents the size effect of the halides on the lead-halide framework, acting as a template for the perovskite structure.
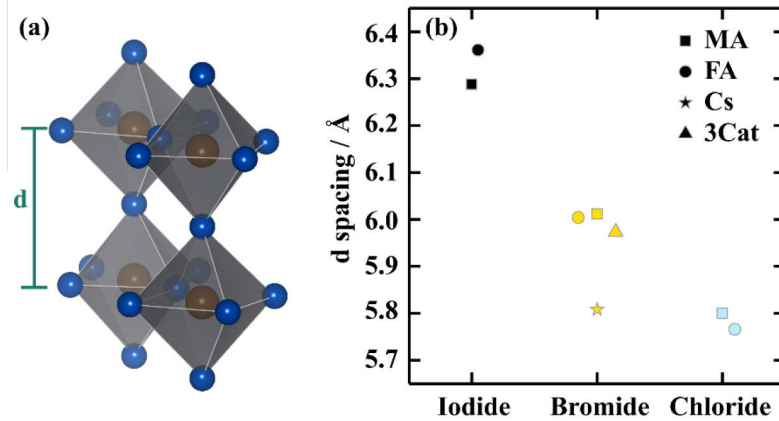
Figure 4.10: *d* **spacing, illustrated as the distance between two lead cations (brown) in two stacked octahedral (a), is presented as a function of the halide composition (b).**

The *d* spacing mainly depends on the halide ionic radii and less on the cation ones. In the case of $CsPbBr_3$, the spacing is given with 5.8 Å and deviates from the other bromide-based perovskites. Due to the strong octahedral tilting in orthorhombic $CsPbBr_3$, the here utilized estimation of the *d* spacing, as a pseudo cubic lattice constant, is not accurate. In the orthorhombic structure, all three lattice constants differ from each other. A LeBail fitting[109] will result in precise spacing parameters. However, such an analysis is out of the scope of this study.

The brief comparison of the structural parameters within a wide composition space of metal halide perovskites illustrates the impact of the ionic radii and their interplay on the exact structure formed. Thus, a strong correlation between composition and properties, here in terms of structure, is described in metal halide perovskites.

4.4.2 Optical and opto-electronic properties

As discussed in Chapter 4.2, the accuracy of absorption measurements strongly rest on their high morphological quality. Thus, a high-quality thin-film morphology over the investigated compositional space is a precondition to detect and evaluate the exciton binding energy (E_B).

Figure 4.11 presents the absorption spectra for the $MAPbX_3$ (a), $FAPbX_3$ (b), and the $APbBr_3$ (c) series with the excitonic contribution fitted by Elliot´s formula.[103] According to the bandgap, the absorption onset shifts with the substitution of the halides (Table A.1.1). For $MAPbI_3$ the absorption starts at 850 nm and for the $MAPbCl_3$ at 420 nm, exemplarily. Comparing the absorption onset in all three perovskite series, confirm a major influence of the halide and a minor one of the cation on the shift in the absorption onset.
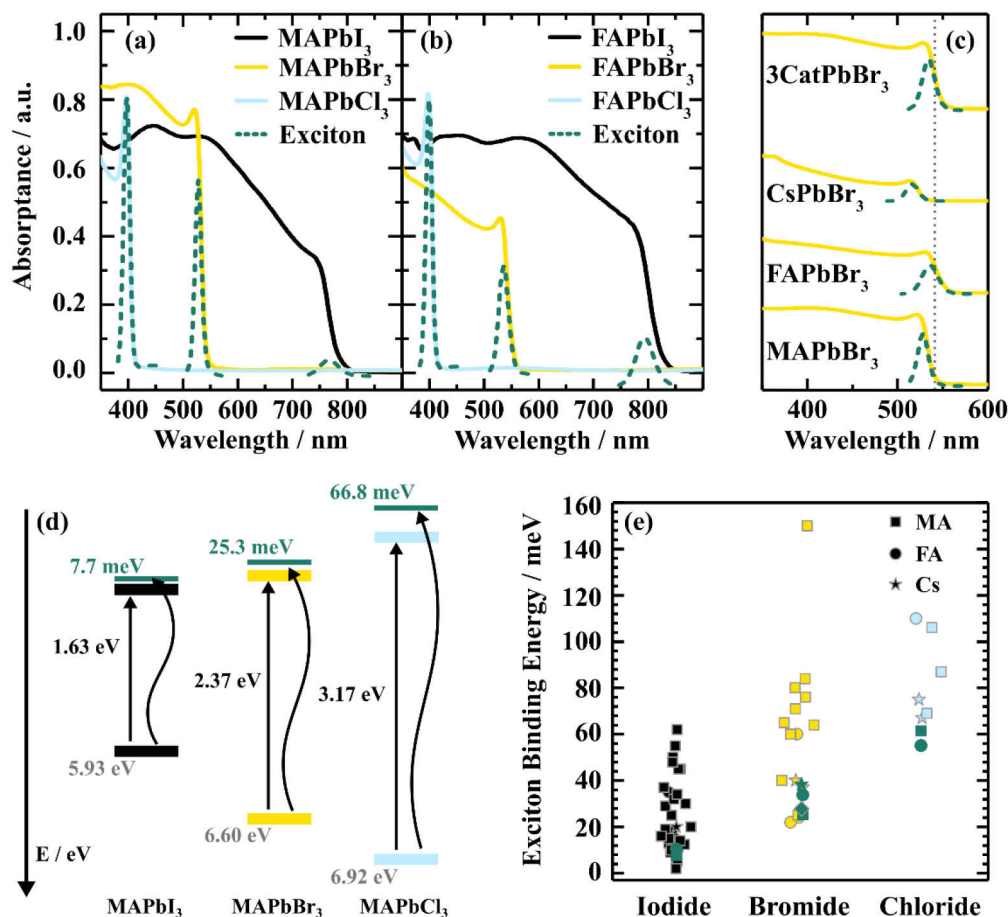
Figure 4.11: Optical and opto-electronic properties for bandgap tuned metal halide perovskites. The absorption onset and fitted excitonic contributions are compared for the MAPbX₃ and FAPbX₃ series, with X = I, Br, and Cl (a) and (b) and the APbBr₃ series, with A = MA, FA, Cs and 3Cat mixture (c). The band alignment in the MAPbX₃ series is illustrated in (d). The valence band maximum is taken from Tao et. al.[31]. The optical bandgap is derived from the absorption measurements (straight line), resulting in an estimated conduction band minimum. In green, the excitonic contribution to the overall absorption (curved line) is demonstrated. (e) presents a literature overview[36] of excitonic binding energies (E_B) in bandgap tuned metal halide perovskites with herein derived values added in green.

All eight perovskite samples show a steep absorption onset and for higher bandgap bromide- and chloride-based perovskites, the excitonic contribution is visible as a peak arising at the onset. The excitonic binding energies increase from ~10 meV in the iodide-based perovskites to ~60 meV for the chloride-based ones (Table A.1.1). The influence of the cation on the exciton binding energy is minimal. Along with bandgap, the exciton binding energy increases with the substitution to smaller halides. Beside the structure, also the electronic structure in metal halide perovskites modifies by ion substitution. Based on a shorter lattice distance and resulting higher band curvature in chloride-based perovskites, the effective mass is reduced and electrons are more delocalized in this case, thus the exciton binding energy increases. Due to the excitonic contribution, the absorption onset does not directly correspond to the optical bandgap in perovskite materials. This error is quite small for iodide-based perovskites, but increases for higher bandgaps due to the clear excitonic contribution at the absorption onset. Figure (4.11 (d)) illustrates the additional absorption share above the optical bandgap within the MAPbX₃ series, stating the calculated values for the optical

bandgap and the exciton binding energy. Thus, especially for higher bandgap perovskites applying a Tauc plot is involving a uncertainty in the bandgap determination.

A spread of exciton binding energies for metal halide perovskites is found in literature (Figure 4.11 (e)). Besides sample quality, this variations are connected to different measurement techniques, their accuracies, and fitting procedures utilized.[36,110] Even within this distribution a trend of increasing exciton binding energies with the substitution from iodide to chloride emerges. The herein determined values (green) follow this established trend, although they are located at the lower limit. The determination of exact exciton binding energy for metal halide perovskites via Elliot´s formula is questioned in accuracy by now.[110] The here determined values, nevertheless, describe a trend following literature. Since the dependency of composition and opto-electronic properties is the main objective here, errors in the determination of the absolute energies can be neglected.

Both absorption onset and exciton binding energy are determined by the exact composition of the metal halide perovskite.

4.4.3 Correlation of structural, optical and opto-electronic properties

Figure 4.12 presents correlative plots of the structural, optical, and opto-electronic properties discussed before. The exciton binding energy increases linearly with the bandgap. Additionally, both bandgap and exciton binding energy decrease with an increase in the lattice spacing. The above-discussed rough estimation of the d spacing explains that $CsPbBr_3$ shows up as an outlier.
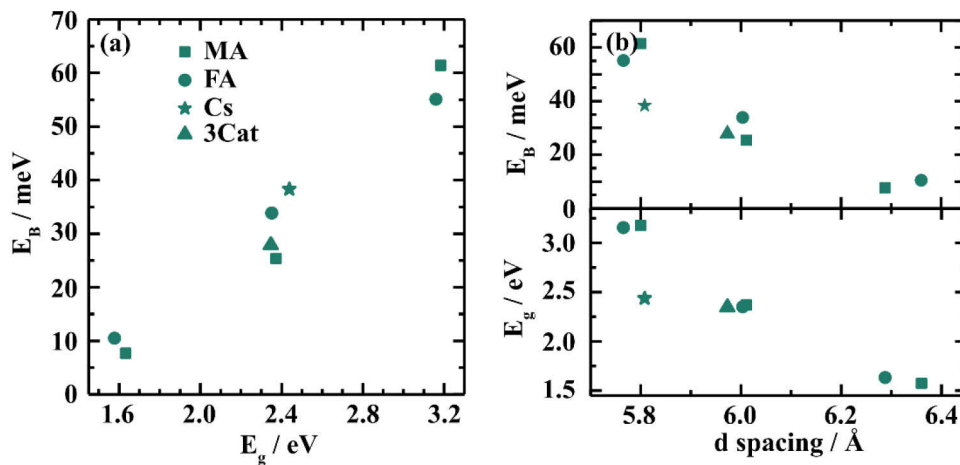
Figure 4.12: Correlation of optical, opto-electronic and structural properties in metal halide perovskites. (a) presents the exciton binding energy (E_B) as a function of the bandgap (E_g) and (b) demonstrates the exciton binding energy (E_B) and the bandgap (E_g) as a function of the d spacing.

This correlation visualizes the interconnection of structural, optical, and opto-electronic properties by the perovskite composition. Therefore, tuning one parameter, e.g. the bandgap, will automatically change the other properties, since composition, structure, and electronic structure are strongly correlated.

4.5 Conclusion

In the case of metal halide perovskites, the structure-property relationship translates to a composition-property relationship. Not only composition and property are interconnect, they also shape, respectively, are shaped by the formation process. Modifying the perovskite composition requires adjustment of preparation parameters due to changed formation processes. Optimized preparation parameters are mandatory to obtain high-quality thin-film samples. Thus, the triangular precursor-process-property space stretches out for metal halide perovskites.

A high quality of thin-film samples is essential for reliable property determination and their application in opto-electronic devices, thus, process optimization is indispensable. Optimizing the thin-film preparation processes over the full compositional space proved as a high expenditure of work and resources by evaluating final film quality, particularly for less investigated compositions. Thus, deeper insights and rationalization of perovskite formation processes and the underlying formation pathways and kinetics will enable time- and resource-saving, target-orientated process design. Such understanding of the formation processes will likewise facilitate optimization of solution-based up-scaling procedures.

A set-up tracking the perovskite formation needs to be compatible with established manufacturing processes in inert atmosphere, namely gloveboxes, since the perovskite preparation is highly dependent on ambient conditions. Due to the optical properties of expectable intermediates and the final perovskites, the application of UV-vis and PL measurements is promising to track formation processes. Thus, a small footprint, optical in-situ set-up is developed and introduced in Chapter 5 to rationalize perovskite formation processes.

5. Origin of ionic inhomogeneity in MAPb(I_xBr$_{1-x}$)$_3$ perovskite thin-films revealed by in-situ spectroscopy during film preparation

The following chapter is based on the peer-reviewed article "Origin of ionic inhomogeneity in MAPb(I_xBr$_{1-x}$)$_3$ perovskite thin-films revealed by in-situ spectroscopy during spin-coating and annealing" by Carolin Rehermann, A. Merdasa, K. Suchan, V. Schröder, F. Mathies and E. L. Unger published in ACS Appl. Mater. Interfaces 2020, 12, 27, 30343–30352.

This chapter presents the description and specifications of a self-built, fiber-optic based spectroscopic in-situ set-up to rationalize perovskite thin-film formation; followed by its application studying the formation processes of the methyl ammonium lead bromide/iodide, MAPb(I_xBr$_{1-x}$)$_3$, series on a sub-second timescale during spin-coating and thermal annealing. While Chapter 4 investigates a variety of different perovskite compositions and demonstrates the influence of individual preparation parameters, here, the formation study is limited to the MAPb(I_xBr$_{1-x}$)$_3$ series to rationalize the influence of the halide ratio on the film formation, as one model process parameter. In-situ UV-vis measurements during spin-coating reveal the influence of different halide ratios (x) in the precursor solution on the phase crystallization. Pure bromide samples directly form a perovskite phase, while samples with high iodide content form a solvate intermediate phase and samples with a mixed stoichiometry between $0.1 \leq x \leq 0.6$ form both. This phenomenon leads to a heterogeneous formation process via two competing reaction pathways, inducing a heterogeneous mixture of phases during spin-coating. The competing formation rationalizes the compositional heterogeneity of mixed bromide/iodide samples even after annealing. Additionally, in-situ UV-vis and XRD measurements reveal halide segregation throughout a slow drying process at room temperature and, therefore, emphasize the importance to quench the as-casted films immediately after spin-coating by thermal annealing.

5.1 Introduction

Mixed bromide-iodide perovskites with bandgaps in the range of 1.75 – 2.20 eV are of interest for multi-junction solar cell applications.[97,99,111,112] However, single-junction devices based on these materials exhibit significant PCE losses compared to their theoretical limits and have a short operating life time.[113–115] These factors are attributed to phase segregation into iodide- and bromide-rich domains within the perovskite film upon light illumination, the so-called *Hoke Effect*.[54] V_{OC} losses are limiting PCEs in those mixed halide perovskite devices (Chapter 2.2). The losses occur due to an iodide-rich, low bandgap minority phase forming during phase segregation and low overall PLQY.[114,116]

It has been postulated that the phenomenon of phase segregation depends on intrinsic ionic (in)homogeneity in samples induced already during film formation.[85,117] Early works from Fedeli *et al.*[85] and Sadhanala *et al.*[117] point out that mixed halide perovskite films are not necessarily homogeneous in terms of their halide distribution directly after preparation, depending on their deposition process. Heterogeneity induced during the film formation will lead to bromide and iodide enriched domains. The latter could act as low-energy sites limiting the V_{OC} and probably play a role in phase segregation due to illumination or electrical bias. The current interpretation of the driving force for phase segregation is local by irradiation induced electric fields that initiate ion migration.[54,56,118–121] Suchan *et al.*[121] reported an initial, temporary low energy emission peak indicating the existence of small pure iodine domains. These domains could play a decisive role in phase segregation, as it can be assumed that holes might get trapped preferentially on these sites resulting in local charge carrier imbalance.[57,89,122–124]

While samples spanning the full range of mixed bromide/iodide ratios in spin-coated MAPb(I$_x$Br$_{1-x}$)₃ films have been reported,[19,125] work on single crystals or powders of mixed bromide/iodide solid solutions of MAPb(I$_x$Br$_{1-x}$)₃, demonstrate a thermodynamic miscibility gap.[55,126,127] Lehmann *et al.*[127] observe immiscibility for halide ratios between x = 0.29 and x = 0.92 (± 0.02) in powders prepared from solution-based, thermodynamic controlled processing. During the spin-coating process, the samples crystallize rapidly and, therefore, it is assumed that meta-stable compositions can be achieved under this kinetic process control. Spin-coated samples with x > 0.2 have been shown to exhibit compositional inhomogeneity evident from sub-bandgap states from Urbach tails[117] and broader FWHM values of XRD reflections or PL peaks.[85]

Ionic inhomogeneity could even be predefined by solution chemistry in terms of solubility, Lewis acidity and coordination complexation with regard to varied lead halide precursors and solvents.[73,128–131] It is expected that the halides have a significant influence on the complex chemistry in solution, hence determining intermediate structures,[76] crystallization processes and the overall film quality. A deeper understanding of the MAPb(I$_x$Br$_{1-x}$)₃ formation processes and the influence of the halide ratio, solvents, and perovskite precursor composition as well as the influence of processing parameters during deposition is still lacking.
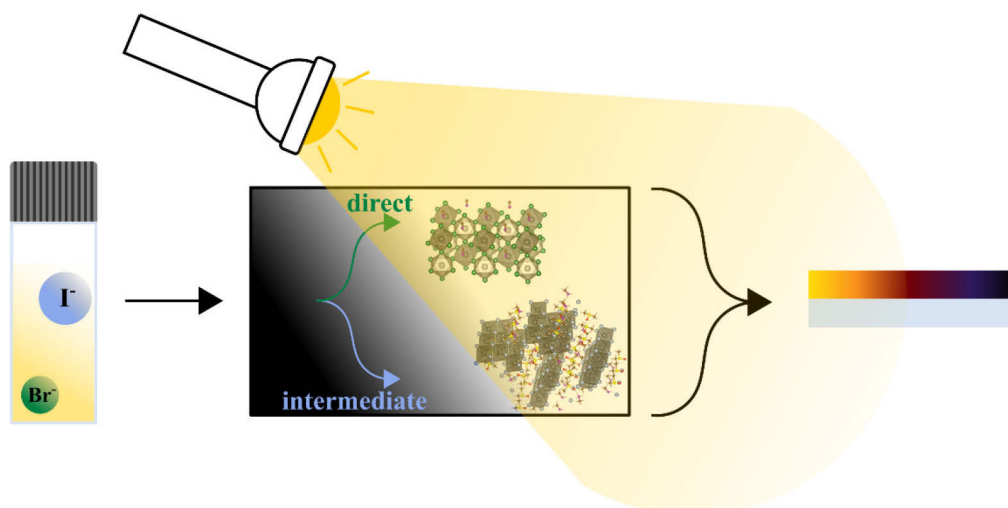
Figure 5.1: Illustrative description of this chapter´s objective to enlighten the black box of the formation processes by in-situ spectroscopy of the MAPb(I_xBr$_{1-x}$)$_3$ series depending on the halide ratio.

Therefore, this chapter focuses on revealing the detailed formation processes of the MAPb(I_xBr$_{1-x}$)$_3$ series during spin-coating and annealing to rationalize the resulting (in)homogeneity of these mixed bromide/iodide perovskite thin-films (Figure 5.1). By spectroscopic in-situ monitoring, the evolution of phase homogeneity is identified as a function of the halide ratio. From these spectral signatures, correlated with ex-situ XRD, the evolution of perovskite and intermediate crystalline phases are observed during film formation and competing pathways in the formation of intermediate phases are identified: the formation of a bromide-rich perovskite phase and the formation of an iodide-rich solvate phase. Their ratio to one another is found to be strongly dependent on the iodide to bromide ratio in precursor solutions. These phases are transformed into mixed bromide/iodide perovskite samples equivalent to the ratio of halides in the precursor solutions upon annealing. However, the ionic homogeneity and sample morphology is strongly affected in cases where samples crystallize from heterogeneous bromide-rich perovskite and iodide-rich solvate intermediate phases. Understanding the detailed formation process of mixed bromide/iodide perovskites regarding the halide ratio is crucial to verify and improve the homogeneity of these materials.

5.2 In-situ Spectroscopy to rationalize metal halide perovskite formation processes from solution to solid thin-films

Throughout the last years, intensive research made metal halide perovskites utilizable in thin-film-based opto-electronic devices, more and more drawing from lab-based to commercialized outdoor applications.[63,132–138] Thereby, the fundamental properties of metal halide perovskites are classified and understood to a large extend (Chapter 2.1). Even though the preparation of these semiconductors via solution-based processes is widely stated to be simple, details about formation processes and pathways is still insufficient. To lift perovskite thin-film preparation from a blind, trial-and-error approach, to an efficient and target-orientated procedure, understanding and rationalization of relevant parameters and their influences on film formation and final film quality

is neccessary. To achieve this, an optical in-situ set-up, tracking the two main process steps, spin-coating and annealing, was developed. The fundamental knowledge gained about the perovskite formation pathways contributes to pave the way from fabrication methods on a laboratory scale such as spin-coating, to reliable and industrial scalable printing and coating techniques.[139]

The fabrication process of thin-film metal halide perovskites is strongly influenced by the surrounding conditions, such as temperature, atmosphere, and humidity.[140–144] Therefore, the objective was to develop an in-situ set-up with a small footprint, directly mountable in a glovebox cluster, in which high efficient solar cells are fabricated. To fulfill these conditions, a fiber-based, modular optical in-situ set-up was designed to track the formation processes by UV-vis and PL spectroscopy on a sub-second timescale. Optical tracking proves to be a suitable method to investigate the formation process, due to high absorption and optically active intermediates.

Other home-built set-ups have been introduced by Buchhorn *et al.*[145], Song *et al.*[146] and Pratap *et al.*[147], however, all these designs either require modification of laboratory equipment, integration into a beamline or are limited to PL measurements. Thereby, the set-up developed here, has the following two advantages: straightforward implementation into standard glovebox equipment and combination of both in-situ UV-vis and PL spectroscopy.

With this spectroscopic set-up, it is possible to systematically investigate and rationalize all the various parameters from (a) solution (solution concentration, precursors and their ratios, and solvents) to (b) spin-coating parameters (spin speed and time, consequential film thinning, the influence of an anti-solvent drop), and (c) annealing parameters (annealing temperature and time). Overall, the spectroscopic analysis of these processes gives information about film formation pathways, intermediates, kinetics, and final morphology. As part of this work, the influence of the X⁻ site anion, namely the bromide to iodide ratio, on the overall formation process and influence on (in)homogeneities (Chapter 5.4), and the solution concentration dependency for pure bromide perovskites (Chapter 6.3) are resolved.

Figure 5.2 pictures a schematic of the developed spectroscopic set-up, to conduct, in-situ UV-vis and PL measurements during film fabrication. It consists of light sources, suitable filters, optical fibers, a reflectance probe, as the centerpiece, and a spectrometer. Based on the fiber optics, the individual building blocks can be connected custom designed and allow the implementation, as shown in a glovebox. In general, the set-up enables a high degree of flexibility due to its modular design and, therefore, adjustment to specific measurements and surrounding conditions. In the following both measurement modes and the detectable signals are described.
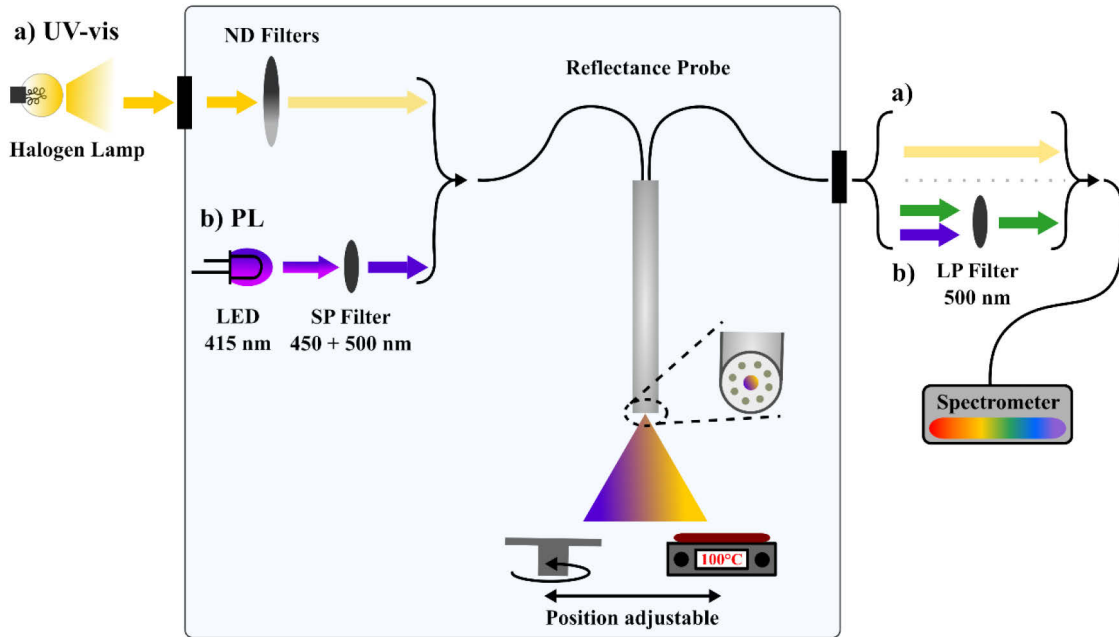
Figure 5.2: Schematic of the in-situ spectroscopy set-up. The centerpiece is the reflectance probe adjustable above the spin-coater or the hot plate to monitor the respective process. (a) represents the light pass for the in-situ UV-vis measurements, using a halogen lamp as the excitation source with ND filters to adjust the light intensity, (b) indicates the light pass for PL measurements. Short and long pass filters are utilized to cut off disruptive parts of the excitation from an LED. Components illustrated within the light blue box are assembled inside the glovebox and connected via optical feedthroughs to the components outside the glovebox.

First, the configuration of the in-situ UV-vis mode is explained (Figure 5.2 (a)): a white light halogen lamp (Thorlabs SLS201L\M)[148] outside the glovebox is utilized as the excitation source. The excitation light is coupled into the glovebox via optical fibers connected to a feedthrough. Different neutral density (ND) filters on the inside allow the adjustment of the light intensity incident on the sample. This intensity modification is necessary to prevent oversaturation of the spectrometer and ensure proper data collection. With additional fibers, the excitation is coupled into the reflectance probe (Ocean Optics QR400-7-UV-BX), placed above the sample to be measured. The sample in turn can be placed either the spin-coater or the hot plate. The excitation light undergoes scattering, absorption, and reflection processes, before being collected by the outer openings in the reflectance probe (enlargement Figure 5.2). This attenuated signal is detected by the fiber-optic spectrometer (Ocean Optics Flame FLMS12200) and processed by the connected computer.

For the reflectance probe, the center fiber is providing the excitation (inner circle, enlargement Figure 5.2), and a second one is collecting the signal reflected from the sample (outer ring, enlargement Figure 5.2). The reflectance probe is placed vertical, ~1 cm above the sample, whereas the exact height is configurable to further adjust the intensity of the incoming light. This way, the probe can only detect reflected and scattered light from the sample and substrate, (compare Chapter 4.2 for other UV-vis measurement assemblies). However, the information about an absorption edge evolving, as soon as the semiconducting phase starts to crystallize (Figure 5.3 (b)) originates from light transmission. The incident excitation light is to some extent directly scattered or reflected, however, the other part undergoes transmission. An additional back-scattering process

needs to take place at the wet-film|substrate interface, thus, the absorption by the wet-film can be detected in the reflection configuration. Therefore, the excitation undergoes transmission twice, since it travels twice through the sample. Since the signal is influenced by absorption and scattering of the sample based on the reflectance probe, this measurement mode is referred to as *transflectance*, a portmanteau of *trans*mission and re*flectance*. To increase the amount of transflected light and, therefore, improving the signal-to-noise ratio, a highly reflective Ag mirror, is evaporated on the backside of the substrate. Overall, the evolution of an absorption edge forming during transflectance measurements indicates the formation of a solid-state semiconductor phase (Figure 5.3 (b), middle and bottom).

Due to the reflectance probe assembly, scattering and reflection over all wavelengths influence the detected signal additionally (Chapter 4.2), especially for rough and non-complete covered samples resulting in an increased baseline or a wavy one during film formation. In extreme cases, this background can mask a clear absorption edge and complicate data analysis. However, the evolution of an overall higher background directly indicates a change in film morphology.[46] In Chapter 5.2, a broadband change in the absorption indicates the formation of a crystalline species with no optical features in the acquired spectral range.

To correctly calculate the transflectance signal (*TF*), a bright reference spectrum $I(\lambda)_B$ is recorded with the substrate beneath the probe and the light source turned on. Additionally, a dark reference spectrum $I(\lambda)_D$ is acquired, with the light source turned off. Each transflectance signal is calculated as followed:

$$TF = 1 - \frac{I(\lambda)_S - I(\lambda)_D}{I(\lambda)_B - I(\lambda)_D} \tag{5.1}$$

where $I(\lambda)_S$ is the dynamic signal measured during the formation process.

If the Ag mirror is pointing upwards and, thus, the solution is directly processed on it, an interference pattern, created by path differences (Figure 5.3 (a) top), indicates the thinning behavior of the solution during spin-coating. However, fast reactions or different wetting behaviors at the solution|Ag interface might slightly influence the formation process. Overall, the solution is mainly thinning during spin-coating. Thus, thinning measurements are not carried out during annealing. A single interference pattern and the evolution of the thinning during spin-coating are presented in Figure 5.3 (a), middle and bottom. Chapter 6.4 presents a detailed analysis of the interference pattern and the associated film thinning. Two different measurements are needed to detect the thinning and the evolution of the absorption edge, due to the positioning of the Ag mirror (Figure 5.3 (a) and (b), top). However, this enables us to decouple the interference pattern and the evolution of the absorption edge, simplifying data analysis to some extent.
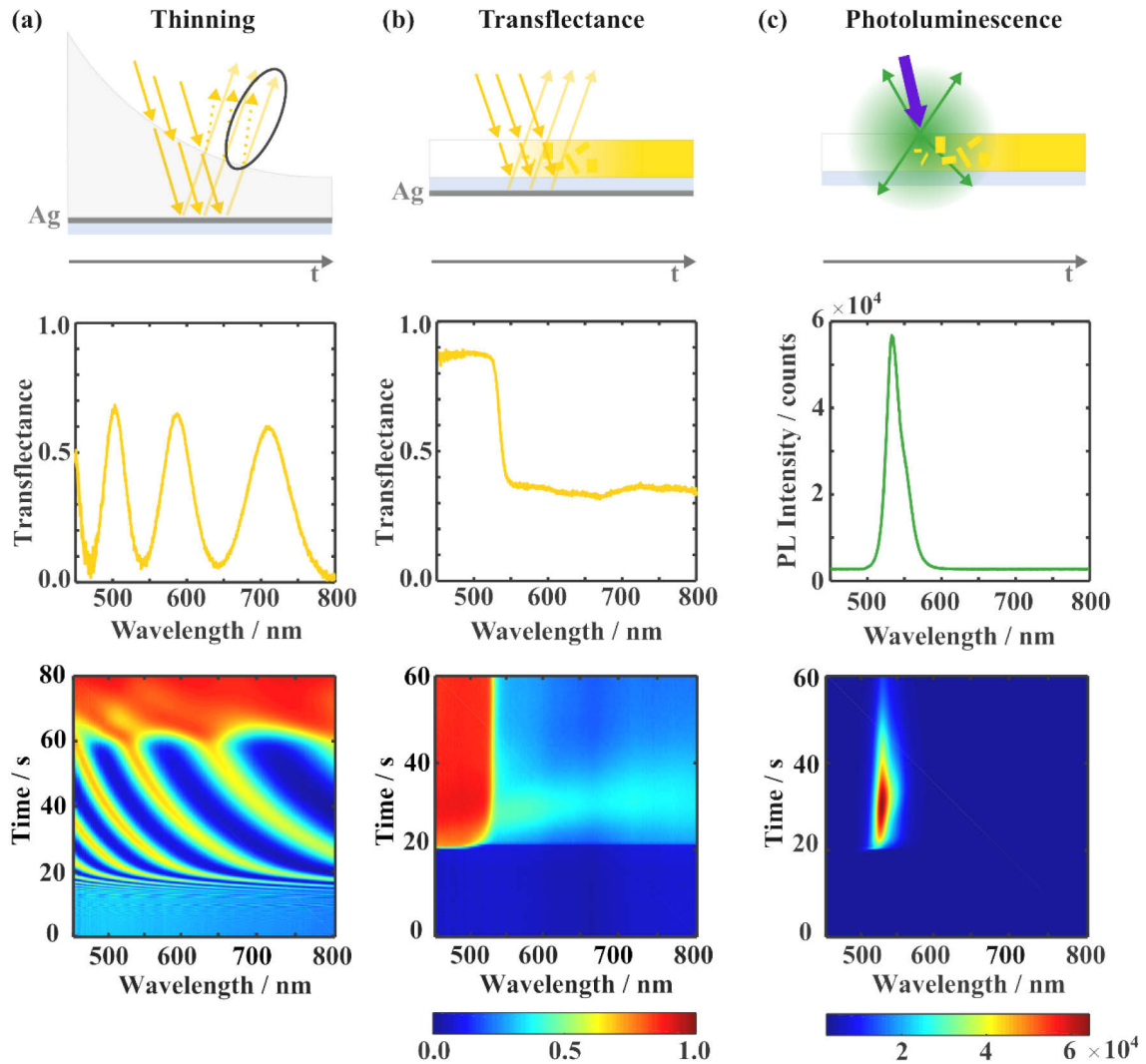
Figure 5.3: Schematic presenting the signal origin for the different measurement modes, (a) Interference, (b) Transflectance, and (c) Photoluminescence. (a) Interference is detected throughout the thinning of the solution during spin-coating with the Ag mirror (grey line) on the front. On the other hand, the evolution of an absorption edge can be detected during the crystallization of a semiconductor if the Ag mirror is on the backside. An Ag mirror is evaporated to increase the transflectance signal. The color scale is the same for Interference and Transflectance in the heat map. The PL signal (c) occurs as soon as the formation of intermediate or perovskite phases starts. For all three modes, the upper part illustrates the origin of the detected signal, the middle one, a single spectrum during the spin-coating process and the lower one, a 2D heat map, presenting the time evolution of the respective signal over the formation process.

Secondly, the configuration of the in-situ PL mode, which is consistent in its basic construction and components with the UV-vis mode, is described; merely the excitation source and optical filters need to be replaced. As excitation sources LEDs, emitting at a suitable wavelength, are utilized. The option of changing the excitation wavelength from 365 nm to 415 nm, 470 nm, or 625 nm is provided within the set-up. The overall functionality and operational principle is the same independently of the LED connected. In the following, the description is based on a LED emitting at 415 nm (Thorlabs M415F3), suitable for bromide-based perovskites discussed in Chapter 6. The excitation wavelength is selected by expected absorption and resulting emissions from intermediate

states and the final perovskite. Separate Photoluminescence Excitation (PLE) measurements on the final perovskite film help with the selection of a relevant excitation wavelength, at least for the expected perovskite phase forming.

The LEDs are not monochromatic and their emission profile has a distribution[149] around the peak emission. Especially longer excitation wavelengths will overlap with the PL signal of the bromide-based perovskites and complicate data analysis. To cut off this low energy tail in the excitation, short pass (SP) filters at 450 and 500 nm are implemented to ensure a sharp edge at a longer wavelength, namely 500 nm, to prevent the described overlap of excitation and emission wavelength. In principle, one SP filter would be enough to cut off longer wavelength. However, to reach a sufficient optical density to ensure the complete cut off at 500 nm, those two SP filters need to be combined. In general, SP and LP filters work as edge pass filters at their specific wavelength. While SP filters cut off all longer wavelength and let shorter wavelength pass through, LP filters cut off shorter wavelength and let the longer ones pass.

The filtered light is coupled into the reflectance probe as for the UV-vis mode and incident on the sample, generating photoluminescence of the optically active components evolving during the formation process. The signal is detected in reflection mode. In this case, excitation from the LED source and the photoluminescence signal are collected, since some parts of the excitation are reflected, too. To prevent the excitation to be detected together with the actual PL signal, an additional long pass (LP) filter at 500 nm is installed outside the glovebox before the spectrometer, to cut off the excitation wavelength shorter than 500 nm. The LP filter should be chosen carefully and close to excitation wavelength to make sure no photoluminescence from intermediate species is cut off. In addition, it is very important to make sure that no self-fluorescence material is placed in the light pass, e.g. a Teflon-based spin-coater chuck or any sample holder that might distort the photoluminescence of the investigated species.

For the in-situ PL measurements, a calibration is necessary and a dark spectrum $I(\lambda)_D$ is recorded with the excitation source turned off. Each PL signal is calculated as:

$$PL = I(\lambda)_S - I(\lambda)_D \tag{5.2}$$

where $I(\lambda)_S$ is the dynamic signal detected during the formation process.

Also for in-situ PL measurements, an Ag mirror might be reasonable to increase the signal intensity due to additional scattering of the PL signal at the backside of the substrate, and, therefore, being directed to the probe. This additional reflection is mainly useful for species with a low PLQY, which otherwise might be hardly detectable. However, in Chapter 6, an Ag mirror was waived, due to an obstacle: the bromide-based perovskite and especially the wet-films after initial crystallization have a comparably high PLQY yield, extremely easily leading to an oversaturation of the detector. Therefore, an artificial increase due to reflection with an Ag mirror would underline this obstacle.

A PL signal is detectable from intermediate phases and perovskite phases as soon as the solidification of the solution starts due to the crystallization of these phases. Figure 5.3 (c) illustrates the in-situ PL signal, detectable as soon as crystallization starts (top), a 1D spectrum after the crystallization started (middle) and the full 2D heat map of the full spin-coating process (bottom) of a MAPbBr₃ film. For the in-situ PL signal, the peak position, possibly double or multiple peaks or broadened peaks, peak shifts and intensity evolution over time are monitored. Analyzing those parameters rationalizes the formation pathways in terms of intermediates and perovskite phases formed and their evolution, film formation kinetics, growth processes, and changes in PLQY give insights into defect formation. In general, the in-situ PL signal is less influenced by a rough

morphology than the in-situ UV-vis measurement with its shifting baseline. However, overall low PLQYs and the thermal quenching of the PLQY upon annealing are an obstacle. In Chapter 5, no in-situ PL analysis was possible, since the excitation at 415 nm used for these measurements induced the phase segregation by light. Consequently it prevented rationalizing the intrinsic formation pathways of mixed halide samples.[150] Thus, light-induced changes, due to the high excitation density in in-situ PL measurements, can influence the formation pathways and direct them over different intermediates or influence the final film. Hence, in-situ UV-vis and PL measurements should always be compared and conclusive. Chapter 6 discusses details of the in-situ PL signal evolution for different bromide-based perovskites and their formation processes, and their meaning for film formation. In pure bromide-based perovskites, no light-induced phase segregation has to be expected.

Overall, the developed optical set-up is a key method to rationalize the perovskite formation during processing. However, one needs to carefully evaluate the detected signal, since high light intensities may influence the crystallization process or induce phase segregation. More technical details and data analysis are described in Merdasa *et al.*[151].

5.3 Experimental

All general cleaning and preparation steps were carried out under the same conditions as described in Chapter 3.2 in N_2 filled gloveboxes. Table 5.1 gives the details for solution preparation applied for the formation study on the $MAPb(I_xBr_{1-x})_3$ series:

Table 5.1: Details of pure MAPbI₃ and MAPbBr₃ solutions prepared for the formation study on the MAPb(IₓBr₁₋ₓ)₃ series with precursors, their ratio, concentration, and solvents utilized.

Solution	Precursor - ratio	Concentration / mol L^{-1}	Solvent
MAPbI$_3$	MAI:PbI$_2$ - 1:1	1.0	4:1 DMF:DMSO
MAPbBr$_3$	MABr:PbBr$_2$ - 1:1	1.0	4:1 DMF:DMSO
MAPbI$_3$	MAI:PbI$_2$ - 1:1	1.0	DMF
MAPbBr$_3$	MABr:PbBr$_2$ - 1:1	1.0	DMF

Pure MAPbI$_3$ and MAPbBr$_3$ solutions from the same solvent composition were mixed accordingly to realize different halide ratios (X_{sol}) several hours before thin-film preparation without any additional heating. The term X_{sol} is introduced, giving the amount of iodide mixed into the solutions with different halide ratios; 1-X_{sol} corresponds to the bromide amount. By blending the pure MAPbI$_3$ and MAPbBr$_3$ solutions, halide ratios were obtained in 0.1 steps from the pure iodide (X_{sol} = 1.0) to the pure bromide (X_{sol} = 0.0).

To investigate primarily the influence of the halide ratio (X_{sol}) on the thin-film formation, spin-coating and annealing parameters were fixed, as stated in Table 5.2, for all blends:

Table 5.2: Details of perovskite thin-film preparation applied to study the thin-film formation of the MAPb(I_xBr_{1-x})₃ series, with the amount of solution, spin-coating, and annealing parameters.

Amount of solution / µL	Spin speed / rpm	Acceleration / rpm s^{-1}	Spin time / s	Annealing Temp. / °C	Annealing time / min
60	4000	4000	60	100	30

Deliberately, no anti-solvent drop was applied during the spin-coating process to investigate the intrinsic formation pathways and kinetics underlying the halide composition and to avoid quenching and influencing the formation process by external factors.

To rationalize the formation process, both spin-coating and annealing were monitored by in-situ UV-vis measurements as specified in Chapter 5.2. To ensure a stable emission spectrum, the halogen lamp should be turned on 30 min before starting the measurements. Individual spectra were collected with an integration time of 500 ms in this study to increase the signal to noise ratio. While monitoring the entire spin-coating process, only the first 30 s of thermal annealing were tracked since detectable changes proceed within the first seconds of this preparation step. The first minute of drying was measured to interpret possible differences in the spectra between both preparation steps and to determine dynamic processes in the as-cast films. Since recalibration is necessary relocating the in-situ set-up in-between spin-coater and hot plate, spin-coating and annealing are not measured on the same sample to avoid dynamic changes within the as-cast film during a drying process and, therefore, mimic a regular preparation with direct annealing after spin-coating.

Irradiation-induced phase segregation can be neglected during the following since the UV-vis signal is not predominantly affected by phase segregation. In addition, the amount of light intensity and exposure time of the sample was minimized using a relatively big spot of ~0.2 cm^2 and measuring of center on the rotating sample.

5.4 Formation study of the MAPb(I_xBr_{1-x})₃ series rationalizing the influence of the halide ratio

In Chapter 5.4 the formation study of the MAPb(I_xBr_{1-x})₃ series is presented and discussed, divided into the formation process during spin-coating, annealing, and slow drying at room temperature. Five representative ratios of halide precursor solutions, namely X_{sol} = 0.0, 0.3, 0.6, 0.7, and 1.0 in 4:1 DMF:DMSO are selected to present three identified formation regimes in detail. Figure A.2.2 and A.2.3 shortly present the remaining halide ratios, X_{sol} = 0.1, 0.2, 0.5, 0.8, and 0.9.

5.4.1 Film formation process during spin-coating

In Figure 5.4 the perovskite formation during spin-coating from a pure bromide solution (X_{sol} = 0.0) is presented. In-situ UV-vis measurements in Figure 5.4 (a) reveal that an absorption onset evolves after 25 s of spin-coating at 550 nm, indicating that the yellow MAPbBr₃ perovskite phase with a bandgap of 2.3 eV forms directly. Three individual line plots at 20, 25, and 60 s, representing the

time before, during, and at the end of the formation process are depicting the transflectance evolution in detail. The evolution of a sharp absorption onset indicates the formation of the pure bromide perovskite sample. XRD measurements of the as-cast samples (Figure 5.4 (b)) only show the desired $MAPbBr_3$ phase indicated by the reflection of the 100 peak of the cubic perovskite phase at $2\theta = 14.9$. Neither additional intermediates nor precursor phases are observed at low 2θ values. $MAPbBr_3$ has an exothermic formation enthalpy ($\Delta_f H$ = - 543.08 kJ/mol[77], Table A.2.1) and no bromide-based intermediate solvate phase has been reported so far, suggesting that it does not form easily.[152] Therefore, it is thermodynamically most favorable that $MAPbBr_3$ forms directly from solution via a fast crystallization process. Nevertheless, this fast crystallization process can lead to several structural and electronic defects integrated into the crystal structure affecting morphology and opto-electronic quality of the as-prepared semiconductor layer.
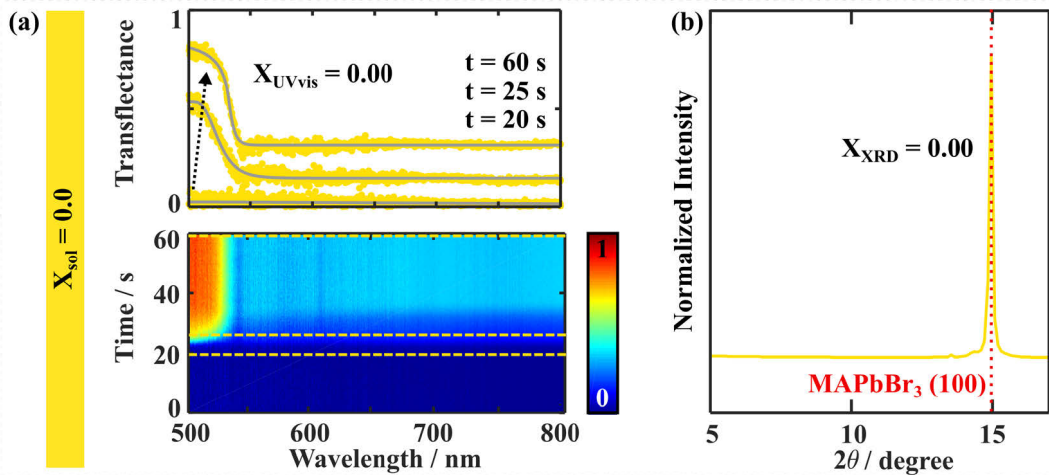

Figure 5.4: Film formation process during spin-coating of MAPbBr₃, X_{sol} = 0.0. In-situ UV-vis measurements (a) during spin-coating for 60 s present the evolution of the transflectance over time (bottom) and selected single-spectra (top) indicating key formation steps. The XRD pattern (b) of the as-cast film reveals the crystalline MAPbBr₃ phase formed during spin-coating. The red dashed line indicates the 100 reflection for cubic MAPbBr₃.[153] X_{UVvis} and X_{XRD} specify the amount of iodide in the perovskite phase derived from the respective measurement according to the calibration curve (Figure A.2.1).

While the pure $MAPbBr_3$ forms directly, for mixed solutions with iodide concentrations of X_{sol} = 0.3 and 0.6 in-situ UV-vis measurements indicate a crystallization of a bromide-rich perovskite phase during spin-coating (Figure 5.5 (a) and (b)). For X_{sol} = 0.3 an absorption edge at 570 nm is formed around 35 s into the spin-coating process. From the relation of absorption onset as a function of halide ratio for ionically homogeneous samples (Figure A.2.1) the experimental absorption onset at 570 nm evolving during spin-coating can be related to an estimated iodide amount of X_{UVvis} = 0.08. For the solution with X_{sol} = 0.6 the absorption edge around 650 nm arising at the end of spin-coating corresponds to an estimated iodide content of X_{UVvis} = 0.38. Instead of the direct crystallization of the perovskite phase with halide composition equivalent to the ratio in the precursor solution, a bromide enriched perovskite phase forms during spin-coating, indicating that compositional heterogeneity in terms of the halide distribution is introduced in the samples during formation. Both halide ratios are located within the thermodynamic miscibility gap described for solid solutions of methyl ammonium lead bromide/iodide perovskites reported by Lehmann *et al.*[127]. This heterogeneous crystallization evokes that mixed bromide/iodide samples are limited in their formation during spin-coating by the miscibility gap identified for powder samples prepared in thermodynamic equilibrium.
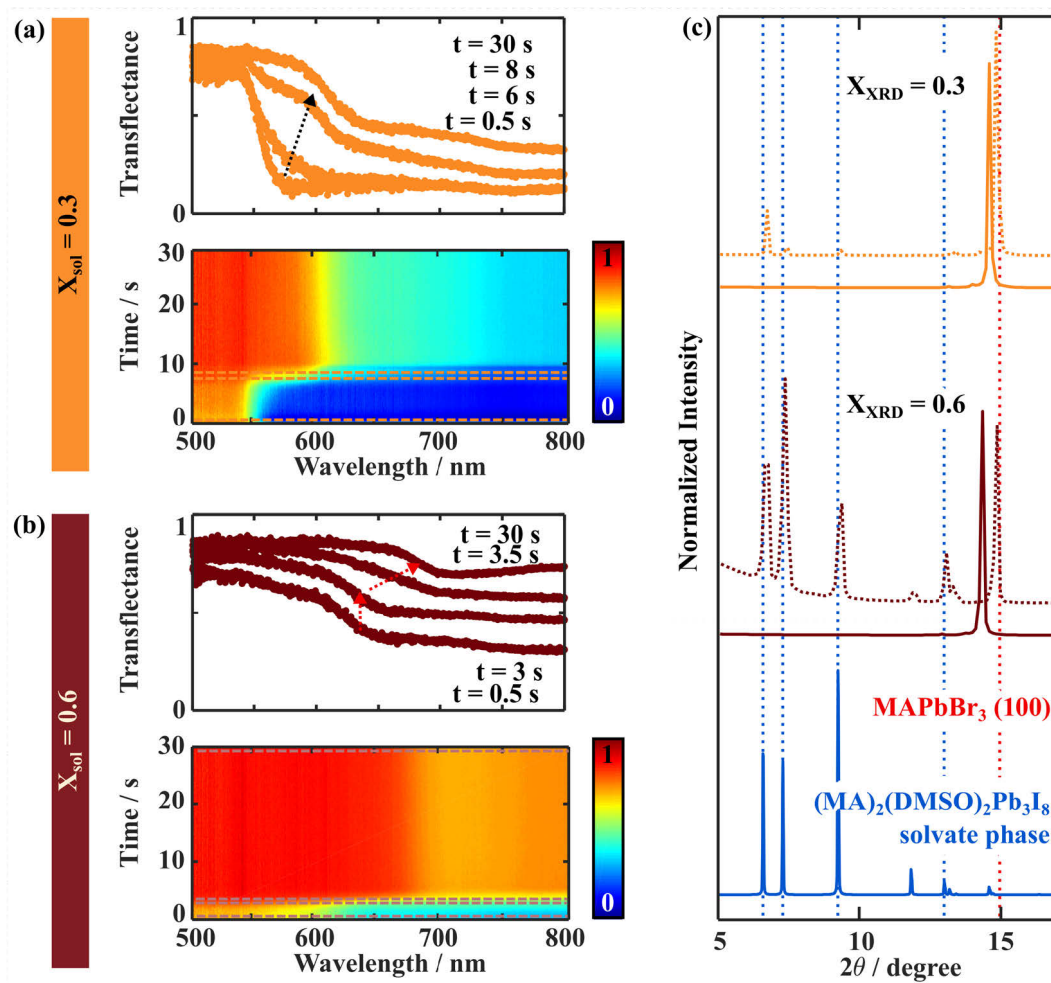
Figure 5.5: Film formation process during spin-coating of X_{sol} = 0.3 and 0.6. In-situ UV-vis measurements (a and b) during spin-coating for 60 s present the evolution of the transflectance over time (bottom) and selected single-spectra (top) indicating key formation steps. The XRD patterns (c) of the as-cast films reveal crystalline phases formed during spin-coating. The red dashed line indicates the 100 reflection for cubic MAPbBr₃.[153] The (MA)₂(DMSO)₂Pb₃I₈ solvate phase[75] is shown in blue at the bottom with the main reflections indicated by dashed blue lines. X_{UVvis} and X_{XRD} specify the amount of iodide in the perovskite phase derived from the respective measurement according to the calibration curves (Figure A.2.1).

XRD measurements of the as-cast samples (Figure 5.5 (c)) confirm the formation of a crystalline bromide enriched perovskite phase for both halide ratios X_{sol} = 0.3 and 0.6. From the position of the cubic 100 reflection, the iodide content of as spin-cast samples can be determined to be X_{XRD} = 0.05 for the X_{sol} = 0.3 and X_{XRD} = 0.15 for the X_{sol} = 0.6 sample. Figure A.2.1 (d) presents the XRD calibration curve for the solid solutions of the MAPb(I$_x$Br$_{1-x}$)₃ series. The discrepancy between the nominal halide ratio between values extrapolated from UV-vis absorption and XRD measurement is attributed to the fact that XRD measurements were carried out ex-situ approximately 5 min after sample preparation. Room temperature in-situ UV-vis drying experiments show a possible change in the composition of the mixed bromide-iodide perovskite phase may change during and after spin-coating. Chapter 5.4.3 discusses this effect of dynamic exchange during drying in more detail. Besides the bromide-rich perovskite phase, a second crystalline phase is identified via ex-situ XRD measurements on the as-cast films, namely the (MA)₂(DMSO)₂Pb₃I₈ solvate phase. (MA)₂(DMSO)₂Pb₃I₈ cannot be detected via the in-situ UV-vis measurements due to its low

absorption coefficient and lack of spectral features in the visible range. Therefore, the combination of in-situ UV-vis and ex-situ XRD measurements reveal the formation of two phases during spin-coating, one bromide-rich perovskite and one iodide-rich intermediate solvate phase.

For solutions with iodide concentrations of $X_{sol} = 0.7$ and 1.0 no evolution of an absorption onset can be observed during spin-coating (Figure 5.6 (a) and (b)). Also for subsequent drying no spectral features indicating the formation of a crystalline perovskite semiconductor phase (Figure A.2.4). However, the shift in the baseline in the measured absorption signal indicates a change in sample scattering and likely the formation of a crystalline phase.
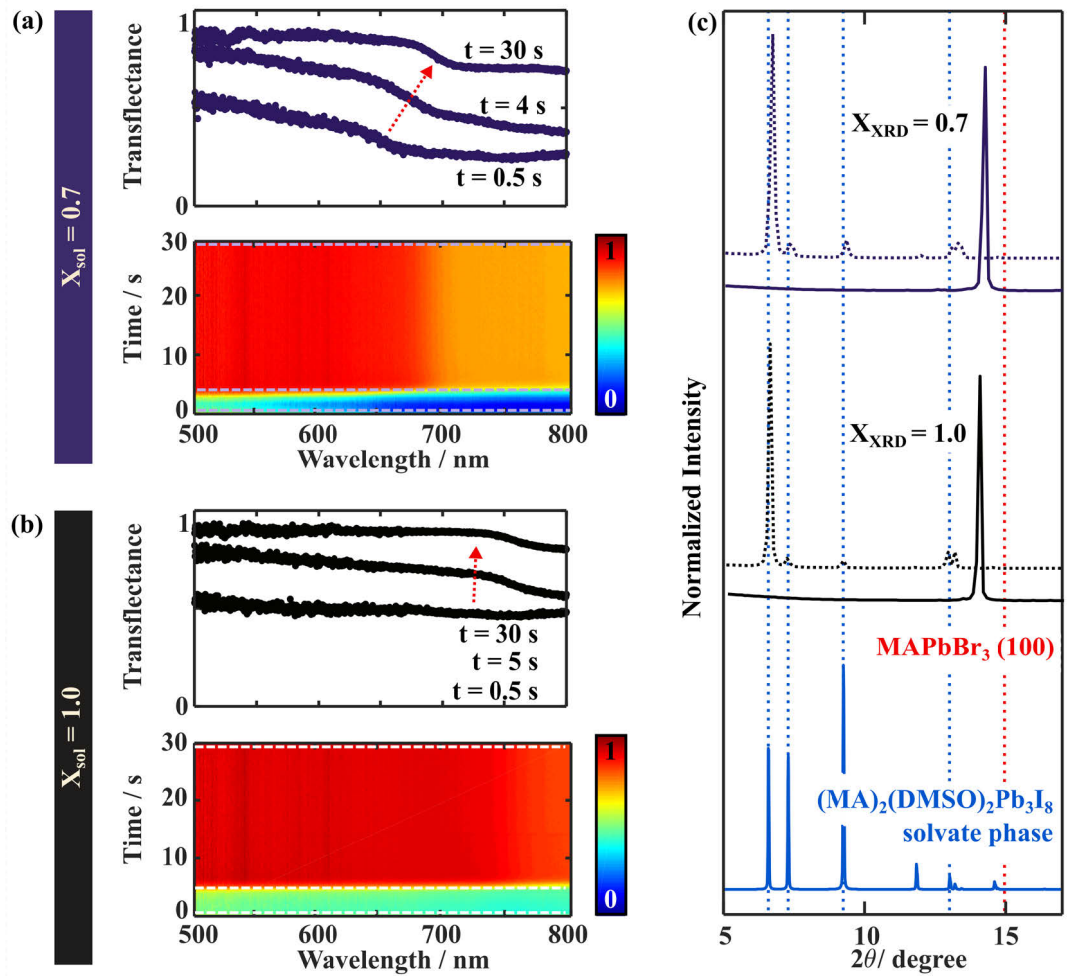

Figure 5.6: Film formation process during spin-coating of $X_{sol} = 0.7$ and 1.0. In-situ UV-vis measurements (a and b) during spin-coating for 60 s present the evolution of the transflectance over time (bottom) and selected single-spectra (top) indicating key formation steps. The XRD patterns (c) of the as-cast films reveal solvate intermediate phases formed during spin-coating. The red dashed line indicates the 100 reflection for cubic MAPbBr₃.[153] The (MA)₂(DMSO)₂Pb₃I₈ solvate phase pattern[75] is shown in blue at the bottom with the main reflections indicated by dashed blue lines. X_{XRD} specifies the amount of iodide in the perovskite phase derived from the XRD measurement according to the calibration curve (Figure A.2.1).

Only from XRD measurements of the as-cast samples, diffraction patterns allow to identify the crystalline phases formed during spin-coating. No perovskite phase is directly formed from iodide-rich solutions (Figure 5.6 (c)), only reflections attributable to the solvate intermediate phase

$(MA)_2(DMSO)_2Pb_3I_8$[75] can be identified. As mentioned above, due to its low absorption coefficient, $(MA)_2(DMSO)_2Pb_3I_8$ cannot be detected via the in-situ UV-vis measurement.

While the formation of a pure $(MA)_2(DMSO)_2Pb_3I_8$ solvate phase can be expected for a film spin-coated from $X_{sol} = 1.0$, the lack of reflections in XRD related to a perovskite phase for a film spin-coated from $X_{sol} = 0.7$ suggests that the bromide is incorporated into the solvate intermediate phase. Comparing the exact reflection positions for the pure iodide $(MA)_2(DMSO)_2Pb_3I_8$ solvate phase published by Cao *et al.*[75] and the solvate phase formed during spin-coating from $X_{sol} = 0.7$, all reflection positions shift about 0.1° to higher 2θ values for the latter case. Table A.2.2 lists the exact reflection positions and the respective shifting. This shift in the XRD peaks indicates a change in the lattice parameter of the solvate intermediate phase and, therefore, the incorporation of a certain amount of bromide in the crystallized solvate phase. The solubility limit of bromide co-existing in the iodide-rich solvate phase is located between $X_{sol} = 0.6$ and $X_{sol} = 0.7$, as a bromide-rich perovskite phase starts to form during spin-coating for the $X_{sol} = 0.6$.

For solutions with iodide contents $X_{sol} \geq 0.7$, the formation process takes place via one intermediate step during spin-coating and no bromide-rich perovskite phase is formed as a second phase. Therefore, this formation is ionically more homogeneous than the divided one for $X_{Sol} \leq 0.6$ since no separated phases form during spin-coating. However, the formation of the solvate intermediate phase predetermines the microstructure of the sample being a potential cause for morphological inhomogeneity (Figure 5.15) and the increased scattering influencing in-situ UV-vis measurements.[75,76]

Introducing iodide in the mixed halide perovskites changes the lead-halide-solvent complex equilibrium in solution since iodide interacts stronger with DMSO and coordinates weaker to lead than bromide. For details on the coordination chemistry in perovskite precursor solutions (Chapter 2.3). As calculated from XRD, with increasing X_{sol}, corresponding to an increasing iodide content, the amount of the $(MA)_2(DMSO)_2Pb_3I_8$ solvate phase rises while the amount of a bromide-rich perovskite phase formed during spin-coating decreases (Figure 5.7).
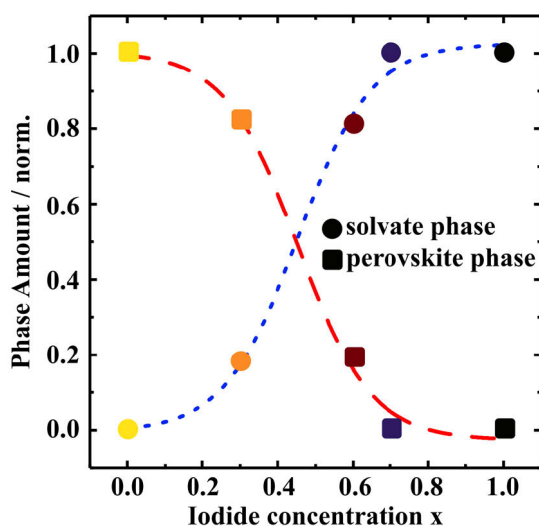

Figure 5.7: Traces of perovskite and solvate phase formed after spin-coating in the as-cast films estimated from XRD pattern as a function of the iodide content (X_{sol}).

Due to a higher Lewis acidity of PbI_2 compared to $PbBr_2$,[129] it is more favorable that the Lewis-base DMSO coordinates to PbI_2. Furthermore, the stronger coordination of DMSO to lead-iodide

complexes energetically favors the formation of the $(MA)_2(DMSO)_2Pb_3I_8$ solvate phase, rather than an iodide-rich perovskite phase.

From theoretical calculations, the formation enthalpy of $(MA)_2(DMSO)_2Pb_3I_8$ was estimated to be $\Delta_fH = -1633.4$ kJ/mol,[76] which is the most exothermic among the known solvate phases (Table A.2.1) and significantly higher than for solid-state $MAPbI_3$ ($\Delta_fH = -371.6$ kJ/mol).[77] In contrast to the extent known as far, it is observed that bromides do not form a stable solvate phase,[152] nor is thermodynamic data on the enthalpy of formation available. The enthalpy of formation of the bromide perovskite phase has been calculated to be $\Delta_fH = -543.08$ kJ/mol,[77] which may rationalize the more favored formation of a bromide perovskite phase compared to iodide perovskite in a mixture of both halides present. However, all formation enthalpies mentioned are theoretically determined and the absolute values must be critically evaluated, as the calculation details are not always described and may be different for individual sources. However, the described overall trend of the calculated formation enthalpies for metal halide perovskites and the solvate phases is reliably reported across different sources.[76,77,154,155]

Further work is needed to fully rationalize the role of solvent coordination strength in determining the preferred crystal phase formed, however, such a study is out of the scope of this work. We conclude that the fundamental differences in halide and solvent coordination strength, as well as differences in the enthalpy of formation of perovskite vs. solvate phases, dictate the phase distribution of thin-films formed upon spin-coating.

Besides the formed intermediate phases during spin-coating, the halide ratio in the $MAPb(I_xBr_{1-x})_3$ series determines the onset of crystallization. The averaged transflectance signal (Figure 5.8) indicates the formation onset of crystalline phases. An increase in transflectance above the respective bandgap is related to the start of the perovskite crystallization. The transflectance is averaged within a relevant wavelength range representing the absorption of the perovskite phase and excluding the influence of the background; specifically $500 - 550$ nm for $X_{sol} = 0.0$, $500 - 580$ nm for $X_{sol} = 0.3$, $500 - 650$ nm for $X_{sol} = 0.6$ and $500 - 800$ nm for $X_{sol} = 0.7$ and 1.0.

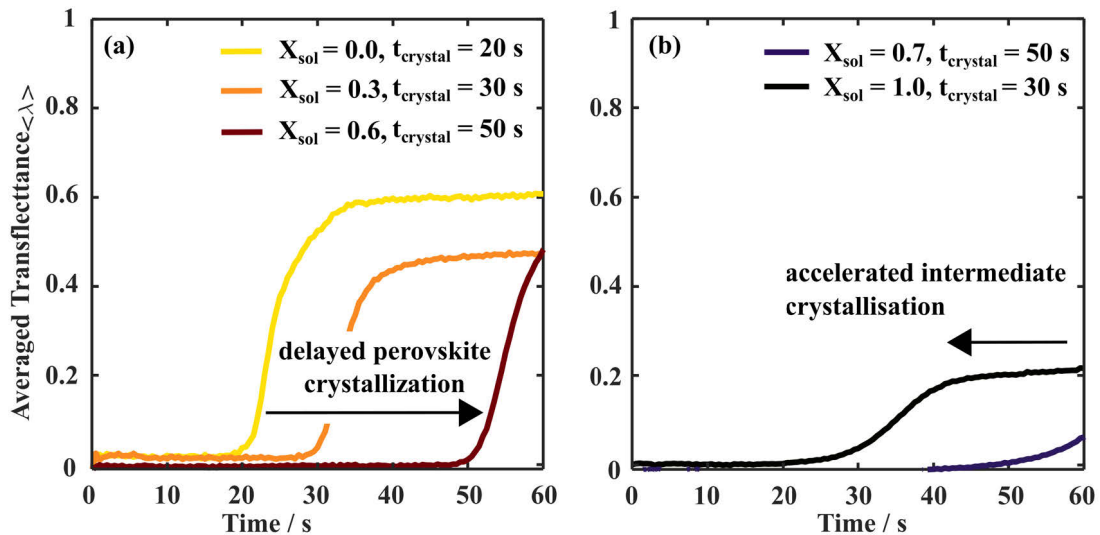**Figure 5.8: Averaged transflectance of (a) $X_{sol} = 0.0$ for $500 - 550$ nm, $X_{sol} = 0.3$ for $500 - 580$ nm and $X_{sol} = 0.6$ for $500 - 650$ nm indicating the perovskite crystallization time and of (b) $X_{sol} = 0.7$ and 1.0 for $500 - 800$ nm indicating solvate intermediate crystallization time, as the transflectance increases.**

The perovskite crystallization for the pure bromide ($X_{sol} = 0.0$) is detectable after $t_{crystal} \sim 20$ s (Figure 5.8 (a)). $t_{crystal}$ defines the time of the crystallization onset. For the mixed halide ratios $X_{sol} = 0.3$ and 0.6, which form a bromide enriched perovskite phase, a delayed crystallization at $t_{crystal} \sim 30$ and ~ 50 s is determined, respectively. The higher the iodide content in the solution, the later the crystallization starts. Due to a higher iodide content, a higher amount of the intermediate solvate phase forms (Figure 5.7).

Although no perovskite phase crystallizes for $X_{sol} = 0.7$ and 1.0 during spin-coating, an overall increase in the transflectance is observed averaging over 500 to 800 nm (Figure 5.8 (b)). This rise in transflectance is based on increased scattering on the sample during the formation of the $(MA)_2(DMSO)_2Pb_3I_8$ solvate intermediate phase. Scattering results in a higher background and increases in the averaged transflectance without any specific features from an absorption onset. As the averaged transflectance for the sample of $X_{sol} = 0.7$ is not reaching a maximum within the 60 s of spin-coating, hence crystallization of the intermediate phase is ongoing. A better homogeneity, in this case, might be caused by thermal quenching, preventing complete crystallization of the intermediate phase and a template morphology. Therefore, thermal quenching and its timing are optimizable parameters to obtain high-quality samples in terms of homogeneity and coverage.

It is observed, that the pure iodide intermediate solvate phase crystallization at $t_{crystal} \sim 30$ s is accelerated compared to the crystallization from the $X_{sol} = 0.7$ with some incorporation of bromide, $t_{crystal} \sim 50$ s. The crystallization for mixed solutions in both cases, the bromide-rich perovskite and the iodide-rich intermediate phase is delayed compared to the crystallization from the mono-halide solution. The delay in crystallization correlates for both processes with the increasing amount of the second halide. This phenomenon of an unfavorable crystallization is well known for solid solutions of mixtures. Therefore, the halide ratio not only determines the formation pathway but also the kinetics and, hence, the processing window.
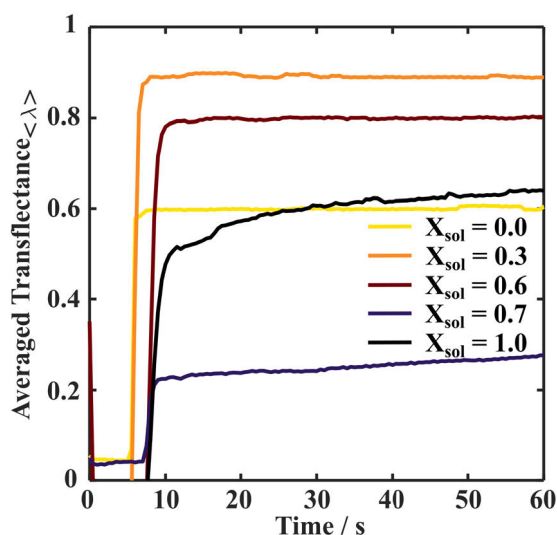

Figure 5.9: Averaged transflectance for 500 – 800 nm over 60 s of spin-coating utilizing solutions with $X_{sol} = 0.0, 0.3, 0.6, 0.7$, and 1.0 in pure DMF.

Besides the halide ratio, the solvents determine the kinetics of the crystallization process. DMSO is a necessary component to slow down the crystallization and, therefore, being able to get control over the formation by an increased process window (Figure 5.8). In comparison, samples spin-coated from DMF show a fast crystallization after 5 - 8 s, having a short process window

independent of the halide ratio (Figure 5.9). Since the absorption spectra for all samples prepared from pure DMF are dominated by scattering, no detailed statement about the specific phase forming can be made. Thus, not only the halide ratio but also a specific solvent system significantly influences the crystallization onset. Due to the complex interplay of lead halide precursors and solvents, the solution chemistry affects the crystallization onset and, thus, the morphology of the final sample. This brief comparison points out the importance of a detailed understanding of the multifaceted formation processes and the optimization of the modified precursor solutions.

5.4.2 Film formation process during annealing

In addition to spin-coating, the subsequent thermal annealing was investigated by in-situ UV-vis measurements and by ex-situ XRD characterization on the final films to track changes in sample composition and (in)homogeneity during this completing preparation step. The UV-vis spectra at the end of spin-coating and beginning of annealing correspond to each other. Small discrepancies in experimental data sets are a result of measurements carried out on different samples and due to calibration effects (Chapter 5.2 and 5.3).

Figure 5.10 illustrates the annealing for the as-cast pure bromide film (X_{sol} = 0.0). During annealing, a stable absorption onset at 550 nm presents no optical changes in the MAPbBr₃, directly formed during spin-coating. For the XRD pattern on the annealed film, the perovskite peak remains at 2θ = 14.9. Hence, during annealing no further (re)formation process appears for the pure MAPbBr₃ and the perovskite formation can be assumed to be completed after spin-coating, mainly residual solvents evaporate from the thin-film. However, slight peaks around 2θ = 13 and 2θ = 14 indicate a small amount of a secondary phase, formed during annealing, which could not be identified due to low peak intensities.
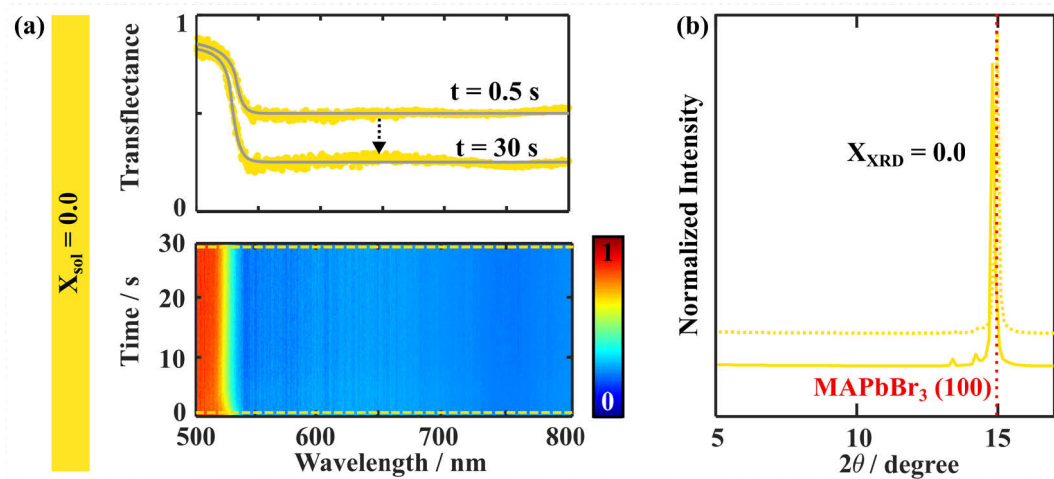

Figure 5.10: Film formation process during annealing of MAPbBr₃, X_{sol} = 0.0. In-situ UV-vis measurements (a) during the first 30 s of annealing present the evolution of the transflectance over time (bottom) and selected single-spectra (top) indicating key formation steps. The XRD patterns (b) of the annealed film (solid line) and the as-cast film (dashed line) compare crystalline phases before and after annealing. The red dashed line indicates the 100 reflection for cubic MAPbBr₃.[153] X_{XRD} specifies the amount of iodide in the perovskite phase derived from the XRD peak position according to the calibration curve (Figure A.2.1).

For the as-cast film from X_{sol} = 0.3 (Figure 5.11(a)) no significant changes in terms of absorption onset are identified between the last scan of the spin-coating and the first scan of the annealing

process. In comparison to the heat map for $X_{sol} = 0.0$ (Figure 5.10 (a)) a significant difference in the evolution of the absorption onset arises after 8 s of annealing. The absorption edge is shifting from 570 nm to longer wavelengths within these first seconds of annealing. The final absorption edge at 630 nm suggests the incorporation of iodide into the perovskite phase from the $(MA)_2(DMSO)_2Pb_3I_8$ solvate phase which disappears upon annealing evidenced by XRD measurements (Figure 5.11 (c)). The amount of iodide in the film determined from UV-vis measurements after annealing is $X_{UVvis} = 0.3$, corresponding to the halide ratio in the precursor solution $X_{sol} = 0.3$. Having a detailed look at the individual spectra, the absorption edge after spin-coating remains at 570 nm corresponding to X_{UVVis} of 0.08. After 6 s, a shoulder starts growing within a time range of 3 s indicating the formation of a perovskite phase with $X_{UVvis} = 0.26$, which quickly grows beside the remaining absorption at 550 nm. After 30 s of annealing, the two perovskite phases are found to equilibrate by an exchange of anions and incorporation of further iodide with an absorption edge of 620 nm. Due to an increase in scattering while annealing, an increase in the baseline and a small amount of a possibly forming iodide-rich perovskite phase cannot be distinguished. While solvent molecules evaporate during annealing the solvent intermediate phase is enabled to form an iodide-rich perovskite phase. However, XRD measurements performed directly after annealing exhibit residual PbI_2 and PbIBr (Figure A.2.5) for all samples containing iodide. Thus, during the fast temperature induced annealing process not all $(MA)_2(DMSO)_2Pb_3I_8$ solvate phase is directly converted to crystalline perovskite and small amounts of PbI_2 remain. Therefore, the reformation into a pure perovskite is not completed immediately after annealing. Only slow phase reconstruction processes at room temperature in N_2 atmosphere overnight result in a pure perovskite phase.
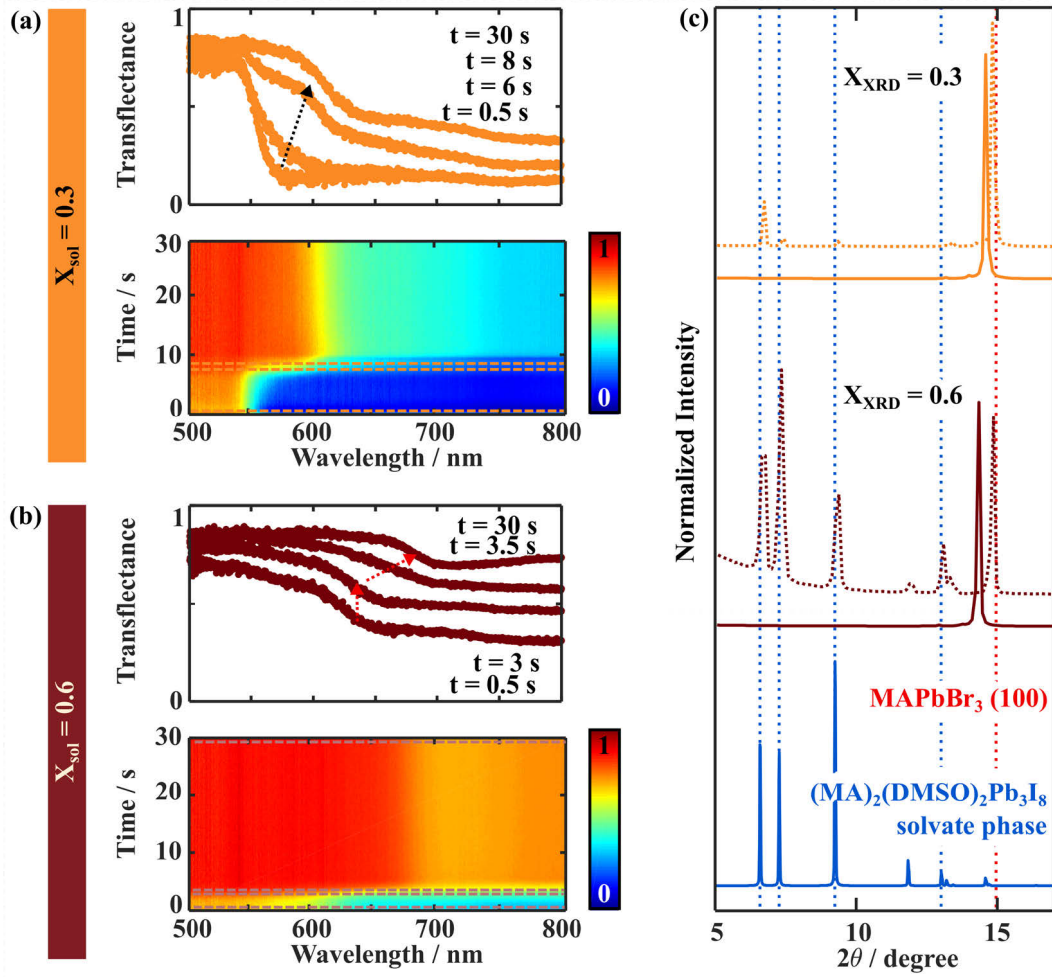
Figure 5.11: Film formation process during annealing of X_{sol} = 0.3 and 0.6. In-situ UV-vis measurements (a and b) during the first 30 s of annealing present the evolution of the transflectance over time (bottom) and selected single-spectra (top) indicating key formation steps. The XRD patterns (c) of the annealed films (solid line) and the as-cast films (dashed line) compare crystalline phases before and after annealing. The red dashed line indicates the 100 reflection for cubic MAPbBr₃.[153] The (MA)₂(DMSO)₂Pb₃I₈ solvate phase[75] is shown in blue at the bottom with the main reflections indicated by dashed blue lines. X_{XRD} specifies the amount of iodide in the perovskite phase derived from the XRD measurement according to the calibration curve (Figure A.2.1).

The XRD pattern of the final film shows the conversion of the iodide-rich solvate intermediate phase and the bromide-rich perovskite phase to the desired perovskite phase with X_{XRD} = 0.3. However, the FWHM of the main perovskite peak is with 0.13 the highest among the MAPb(IₓBr₁₋ₓ)₃ series, indicating a certain heterogeneity in the films prepared from X_{sol} = 0.3 (Figure 5.12).

Tracking the annealing of the films spin-coated for X_{sol} = 0.6 by in-situ UV-vis measurements (Figure 5.11 (b)) the same stepped shift of the absorption edge can be identified as for X_{sol} = 0.3. The shift of the absorption onset from 650 nm to 700 nm again confirms the incorporation of iodide in the perovskite phase. Here as well, mixed-in and measured iodide concentration from in-situ UV-vis match at $X_{sol/UVvis}$ = 0.6.

After annealing, no XRD reflections of the $(MA)_2(DMSO)_2Pb_3I_8$ solvate phase are visible and the reflections related to the perovskite crystal phases are shifted from $2\theta = 14.8$ to $2\theta = 14.3$ (Figure 5.11 (c)). These changes indicate the incorporation of the iodide remaining in the solvate phase after spin-coating into the bromide-rich perovskite phase forming a more mixed phase with $X_{XRD} = 0.6$. The FWHM of the 100 reflection in the XRD pattern of annealed films for perovskite phases forming via a bromide-rich perovskite phase and an iodide-rich solvate phase show a slightly higher FWHM of 0.11 to 0.13 compared to films that form directly or via the intermediate phase with a FWHM of 0.10 (Figure 5.12). These results indicate that the formation of mixed bromide/iodide thin-films via the intermittent formation of bromide-rich perovskite and iodide-rich solvate phases is detrimental. The increase in FWHM indicates a certain level of structural and ionic inhomogeneity even after annealing. The halide intermixing during annealing could not completely compensate for the halide separation caused by the heterogeneous formation during spin-coating.
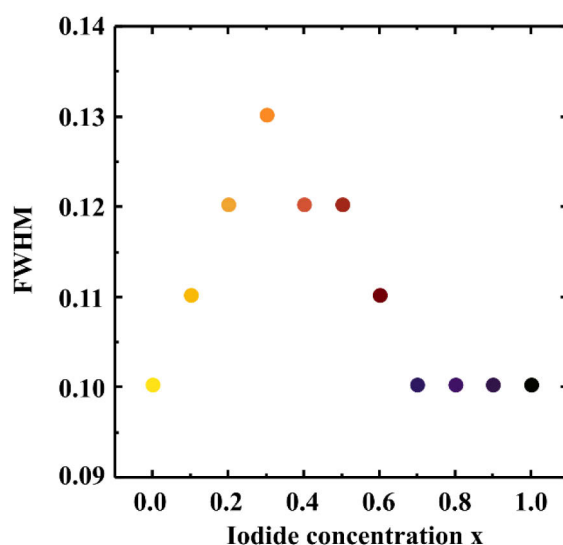

Figure 5.12: FWHM of the 100/ 110 perovskite reflection in the MAPb(IₓBr₁₋ₓ)₃ series of the annealed films.

For the as-cast films from $X_{sol} = 0.7$ and 1.0 no perovskite phase crystallized during spin-coating and, therefore, no absorption edge was detected. During annealing for both samples, an absorption edge grows within the first seconds of annealing at 710 nm and 770 nm, respectively (Figure 5.13 (a) and (b)). The perovskite phase for these high iodide concentrations is only formed upon annealing, making it a necessary step for the formation process. This observation is confirmed by ex-situ XRD measurements (Figure 5.13 (c)) showing only reflections corresponding to the $(MA)_2(DMSO)_2Pb_3I_8$ solvate phase after spin-coating, which disappear entirely upon annealing in favor of reflections attributable to crystalline perovskite phases at $2\theta = 14.2$ and $2\theta = 14.0$, for $X_{sol} = 0.7$ and $X_{sol} = 1$, respectively.
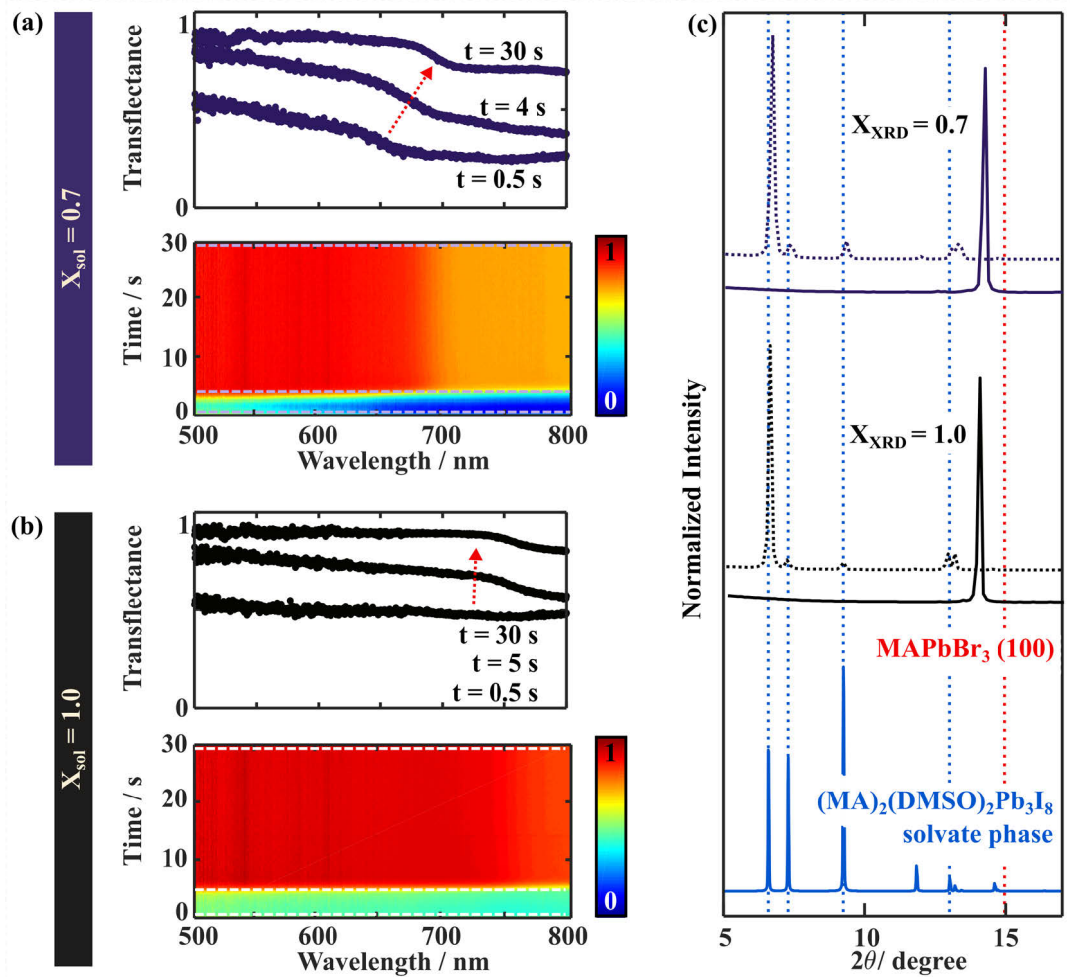
Figure 5.13: Film formation process during annealing of X_{sol} = 0.7 and 1.0. In-situ UV-vis measurements (a and b) during the first 30 s of annealing present the evolution of the transflectance over time (bottom) and selected single-spectra (top) indicating key formation steps. The XRD patterns (c) of the annealed films (solid line) and the as-cast films (dashed line) compare crystalline phases before and after annealing. The red dashed line indicates the 100 reflection for cubic MAPbBr₃.[153] The (MA)₂(DMSO)₂Pb₃I₈ solvate phase[75] is shown in blue at the bottom with the main reflections indicated by dashed blue lines. X_{XRD} specifies the amount of iodide in the perovskite phase derived from the XRD measurement according to the calibration curve (Figure A.2.1).

At first glance, the absorption features seem to decrease over time while annealing, comparing the baseline and the height of the transflectance signal. However, this is mainly an artifact, caused by increased light scattering. The latter happens because the sample roughness is increased during annealing. This results in a rise of the background signal observed during the in-situ measurements. Besides, changes in sample coverage due to perovskite crystallization and pinhole formation are observed in SEM images of samples shown in Figure 5.14. A non-unity coverage will reduce the absorptivity of the sample as discussed in Chapter 4.2. The apparent reduction in sample absorption is therefore not indicative of a decrease in perovskite semiconductor concentration during annealing but rather reflects changes in light scattering and sample coverage.
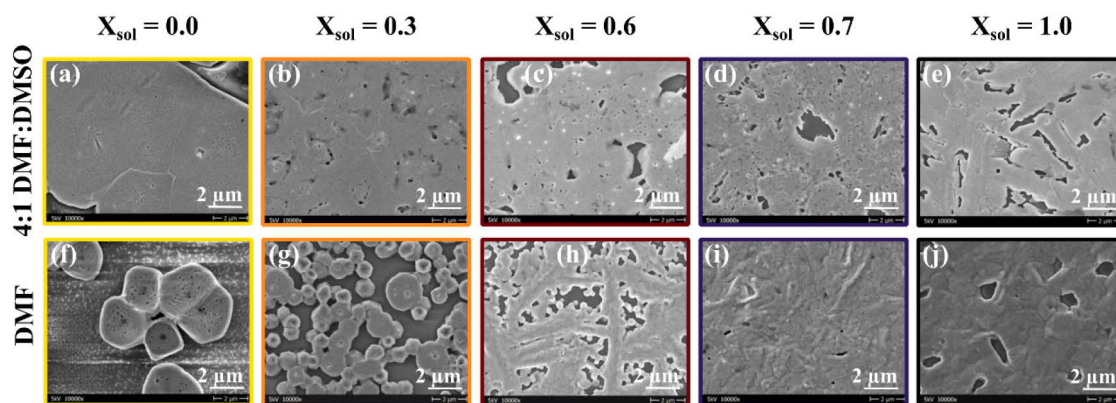
Figure 5.14: SEM top view images of perovskite thin-films prepared from 4:1 DMF:DMSO solvent system (a – e) and pure DMF (f – j), for halide ratios of X_{sol} = 0.0, 0.3, 0.6, 0.7, and 1.0.

The SEM images reveal modifications in morphology due to a varied halide ratio and the solvent system utilized. Both 4:1 DMF:DMSO (Figure 5.14 (a – e)) and the pure DMF (Figure 5.14 (f – j)) present the trend of morphology changes from more or less flat, cornered grains to a more needle-like morphology while increasing the iodide amount. Overall, this tendency is more pronounced in the pure DMF system. This template morphology is defined by the needle-like morphology of the solvate intermediate phases.[76] The template effect might be blurred out for samples prepared from 4:1 DMF:DMSO since the crystallization is delayed for all halide ratios compared to the crystallization from pure DMF (Figure 5.8 and Figure 5.9) likely resulting in a reduced template morphology.

Since no splitting of the reflection at 2θ ~ 14 - 15 (Figure A.2.1 (c)) can be identified for the full range of the MAPb(I$_x$Br$_{1-x}$)$_3$ annealed films, it is assumed that the inhomogeneity in the halide distribution is equalized during the annealing process to a certain extent. However, as shown in Figure 5.12, and established for preparation from X_{sol} = 0.3 and 0.6 above, the FWHM increases slightly for films prepared from $0.1 \leq X_{sol} \leq 0.6$, represented by a broadening of the XRD peak. This broadening can be rationalized with some compositional inhomogeneity retained in the films after the annealing process. Indeed the motivation and hypothesis of this work were to rationalize this compositional inhomogeneity often observed in mixed bromide/iodide samples and, therefore, with these findings, it is possible to explain its origin to be due to heterogeneous crystallization as evidenced by the conducted measurements.

Expect for the pure bromide perovskite, the annealing is a necessary formation step to go to the desired mixed halide perovskite phase: for $X_{sol} \leq 0.6$ the reformation of bromide-rich perovskite and the iodide-rich solvate phase proceeds, while for samples prepared from $X_{sol} \geq 0.7$ annealing includes the final perovskite formation from the intermediate solvate phase.

5.4.3 Halide exchange during slow drying process at room temperature

During the two common preparation steps spin-coating and annealing, a dynamic exchange of halides occurs between the two enriched phases for samples prepared from $0.1 \leq X_{sol} \leq 0.6$, which leads to increased heterogeneity in the film. To investigate this phenomenon more, a slow drying process upon room temperature was investigated with in-situ UV-vis measurements on a short (60 s) and with XRD measurements on a longer (3 h) time scale.
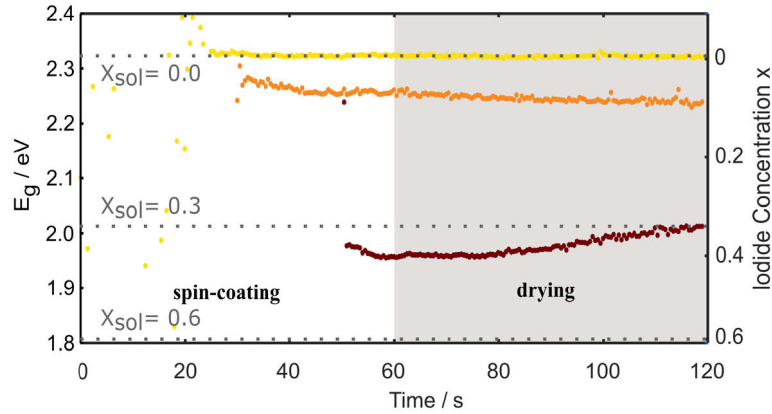
Figure 5.15: Fitted bandgap (E_g) evolution (left axis) and corresponding iodide concentration x (right axis) of the crystallized perovskite phase over 60 s of spin-coating and direct drying of additional 60 s in an inert atmosphere.

After the start of the perovskite crystallization, the corresponding bandgap from the absorption onset and thus, the halide ratio in this phase can be determined as described by Suchan *et al.*[156] as shown in Figure 5.15.

For the pure MAPbBr₃ forming from X_{sol} = 0.0 a bandgap of 2.33 eV is determined after 24 s of spin-coating. For the formed MAPbBr₃ the bandgap is stable at 2.33 eV over the entire spin-coating and subsequent drying process. As described above, MAPbBr₃ directly forms from solution and no changes in the crystallized phase occur anymore.

Films formed from X_{sol} = 0.3 and 0.6 show a shift in the bandgap and, therefore, in the halide composition of the as-cast film. For the bromide-enriched perovskite phase crystallizing from X_{sol} = 0.3 a first bandgap of 2.26 eV is determined, decreasing to 2.23 eV during spin-coating and drying. Therefore, the amount of iodide incorporated in the bromide-rich perovskite phase increases from 0.05 to 0.10. The perovskite phase crystallizing from X_{sol} = 0.6 behaves differently. First, the bromide-rich perovskite phase has a bandgap of 1.97 eV, which decreases to 1.95 eV. However, over the drying process, the bandgap increases to 2.01 eV. All these effects considered, the iodide content of the bromide-rich perovskite phase decreases from 0.38 to 0.33 during drying leading to a perovskite phase with even higher bromide content. Changes in halide composition during drying explain the difference between the iodide content determined from in-situ UV-vis and XRD on the as-cast films since around 5 min lies between the end of spin-coating and the ex-situ XRD measurement. Both samples tend towards a common stable bromide-rich perovskite phase over a longer time. This is supported by the X_{XRD} = 0.15 for the film prepared from X_{sol} = 0.6, likely aspiring to the limit of the miscibility gap determined by Lehmann *et al.*[127] to be x = 0.08 (± 0.02) for iodide incorporated in the bromide-rich phase.

The drying process over several minutes and up to 3 hours was tracked by XRD measurements in ambient conditions. The films spin-coated from X_{sol} = 0.0 show no significant changes during drying (Figure 5.16 (a)). The MAPbBr₃ is stable under these drying conditions; no reformation, degradation, or evolution of additional secondary phases is detected. The FWHM during and after this slow drying process is increased to 0.15, compared to 0.10 after a rapid annealing process (Figure 5.17). Since no ionic inhomogeneity may exist in these samples, the higher FWHM indicates defects in terms of strain and disorder in the film. Therefore, annealing in bromides seems to be a necessary step to end up with high-quality films.

During the drying process of as-cast films from $X_{sol} = 0.3$, the $(MA)_2(DMSO)_2Pb_3I_8$ solvate intermediate phase reflection intensity at $2\theta = 6.7$ and 7.2 decreases within the first 9 min of drying and these reflections have completely disappeared after 3 h (Figure 5.16 (b_1)) indicating the decomposition of the crystalline intermediate solvate phase upon slow solvent evaporation. At the same time, the perovskite reflection remains at $2\theta = 14.8$ (Figure 5.16 (b_2)). However, in the first scan, a shoulder to higher 2θ values appears. After 3 h of drying and the complete disappearance of the solvate phase, a shoulder to lower 2θ values appears. Although the shoulder shifts and indicates the incorporation of the iodide from the solvate phase into the perovskite structure, the FWHM decreases slightly from 0.12 to 0.11 over the drying process (Figure 5.17 (b)) and is overall a bit lower than for the rapid annealing process. Additionally, no significant peak shift can be overserved for 3 h of drying compared to the rapid annealing process (Figure 5.11 (c)). These observations may indicate a broad distribution of different bromide/iodide ratios in the crystallites in very small quantities, represented at low peak intensity.
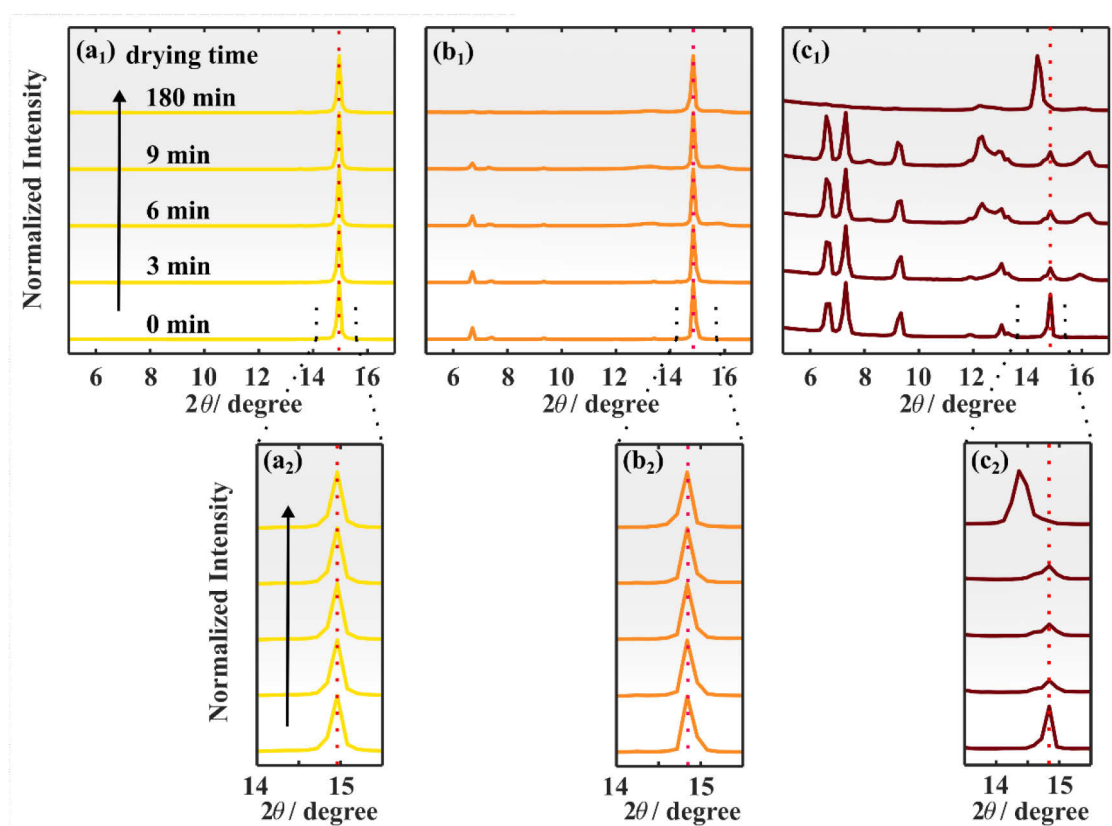

Figure 5.16: XRD patterns of as-cast films from (a) $X_{sol} = 0.0$, (b) $X_{sol} = 0.3$ and (c) $X_{sol} = 0.6$ during the slow drying process at room temperature, measured at the start (5 min after finishing spin-coating) and 3 min, 6 min, 9 min and roughly 3 h after the first scan in ambient atmosphere. In (1) the XRD pattern from $2\theta = 5 - 17$ present the main reflections for the $(MA)_2(DMSO)_2Pb_3I_8$ solvate and perovskite phase, while (2) shows a zoom on the 100/ 110 perovskite reflection, respectively.

The drying process for the films spin-coated from $X_{sol} = 0.6$ starts from the bromide-rich perovskite phase and the $(MA)_2(DMSO)_2Pb_3I_8$ intermediate solvate phase. After 9 min of drying the solvate phase is still clearly present and only disappears after 3 h of drying. Due to the higher amount of the $(MA)_2(DMSO)_2Pb_3I_8$ solvate intermediate phase formed during spin-coating (Figure 5.7) overall more solvent is strongly coordinated within the as-cast film, likely slowing down the drying process. The drying process for $X_{sol} = 0.6$ is more complex since the perovskite reflection decreases

while drying and several reflections around 2θ = 12 - 13 and 2θ = 15 – 16 arise, indicating different solvate phases.[75,76] Hence, the intermediate solvate phase is not directly transformed into a perovskite phase. The perovskite reflection intensity is decreasing while drying, indicating that the formed perovskite phase is dissolving or getting amorphous during this slow process. Additionally, the perovskite peak has shifted from 2θ = 14.7 to 2θ = 14.2 while drying and, therefore, the iodide is incorporated into the perovskite phase. However, heterogeneity increases during the slow drying process, represented by the FWHM of the perovskite peak increasing strongly from 0.12 to 0.26 (Figure 5.17).

In total, the kinetically formed bromide-enriched perovskite phase is not stable upon a slow drying process at room temperature. Altogether, the intermediate solvate phase is slowly decomposed and perovskite forms due to slow solvent evaporation. Depending on the mixed-in halide ratio, different re-formation processes proceed to some extent increasing heterogeneity and lower film quality.
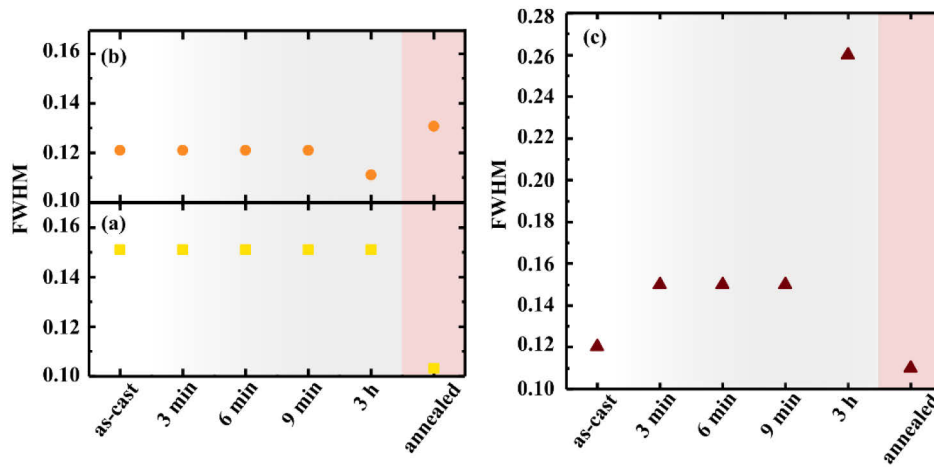

Figure 5.17: FWHM for the main (100/ 110) perovskite reflection of the as-cast film, all drying stages and the annealed film. Samples have been spin-coated from (a) X_{sol} = 0.0, X_{sol} = 0.3 and (c) X_{sol} = 0.6.

For the drying process of the films from X_{sol} = 0.7 and 1.0 no significant changes are identified during the first 9 min of drying (Figure 5.18) indicating the $(MA)_2(DMSO)_2Pb_3I_8$ intermediate solvate phase is stable under these drying conditions in room temperature and air. Only after 3 h, a perovskite reflection arises in both cases, at 2θ = 14.2 and 14.0, respectively. However, the reflections for the $(MA)_2(DMSO)_2Pb_3I_8$ solvate intermediate phase are still clearly identified. Overall, the strongly coordinating solvent DMSO slows down the drying process for theses samples compared to the ones with a lower iodide content and the re-formation into a perovskite is not completed after 3 h. Therefore, the solvate intermediate phase is stable in this time regime under the given conditions, strengthening that annealing is a necessary step to convert the solvate intermediate phase quickly into the desired perovskite.
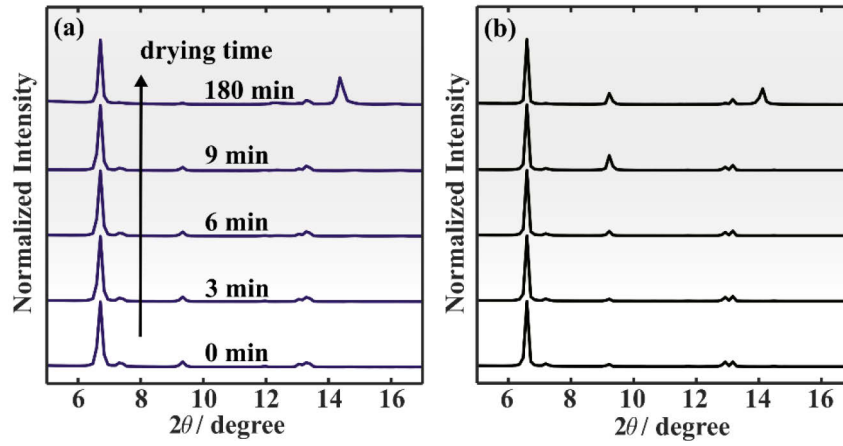
Figure 5.18: XRD patterns during a slow drying process at room temperature measured at the start (5 min after finishing spin-coating) and after 3 min, 6 min, 9 min and roughly 3 h in ambient atmosphere for (a) $X_{sol} = 0.7$ and (b) $X_{sol} = 1.0$.

5.5 Conclusion

In the model system $MAPb(I_xBr_{1-x})_3$ prepared from 4:1 DMF:DMSO the formation process is highly influenced by the halides and their ratio (X_{sol}). Coordination and binding interactions between molecules in solution are accountable for different formation pathways and competing formation processes. This is sketched in Figure 5.19.
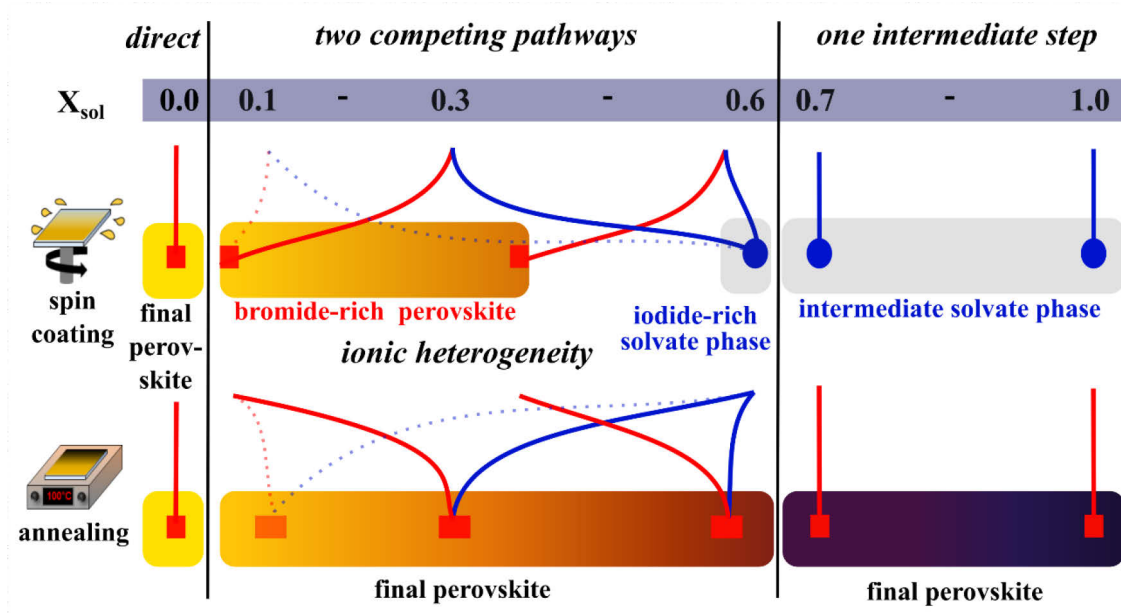

Figure 5.19: Schematic overview of the $MAPb(I_xBr_{1-x})_3$ formation processes from 4:1 DMF:DMSO indicating key steps during spin-coating and annealing from $X_{sol} = 0.0$ to $X_{sol} = 1.0$. Mixed in iodide amounts (X_{sol}) are given in the upper panel. Solid lines state formation pathways of $X_{sol} = 0.0$, 0.3, 0.6, 0.7, and 1.0 discussed in detail, while the formation pathway of $X_{sol} = 0.1$, only briefly discussed in Appendix A.2, is indicated in dashed lines. Red represents the formation of a perovskite phase, and blue the formation of the $(MA)_2(DMSO)_2Pb_3I_8$ intermediate solvate phase.

The pure bromide ($X_{sol} = 0.0$) forms via a *direct crystallization* into the desired perovskite phase, directly during spin-coating without any intermediate solvate phase due to weak bromide-solvent interactions. No further phase transition takes place upon annealing; only residual solvent evaporates.

For mixed halide ratios of $0.1 \leq X_{sol} \leq 0.6$ a heterogeneous formation proceeds with *two competing pathways*, one favoring the direct crystallization of a bromide-rich perovskite, the other favoring the crystallization of the iodide-rich $(MA)_2(DMSO)_2Pb_3I_8$ solvate intermediate phase. The exact bromide amount in the bromide-rich perovskite varies with X_{sol}. Ionic heterogeneity of annealed samples stems from this inhomogeneous intermediate state of the sample when solvate and perovskite phase co-crystallize during spin-coating. By halide incorporation and phase reconstruction during annealing, the degree of heterogeneity after spin-coating is decreased as the solvate phase decomposes into an iodide-rich perovskite phase that equilibrates with the bromide-rich perovskite phase by ion exchange and diffusion. This is the reason for the intrinsic heterogeneity introduced during the formation process. Interestingly, samples within a similar halide ratio show strong phase segregation and high losses in V_{OC} when implemented in perovskite

solar cell devices. A higher degree of ionic heterogeneity in thin-films formed via these two contrary pathways might go along with phase segregation and V_{OC} losses.

Mixed halide perovskite from solutions with $X_{sol} \geq 0.7$ only forms an *intermediate solvate phase* upon spin-coating. The preferred formation of $(MA)_2(DMSO)_2Pb_3I_8$ determines the overall formation process and the perovskite phase grows from this phase upon annealing. Therefore, the formation results in an ionically more homogenous film, compared to films prepared from $0.1 \leq X_{sol} \leq 0.6$ forming via two competing processes. Crystallization kinetics allowing thermal quenching for a late crystallization might additionally increase homogeneity. However, the $(MA)_2(DMSO)_2Pb_3I_8$ intermediate phase crystallizes in a more needle-like structure predefining the morphology of the final perovskite thin-film even after annealing.

Concluding, thermal annealing is a detrimental step to transform the as-cast heterogeneous films into a more homogeneous perovskite film. Drying processes under room temperature convert the intermediates of the as-cast films only slowly into a perovskite film with increased heterogeneity and decreased film quality, supporting the relevance of a fast thermal quenching via annealing.

Therefore, future research should focus on solvent and additive engineering to further improve the perovskite film formation and layer morphology. One way might be to develop solvent systems accounting for the different binding constants, resulting in chemical equilibria and crystalline solvate intermediate phases of iodide and bromide to support homogeneous crystallization and to avoid disruptive intermediates. Studies on iodide based perovskite solutions already show, how the use of high coordinating solvents tailoring complexes and colloids formed in solution and the use of low coordinating solvents enabling control over solution and process properties improves the formation of perovskites.[157,158] A new or improved solvent system for mixed halide solutions can prevent competing formation processes resulting in homogenous films.

6. Role of the precursor solution composition on the formation process of bromide-based perovskite during spin-coating

This chapter rationalizes the individual influence of chemical preparation parameters on the formation process of bromide-based perovskite thin-films to simplify and target the preparation optimization of requested perovskite thin-film characteristics. Gaining an understanding of each parameter is key to design a successful preparation routine with minimal experimental effort and resources.

With in-situ spectroscopy, the influence on the formation process of the following chemical preparation parameters is evaluated: the anti-solvent drop, the solvent system, the A^+ site cation, and the solution concentration. Based on the strong dependency of the crystallization onset during film formation on the solution concentration, modifications in the wet-film thinning behavior and the solution characteristics are investigated in more detail. Complex and colloid chemistry varies with the concentration and affects the formation process. Wet-film thinning is identified as a critical step during perovskite formation, though, up to now just streamlines for these systems. Thus, a model for multi-layer thinning during perovskite preparation is drawn to fully rationalize the perovskite formation process with the gained insights on the impact of each chemical preparation parameter.

6.1 Introduction

The reliability and reproducibility of high-quality perovskite thin-films are essential for manufacturing and improvement in perovskite-based opto-electronic devices.[159–161] In addition, accurate and trustworthy characterization of perovskite thin-film properties requires a high material quality for all possible compositions. Sample quality strongly influences already relatively simple UV-vis measurements.[46] Another example are ellipsometry measurements. Here, homogeneous and smooth thin-films are necessary to determine solid optical properties, namely *n,k* values. Those optical characteristics enter device simulation,[112] as well as wet-film thinning discussed in Chapter 6.4.5. Hence, they are a critical feature for accurate calculations. Overall, the preparation and the connected formation pathway dictate the perovskite thin-film quality. Thus, rationalizing perovskite formation is key to reliable high-quality thin-films.

Lately, studies focus on clarifying the formation process of $MAPbI_3$ and $(Cs_{0.08}MA_{0.15}FA_{0.77})Pb(Br_{0.15}I_{0.90})_3$ thin-films that are widely utilized and investigated in solar cell devices.[146,151,162] This top-down approach aims for the evaluation of established preparation routines and reasoning device performance. However, a bottom-up approach rationalizing the influence of individual preparation parameters will enable targeted process development for solution-based perovskite deposition. The perovskite preparation depends on a multitude of parameters classified within this study into technical parameters such as spin speed and time, temperature, atmosphere, annealing temperature and time, and chemical parameters like solvent, anti-solvent, precursor salts defining the composition, and solution concentration.

The defined chemical parameters are expected to have a major influence on the formation process due to complex formation in solution[15,163] and stable solvate phases.[75,76,164] Especially, solvate phases introduces an intermediate step in the formation of iodide-based perovskites.[165] On the contrary, as discussed in Chapter 5, bromide-based perovskites form directly from solution during the spin-coating as they interact weaker with solvents[74] and only the specific $FA_2PbBr_4\cdot2DMSO$ solvate phase is identified recently.[164] Therefore, a first rationalization of chemical parameters influencing the perovskite formation process by optical in-situ data appears suitable on bromide-based perovskites.

Furthermore, wide bandgap, bromide-based perovskites are studied less, compared to their low bandgap, iodide-based counterparts (Chapter 2.3). The $3CatPbBr_3$ perovskite, introduced by Kulbak *et al.*[166], demonstrates the most promising results for wide bandgap, high-efficiency solar cell devices. Major improvements are postulated upon optimization of the $3CatPbBr_3$ thin-film. To achieve this objective target-orientated evaluation, the underlying film formation processes is essential to optimize and increase performance of bromide-based, opto-electronic devices.
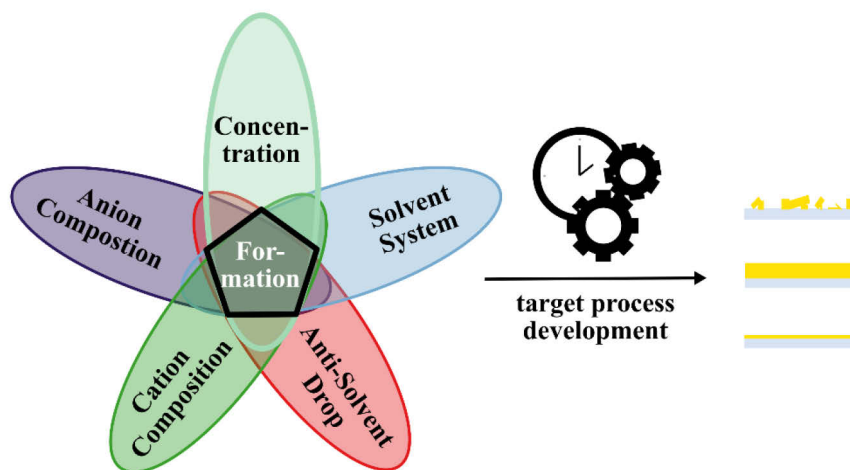
Figure 6.1: Schematic overview illustrating the investigated chemical preparation parameters influencing the perovskite formation process. Rationalizing their impact paves the way to targeted process development. A special focus is on the rationalization of the solution concentration.

Therefore, this chapter focuses on ways to rationalize the effect of chemical preparation parameters on the formation process of bromide-based perovskite with in-situ spectroscopy (Figure 6.1). One chemical parameter is varied at a time, while the technical ones, such as spin-coating parameters, are kept constant. While an overview on the influence of applying an anti-solvent, the utilized solvent system, and the impact of the cation is given, the focus lies on the concentration dependency of the formation process. A reduced solution concentration, compared to concentrations applied for solar cell fabrication, is practical in printing and LED manufacturing. An earlier crystallization onset for lower concentrated solutions is determined, reasoned from connected changes in the complex and colloid solution chemistry. Thus, the concentration dictates the solution chemistry and predefines critical factors, e.g. the saturation concentration, in the formation process. Additionally, obstacles in the wet-film thinning calculation are identified and a possible model, including the thinning of multiple layers, is drawn. Such a model is relevant to evaluate complex formation processes, e.g. by dropping the anti-solvent, in detail. Overall, this study is a first contribution to rationalize preparation parameters systematically and highlights the importance of underlying solution chemistry.

6.2 Experimental

All general cleaning and preparation steps were carried out under the same conditions as described in Chapter 3.2 in N_2 filled gloveboxes. Table 6.1 gives the details for solutions prepared for the formation study on the bromide-based perovskites, depending on the influence of chemical preparation parameters.

For the solution concentration-dependent formation study a mixed cation, bromide-based perovskite was investigated introduced by Kulbak *et al.*[166], containing FA^+, MA^+, and Cs^+ as A^+ site cations. The exact composition is given in Table 6.1. Instead of $FA_{0.85}MA_{0.10}Cs_{0.05}PbBr_3$, this perovskite is stated as $3CatPbBr_3$ for easier readability.

Table 6.1: Details of bromide-based solutions prepared for the formation study, depending on the solvent system, A^+ site cation, and the solution concentration, with precursors, their ratio, concentration, and solvents utilized.

Solution	Precursor - ratio	Concentration / mol L^{-1}	Solvent
PbBr$_2$	-	1.2	7:3 DMF:DMSO
MAPbBr$_3$	MABr:PbBr$_2$ - 1:1	1.2	7:3 DMF:DMSO
MAPbBr$_3$	MABr:PbBr$_2$ - 1:1	1.2	DMF
MAPbBr$_3$	MABr:PbBr$_2$ - 1:1	1.2	4:1 DMF:DMSO
MAPbBr$_3$	MABr:PbBr$_2$ - 1:1	1.2	DMSO
FAPbBr$_3$	FABr:PbBr$_2$ - 1:1	1.2	7:3 DMF:DMSO
CsPbBr$_3$	CsBr:PbBr$_2$ - 1:1	0.4	DMSO
3CatPbBr$_3$	FABr:MABr:CsBr:PbBr$_2$ - 0.85:0.10:0.05:1.1	1.2	7:3 DMF:DMSO
3CatPbBr$_3$	FABr:MABr:CsBr:PbBr$_2$ - 0.85:0.10:0.05:1.1	0.8	7:3 DMF:DMSO
3CatPbBr$_3$	FABr:MABr:CsBr:PbBr$_2$ - 0.85:0.10:0.05:1.1	0.5	7:3 DMF:DMSO
3CatPbBr$_3$	FABr:MABr:CsBr:PbBr$_2$ - 0.85:0.10:0.05:1.1	0.1	7:3 DMF:DMSO

For the 3CatPbBr$_3$ solution, first a PbBr$_2$ stock solution was prepared. MAPbBr$_3$ and FAPbBr$_3$ solutions were realized by mixing corresponding amounts of the PbBr$_2$ solution with the respective ABr salt. Since CsBr has comparatively low solubility to FABr and MABr, the CsBr was directly mixed with corresponding amounts of FAPbBr$_3$, MAPbBr$_3$, and additional PbBr$_2$ solutions to obtain the final 3CatPbBr$_3$ solution. According to Kulbak *et al.*[166] 10 % excess of PbBr$_2$ is added into the solution. For the concentration series, the 1.2 M 3CatPbBr$_3$ solution was diluted with corresponding amounts of 7:3 DMF:DMSO to obtain concentrations of 0.8 M, 0.5 M, and 0.1 M.

Table 6.2 lists the preparation parameters for the MAPbBr$_3$, FAPbBr$_3$, and CsPbBr$_3$ films prepared with and without an anti-solvent drop:

Table 6.2: Details of perovskite thin-film preparation applied to prepare all mono-cation perovskite thin-films with and without dropping an anti-solvent, with the amount of solution, spin-coating, and annealing parameters.

Amount of solution / μL	Spin speed / rpm	Acceleration / rpm s^{-1}	Spin time / s	Annealing Temp. / °C	Annealing time / min
60	4000	4000	60	100	30

For these different chemical parameters, preparation conditions as in Chapter 5 were utilized. The perovskite thin-films were prepared without as well as with setting an anti-solvent drop of 150 μL toluene 30 s within the spin-coating process. Directly after spin-coating the films were thermally annealed.

To investigate primarily the influence of the solution concentration on the formation process of 3CatPbBr$_3$, the spin-coating and annealing parameters were kept the same within the concentration series, as stated in Table 6.3:

Table 6.3: Details of perovskite thin-film preparation applied to study the concentration dependency of the film formation of 3CatPbBr$_3$, with the amount of solution, spin-coating, and annealing parameters.

Amount of solution / µL	Spin speed / rpm	Acceleration / rpm s^{-1}	Spin time / s	Annealing Temp. / °C	Annealing time / min
60	1000 | 4000	1000 | 4000	10 | 30	100	30

The spin-coating process was performed in two steps, a slow one at 1000 rpm and a subsequent fast one at 4000 rpm. Only for the 1.2 M solution, an anti-solvent drop of 150 µL toluene was set after 17 s within the spin-coating process. Thus, for this concentration additionally, the influence of an anti-solvent drop is investigated. Here as well, the films were thermally annealed directly after finishing the spin-coating. Generally, the preparation process is following the instructions established by Kulbak *et al.*[166] for this particular 3CatPbBr$_3$ perovskite.

To rationalize the formation process of bromide-based perovskites for the above-described material compositions and preparation routes, both spin-coating and annealing were monitored by in-situ UV-vis and in-situ PL measurements; Chapter 5.2 explains these techniques.

For in-situ UV-vis measurements, substrates with an Ag mirror were utilized. Depending on the orientation of the Ag mirror, either the absorption edge evolution or the thinning behavior was investigated. To ensure a stable emission spectrum, the halogen lamp was turned on 30 min before starting the measurements. Individual spectra were collected with an integration time of 500 ms. Since no major influences in terms of phase segregation are expected for pure bromide-based perovskites, in-situ PL analysis is possible in this study. However, integration times for individual spectra needed to be adjusted for every measurement, in consequence of strongly different PLQY, especially when applying an anti-solvent drop, to avoid oversaturation of the spectrometer. Integration times of 100, 200, and 500 ms were applied during spin-coating. Longer integration times of 500, 1000, and 2000 ms were necessary during annealing due to thermal quenching and an overall lower PLQY of the solid films. In addition, no Ag mirror on the substrates was utilized due to possible oversaturation.

While monitoring the entire spin-coating process, only the first 60 sec of thermal annealing were tracked since detectable changes proceed within the first seconds of this preparation step. Recalibration is necessary after relocating the in-situ set-up in-between spin-coater and hot plate. Therefore, formation upon spin-coating and annealing are not tracked on the same sample.

6.3 Routines for in-situ spectroscopy data analysis and evaluation on the basis of chemical preparation parameters

The following provides an overview of the continuative in-situ UV-vis and in-situ PL data analysis for a detailed rationalization of perovskite formation processes. Based on varying chemical preparation parameters such as dropping an anti-solvent, changing the utilized solvents, and replacing the A$^+$ site cation, analytic routines are established. The three investigated parameters primarily influence the formation kinetics in the case of bromide-based perovskites. Additionally, obstacles in in-situ UV-vis and in-situ PL data fitting are discussed and the complementarity of the two methods is highlighted.

6.3.1 Introduction to analysis routines for in-situ spectroscopy

While the 2D heat maps of in-situ UV-vis and in-situ PL measurements give a robust overview of the general formation process (Figure A.3.1, Chapter 5), detailed data analysis and fitting are key to rationalize the perovskite formation processes in all detail.

Identifying the bandgap evolution is a crucial step to rationalize perovskite formation upon nucleation, crystallite growth, and perovskite composition. As discussed by Kückemeier *et al.*[43] the inflection point of the absorption onset can be utilized to identify the perovskite bandgap. Calculating the first derivative of each spectrum and identifying the resulting peak position via curve fitting (Figure 6.2 (b)) returns the inflection point in the transflectance spectra (Figure 6.2 (a)).
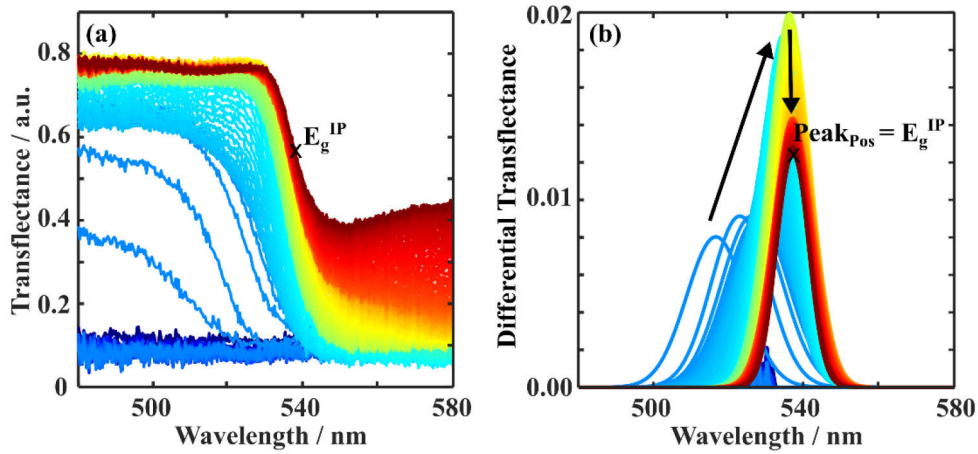

Figure 6.2: Transflectance spectra (a) and the corresponding Gaussian fit of the first derivative (b) by the example of a MAPbBr₃ film during spin-coating with dropping an anti-solvent. Based on the first derivative the bandgap evolution is determined over the spin-coating process. The color scheme represents the in-situ spectra and fitted derivative from the start (blue) to the end (red) of the spin-coating process.

The first derivative of the smoothed transflectance spectra is calculated by the numerical approximation:

$$y = [(x_2 - x_1), (x_3 - x_2), \dots]$$ (6.1)

where the elements of *y* are the differences between adjacent elements of *x*, corresponding to the difference in transflectance as a function of wavelength. This numerical approximation is preferred to an actual derivative of Lambert-Beer´s law depending on the wavelength-dependent absorption coefficient α. The actual perovskite composition, to be determined at this stage, defines the precise absorption coefficient α. Therefore, the absorption coefficient can only be estimated and Lambert-Beer´s law is not applied here.

This first derivative, calculated by a numerical approximation, is fitted with a Gaussian curve (Figure 6.2 (b)):

$$I(\lambda) = a \cdot e^{(-\frac{x - x_0}{b})^2}$$ (6.2)

where *a* is the peak amplitude, x_0 the peak position, and *b* the peak width at Full Width Half Maximum (FWHM). In principle, amplitude *a* is a measure for the quantity of semiconductor taking part in the absorption process. As discussed in Chapter 5.4.1, alterations in light scattering influence

the baseline. Therefore, the amplitude a, describing the height in transflectance, does not reflect the semiconductor quantity formed in these measurements. The peak position x_0 represents the inflection point of the respective transflectance spectrum and, thus, the bandgap of the absorbing species. The FWHM of the peak gives a value for the slope of the absorption onset. A narrow FWHM translates into a steep slope indicating a rather homogeneous film nature. A wide FWHM represents a flat slope and, thus, a more inhomogeneous perovskite film condition.

An obstacle of this bandgap analysis are in-situ UV-vis measurements mainly dominated by scattering. In such cases, the derivative of the bandgap evolution is not successful due to the low absorption above the bandgap. As an empirical value, an absorption above the bandgap ≥ 0.1 enables a reasonable determination of the bandgap and connected parameters from transflectance spectra.

Both in-situ UV-vis and in-situ PL spectra are detected in units of wavelength. In-situ PL spectra are converted into units of energy, namely eV, before data analysis by utilizing the Jacobian transformation (Figure 6.3 (a)). The Jacobian transformation involves the logarithmic dependency of wavelength and energy scale by additionally re-scaling the signal intensities:

$$f(E) = -f(\lambda)\frac{hc}{E^2} \tag{6.3}$$

where E is the respective energy in eV, h is the Planck constant, and c the speed of light. The Jacobian transformation becomes important for PL emissions at shorter wavelengths respectively higher energy. Due to the calibration by dark and bright reference spectra, such a transformation is not necessary for converting UV-vis data into the energy scale.[167,168]

In-situ PL spectra are fitted with an asymmetric Voigt curve (Figure 6.3 (b)),[151] assuming a mixture of Gaussian and Lorentzian shares:

$$f(x) = \frac{a}{\left[1+\frac{m(x-x_0)^2}{b^2}\right]exp\left[\frac{(1-m)\{ln2(x-x_0)^2\}}{b^2}\right]} \tag{6.4}$$

where a is the peak amplitude, x_0 the peak position, m the mixing ratio of Gaussian and Lorentzian proportion, and b is the peak width corresponding approximately to the Half Width Half Maximum (HWHM).[169] By replacing the term $(x-x_0)$ with:

$$\frac{x-x_0}{\left\{\left(1+\frac{\alpha(x-x_0)}{b}\right)\right\}} \tag{6.5}$$

where α as the asymmetry coefficient assuming values between -2 and 2[170], peak asymmetry is taken into account.
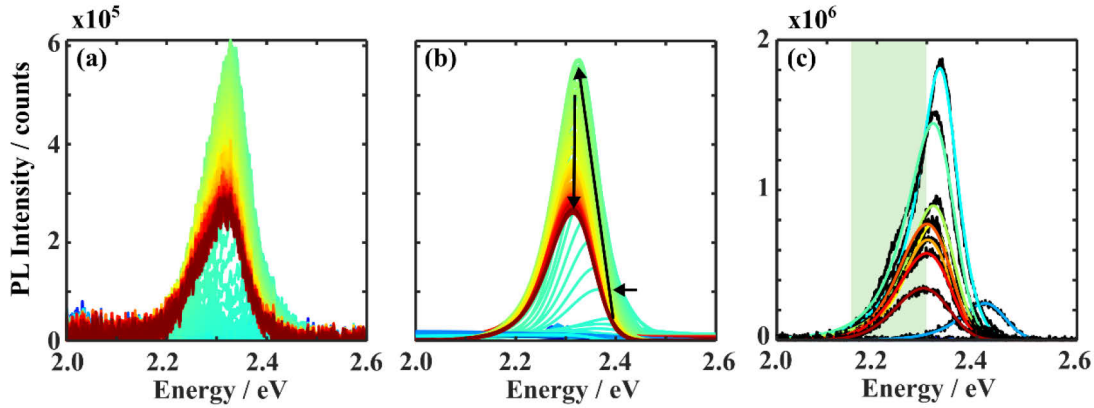
Figure 6.3: (a) PL spectra and the corresponding (b) Voigt fit by the example of a MAPbBr₃ film during spin-coating without setting an anti-solvent drop. Based on the peak intensity, position, and shape, nucleation and growth during the formation process is described. (c) presents individual PL spectra (black) with a Voigt fit (color) for spin-coating a MAPbBr₃ film with setting an anti-solvent drop. The green area marks the low energy region where one Voigt curve is not universally sufficient to model the PL signal. The color scheme represents the in-situ spectra and fitted derivative from the start (blue) to the end (red) of the spin-coating process.

The peak amplitude a corresponds to the PL intensity and, hence, to a certain extent to the relative PLQY. For a fixed working distance between the sample and reflectance probe, PL intensities are comparable. As for the averaged transflectance, an initial increase in the PL intensity indicates the crystallization onset. The peak position x_0 represents the PL emission center and its shift and is, thus, significant for the signal evolution over time. The PL peak position gives insides about nucleation and crystallite growth as well as the formed emitting phase during the formation process. The peak width b, given as the FWHM by doubling the HWHM, corresponds to the homogeneous nature of the film during crystal growth. For perovskites forming intrinsically during spin-coating, an asymmetric Voigt fit describes the PL shape satisfyingly (Figure 6.3 (a) and (b)). However, induced crystallization by dropping anti-solvent results in a pronounced shoulder towards lower energies (Figure 6.3 (c), black). In this case, fits assuming one Voigt curve do not represent the data in all details. Here, a fit with two or multiple curves would result in a more accurate representation. In general, broad peak widths and pronounced shoulders indicate a non-uniform size distribution of crystallites within the film. Since scattering has a negligible influence on the PL signal, the shape and evolution of the PL signal enable the rationalization of formation processes also for low-quality film morphologies causing a high scattering. Thus, in-situ PL provides complementary information to in-situ UV-vis data.

6.3.2 Evaluation of chemical preparation parameters on the perovskite formation process

The following chapter successively and briefly describe the individual influence of applying an anti-solvent drop, utilizing different solvent systems and varying the A^+ site cation composition on the bromide-based perovskite formation process by the above implemented analysis routines.

Influence of applying an anti-solvent drop

The 2D heat maps (Figure A.3.1) visualizing the formation of MAPbBr$_3$ (Table 6.1) without and with an anti-solvent drop, give an overview of the two processes and reveal its impact on the formation. To review this influence in more detail, analytic routines introduced in Chapter 6.3.1 are applied.

As one striking aspect, dropping an anti-solvent reduces the background in in-situ UV-vis measurements by minimizing diffuse scattering due to a more homogeneous film morphology (Figure A.3.2). While scattering dominates the transflectance signal without an anti-solvent drop, the absorption share increases setting an anti-solvent (Figure 6.4 (a) and (d)) and fitting the bandgap evolution is possible. The transflectance increases simultaneously with dropping the anti-solvent and demonstrates an induced crystallization of the pure MAPbBr$_3$ perovskite, evident from the absorption onset around 550 nm.

A look at the PL emission shows a shift from high energies in the peak position over the first seconds of crystallization, then flattening until the end of spin-coating (Figure 6.4 (b) and (e)). The fast decay in peak position upon crystallization is connected to the nucleation of small seed crystals emitting at higher energies. During crystallite growth, their emission shifts to lower energies. Since a pure MAPbBr$_3$ directly forms, inhomogeneities in the composition are excluded and do not play a role in this shift. However, re-absorption and a related filter-effect influence the peak position (Chapter 6.4.2). Thus, the largest nuclei and crystallites dominate the PL emission. The PL peak position progresses wave-like in the flat part starting ~32 s for dropping an anti-solvent, namely 2 s after setting the anti-solvent drop (Figure 6.4 (e)). This process indicates a more complex nucleation and growth mechanism, supported by a similar development in the signal derived from UV-vis measurements. Additionally, a non-uniform size distribution of crystallites based on continued nucleation and Ostwald ripening evokes the undulating FWHM (Figure 6.4 (f)). Without an anti-solvent drop the FWHM stabilizes with the flattening of the PL peak position (Figure 6.4 (c)), indicating a homogenous size distribution of crystallites.
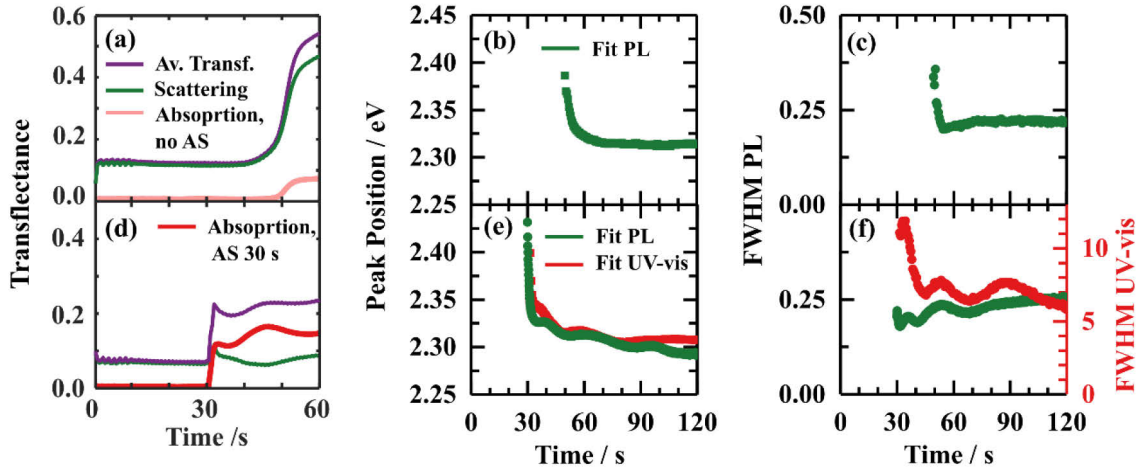
Figure 6.4: Overview of exemplary fit parameters from in-situ UV-vis and in-situ PL measurements during spin-coating MAPbBr$_3$ without (top row) and with (bottom row) dropping an anti-solvent. (a) and (d) present the averaged transflectance with scattering and absorption shares. The PL peak position (b) and the FWHM of the PL peak (c) are shown for the MAPbBr$_3$ formation without an anti-solvent drop, while (e) and (f) represent the same parameters for setting an anti-solvent. The fitted bandgap and the corresponding peak width are added in this case.

In both cases, phase pure MAPbBr$_3$ forms. The anti-solvent drop primarily improves the film morphology in terms of coverage and consequently higher-quality absorption spectra are collected (Figure A.3.2).

Overall, dropping an anti-solvent induces crystallization, affects nucleation and ongoing crystallite growth, thus, defining the film morphology. Optimizing the anti-solvent drop time allows tailoring the crystallite size of the final films (Chapter 4.3).

Influence of utilized solvent system

To evaluate the influence of the solvent system, the two common solvents DMF, DMSO, and a commonly used 4:1 mixture of both are utilized for solution preparation.

The correlated increase in PL peak intensity and averaged transflectance (Figure 6.5 (a) and (b)) demonstrates a delayed crystallization onset for solutions containing higher shares of polar DMSO. The absorption onset confirms the direct formation of MAPbBr$_3$. For all three solvent systems, the PL peak position as well as the bandgap shift from high energies after the onset of crystallization and process linearly during the ongoing spin-coating (Figure 6.5 (c) - (e)). This shift indicates fast crystallite growth from seed crystals. A flattened slope in the PL shift, accompanied by a flattened increase in transflectance with increasing amounts of DMSO, indicates a slower crystallite growth. The stable FWHM, demonstrate a homogeneous size distribution of the crystallites independent from the utilized solvent system (Figure 6.5 (f)). A fluctuation in the first seconds is most likely connected to a fitting issue due to the strong increase of the signal.
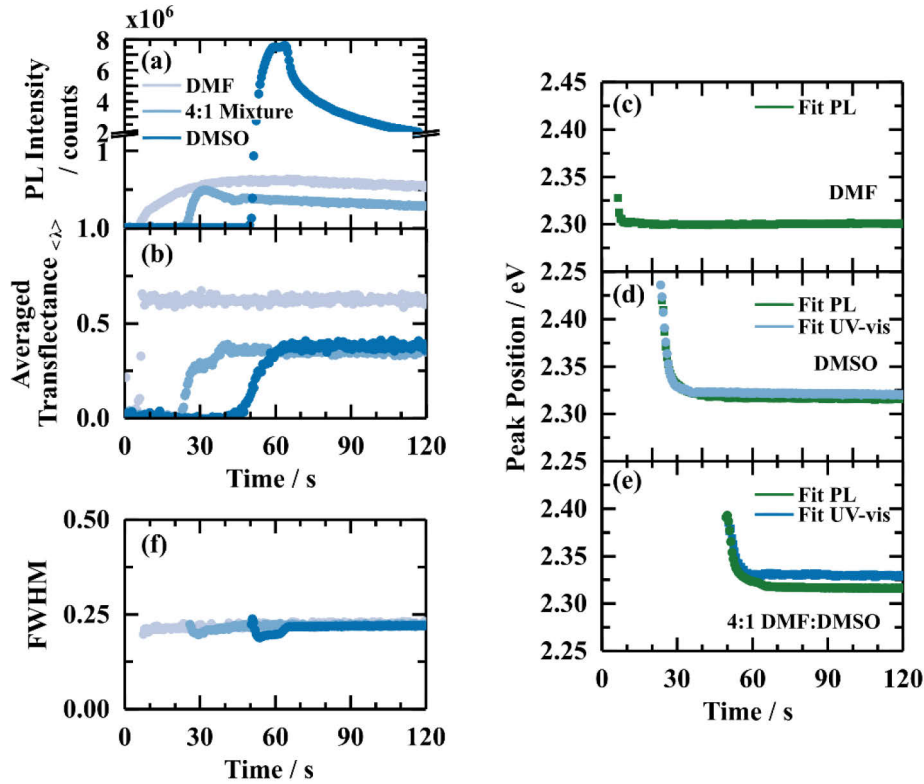
Figure 6.5: Overview of fit parameters from in-situ UV-vis and in-situ PL measurements during spin-coating MAPbBr$_3$ for 120 s utilizing the solvent systems DMF (grey), 4:1 DMF:DMSO (light blue), and DMSO (dark blue). (a) and (b) present the PL intensity and the averaged transflectance for all three solvent systems, respectively. The PL peak positions of (b) DMF, (c) 4:1 DMF:DMSO, (e) DMSO is demonstrated, for (d) and (e) the bandgap evolution is added. (f) shows the FWHM of the PL peaks.

Pure MAPbBr$_3$ thin-films can be obtained from all three solvent systems. A rising share of DMSO results in a slower formation process and increased coverage, thus improving the morphology. The latter accompanies higher quality absorption spectra (Figure A.3.3).

The solvent system influence mainly the time of intrinsic crystallization and, thus, opens up a larger process window for higher ratios of DMSO utilized. The crystallite growth is slowed down, resulting in higher film quality. However, the solvent system will have a major impact on the formation process in iodide-containing perovskites[165] due to different solvate phases forming due to the available solvent molecules.

Influence of the A$^+$ site cation

Compared to MAPbBr$_3$ crystallizing ~50 s within the spin-coating process, the PL intensity and the averaged transflectance (Figure 6.6 (a) and (b), light green) demonstrate a delayed crystallization onset ~60 s for FAPbBr$_3$. Similarly, the PL emission position decays from high energies due to crystallite growth after nucleation (Figure 6.6 (c)). However, the slope in the case of FAPbBr$_3$ runs flatter and, thus, crystallites grow slower. The PL peak position decays slowly even for later spin-coating times, indicating ongoing growth. The FWHM (Figure 6.6 (e)) progresses stable for these later spin-coating times, presenting a homogeneous crystallite size.

Also, in the case of $FAPbBr_3$, dropping an anti-solvent induces crystallization evident by an increase in PL intensity (Figure 6.6 (a)). An increase in the averaged transflectance is detected only 10 s later. The PL peak position increases from 2.35 eV to 2.39 eV connected to a shrinking of seed crystals. A high amount of residual solvent might cause the dissolution of the seed crystals. The peak in the FWHM, parallel with the increase in the PL emission (Figure 6.6 (f)), indicates a variation in the crystallite size distribution. Only after 48 s within the spin-coating process, the PL signal starts shifting to lower energies and crystallite growth starts. A second increase in the averaged transflectance accompanies the starting growth.
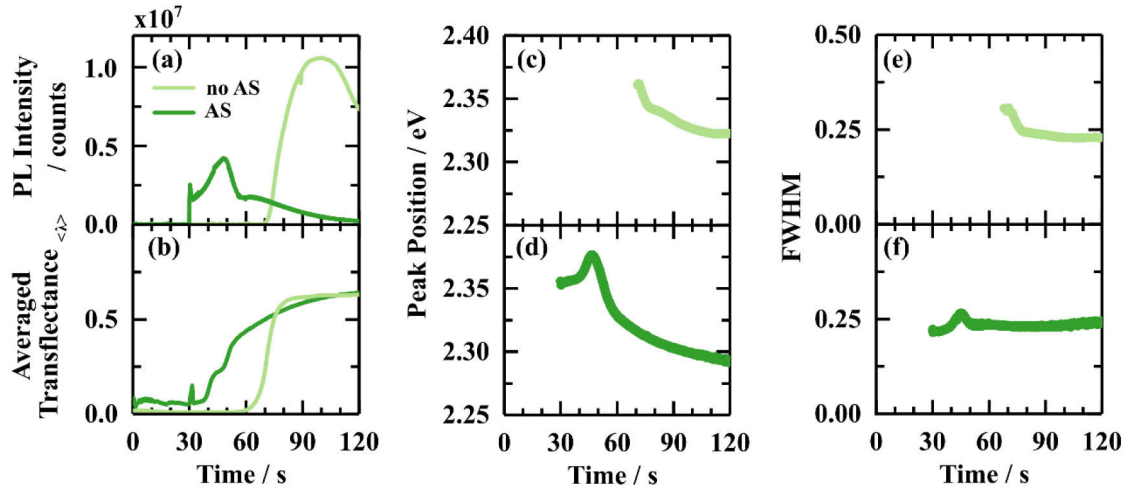

Figure 6.6 Overview of exemplary fit parameters from in-situ UV-vis and in-situ PL measurements during spin-coating process $FAPbBr_3$. (a) and (b) present the PL intensity and the averaged transflectance without (light green) and with (dark green) dropping an anti-solvent. The PL peak position (c) and the FWHM of the PL peak (e) are shown for the $FAPbBr_3$ formation without an anti-solvent drop, while (d) and (f) represent the same parameters for setting an anti-solvent.

Dropping the anti-solvent also improves the film morphology of $FAPbBr_3$. However, with and without an anti-solvent drop, no phase pure $FAPbBr_3$ is formed, indicating the necessity of further preparation optimization in this case (Figure A.3.4).

For $CsPbBr_3$ the transflectance signal is not increasing during 120 s of spin-coating without and with dropping an anti-solvent (Figure A.3.5). Nevertheless, in both cases a PL signal arises ~80 s within the process, indicating the start of a crystallization process. The formation of comparably small nucleation centers fully embedded in the wet-film might minimize the modification in scattering and, thus, not be detectable by in-situ UV-vis measurements. Overall, it is striking that dropping an anti-solvent in this specific case does not induce crystallization. Hence, the anti-solvent drop is optimizable in terms of chosen anti-solvent and timing. Due to the low solubility of CsBr, the concentration and the solvent system had to be adjusted and a direct comparison of the A^+ cation influence with $MAPbBr_3$ and $FAPbBr_3$ should not be made here. Since the anti-solvent drop is not inducing crystallization, no significant differences in the final film characteristics are identified (Figure A.3.6).

Exchanging MA^+ with FA^+ delays the crystallization onset accompanied by slowed nucleation and growth kinetics. In this special case, first, a size reduction of the induced seed crystals is identified, possibly evoked by a non-optimized timing in the drop.

Concluding, for each of the three presented chemical parameters, an individual impact on the overall bromide-based perovskite formation process is identified. Only the separate review of these three chemical parameters helps with the evaluation and rationalization of the concentration influence on the formation process in Chapter 6.4.

6.4 Rationalizing the concentration dependency of the 3CatPbBr₃ formation process

Chapter 6.4 presents and discusses the concentration dependent 3CatPbBr$_3$ film properties and the underlying formation processes based on the solution concentration series of 0.1 M, 0.5 M, 0.8 M, and 1.2 M. With in-situ spectroscopy, the formation process is evaluated in terms of crystallization onset, formation kinetics, and thinning behavior. Furthermore, differences in these formation characteristics are rationalized by concentration dependent colloid and complex solution chemistry.

6.4.1 Properties of 3CatPbBr₃ perovskite thin-films

Figure 6.7 presents SEM images highlighting differences in morphology and thickness for 3CatPbBr$_3$ films in consequence of solution concentration and dropping an anti-solvent. All films prepared from the established concentration series without an anti-solvent drop (Figure 6.7 (a) - (c)) show low coverage with isolated grains. While grains formed from the 0.5 M solution exhibit an undefined shape, grains formed from the 0.8 M and especially from the 1.2 M solution are square-shaped. Such shapes are expected for cubic MAPbBr$_3$ and FAPbBr$_3$ single crystals grown under controlled conditions. The film thickness decreases from 900 – 1000 nm for spin-coating the 1.2 M solution to 300 – 600 nm for the 0.5 M solution. For all three samples, the film thickness is very inhomogeneous and rough. Thus, SEM images demonstrate an overall low-quality morphology of the 3CatPbBr$_3$ films of the concentration series prepared without dropping an anti-solvent. Despite this low-quality morphology, the samples are still referred to as films for consistency.
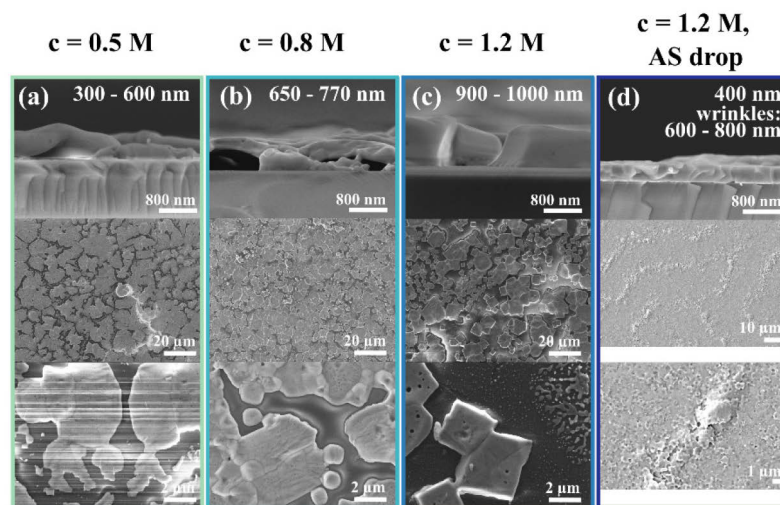

Figure 6.7: SEM images of the 3CatPbBr₃ films prepared from the solution concentration series, (a) 0.5 M, (b) 0.8 M, (c) 1.2 M, and (d) 1.2 M with an anti-solvent drop applied. The top row presents the cross section with film thickness, while the middle and bottom row present top view images at two different magnifications.

In contrast, 3CatPbBr$_3$ films prepared with an anti-solvent drop exhibit a high coverage with connected grains and no pinholes. However, a wrinkled morphology develops upon setting an anti-solvent drop. While the film itself is ~ 400 nm thick, the wrinkles reach heights of 600 – 800 nm. Braunger *et. al.*[171] and Bush *et. al.*[172] describe such a wrinkled morphology for the Cs$_{(1-y)}$FA$_y$Pb(I$_{(1-x)}$Br$_x$)$_3$ system and designate processing parameters as a reason for the formation of wrinkles. Herein, a pure bromide-based perovskite presents wrinkles, even if only weakly pronounced, for the first time.

Figure 6.8 (a) summarizes the optical properties of the 3CatPbBr$_3$ film. As expected and discussed before in Chapter 4.2, the films with a low-quality morphology, namely the ones prepared without setting an anti-solvent drop, present a feature-less, low absorption above the bandgap. Likewise, the closed 3CatPbBr$_3$ film prepared setting an anti-solvent drop exhibits a feature-full absorption above the bandgap. For all films, the absorption arises from 550 nm. The PL emission is centered at 545 nm, the sample prepared from the 1.2 M solution without an anti-solvent drop shows a minor shift to 550 nm. Overall, all four samples show a low PLQY in the range from 0.30 – 0.37 %, indicating a high concentration of defect states.

Figure 6.7 (b) presents the XRD pattern for all four 3CatPbBr$_3$ samples and confirms the formation of the perovskite phase with reflections at 2θ = 14.8, 21.0, and 29.7, comparable to the positions of cubic FAPbBr$_3$ (Chapter 4.4.1). For samples prepared without dropping an anti-solvent, an additional reflection at 2θ = 12.3 arises. Due to missing further reflections with sufficient intensities, this secondary phase is not identifiable. This reflection at 2θ = 12.3 disappears for the sample dropping an anti-solvent. Therefore, the wrinkled morphology is not evoked by a secondary phase formed and setting an anti-solvent drop results in phase pure 3CatPbBr$_3$ film. No reflections of crystalline PbBr$_2$ are identified, thus, the excess PbBr$_2$ mixed in the precursor solution probably exists in an amorphous state.
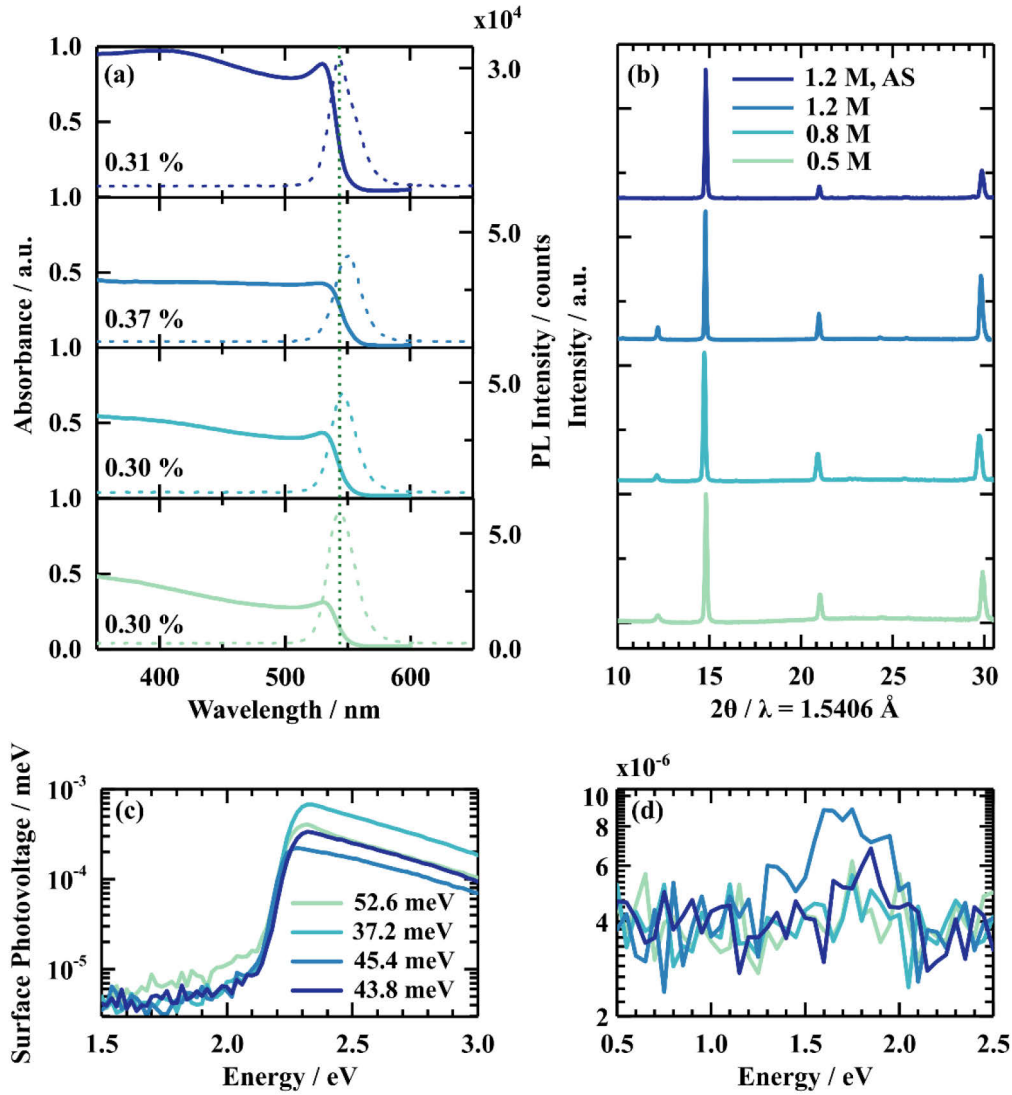
Figure 6.8: Comparison of final 3CatPbBr₃ film properties of the established solution concentration series. UV-vis and PL spectra with the PLQY (a) and the XRD pattern (b) are presented. Furthermore, (c) demonstrates the SPV overview measurements, while (d) visualizes defect sensitive measurements with a long pass filter at 610 nm in the light path.

Figure 6.8 (c) and (d) present the modulated SPV signal for the 3CatPbBr₃ concentration series measured without and with a long pass (LP) filter. Regular, modulated SPV measurements are sensitive to the bandgap and the Urbach tail (Figure 6.8 (c)). Whereas measurements with a LP filter cutting the illumination just under the bandgap are sensitive for sub-bandgap states (Figure 6.8 (c)), in case of bromide-based perovskites mid-gap defect states.[52] For all four samples, a bandgap of ~2.25 eV is determined from the increase in SPV signal. High Urbach energies varying from 37.2 - 52.6 meV, twice to triple as high as reported in literature,[52,173] are determined, indicating a high density of tail states in these samples.

Figure 6.8 (d) exhibits only a small increase in the SPV signal below the bandgap around 1.5 – 2.0 eV for samples prepared from a 1.2 M solution with and without dropping an anti-solvent, indicating the presence of mid-gap defects. The signal is not pronounced and almost vanishing in the background. Overall, the SPV signal arising from the bandgap (Figure 6.8 (c)) is one order of magnitude lower as for comparable perovskite films (Figure A.3.7). Therefore, the modulated SPV

works at its resolution limit for the detection of sub-bandgap states and no clear statement about mid-gap defect can be made for this specific set of samples. A significant difference in this set of samples is the absence of an additional conducting layer between the ITO and the $3CatPbBr_3$ perovskite film compared to others. This missing conducting interlayer might impede charge separation, reduce the overall detected photovoltage, and explain the low sensitivity for defects in this case. Therefore, previously reported defect states in $3CatPbBr_3$ samples, prepared in the same way, are not clearly identified, although low PLQY indicate a high defect concentration.

In principle, modulated SPV operates as a method to investigate in-gap defect states in wide bandgap perovskites. However, SPV results are still puzzling since measurements on different samples, prepared with the same routines, often demonstrate varied signals. In the case of perovskites, the influence of e.g. contact layers, film thickness and morphology on the SPV signal (Figure A.3.7) requires deeper insights to fully rationalize mid-gap defects in bromide-based perovskites. However, such a study is out of the scope of this work.

Evaluating the $3CatPbBr_3$ thin-film properties demonstrates the influence of the solution concentration and dropping an anti-solvent mainly on morphology and structure, and consequently on optical properties. Therefore, the following Chapters 6.4.2 and 6.4.3 focus on rationalizing the concentration dependency of the formation process. In Chapter 6.5 the influence of the anti-solvent drop on the $3CatPbBr_3$ formation is discussed in detail.

6.4.2 Concentration dependency of the 3CatPbBr₃ formation process

Figure 6.9 presents in-situ UV-vis measurements while spin-coating for the three 3CatPbBr₃ solution concentrations, 0.5 M, 0.8 M, and 1.2 M. To investigate the intrinsic formation processes, the films are spin-coated without an anti-solvent drop. For comparability spin speeds and acceleration time are kept constant, while the overall spin-coating time is increased from 40 s to 60 s or respectively 120 s compared to the recipe established by Kulbak *et al.*[166].
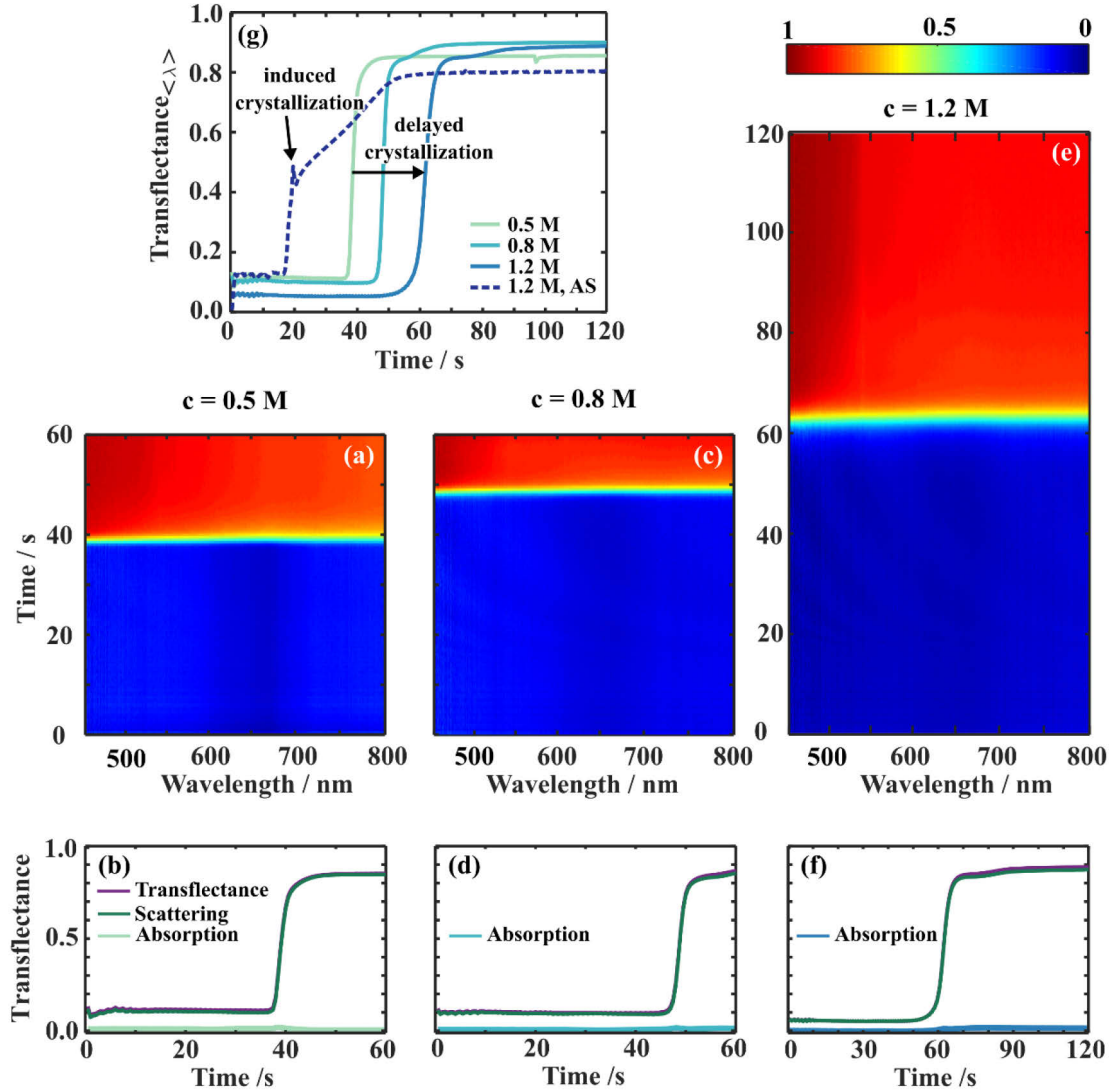

Figure 6.9: In-situ UV-vis measurements on the concentration series of 3CatPbBr₃ solutions during spin-coating. The 2D heat maps present the transflectance data over 60 s or 120 s of spin-coating for the (a) 0.5 M, (c) 0.8 M, and (e) 1.2 M solution while (b), (c), and (d) represent the averaged transflectance from 450 – 800 nm (purple), with the fitted scattering (green) and absorption shares over the process time. Averaged transflectance over time is compared in (g) for all three concentrations. A rise in transflectance indicates the time of crystallization. Higher concentrated solutions crystallize delayed. The crystallization can be induced by setting an anti-solvent drop, as shown for the 1.2 M solution, see Chapter 6.5.

The 2D heat maps of the 0.1 M and 0.5 M solution (Figure 6.9 (a) and (c)) display an increase in the transflectance signal during 60 s of spin-coating. For the higher concentrated 1.2 M solution, an increase in the transflectance signal is only detected extending the regular spin-coating time to 120 s (Figure 6.9 (e)). Although a transflectance signal evolves for the three concentrations, no explicit

absorption edge around 500 - 550 nm is identified. Scattering (green) dominates the mean transflectance signals (purple, Figure 6.7 (b, d, and f)) for the concentration series over the entire wavelength region. Therefore, only a minor part of the detected light undergoes a transmission process. Even though the amount of absorbed light increases slightly for a higher concentrated solution, its share is vanishingly small and not giving conclusive insides in the perovskite phase evolution. In this particular $3CatPbBr_3$ series, low-quality morphology (Chapter 6.4.1) arises from the specific formation parameters, favors scattering and lowers absorption (Chapter 4.2). Since the absorption share is < 0.1, the bandgap evolution is not determinable via the first derivative. Based on previous chapters, it is assumed that also this pure bromide perovskite forms directly from solution. The poor morphology explains the high background due to scattering in the in-situ UV-vis measurements during annealing (Figure A.3.8). The high background prevents any interpretation of the annealing process.

Thus, in-situ UV-vis measurements only identify the crystallization onset through the averaged transflectance (Figure 6.9 (g)). The crystallization of the 0.5 M solution starts ~ 37 s within the spin-coating process, increasing the concentration to 0.8 M and 1.2 M delays the crystallization onset to ~45 s and ~60 s. The time dependent behavior is at the first glance contrary to expected crystallization from the LaMer model.[174] Within this model, super-saturation initializes nucleation and subsequent crystal growth. Higher concentrated solutions should reach the saturation limit faster upon solvent evaporation and, thus, crystallize earlier. These assumptions do not appear accurate for the presented perovskite system. Chapters 6.4.3 and 6.4.4 rationalize and discuss this phenomenon via supplementary in-situ measurements and solution characterization.

To rationalize the formation process of the $3CatPbBr_3$ system comprehensively, in-situ PL measurements during spin-coating are discussed in the following. In-situ PL measurements give complementary insights since the PL signal is influenced less by scattering and light-induced phase-segregation plays no role in the pure bromide-based perovskites.

Figure 6.10 (a, b, and c) present the recalculated in-situ PL measurements for the 0.5 M, 0.8 M, and 1.2 M solution in 2D heat maps. The energy scale covers the range from 1.55 - 2.75 eV, equivalent to the wavelength range of 450 - 800 nm visualized in the in-situ UV-vis measurements. All three concentrations display a comparable evolution of the PL emission over time. Due to the direct perovskite crystallization, a PL signal around 2.35 eV arises with a rapid increase in intensity, decreases as fast and vanishes over the spin-coating process. With longer integration times, the in-situ PL measurements would be more sensitive to the vanishing signal. However, increasing the integration time will face two downsides: simply a loss in time resolution and an oversaturation for early, more significant spin-coating times. Oversaturation is an issue especially faced with monitoring the formation of bromide-based perovskites during crystallization. Beside possible detector damage, a saturated signal rules out curve fitting. Therefore, the integration time is set to 500 ms for these measurements to compensate between signal intensity and time resolution.
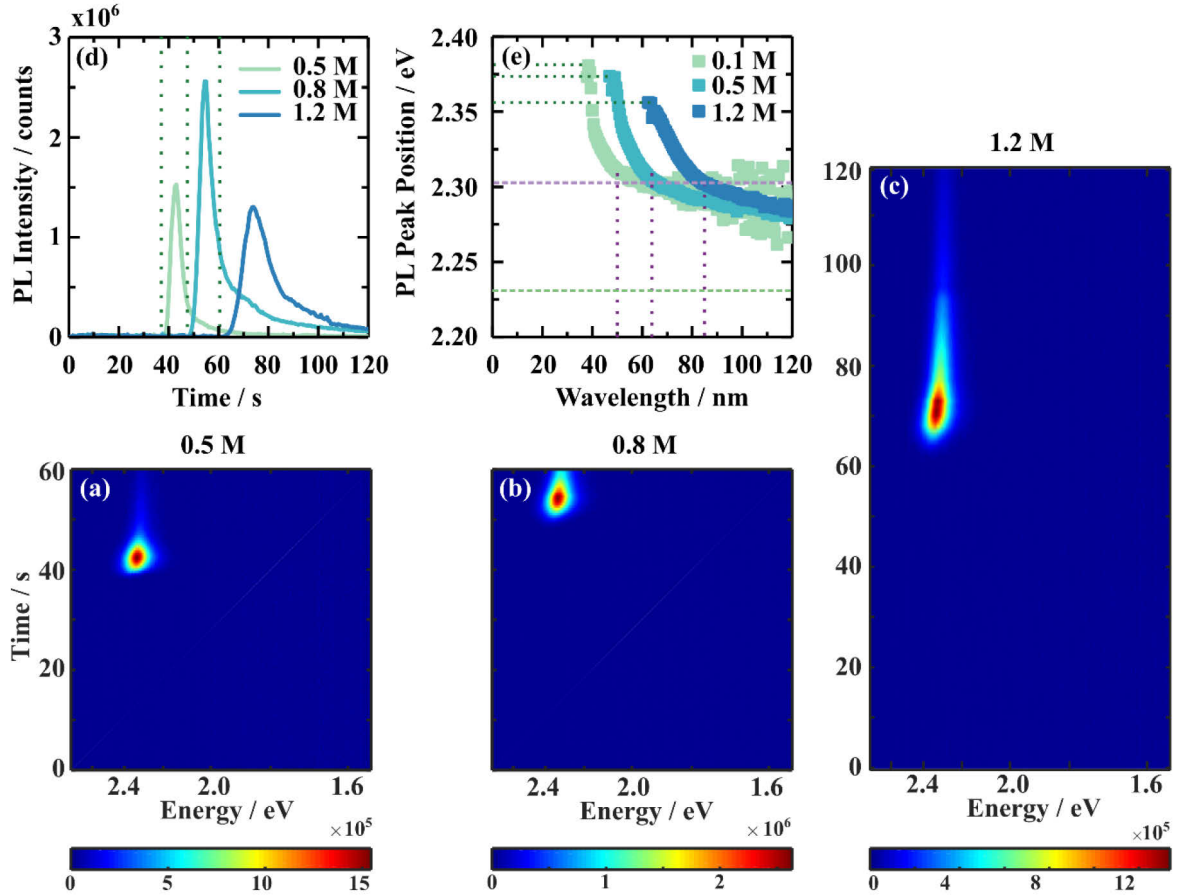
Figure 6.10: In-situ PL measurement for the 3CatPbBr₃ solution concentration series during the spin-coating process presented in 2D heat maps for the (a) 0.5 M, (b) 0.8 M, and (c) 1.2 M solution. All three processes are measured with an integration time of 500 ms. (d) presents the concentration dependent time evolution of the PL intensity. The green dashed lines mark the respective increase in transflectance during in-situ UV-vis measurements. The PL peak position is presented in (e), while the green dotted line is marking the initial peak position and the green dashed line indicates the PL peak position of the final 3CatPbBr₃ films. The purple dotted line visualizes the time when the shift in PL peak position flattens, and the purple dashed line indicates the energy around this turnover point.

PL intensities and PL emission positions, derived via Voigt fit, are the two main parameters discussed in this study. Figure 6.10 (d) presents the evolution of the PL intensity at the main peak position for the three different concentrations during spin-coating. For all three concentrations, the PL intensity rises around the same time as the averaged transflectance increases (green dashed lines), namely at 38 s, 48 s, and at 61 s for the concentrations 0.5 M, 0,8 M, and 1.2 M (Table 6.4). Thus, PL measurements verify a delayed crystallization onset for higher concentrated solutions. Measurements on different samples and a human error coordinating the start of measurements and spin-coating generate slight differences in timing.

The fit strengthens the impression of PL intensity progress from the 2D heat maps with a huge signal increase whilst the onset of crystallization followed by an immediate decay (Figure 6.10 (d)). This pointed shape in PL intensity indicates nucleation and growth processes: During the crystallization onset, a large number of small seed crystals or nucleation centers precipitate simultaneously. Such nucleation centers, similar to perovskite nanocrystals, would result in the described strong rise in PL intensity. Very rapid crystal growth of these nucleation centers correlates

with the immediate decrease of the PL intensity. During ongoing spin-coating, a low PL intensity, being following the overall low PLQY of the final 3CatPbBr$_3$ films (Figure 6.8), is associated mainly with solvent evaporation from the wet perovskite film and re-absorption by the already formed crystallites.

Table 6.4: Key features in the PL intensity evolution over time depending on the solution concentration, giving the onset of the PL signal, the PL Maximum, the time the PL Maximum is reached and the FWHM of the PL signal over time. For FWHM estimation, the low intensity tail at longer spin-coating times is neglected.

Concentration / mol L^{-1}	Onset PL signal / s	PL Maximum / counts	Maximum Position / s	FWHM of PL signal evolution / s
0.5	38	1.5x10^6	42	4
0.8	48	2.5x10^6	54	6
1.2	61	1.3x10^6	74	13

Although the shape follows the same trend for all concentrations, the maximum in PL intensity and the time evolution differ with the concentration (Table 6.4). The maximum PL intensity increases from 1.5x10^6 counts for the 0.5 M solution to 2.5x10^6 counts in case of spin-coating the 0.8 M solution. This significant difference in maximum intensity points to a larger number of nucleation centers forming during initial crystallization. However, this trend does not continue for the 1.2 M solution with a reduced maximum PL intensity of 1.3x10^6 counts. This reduced maximum intensity indicates the formation of fewer seed crystals or already lager nucleation centers. Surprisingly, the time from the PL onset until reaching the PL maximum and the FWHM extend with increased solution concentrations; namely from 4 s for the 0.5 M solution to 13 s for the 1.2 M one (Table 6.4). These timings suggest slower nucleation and crystal growth for higher concentrated solutions. However, faster formation kinetics would be anticipated for higher concentrations. The slowed down nucleation and crystal growth accompanies the likewise unexpected crystallization onset. Chapters 6.3.3 and 6.3.4 discuss these phenomena further. The decelerated formation kinetics explain the defined growth of square-shaped crystallites for film prepared from higher concentrated solutions (Figure 6.7).

Figure 6.10 (e) presents the evolution of the PL peak position for the three established 3CatPbBr$_3$ concentrations. The PL peak positions proceed similarly independent from the solution concentration. They arise at high energies and drop rapidly to lower energies over a few seconds, after this turnover point the emission peak shifts only slightly to lower energies during further spin-coating. This development supports the conclusion that small nucleation centers form upon crystallization and rapidly grow to larger crystallites. Due to quantum confinement, nucleation centers demonstrate PL emissions at higher energies, while the PL peak position shifts to lower energies during crystal growth. The initial emission position moves slightly from 2.38 eV for the 0.5 M solution to 2.36 eV for the 1.2 M solution (green dashed lines), correlation to crystallite sizes of 7.52 nm and 8.26 nm, respectively, extrapolating literature values of MAPbBr$_3$ nanoparticle films.[175] However, these values only represent a size estimation since literature values vary and depend strongly on additional parameters like temperature, capping ligands and constitution.[176–179] The initial emission peak reduction indicates larger nucleation centers forming from the higher concentrated solutions, as discussed for the lowered maximum PL intensity of the 1.2 M solution.

Table 6.5: Key features in the PL emission position evolving over time depending on the solution concentration, giving the initial PL peak position, the turnover point in growth kinetics, and the time window for nucleation and crystal growth.

Concentration / mol L^{-1}	Initial PL Peak Position / eV	Turnover Point / s	Main Nucleation and Growth window / s
0.5	2.38	45	7
0.8	2.37	64	16
1.2	2.36	85	24

Fast crystal growth continues until the turnover point (purple dashed lines) is reached. The timing of the turnover point roughly corresponds to the time when the PL intensity starts vanishing. This correlation in PL intensity and position emphasizes that nucleation and crystal growth mainly take place in the first seconds after the crystallization onset. As identified from the PL intensity the nucleation and growth window opens up from 7 s to 24 s increasing the concentration from 0.5 M to 1.2 M (Table 6.5). The same trend in slowed down nucleation and crystal growth process is derived from PL intensity and peak position though absolute timings vary due to different anchor points in both parameters. The fast shift in the PL emission to lower energies is also observed for pure, homogeneous crystallizing MAPbBr$_3$ (Chapter 6.3.2). Thus, grain growth dominates this shift rather than inhomogeneities caused by the cation distribution.

Due to high absorption coefficients in metal halide perovskites, the high-energy part of the PL emission spectrum is reabsorbed and, thus, cut off. The resulting sharp PL onset on the high-energy side becomes more important for ongoing formation since this effect increases with the perovskite thickness. Additionally, a decay in PL intensity connects to increased reabsorption caused by ongoing solidification of the perovskite film.[180] Even at early stages reabsorption affects the PL emission peak to a certain extent. Larger particles with a lower bandgap reabsorb the high-energy emission of smaller particles. Thus, the PL emission peak represents the maximum crystallite size at the early stages of nucleation and crystal growth. Especially for films prepared with an anti-solvent drop (Chapter 6.3), shoulders at the low-energy side are evident. Due to quantity distribution, the size distribution is not fully masked by reabsorption. Therefore, an increased FWHM of the PL emission indicates an inhomogeneity in size distribution to some extent. In-situ PL measurements in transmission mode as described by Staub *et al.*[181] would give detailed insights on the effect of reabsorption during film formation and about the crystallization direction, either proceeding from the substrate or the solution|atmosphere interface. However, implementing such a set-up and conducting such a study lies out of the scope of this work.

The PL peak position for all three concentrations is located around 2.30 eV at the turnover point, indicating a comparable crystal size at this stage of the formation process. The flattening PL peak position lies at higher energies than the PL emission of the final 3CatPbBr$_3$ film (2.23 eV, green dashed line) also at the end of the spin-coating process. Slowly ongoing grain growth and residual polar solvent, causing a solvatochromic shift, in the wet-film are accountable for the offset. The annealing step finally removes residual solvents.

The formation during annealing is monitored by in-situ PL measurements (Figure A.3.8). Although integration times are extended to 1000 – 2000 ms, PL emissions are only detectable for the first second(s). An increase in temperature generally quenches the PLQY. Bleaching and degradation may affect the PL signal since annealing measurements are carried out on one spot, due to the absence of the natural sample rotation during spin-coating. Therefore, no insights are given about

the ongoing formation during the annealing step. Based on Chapter 5, it is assumed that the $3CatPbBr_3$ formation is completed during the utilized spin-coating times and only residual solvent evaporates.

In summary, complementary in-situ UV-vis and in-situ PL measurements reveal a strong dependency of the $3CatPbBr_3$ formation kinetics on the precursor solution concentration. The extent of solutions considered exhibits that higher concentrated solutions delay the crystallization onset and result in slowed down nucleation and growth processes.

6.4.3 Concentration dependency of the $3CatPbBr_3$ wet-film thinning behavior

Rationalizing the concentration dependent formation process of the $3CatPbBr_3$ reveals the unexpected, accelerated crystallization onset for lower concentrated precursor solutions. Additional in-situ UV-vis measurements sensitive to interference patterns classify this behavior in more detail. Resolving the interference pattern provides insights into wet-film thinning and connected solvent evaporation rates. Besides the three established solutions of 0.5 M, 0.8 M, and 1.2 M, supplementary a diluted 0.1 M solution is investigated.

Figure 6.11 presents the interference pattern evolving during the spin-coating process in 2D heat maps. Independently from the solution concentration, a high number of fringes causes a very fine interference pattern during the initial period of spin-coating. The spin speed acceleration from 1000 to 4000 rpm at 10 s within the process evokes an abrupt modification in the interference pattern (dashed green lines). During spinning at a faster speed, the number of fringes reduces remarkably and the interference pattern start to deviate strongly as a function of solution concentration. The higher the concentration of the solutions, the slower the number of fringes reduces and overall the number of fringes increases from one to three before the crystallization onset occurs. As soon as crystallization starts, the interference pattern is not resolved anymore and scattering dominates the detected signal. Crystallization onsets from interference sensitive in-situ UV-vis measurements demonstrate consistency in timing with Chapter 6.4.3. Therefore, spin-coating directly on the Ag mirror is not influencing the determined formation kinetics. As an additional note, scattering dominates the signal after 25 s within the spin-coating process of the 0.1 M solution (Figure 6.11 (a)) indicating the crystallization onset. This accelerated crystallization onset of the 0.1 M solution verifies the trend discussed before.
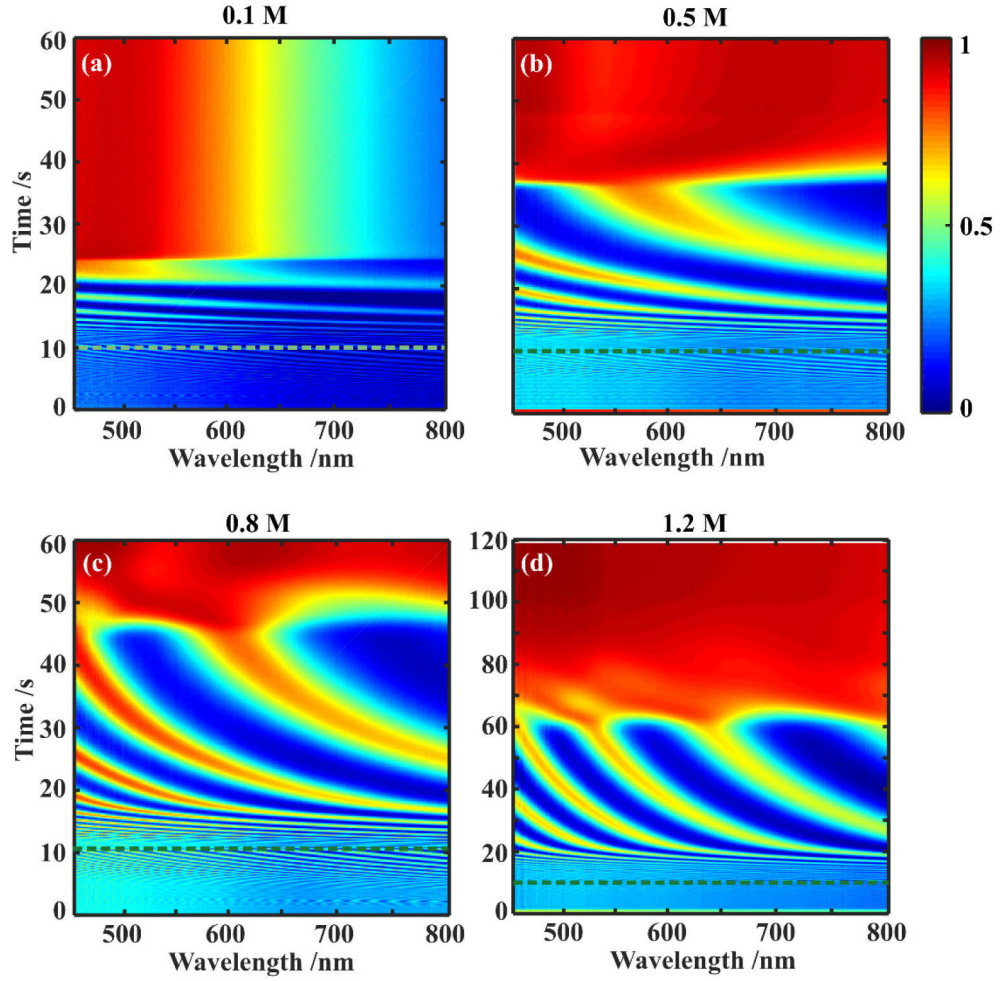
Figure 6.11: 2D heat maps of in-situ UV-vis measurements during 60 s or 120 s of spin-coating, respectively. Since the solutions are directly spin-coated on a silver mirror, these measurements are sensitive for interference patterns while the ejection of the solution and thinning of the wet-film before crystallization. The green dashed lines indicate the acceleration of the spin speed from 1000 rpm to 4000 rpm at 10 s within the process. The thinning of the following concentrations is presented: (a) 0.1 M, (b) 0.5 M, (c) 0.8 M, and (d) 1.2 M.

From the interference pattern, the wet-film thickness d is determined by:[182]

$$d = \frac{m}{2\sqrt{(n^2 + \sin^2\theta)}\Delta v}$$ (6.6)

for every spectrum in the time series, where m is the number of fringes per period in a spectral interval Δv (in cm^{-1}), n is the refractive index and θ is the angle of incidence of the white light.

To classify the concentration dependent thinning behavior, already visible from different evolution of the interference pattern (Figure 6.11), the solutions are characterized by determining the refractive index n, the density ρ, and the dynamic viscosity η (Table 6.6). The refractive index is specified wavelength independent and averaged based on the determination by an Abbé refractometer. While the refractive index and the density increase linear with the solution concentration, the dynamic viscosity increases exponentially (Figure A.3.9).

Table 6.6: Solution characteristics for the 3CatPbBr$_3$ concentration series, listing the refractive index, the density, and the dynamic viscosity.

3CatPbBr$_3$ Concentration / mol L^{-1}	Refractive Index	Density ρ / g cm^{-3}	Dyn. Viscosity η / cP
0.1 M	1.450	1.02 ± 0.03	1.26 ± 0.01
0.5 M	1.473	1.15 ± 0.01	2.05 ± 0.01
0.8 M	1.489	1.24 ± 0.03	3.13 ± 0.01
1.2 M	1.511	1.38 ± 0.02	5.84 ± 0.01

Figure 6.12 presents the evolution of the wet-film thickness fitted from the interference patterns indicating four different regimes in the thinning process for the 0.1 M, 0.5 M, 0.8 M, and 1.2 M concentration. In the first stage of spin-coating flow dominates ejection and planarization of the solution thinning. Thinning mainly is executed by solution flowing off at the sides of the substrate. The flow constant K describes this process:[183]

$$K = \frac{\omega^2 \rho}{3\eta} \qquad (6.7)$$

where ω is the angular velocity, ρ the density and η the dynamic viscosity of the solution. The flow constant K depends on the actual spin speed and is larger for higher spin speeds, resulting in an intensified film thinning due to flow at higher spin speeds (Table 6.7). The film thickness decreases abruptly for all concentrations. Thus, two flow regimes are identified for the utilized spin-coating process with acceleration in spin speed (Figure 6.12). While acceleration, the interference pattern change dramatically resulting in a noisy fit for the wet-film at these times.

Furthermore, K takes higher values for lower concentrated solutions (Table 6.7) due to the change in density and dynamic viscosity. Especially in the second flow regime (Flow 2) lower concentrated solutions thin faster. Hence, wet-films prepared from the lower concentrated solutions are thinner at the transition from flow to the evaporation regime.
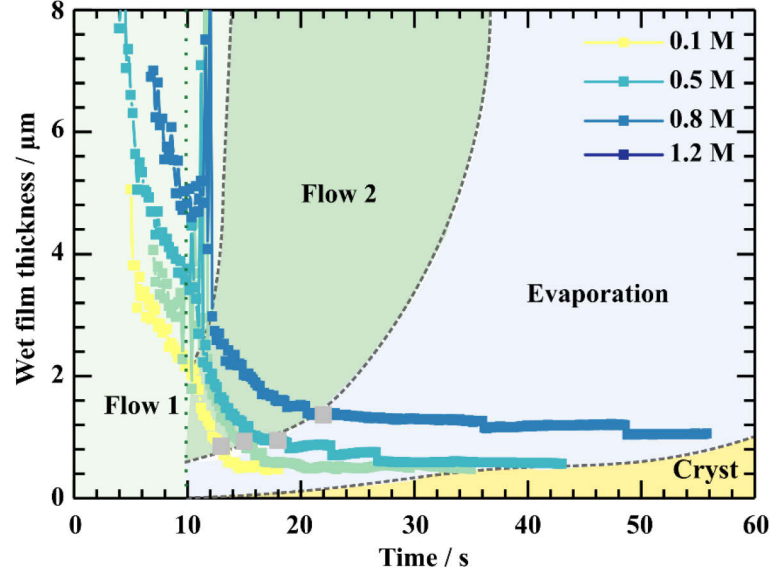
Figure 6.12: Fitted wet-film thinning for the established 3CatPbBr$_3$ concentration series. Two different flow regimes (green) depending on the spin speed, the evaporation (blue), and crystallization (yellow) regime are indicated. The green dotted line displays the time of spin speed acceleration. The grey squares mark the respective transition height (h_{tr}) for all concentrations, drawing the line between flow and evaporation regime.

In the evaporation regime, the wet-film thins down slower due to the domination by solvent evaporation and not by flow anymore. Grey squares indicate the concentration dependent transition height (h_{tr}) highlighting the crossover between the two regimes. The evaporation rate E is calculated by:

$$E = \frac{\Delta d}{\Delta t} = \frac{h_{tr} - h_{sat}}{\Delta t} \tag{6.8}$$

where Δd is the variation in wet-film thickness from the transition height (h_{tr}) until the thickness saturates (h_{sat}) in the time interval Δt. The evaporation rate decreases from 0.1 µm s^{-1} for the 0.1 M solution to 0.01 µm s^{-1} for the 1.2 M solution. In the lower concentrated solutions, less solvent molecules coordinate to the precursor salts and, therefore, evaporate easier. Since the wet-film is already thinner for the lower concentrated solution, the surface for solvent evaporation is also higher compared to the wet-film thickness, supporting fast solvent evaporation. Thus, the wet-film thickness decreases faster for lower concentrations due to enhanced solvent evaporation and the connected precursor concentration increases faster. This rationalizes the delayed crystallization onset for higher concentrated perovskite precursor solutions.

Table 6.7: Concentration dependent thinning parameters for the 3CatPbBr$_3$ solutions, listing the flow coefficient at 1000 rpm (left) and 4000 rpm (right), the determined evaporation rate, the saturated concentration (c_{sat}) when the crystallization starts, and the ratio of transition (h_{tr}) and saturation height (h_{sat}).

Concentration / mol L^{-1}	Flow Coefficient K / cm^{-2} s^{-1}	Evaporation Rate / µm s^{-1}	c_{sat} / mol L^{-1}	h_{tr}/h_{sat}
0.1 M	74.96 | 1199.29	0.10	0.19	1.89
0.5 M	51.94 | 831.07	0.06	0.93	1.86
0.8 M	36.68 | 586.91	0.03	1.30	1.62
1.2 M	21.88 | 350.08	0.01	1.57	1.31

Due to the change in the wet-film thickness by evaporation, the saturation concentration c_{sat} is estimated by:[184]

$$c_{sat} \simeq c_0 \cdot \frac{h_{tr}}{h_{sat}} \qquad (6.9)$$

where c_0 is the starting solution concentration, h_{tr} is the transition height and h_{sat} is the saturated height of the wet-film. The saturation concentration c_{sat}, defines the concentration at which nucleation starts upon spin-coating. For all four starting concentrations, the concentration increases due to solvent evaporation. However, the different starting concentrations do not reach the same saturation concentration at the point of nucleation (Table 6.7). Thus, the assumption of a consistent c_{sat} is not valid to rationalize the crystallization onset. While the concentration increases around 90 % for the 0.1 M solution up to 0.19 M, this enhancement is only around 30 % for the 1.2 M solution up to 1.57 M. This concentration dependent crystallization behavior indicates additional factors within the solution chemistry influencing the crystallization onset. It should be noted, that these calculations are estimations and the actual values might not be accurate, however, the overall trend is.

In total, the wet-film thinning is strongly concentration dependent and, thus, influences the crystallization behavior. Wet-films thin faster for lower concentrations during flow and evaporation. A fixed saturation concentration could not be defined. Also, the saturation concentration depends on the starting solution concentration of the precursor solution.

6.4.4 Colloid and complex solution chemistry in the 3CatPbBr$_3$ concentration series

Since the solution concentration is not a sufficient parameter to fully rationalize perovskite formation processes, further insights into the respective solution chemistry are required.

SAXS (Small Angle X-ray scattering) measurements are performed to investigate the 3CatPbBr$_3$ solution concentration series on a structural level. A first study, by Flatken *et al.*[185] demonstrates the applicability of SAXS measurements on perovskite solutions and presents the existence of structured colloids and their interaction in solution, resulting in pre-crystalline arrangements. The form factor, giving insides into the colloidal assembly itself, and the structural factor, describing the inter-particle interference, affect the scattering profile of the solution.

Figure 6.13 (a) presents the scattering cross section for the 0.5 M, 0.8 M, and 1.2 M solution. The black dotted lines demonstrate the actual measured data, while the solid lines show the fit obtained with the software SASfit©.[186] A broad, but strong maximum evolves for higher concentrated

solutions. This specific increase in the signal demonstrates the domination of the structural factor and indicates a pre-organization of the observed particles in the solution. The stronger the maximum the more particles are involved in the formation of these pre-organized clusters. The volume fraction derived assuming a hard-sphere model, expresses the measure. Figure 6.13 (b) presents its concentration dependency of the volume fraction, increasing from 1.1 % in the 0.5 M solution to 5.6 % in the 1.2 M one. Thus, higher concentrated solutions possess a higher structural pre-organization of colloids.
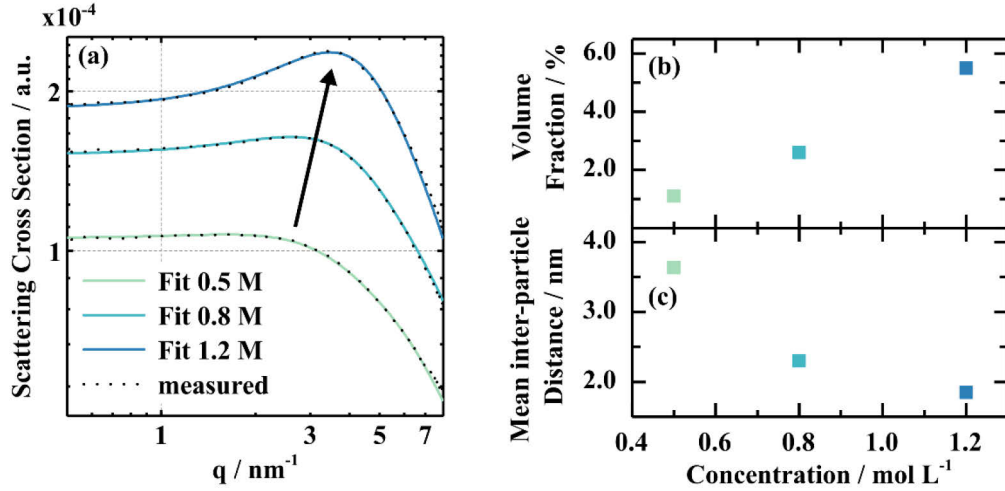
Figure 6.13: SAXS data on the 3CatPbBr$_3$ solution concertation series. The scattering cross section is illustrated in (a) for 0.5 M, 0.8 M, and 1.2 M concentrated solution with black dots as the raw data and in solid lines the fit, while (b) demonstrates the concentration dependency of the structural factor, namely the volume fraction and the mean inter-particle distance.

Using the extended Bragg equation:[187]

$$d_{ip} = \frac{2\pi}{q} \tag{6.10}$$

where q is the position of the peak maximum in q-space, the mean inter-particle distance d_{ip} between the mass centers of these colloids is described. Figure 6.13 (c) shows the concentration dependent inter-particle distance. The mean inter-particle distance reduces from 3.63 nm in the 0.5 M solution to 1.85 nm in the 1.2 M one. Thus, the individual colloids on average come closer together and interact stronger within the higher concentrated 3CatPbBr$_3$ solutions.

The concentration dependency of pre-organized clusters and inter-particle interaction gives deeper insights into the above described formation process. As discussed in Chapter 2.3 high coordinated lead-halide species form as building blocks in solution and will pre-organize in the colloids identified here. Thus, to form the desired bromide-based perovskites, these colloids need to re-organize and partially split, to take part in the formation of crystalline perovskite film. Since these colloids are more pre-organized and interact stronger in higher solutions, the process of re-organization and -formation is impeded and, hence, explains delayed crystallization from higher concentrated solutions and a slowed down crystallization process.

Since the scattering profile is influenced by the structural and the form factor at a time, characteristics from the dominating structure factor are extracted straightforwardly. To gain more insides into the assembly of the individual colloids from the form factor, robust fitting procedures

need to be developed first. However, in the following discussed solution based UV-vis measurements enable the estimation of lead-halide complexes formed depending on the concentration. At this point it worthwhile to distinguish between the definition *colloid* and *complex* in the discussed context. The term *complex* describes the chemical composition of the individual building blocks on an atomic/molecular level, namely the interaction between lead-halide-solvent. On the other hand, *colloid* characterizes the higher-level interaction between complexes.

Figure 6.14 (a) presents the wavelength dependent absorption coefficient α of the solvent mixture 7:3 DMF:DMSO, the 0.1 M, and 0.5 M 3CatPbBr$_3$ solution. The absorption coefficient is calculated from the respective absorbance spectrum by converting Lambert-Beer´s Law:

$$\alpha(\lambda) = \frac{A(\lambda)}{c \cdot d} \tag{6.10}$$

with $A(\lambda)$ as the wavelength dependent absorbance, c the solution concentration and d the path length, here 10 µm. The pure solvents absorb below 250 nm and do not overlap with the absorption features of the precursor solutions located above 280 nm. A red shift in the peak position and the absorbance onset for the 0.5 M 3CatPbBr$_3$ solution indicates changes in the complex composition.

Perovskite solutions demonstrate high absorption coefficients. The low concentrated solutions, 0.1 M and 0.5 M, exhibit values in the range of 10^5 - 10^6 and for the two higher concentrated solutions no reliable absorbance spectra are detected (Figure 6.14 (b), solid lines). Utilizing Lambert-Beer´s law with the two known absorption coefficients, the absorbance spectra are re-calculated. Since the known absorption coefficients differ, also the re-calculated absorbance values differ from each other (dashed and dotted lines). Assuming the absorption coefficient of the 0.1 M solution, a clear discrepancy at the absorption onset is visible. While the reliable onset for the 0.8 M and 1.2 M solution arises from ∼ 360 nm, the re-calculated one only occurs ∼ 340 nm. With the absorption coefficient of the 0.5 M solution the absorbance onsets for both, measured and calculated spectra, arise from 360 nm, anyway the rising flanks deviate slightly below 340 nm. Thus, the 0.5 M solution describes the chemical composition in the higher concentrations more accurately. Re-calculation accounts for intensity increases, not for changes in the chemical composition represented by the absorption coefficient, which evokes the discrepancies at the flanks. Shifts in the absorbance onset indicate a concentration dependent complex chemistry.
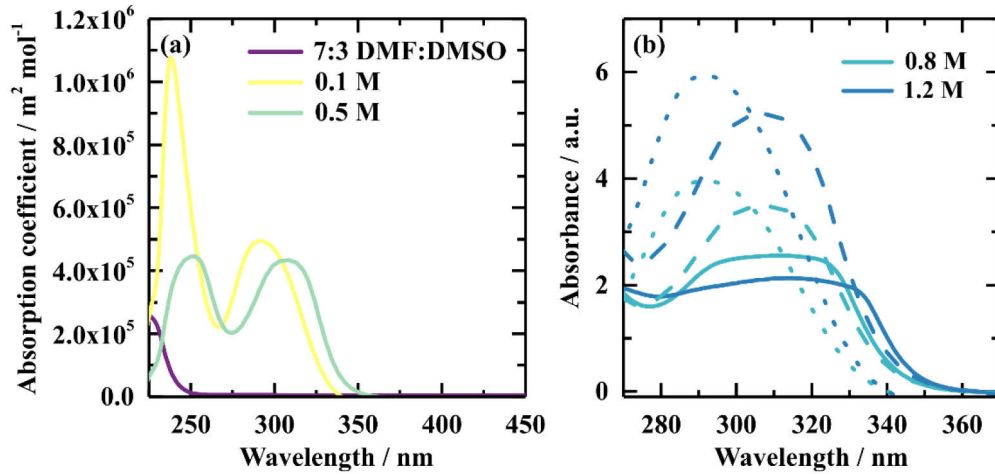
Figure 6.14: Concentration dependent UV-vis data on the 3CatPbBr$_3$ solutions. The wavelength dependent absorption coefficient (α) for the solvent system 7:3 DMF:DMSO, the 0.1 M, and the 0.5 M solution is presented in (a). Due to the overall high absorption coefficients, the higher concentrated solutions of 0.8 M and 1.2 M, shown in (b), saturate the detector (solid lines). Therefore, their absorbance is re-calculated using α of the 0.1 M (dotted lines) and the 0.5 M solution (dashed lines), respectively.

Figure 6.15 (a) presents the measured and re-calculated absorbance on a logarithmic scale, more sensitive to slight increases of absorbance below 400 nm. While PbBr$_2$ and [PbBr$_3$]$^-$ influence the absorbance around 285 nm and 310 nm, an increase in absorbance ~ 360 nm is attributed to [PbBr$_4$]$^{2-}$ (Figure 6.15 (a), grey dashed lines). Literature values are given for diluted solutions of MAPbBr$_3$ in pure DMF.[74] Exact absorbance positions will change due to composition and solvent system, e.g. by solvatochromic effects. For instance, Oldenburg and Vogler[188] report absorption bands for [PbBr$_3$]$^-$ and [PbBr$_4$]$^{2-}$ at 306 nm and 343 nm, in acetonitrile with [Et$_4$N]$^+$ (tetraethyl ammonium) as the counter ion.
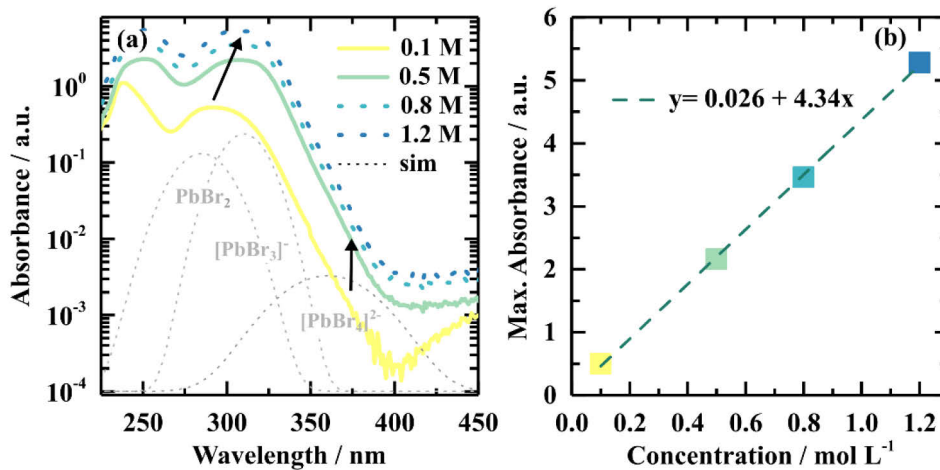
Figure 6.15: Solution characteristics from UV-vis measurements on the 3CatPbBr$_3$ solution concentration series. The absorbance for all four concentrations is plotted in (a), while solid lines present actual measurements and dashed lines re-calculated absorbance spectra utilizing α of the 0.5 M solution. The grey dotted lines indicate solution species of MAPbBr$_3$ in pure DMF from Yoon *et al.*[74]. (b) demonstrates the concertation dependency of the maximum absorbance.

The absorbance spectra indicate the main contribution of $PbBr_2$ and $[PbBr_3]^-$ complexes for the 0.1 M 3CatPbBr$_3$ solution with a peak center around 295 nm. A shift in the main absorbance peak to 310 nm occurs for the higher concentrated solutions and indicates an increasing amount of higher coordinated $[PbBr_3]^-$ and $[PbBr_4]^{2-}$ complexes. The overall maximum absorbance (Figure 6.15 (b)) rises for higher concentrated solutions, thus, the amount of the absorbing species increases. Hence, solution based UV-vis measurements indicate a shift in the chemical equilibrium to higher coordinated lead-bromide complexes for higher concentrated solutions:

$$PbBr_2 \rightleftharpoons [PbBr_3]^- \rightleftharpoons [PbBr_4]^{2-}$$

increasing solution concetration →
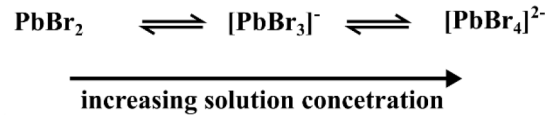
The ideal building block from solution would be the $[PbBr_3]^-$ complex, since each $PbBr_6$ octahedron in the perovskite structure shares all halides with the lead of neighboring octahedrons. This results in $PbBr_{6/2}$ units, corresponding to $PbBr_3$, whereby the negative charge is delocalized over the lead-halide framework. While for lower concentrated solutions the ideal building block dominates and favors a perovskite formation, the shift in chemical equilibrium to $[PbBr_4]^{2-}$ hampers the perovskite crystallization from higher concentrated solutions. Thus, besides colloid formation, complex formation involves additional reconstruction to form perovskites and, thus, impedes fast crystallization from higher concentrated solutions.

The 3CatPbBr$_3$ solution concentration series reveals fundamental modifications in their chemical nature. Higher concentrated solutions possess a higher structural pre-organization in colloids and higher coordinated lead-bromide complexes tend to form. Therefore, the concentration is a necessary but not a sufficient parameter to rationalize perovskite formation processes. The underlying solution chemistry influences the formation process and pathways (Chapter 5), which needs to be taken to hand and understood in detail, to fully rationalize those processes. Thus, the solution concentration and the connected colloid and complex chemistry are identified as an additional optimizable parameter in the perovskite preparation, especially influencing the process window and formation kinetics.

6.4.5 Discussion of errors in applied thinning calculations

As established in Chapter 6.4.3 the solution concentration increases during the spin-coating process and, thus, characteristic solution parameters change. The following discusses the error associated with holding on to the initial characteristic by the example of the refractive index.

Figure 6.16 presents the linear dependency of the refractive index as a function of the solution concentration and extrapolates refractive indices up to 2.0 M solutions. Perovskite solution concentrations up to 2.0 M, with n = 1.555, are unlikely due to solubility limits. The solubility limit for a pure MAPbBr$_3$ solution in DMF deploys ~ 1.4 M (grey underlined zone). Literature values are not consistent. For instance solubility limits of 1.36 M and 1.67 M (green dashed lines) are given for the named system.[189,190] Therefore, the identified insolubility region demonstrates a benchmark rather than a fixed solubility limit.

The extrapolated refractive index of a 1.7 M solution (n = 1.554) is chosen as a comparative value to evaluate its influence on the wet-film thinning calculation. Figure 6.16 (b) presents three evaluated data points for the 0.1 M and 1.2 M solution, respectively, overlaid on the fit. For both concentrations, no drastic difference in the calculated wet-film thickness occurs due to a changed

refractive index. For early spin-coating times, the film thickness differs ~ 200 nm for both concentrations and ~ 50 nm for 16 s within the spin-coating process. Compared to the wet-film thickness of several µm and a hundred nm, respectively, the error is minimal and, thus, negligible for these comparable simple systems regarding one thinning layer. Nevertheless, it has to be considered that the refractive index in the specific system changes slightly, and the effect might change for other systems. The minimization of the absolute error for later spin-coating times, where a change in solution characteristics is stronger, has to be highlighted positively.
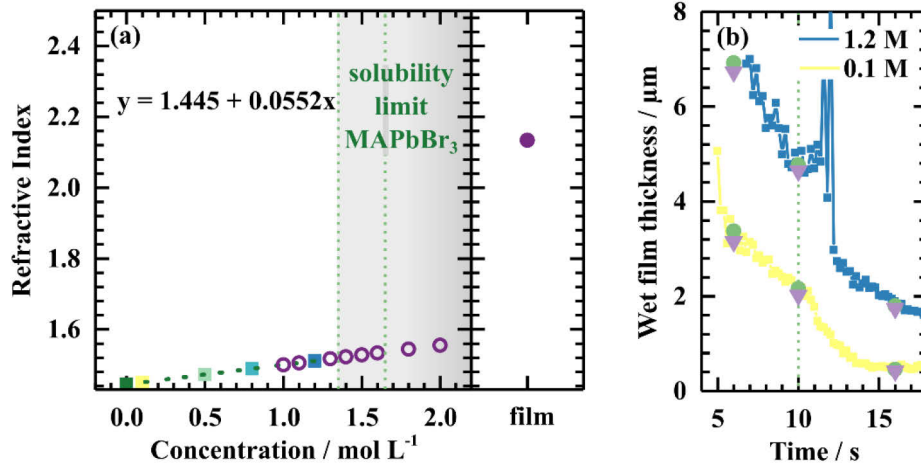
Figure 6.16: Error estimation of the wet-film thinning based on the refractive index (*n*). The concentration dependent *n* of the 3CatPbBr₃ solution series (a, left) and of the final thin-film (right) are demonstrated. Solid squares represent measurement points, fitted by the green dashed line, and open purple circles represent additional extrapolated *n*. The light green dotted lines indicate solubility limits of MAPbBr₃ in DMF from Saidaminov *et al.*[189,190]. The grey area present a rough regime of concentrations above the solubility limit. *n* for the final 3CatPbBr₃ film (solid purple circle) is averaged from 450 – 800 nm from wavelength dependent measurements (Figure A.3.9). In (b) the error in fitting the wet-film thickness is estimated using the fixed *n* of the starting solution concentration for the 0.1 M and 1.2 M solution. Green dots mark thicknesses calculated with the coefficient of the starting concentration of the solution, while purple triangles indicate thickness calculated utilizing n = 1.554 for a 1.7 M solution within the solubility limit. The green dotted line visualizes the acceleration of the spin speed.

Throughout this error estimation, it became clear that the detailed determination of numbers of fringes and the respective spectral interval is crucial for an accurate thinning calculation. Harrick[182] assumes an even distribution of fringes within a spectral interval due to a linear correlation of refractive index and wavelength. Especially for later spin-coating times (Figure A.3.10) the spacing between two fringe maxima deviates strongly, possibly introducing an error in the absolute film thickness calculation.[191] For early spin-coating times such an error is minimalized due to the possibility of averaging over several fringes, however becomes important at later stages only picturing a low number of fringes. Thus, determining an accurate absolute wet-film thickness requires the determination of a time and wavelength dependent refractive index, complicating the calculation. Additionally, a way of determining a wavelength and time dependent refractive index for wet-films has to be established.

Furthermore, the refractive index increases dramatically from the precursor solution (n ~1.5) to the solid 3CatPbBr₃ thin-film with n = 2.13 (Figure 6.16 (a)). Figure A.3.8 (d) presents the wavelength dependent *n,k* values for the final 3CatPbBr₃ thin-film determined by ellipsometry. Since the

refractive indices of the solutions are measured by a conventional Abbé refractometer, comparing averaged values between solution and film is reasonable. This drastic change in the refractive index additionally complicates the thinning analysis upon perovskite formation (Chapter 6.5).

In ongoing work, an optical monitoring set-up, specialized on interference pattern, allows following thinning of the wet-solid film after the crystallization onset.[192] At this point the modification in the refractive index upon crystallization becomes a critical parameter and influences the calculation of the film thickness. To gain conclusive and significant information from this specialized measurement, the discussed change in refractive index from starting solution to the final perovskite film gives insights into the rise in complexity of absolute thinning calculations. An accurate wet-film thickness is the foundation to derive further parameters such as an evaporation rate and a saturation concentration to fully rationalize perovskite formation processes.

Figure 6.17 illustrates the dependency and influences of solution characteristics, thinning, and the composition change during the early stages of spin-coating. The exact and detailed analysis of the complex interference pattern has to consider changes in the entering parameters. Therefore, the analysis raises itself from an analytical to a numerical problem, solvable by an iterative process. A next step in the ongoing work is the development of a robust algorithm evaluating film thickness and related parameters, especially for more complex systems (Chapter 6.5).
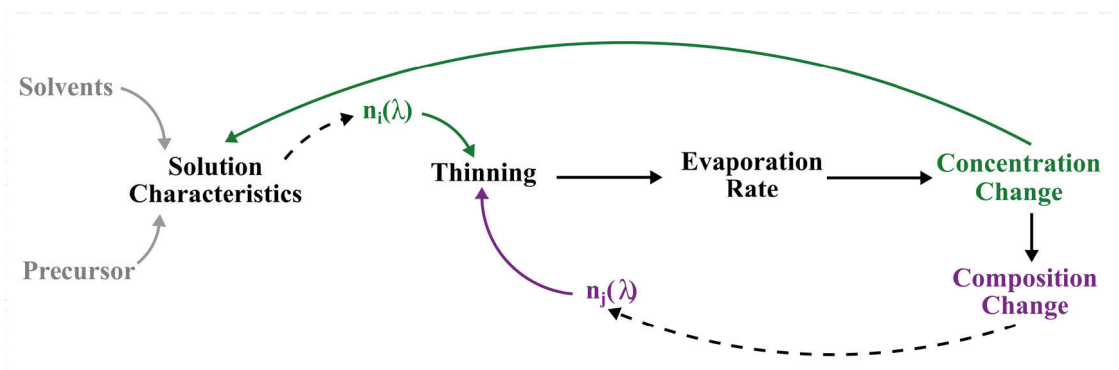
Figure 6.17: Schematic overview of calculating the interconnected solution characteristics and their impact on modelling the film thinning process. For an exact thinning model, an iterative algorithm is required.

In the case of perovskite thin-film preparation, spin-coating is utilized as a deposition technique, but simultaneously acts as a chemical reaction chamber. Due to shifts in chemical equilibria and proceeding chemical reactions, the thin-film thickness calculation and connected rationalization require the development of a complex algorithm considering those changes in characteristic parameters.

6.5 Insights into the established 3CatPbBr₃ film preparation including an anti-solvent drop

To achieve a high-quality morphology in perovskite thin-films, required for implementation in opto-electronic devices, dropping an anti-solvent during the spin-coating process is established as the standard methodology on a laboratory scale. Therefore, the formation process of a 1.2 M 3CatPbBr₃ solution with dropping an anti-solvent is investigated as a case study to rationalize the formation process of a device relevant preparation routine.[52,166] The main film formation process for the 3CatPbBr₃ system takes place during spin-coating (Chapter 6.4.2) and the anti-solvent drop mainly induces and influences the crystallization, thus, the discussion focuses on the spin-coating process.

Figure 6.18 summarizes the optical in-situ, namely UV-vis, PL, and interference sensitive measurements during spin-coating. Fundamental differences appear in the signal evolution for all three measurements comparing them to the intrinsic formation process without setting an anti-solvent (Chapter 6.4.2 and 6.4.3). The in-situ UV-vis and the in-situ PL heat map (Figure 6.18 (a) and (b)) indicate an induced crystallization by dropping the anti-solvent at 17 s within the process (green dashed line) based on the rise of the respective signal. A more detailed look at the mean transflectance and the PL intensity (Figure 6.18 (d)) confirms the induced crystallization (compare Figure 6.9 (g)). Thus, dropping the anti-solvent induces the crystallization at the interface wet-film|anti-solvent by extracting solvent.

In contrast to previous measurements with dropping an anti-solvent, a clear absorption edge evolves after setting the anti-solvent. The absorption share of the overall transflectance increases in this case (Figure 6.18 (c)) and allows deriving the bandgap evolution. The initially low background after dropping the anti-solvent indicates the formation of a very smooth surface and a closed wet-film, preventing scattering. However, around 27 s (purple dashed line) the background rises, due to increased scattering and lowers the absorption share. The enhanced solidification of the film and the growth of a wrinkled structure (Chapter 6.4.1) justify increased scattering. Figure 6.18 (e) presents the evolution of the bandgap and the PL peak position during the formation process. Both bandgap and PL emission position arise from higher energies, decay strongly over ~ 10 s and flatten from around 27 s within the process. This suggests the before described crystallite growth from nucleation centers during spin-coating. The amplified scattering ~ 30 s likely evokes the dip in the bandgap evolution at the same time. Since the PL peak position proceeds continuously, the dip is rather an artifact than a real change in the bandgap.

In-situ PL measurements do not present the short, pointy shape of the PL evolution discussed for not dropping an anti-solvent, in fact, the PL signal persists after dropping the anti-solvent over the whole spin-coating process. The integration time is reduced to 100 ms due to a much higher PL intensity. To compare the PL intensity at the peak center with Chapter 6.4.3, Figure 6.18 (d) presents the PL intensity re-calculated to 500 ms integration time. Already this brief review of the PL evolution indicates a modification in the detailed formation process by applying an anti-solvent.

The PL intensity evolution displays a maximum PL intensity of 3.1×10^6 counts, while the maximum counts are limited to 1.3×10^6 without an anti-solvent drop. The formation of smaller or a higher number of seed crystals, and a greater amount of residual solvent in the film can give a reason for this significant increase in the PL intensity. The initial PL peak position at 2.38 eV (Figure 6.18 (d), green) and the initial high bandgap of 2.43 eV (purple) suggest that slightly

smaller seed crystals are formed dropping an anti-solvent, compared to the initial PL position at 2.35 eV without dropping an anti-solvent (Figure 6.10 (e)). In addition, the PL intensity reveals a steep increase over ~10 s, comparable to the steep increase for films without an anti-solvent drop, until 27 s within the process. However, the PL intensity rises lower until 50 s of spin-coating before gently decreasing. This long progress of the PL signal indicates a slowed down nucleation and crystal growth because of dropping an anti-solvent. A different chemical composition of colloids and complexes in the wet-film, compared to intrinsic crystallization, may reason the slowed down formation

The formation of a wrinkled morphology (Chapter 6.4.1) can be traced back to a slowed down crystallization process. Setting an anti-solvent drop induces crystallization from the top of the wet-film. Due to a slow crystallite growth, a second, parallel crystallization might proceed from the wet-film|substrate interface at later spin-coating times evoking the wrinkles. Therefore, optimized timing in setting an anti-solvent might prevent wrinkle formation.
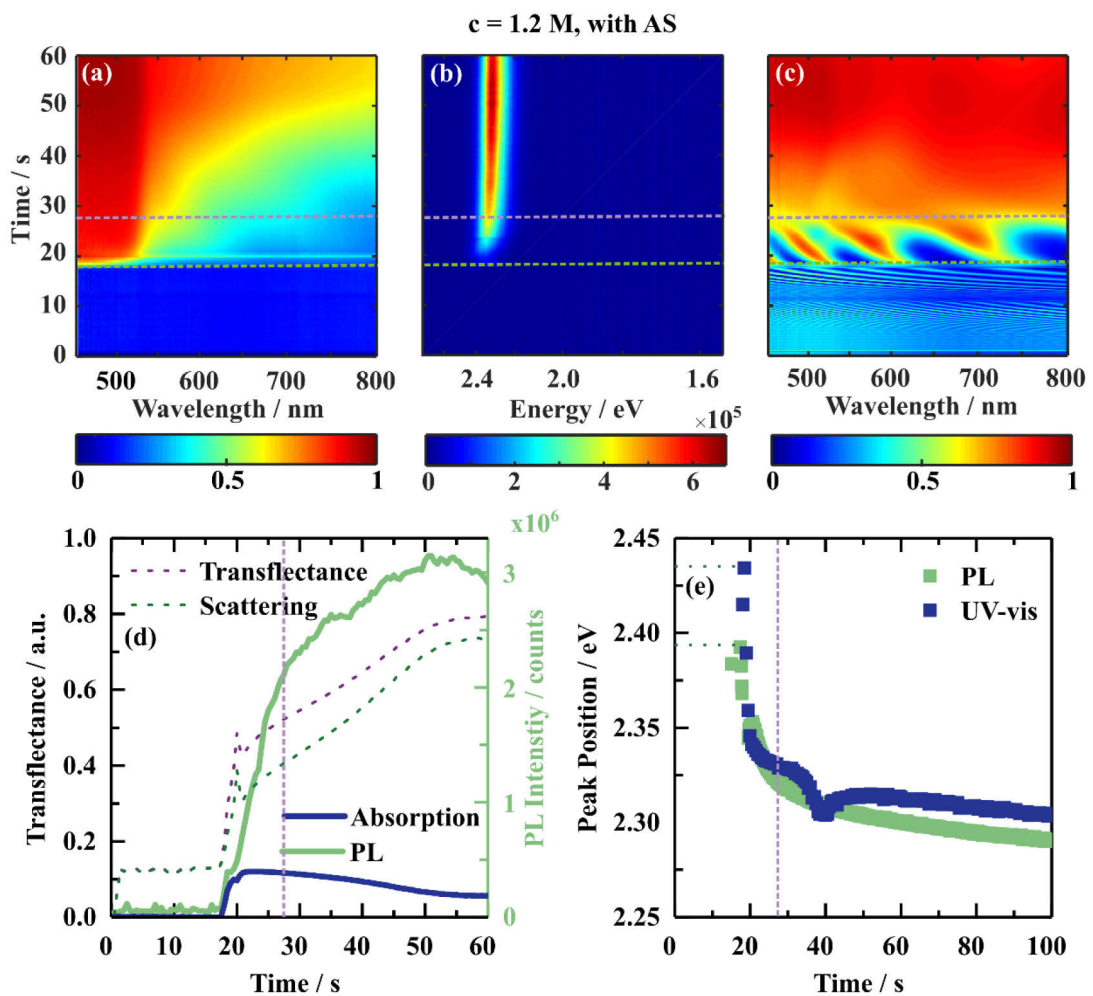
Figure 6.18: 2D heat maps of (a) in-situ UV-vis, (b) in-situ PL measurements, and (c) interference sensitive in-situ UV-vis measurements during spin-coating of the 1.2 M 3CatPbBr₃ solution with dropping the anti-solvent 17 s within the process (light green dashed line). The purple dashed line indicates the time when no thinning of the wet-film is detected anymore. The shares of scattering and absorption of the averaged transflectance and the PL intensity evolution over the spin-coating process are shown in (d), while (e) presents the evolution of the PL peak position and the derived bandgap from the absorption onset.

Figure 6.18 (c) demonstrates the thinning behavior for the 1.2 M solution by applying an anti-solvent. The interference pattern equals the one of the 1.2 M solution discussed in Chapter 6.3.3 in the beginning. However, dropping the anti-solvent causes a second abrupt modification in the interference pattern (green dashed line). Although the anti-solvent induces crystallization, an interference pattern with a reduced number of fringes is detected. Only 27 s within the spin-coating process scattering arising from ongoing crystallization starts to dominate the signal. Thus, it seems setting an anti-solvent drop reduces the wet-film thickness. Calculations (Figure A.3.11) indicate a film thinning of around 700 nm. However, utilizing the thinning calculations from Chapter 6.3.3 only allows reasonable fitting data until 20 s within the spin-coating process.

Here, obstacles, discussed in Chapter 6.3.5, become evident for the thinning calculation since the system complicates with dropping an anti-solvent. Figure 6.19 outlines the wet-film evolution during spin-coating and serves as a draft and outlook for ongoing work and collaboration[192] to measure, model, and rationalize such complicated formation processes in detail.
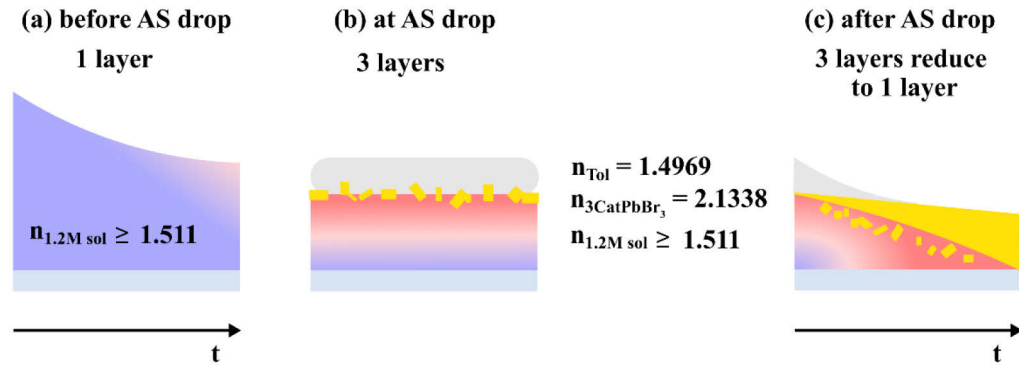
Figure 6.19: Schematic demonstrating the layer evolution during the spin-coating process (a) before, (b) at, and (c) after the anti-solvent drop. Since the number of layers and the exact refractive within and between the layers changes, a complex optical model is required to determine the exact thinning behavior of all involved layers.

Before the anti-solvent drop (Figure 6.19 (a), one thinning layer, as previously implemented, can describe the wet-film thickness. In the moment of dropping the anti-solvent, a stack of three different layers would correctly describe the system, namely the precursor solution, the anti-solvent, and seed crystals at their interface (Figure 6.19 (b)). The layers hold different, in part strongly wavelength dependent refractive indices. Precisely, a concentration gradient and, therefore, a connected gradient in the refractive index of the precursor solution should be taken into account. During the ongoing spin-coating, the system reduces again from three different layers to one (Figure 6.19 (c)). Namely, the anti-solvent flows and evaporates and the wet-film is converted via crystallization into perovskite. Thus, at the end of spin-coating the system consists of a perovskite film embedding residual solvent. The herein-drawn model assumes clear interfaces between the layers and does not consider the intermixing of the layers. Through developing an analytical model, the influences of the individual layers and their optical properties on the overall interference pattern need to be evaluated. Additionally, the influence on the in-situ UV-vis and in-situ PL signal by the anti-solvent layer has to be classified due to conspicuous time correlation in signal changes for all three measurements.

Overall, setting an anti-solvent drop induces the perovskite crystallization at the wet-film surface and formation kinetics appear to slow down. However, an anti-solvent drop complicates the data

evaluation and interpretation, especially in terms of wet-film thinning. Thus, at this stage, the film formation process is estimated and the ongoing work will be key to rationalize the perovskite formation by dropping an anti-solvent in more detail.

6.6 Conclusion

Investigating the formation process of bromide-based perovskites with in-situ spectroscopy in terms of chemical preparation parameters revealed an influence of each parameter on the overall process. The system under consideration shows the following influences: an adequate anti-solvent drop induces crystallization, the solvent system defines the process window, and the cation composition influences formation kinetics. Each parameter needs to be evaluated and understood individually to fully rationalize their interplay and the overall perovskite formation processes.

The 3CatPbBr$_3$ formation process demonstrates a strong dependency on the solution concentration. The solution chemistry changes with the concentration, complex and colloid differ and affect the saturation concentration at the crystallization onset. Thus, the underlying solution chemistry predetermines the formation process, opening up a great potential to tailor and optimize perovskite thin-film deposition from solution-based techniques. However, this first requires a deeper understanding of perovskite-based solution chemistry.

Evaluating the concentration dependent thinning behavior reveals the usability of established models for quantitative thinning calculations of simple one-layer systems. However, these models do not hold for multi-layer thinning, e.g. occurring dropping an anti-solvent. Iterative algorithms including various layers with different and changing optical parameters are required and need to be implemented for adequate thinning calculations. The described ongoing development in in-situ data modulation and analysis, in combination with the herein acquired understanding of individual chemical preparation parameters, will allow the detailed rationalization of complex, device-relevant perovskite formation processes.

7. Conclusion and Outlook

The material class of metal halide perovskites is characterized by their solution-based processing, bandgap tunability by ion substitution, and the associated possibility for application in various opto-electronic devices. The reliable and reproducible fabrication of high-quality thin-films is critical for their application. The crystallization behavior during processing determines the thin-film quality. However, the formation processes of metal halide perovskites from precursor solutions during their preparation are not clarified. It is only known that the formation depends on the composition of the precursors in solution and can be influenced by process engineering. Rationalizing the formation processes from solution will enable target-orientated process design for high-quality thin-film deposition over the broad compositional range on a laboratory and, in the long-term, on an industrial scale. Thus, this work focuses on the evaluation of the precursor-process-property space to rationalize solution-based perovskite formation.

Chapter 4 meets the initial challenge:

- How can we fabricate high-quality perovskite thin-films over their broad compositional range of $APbX_3$, with $A^+ = Cs^+$, MA^+, FA^+ and $X^- = Cl^-$, Br^-, I^-, in order to determine reliable optical properties?

High-quality perovskite thin-film samples are required to determine accurate and detailed absorption spectra by UV-vis measurements. Due to the differences in the film quality, especially in morphology, sample properties may differ from material properties. The comparison of two pure $MAPbBr_3$ thin-films with varied morphology presents obvious differences in their absorption spectra. A feature-less absorption spectrum arises from the low-quality morphology, while the high-quality one presents a detailed, feature-full absorption spectrum, expected for $MAPbBr_3$. From such feature-full absorption spectra, the exciton binding energy is determined. This comparison emphasizes, that high-quality samples are essential to determine optical properties of metal halide perovskite thin-films. The preparation process has a major impact on the final film morphology, thus, process and property are strongly interconnected in metal halide perovskites.

By adjusting the variety of preparation parameters, the fabrication of the mentioned $APbX_3$ compositions has been optimized in terms of phase purity, morphology and optical absorption. From the resulting high-quality films, structural, optical, and opto-electronic parameters are

determined and correlated among each other in relation to their composition. In metal halide perovskites, the substitution of iodide with bromide and chloride results in a smaller unit cell, presented by a smaller *d* spacing. This decrease in the structural parameters correlates with an increase in the bandgap and the exciton binding energy. Thus, the ionic composition interconnects structural, optical, and opto-electronic properties. Tuning one characteristic property by modifying the composition automatically changes all the other ones, due to the correlation of precursor and property.

The fabrication of high-quality thin-films over the broad compositional space of $APbX_3$ required the re-optimization of the fabrication process for every precursor composition. Already slight changes in, e.g. the drop time of the anti-solvent evoke different morphologies. Thus, the exact precursor composition influences the formation process of metal halide perovskites and precursor and process correlate with each other. Overall, a strong mutual dependency of the precursor-process-property triangle is demonstrated in this work.

Hence, the key to fabricating high-quality thin-films is the optimization of every process parameter for each individual composition. However, the blind optimization of preparation parameters turns out between other things to be time consuming and an excess of source consumption. Thus, detailed understanding and rationalization of the perovskite formation processes are essential to simplify and control the fabrication of high-quality thin-films. These insights encouraged the development and construction of an optical in-situ set-up, acting as an "eye" in the formation process of metal halide perovskites. Implemented into a glovebox, this set-up allows monitoring and evaluating the formation process by UV-vis and PL measurements within established laboratory routines and equipment. Identifying and rationalizing the formation processes and critical preparation parameters will be a first step towards target-orientated optimization of fabrication routines.

Chapter 5 answers the scientific question:

- How and why determine the solution composition and the process the final perovskite thin-film composition in terms of homogeneity in the mixed halide $MAPb(I_xBr_{1-x})_3$ series?

Based on the development of the optical in-situ set-up, the possibility is given to bring light into the black box of formation processes of metal halide perovskites. Here, the influence of the composition in the mixed halide $MAPb(I_xBr_{1-x})_3$ series on the crystallization behavior from solution during spin-coating and subsequent annealing is discussed. Monitoring the crystallization process by in-situ UV-vis measurements rationalizes the (in)homogeneity of those thin-films throughout the formation process.

Rationalizing the formation process of the $MAPb(I_xBr_{1-x})_3$ series maps three different formation pathways appearing during film preparation dependent on the halide ratio (x). While the pure bromide-based perovskite forms directly during spin-coating, the pure iodide and solutions containing $x \geq 0.7$ form via the $MA_2(DMSO)_2Pb_3I_8$ intermediate solvate phase. In this case, the final perovskite only forms during annealing. For halide mixtures between $0.1 \leq x \leq 0.6$, both pathways are taken during spin-coating, namely a bromide-rich perovskite and an iodide-rich solvate phase form. Hence, an intrinsic, ionic inhomogeneity is introduced for these mixed halides.

Annealing converts the two phases into perovskite and compensates the inhomogeneity to a certain extent. Thus, the mixed halide composition of the precursor solution introduces a heterogeneous crystallization during spin-coating and rationalizes inhomogeneities in the final thin-films.

In addition, the solvent system has a major influence on the formation process, due to different binding strengths between the solvents and the lead-halide precursors. Thus, preferably iodide-based solvent complexes are formed that act as intermediate species, having a template effect on the morphology. The solvent system also affects the formation kinetics. Compared to weakly coordinating, pure DMF, the crystallization process utilizing stronger coordinating DMSO as a co-solvent is delayed and varies with respect to the halide composition. Therefore, the use of DMSO opens a wider process window due to slowed down formation kinetics.

Therefore, further work should aim to investigate and develop new or modified precursor solutions, including solvents and additives, to inhibit different complexation of precursor salts and, thus, competing formation pathways. Such modified precursor solution will enable a homogeneous formation process. In an ideal case, halide-balanced complexes form in solution and convert directly into a homogenous mixed perovskite thin-film.

Chapter 6 faces the scientific question:

- How does the precursor solution, in terms of concentration and solvent, in combination with an anti-solvent drop affect the thin-film formation in the pure bromide $APbBr_3$ series, with $A^+ = Cs^+$, MA^+, FA^+ and their mixture?

By walking along different axis of the preparation parameter space, the influences of the precursor solution, in terms of solvent, cation composition and concentration, in combination with an anti-solvent drop, on the formation process of the $APbBr_3$ system, with $A^+ = Cs^+$, MA^+, FA^+ and mixtures, is revealed. In-situ UV-vis and PL measurements follow the formation process and in-situ interference measurements give insights into the wet-film thinning. Additionally, SAXS and UV-vis measurements examine the solution chemistry of the $3CatPbBr_3$ concentration series.

The drop of an adjusted anti-solvent induces the crystallization of the desired bromide-based perovskite at the anti-solvent|wet-film interface and increases the quality of the thin-film morphology. Thus, the anti-solvent drop has to be aligned with the crystallization mechanism. Due to different precursor chemistry and evaporation rates, the solvent system and the cation composition affect the crystallization kinetics. Utilizing DMSO and FA^+ in the precursor solution results in a delayed crystallization.

In addition, the solution concentration affects the crystallization kinetics of the formation process due to differences in the colloid chemistry. Lower concentrated solutions crystallize earlier during the spin-coating process in consequence of smaller colloids with less particle interaction and higher evaporation rates. Thus, different saturation concentrations, depending on the starting concentration, are determined from wet-film thinning behavior.

Modifications in the precursor composition change the solution chemistry, which predefines the overall formation process. Even for low lead-halide-solvent interactions causing the direct formation of bromide-based perovskites, different precursor compositions in solution affect the

crystallization kinetics. Thus, the impact of precursor modification is expected to be more pronounced in iodide-based perovskites, due to stronger lead-halide-solvent interactions, and stable intermediates. Therefore, future process rationalization should go hand in hand with solution characterization and optimization.

Outlook

This work evaluates the strong correlation within the precursor-process-property space of metal halide perovskites. The individual precursor solution is identified to predefine the formation process and, thus, the final thin-film properties. In-situ spectroscopy, acting as an "eye" in the process, is introduced as a strong tool to monitor and rationalize perovskite formation from solution. Thus, as a first basis to gain fundamental knowledge about solution-based formation processes, the influences of the halide ratio, the cation composition, the solvent system, the solvent concentration, and the anti-solvent drop are evaluated and rationalized. In order to fully rationalize the entire complex formation processes in metal halide perovskites, future work should focus on:

The rationalization of further individual process parameters, such as less established solvent system, the influence of additives or the detailed mechanism of dropping an anti-solvent. These insights will complete the picture of the complex formation processes in metal halide perovskites. All studies within this work, presented the strong correlation between precursor solution composition and the detailed formation process. Thus, future studies should combine the rationalization from solution chemistry, over the resulting formation process towards the influence of quenching methods, like an anti-solvent drop. This will enable to rationalize the full picture behind the precursor-process-property correlation and allow the targeted design of new solution compositions and process parameters.

An ongoing collaboration aims to improve in-situ spectroscopy and associated data analysis routines in particular for wet-film thinning. Those improvements give the opportunity to evaluate e.g. the anti-solvent drop, way beyond induced crystallization and modified morphology. A detailed thinning analysis of a multi-layer stack will allow rationalizing the precise chemical mechanism of dropping an anti-solvent. This gives the possibility to optimize systematically the choice, amount, and timing of the anti-solvent drop. Additionally, such a rationalization of the anti-solvent drop will enable the replacement in upscaling techniques, where quenching by an anti-solvent drop cannot be applied.

Upscaling the fabrication of high-quality thin-films by solution-based deposition techniques is a critical parameter for market maturity of opto-electronic devices based on metal halide perovskites. Thus, the implementation of in-situ spectroscopy in e.g. inkjet printers or slot-die coaters will give the opportunity to rationalize the perovskite formation based on these methods. The formation process differs among various deposition techniques e.g. due to the different deposition of the precursor solution. Thus, process parameters need to be modified for upscaling. Applying in-situ spectroscopy will identify critical points in the perovskite preparation and allow the targeted optimization of ink composition and deposition parameters in the printing process.

In addition, in-situ spectroscopy can be applied as process control. As presented, an undesired low-quality morphology distinguishes itself by a high background signal in UV-vis measurements. Evaluating such conspicuities by simultaneous process tracing and data analysis will allow the identification of deficient film deposition. Such a process control becomes particularly important for large-scale, industrial perovskite fabrication.

This work paves the way for a complete rationalization and, thus, targeted and hasten optimization of formation processes over the entire compositional space of metal halide perovskites, especially in upscaling techniques. Optimization of the fabrication of high-quality thin-films is accelerated as new solution compositions and process parameters can be evaluated directly during the fabrication process. This is essential for the fabrication of perovskite-based opto-electronic devices on a large, industrial scale.

8. Bibliography

[1]   M. R. Filip, F. Giustino, *Proc. Natl. Acad. Sci. U. S. A.* **2018**, *115*, 5397–5402.

[2]   H. Jin, S. H. Rhim, J. Im, A. J. Freeman, *Sci. Rep.* **2013**, *3*, 1651–1651.

[3]   D. B. Mitzi, C. A. Feild, W. T. A. Harrison, A. M. Guloy, *Nature* **1994**, *369*, 467–469.

[4]   S. Hui, A. Petric, *Solid State Ionics* **2001**, *143*, 275–283.

[5]   G. Rose, *J. für Prakt. Chemie* **1840**, *19*, 459–468.

[6]   H. L. Wells, *Am. J. Sci.* **1893**, *s3-45*, 121–134.

[7]   D. Weber, *Zeitschrift fur Naturforsch. - Sect. B J. Chem. Sci.* **1978**, *33*, 1443–1445.

[8]   K. Chondroudis, D. B. Mitzi, *Chem. Mater.* **1999**, *11*, 3028–3030.

[9]   A. Kojima, K. Teshima, Y. Shirai, T. Miyasaka, *J. Am. Chem. Soc.* **2009**, *131*, 6050–6051.

[10]   E. Riedel, C. Janiak, *Anorganische Chemie*, De Gruyter, **2007**.

[11]   V. M. Goldschmidt, *Naturwissenschaften* **1926**, *14*, 477–485.

[12]   G. Kieslich, S. Sun, A. K. Cheetham, *Chem. Sci.* **2014**, *5*, 4712–4715.

[13]   R. D. Shannon, C. T. Prewitt, *Acta Crystallogr. Sect. B Struct. Crystallogr. Cryst. Chem.* **1969**, *25*, 925–946.

[14]   W. Travis, E. N. K. Glover, H. Bronstein, D. O. Scanlon, R. G. Palgrave, *Chem. Sci.* **2016**, *7*, 4548–4556.

[15]   E. L. Unger, O. Shargaieva, S. Braunger, P. Docampo, **2019**, pp. 153–192.

[16]   A. M. Glazer, *Acta Crystallogr. Sect. B Struct. Crystallogr. Cryst. Chem.* **1972**, *28*, 3384–3392.

[17]   T. J. Jacobsson, M. Pazoki, A. Hagfeldt, T. Edvinsson, *J. Phys. Chem. C* **2015**, *119*, 25673–25683.

[18]   A. Poglitsch, D. Weber, *J. Chem. Phys.* **1987**, *87*, 6373–6378.

[19]   J. H. Noh, S. H. Im, J. H. Heo, T. N. Mandal, S. Il Seok, *Nano Lett.* **2013**, *13*, 1764–1769.

[20]   M. R. Linaburg, E. T. McClure, J. D. Majher, P. M. Woodward, *Chem. Mater.* **2017**, *29*, 3507–3514.

[21]   C. C. Stoumpos, C. D. Malliakas, M. G. Kanatzidis, *Inorg. Chem.* **2013**, *52*, 9019–9038.

[22] M. T. Weller, O. J. Weber, J. M. Frost, A. Walsh, *J. Phys. Chem. Lett.* **2015**, *6*, 3209–3212.

[23] M. Saliba, T. Matsui, J.-Y. Seo, K. Domanski, J.-P. Correa-Baena, M. K. Nazeeruddin, S. M. Zakeeruddin, W. Tress, A. Abate, A. Hagfeldt, et al., *Energy Environ. Sci.* **2016**, *9*, 1989–1997.

[24] N. J. Jeon, J. H. Noh, W. S. Yang, Y. C. Kim, S. Ryu, J. Seo, S. Il Seok, *Nature* **2015**, *517*, 476–480.

[25] C. Li, X. Lu, W. Ding, L. Feng, Y. Gao, Z. Guo, *Acta Crystallogr. Sect. B Struct. Sci.* **2008**, *64*, 702–707.

[26] C. J. Bartel, C. Sutton, B. R. Goldsmith, R. Ouyang, C. B. Musgrave, L. M. Ghiringhelli, M. Scheffler, *Sci. Adv.* **2019**, *5*, eaav0693.

[27] J. Breternitz, S. Schorr, *Adv. Energy Mater.* **2018**, 1802366.

[28] S. N. Ruddlesden, P. Popper, *Acta Crystallogr.* **1957**, *10*, 538–539.

[29] A. Jodlowski, D. Rodríguez-Padrón, R. Luque, G. de Miguel, *Adv. Energy Mater.* **2018**, *8*, 1703120.

[30] L. Vegard, *Zeitschrift für Phys.* **1921**, *5*, 17–26.

[31] S. Tao, I. Schmidt, G. Brocks, J. Jiang, I. Tranca, K. Meerholz, S. Olthof, *Nat. Commun.* **2019**, *10*, 1–10.

[32] R. E. Brandt, V. Stevanović, D. S. Ginley, T. Buonassisi, *MRS Commun.* **2015**, *5*, 265–275.

[33] T. Umebayashi, K. Asai, T. Umebayashi, K. Asai, T. Kondo, T. Kondo, A. Nakao, *Phys. Rev. B - Condens. Matter Mater. Phys.* **2003**, *67*, 155405.

[34] N. H. Nickel, F. Lang, V. V. Brus, O. Shargaieva, J. Rappich, *Adv. Electron. Mater.* **2017**, *3*, 1700158.

[35] A. Walsh, *J. Phys. Chem. C* **2015**, *119*, 5755–5760.

[36] Y. Jiang, X. Wang, A. Pan, *Adv. Mater.* **2019**, *31*, 1806671.

[37] M. Saba, M. Cadelano, D. Marongiu, F. Chen, V. Sarritzu, N. Sestu, C. Figus, M. Aresti, R. Piras, A. Geddo Lehmann, et al., *Nat. Commun.* **2014**, *5*, 5049.

[38] "Perovskite Database Project," can be found under www.perovskitedatabase.com, **n.d.**

[39] "Best Research-Cell Efficiency Chart | Photovoltaic Research | NREL," can be found under https://www.nrel.gov/pv/cell-efficiency.html, **n.d.**

[40] Q. Jiang, Y. Zhao, X. Zhang, X. Yang, Y. Chen, Z. Chu, Q. Ye, X. Li, Z. Yin, J. You, *Nat. Photonics* **2019**, *13*, 460–466.

[41] M. Abdi-Jalebi, Z. Andaji-Garmaroudi, S. Cacovich, C. Stavrakas, B. Philippe, J. M. Richter, M. Alsari, E. P. Booker, E. M. Hutter, A. J. Pearson, et al., *Nature* **2018**, *555*, 497–501.

[42] S. Yang, J. Dai, Z. Yu, Y. Shao, Y. Zhou, X. Xiao, X. C. Zeng, J. Huang, *J. Am. Chem. Soc.* **2019**, *141*, 5781–5787.

[43] L. Krückemeier, U. Rau, M. Stolterfoht, T. Kirchartz, *Adv. Energy Mater.* **2020**, *10*, 1902573.

[44] J. Tauc, *Mater. Res. Bull.* **1968**, *3*, 37–46.

[45] M. A. Green, Y. Jiang, A. M. Soufiani, A. Ho-Baillie, *J. Phys. Chem. Lett.* **2015**, *6*, 4774–

4785.

[46]   Y. Tian, I. G. Scheblykin, *J. Phys. Chem. Lett.* **2015**, *6*, 3466–3470.

[47]   M. Saliba, J. P. Correa-Baena, C. M. Wolff, M. Stolterfoht, N. Phung, S. Albrecht, D. Neher, A. Abate, *Chem. Mater.* **2018**, *30*, 4193–4201.

[48]   S. Rühle, *Sol. Energy* **2016**, *130*, 139–147.

[49]   W. Shockley, H. J. Queisser, *J. Appl. Phys.* **1961**, *32*, 510–519.

[50]   F. Lang, M. Jošt, K. Frohna, E. Köhnen, A. Al-Ashouri, A. R. Bowman, T. Bertram, A. B. Morales-Vilches, D. Koushik, E. M. Tennyson, et al., *Joule* **2020**, *4*, 1054–1069.

[51]   P. Kaienburg, P. Hartnagel, B. E. Pieters, J. Yu, D. Grabowski, Z. Liu, J. Haddad, U. Rau, T. Kirchartz, *J. Phys. Chem. C* **2018**, *122*, 27263–27272.

[52]   I. Levine, O. G. Vera, M. Kulbak, D. R. Ceratti, C. Rehermann, J. A. Márquez, S. Levcenko, T. Unold, G. Hodes, I. Balberg, et al., *ACS Energy Lett.* **2019**, *4*, 1150–1157.

[53]   F. Gao, Y. Zhao, X. Zhang, J. You, *Adv. Energy Mater.* **2020**, *10*, 1902650.

[54]   E. T. Hoke, D. J. Slotcavage, E. R. Dohner, A. R. Bowring, H. I. Karunadasa, M. D. McGehee, *Chem. Sci.* **2015**, *6*, 613–617.

[55]   F. Brivio, C. Caetano, A. Walsh, *J. Phys. Chem. Lett.* **2016**, *7*, 1083–1087.

[56]   C. G. Bischak, C. L. Hetherington, H. Wu, S. Aloni, D. F. Ogletree, D. T. Limmer, N. S. Ginsberg, *Nano Lett.* **2017**, *17*, 1028–1033.

[57]   A. J. Knight, A. D. Wright, J. B. Patel, D. P. McMeekin, H. J. Snaith, M. B. Johnston, L. M. Herz, *ACS Energy Lett.* **2019**, *4*, 75–84.

[58]   S. Draguta, O. Sharia, S. J. Yoon, M. C. Brennan, Y. V. Morozov, J. M. Manser, P. V. Kamat, W. F. Schneider, M. Kuno, *Nat. Commun.* **2017**, *8*, 1–8.

[59]   C. Momblona, L. Gil-Escrig, E. Bandiello, E. M. Hutter, M. Sessolo, K. Lederer, J. Blochwitz-Nimoth, H. J. Bolink, *Energy Environ. Sci.* **2016**, *9*, 3456–3463.

[60]   D. Liu, M. K. Gangishetty, T. L. Kelly, *J. Mater. Chem. A* **2014**, *2*, 19873–19881.

[61]   M. Mateen, Z. Arain, C. Liu, Y. Yang, X. Liu, Y. Ding, P. Shi, Y. Ren, Y. Wu, S. Dai, et al., *ACS Sustain. Chem. Eng.* **2019**, *7*, 11760–11768.

[62]   N. Mohammadian, A. H. Alizadeh, A. Moshaii, S. Gharibzadeh, A. Alizadeh, R. Mohammadpour, D. Fathi, *Thin Solid Films* **2016**, *616*, 754–759.

[63]   F. Mathies, H. Eggers, B. S. Richards, G. Hernandez-Sosa, U. Lemmer, U. W. Paetzold, *ACS Appl. Energy Mater.* **2018**, *1*, 1834–1839.

[64]   J. H. Heo, M. H. Lee, M. H. Jang, S. H. Im, *J. Mater. Chem. A* **2016**, *4*, 17636–17642.

[65]   D. Moghe, L. Wang, C. J. Traverse, A. Redoute, M. Sponseller, P. R. Brown, V. Bulović, R. R. Lunt, *Nano Energy* **2016**, *28*, 469–474.

[66]   N. J. Jeon, J. H. Noh, Y. C. Kim, W. S. Yang, S. Ryu, S. Il Seok, *Nat. Mater.* **2014**, *13*, 897–903.

[67]   Q. Jiang, D. Rebollar, J. Gong, E. L. Piacentino, C. Zheng, T. Xu, *Angew. Chemie* **2015**, *127*, 7727–7730.

[68]   P. Patnaik, *Handbook of Inorganic Chemicals*, **2003**.

[69]   S. E. Denmark, G. L. Beutner, *Angew. Chemie - Int. Ed.* **2008**, *47*, 1560–1638.

[70]   Y. Rakita, N. Kedem, S. Gupta, A. Sadhanala, V. Kalchenko, M. L. Böhm, M. Kulbak, R. H. Friend, D. Cahen, G. Hodes, *Cryst. Growth Des.* **2016**, *16*, 5717–5725.

[71]   J. Stevenson, B. Sorenson, V. H. Subramaniam, J. Raiford, P. P. Khlyabich, Y. L. Loo, P. Clancy, *Chem. Mater.* **2017**, *29*, 2435–2444.

[72]   S. Rahimnejad, A. Kovalenko, S. M. Forés, C. Aranda, A. Guerrero, *ChemPhysChem* **2016**, *17*, 2795–2798.

[73]   K. G. Stamplecoskie, J. S. Manser, P. V. Kamat, *Energy Environ. Sci.* **2015**, *8*, 208–215.

[74]   S. J. Yoon, K. G. Stamplecoskie, P. V. Kamat, *J. Phys. Chem. Lett.* **2016**, *7*, 1368–1373.

[75]   J. Cao, X. Jing, J. Yan, C. Hu, R. Chen, J. Yin, J. Li, N. Zheng, *J. Am. Chem. Soc.* **2016**, *138*, 9919–9926.

[76]   A. A. Petrov, I. P. Sokolova, N. A. Belich, G. S. Peters, P. V. Dorovatovskii, Y. V. Zubavichus, V. N. Khrustalev, A. V. Petrov, M. Grätzel, E. A. Goodilin, et al., *J. Phys. Chem. C* **2017**, *121*, 20739–20743.

[77]   I. L. Ivanov, A. S. Steparuk, M. S. Bolyachkina, D. S. Tsvetkov, A. P. Safronov, A. Y. Zuev, *J. Chem. Thermodyn.* **2018**, *116*, 253–258.

[78]   A. S. Tutantsev, N. N. Udalova, S. A. Fateev, A. A. Petrov, A. A. Petrov, W. Chengyuan, E. G. Maksimov, E. A. Goodilin, E. A. Goodilin, A. B. Tarasov, et al., *J. Phys. Chem. C* **2020**, *124*, 11117–11123.

[79]   J. Burschka, N. Pellet, S.-J. Moon, R. Humphry-Baker, P. Gao, M. K. Nazeeruddin, M. Grätzel, *Nature* **2013**, *499*, 316–319.

[80]   A. Binek, I. Grill, N. Huber, K. Peters, A. G. Hufnagel, M. Handloser, P. Docampo, A. Hartschuh, T. Bein, *Chem. - An Asian J.* **2016**, *11*, 1199–1204.

[81]   M. Krumrey, G. Ulm, *Nucl. Instruments Methods Phys. Res. Sect. A Accel. Spectrometers, Detect. Assoc. Equip.* **2001**, *467*, 1175–1178.

[82]   A. Hoell, I. Zizak, H. Bieder, L. Mokrani, *DE102006029449* **2007**.

[83]   U. Keiderling, *Appl. Phys. A* **2002**, *74*, s1455–s1457.

[84]   G. E. Eperon, S. D. Stranks, C. Menelaou, M. B. Johnston, L. M. Herz, H. J. Snaith, *Energy Environ. Sci.* **2014**, *7*, 982–988.

[85]   P. Fedeli, F. Gazza, D. Calestani, P. Ferro, T. Besagni, A. Zappettini, G. Calestani, E. Marchi, P. Ceroni, R. Mosca, *J. Phys. Chem. C* **2015**, *119*, 21304–21313.

[86]   A. Sadhanala, S. Ahmad, B. Zhao, N. Giesbrecht, P. M. Pearce, F. Deschler, R. L. Z. Hoye, K. C. Gödel, T. Bein, P. Docampo, et al., *Nano Lett.* **2015**, *15*, 6095–6101.

[87]   T. Jesper Jacobsson, J.-P. Correa-Baena, M. Pazoki, M. Saliba, K. Schenk, M. Grätzel, A. Hagfeldt, *Energy Environ. Sci.* **2016**, *9*, 1706–1724.

[88]   M. Saliba, T. Matsui, J.-Y. Seo, K. Domanski, J.-P. Correa-Baena, M. K. Nazeeruddin, S. M. Zakeeruddin, W. Tress, A. Abate, A. Hagfeldt, et al., *Energy Environ. Sci.* **2016**, *9*, 1989–1997.

[89]   R. E. Beal, D. J. Slotcavage, T. Leijtens, A. R. Bowring, R. A. Belisle, W. H. Nguyen, G. F. Burkhard, E. T. Hoke, M. D. McGehee, *J. Phys. Chem. Lett.* **2016**, *7*, 746–751.

[90]   R. J. Sutton, G. E. Eperon, L. Miranda, E. S. Parrott, B. A. Kamino, J. B. Patel, M. T.

Hörantner, M. B. Johnston, A. A. Haghighirad, D. T. Moore, et al., *Adv. Energy Mater.* **2016**, *6*, DOI 10.1002/aenm.201502458.

[91]   C. C. Boyd, J. Xu, K. A. Bush, J. A. Raiford, R. Cheacharoen, M. D. McGehee, in *Opt. InfoBase Conf. Pap.*, OSA - The Optical Society, **2019**, p. PM4C.1.

[92]   R. Lin, K. Xiao, Z. Qin, Q. Han, C. Zhang, M. Wei, M. I. Saidaminov, Y. Gao, J. Xu, M. Xiao, et al., *Nat. Energy* **2019**, *4*, 864–873.

[93]   F. Hermerschmidt, F. Mathies, V. R. F. Schröder, C. Rehermann, N. Z. Morales, E. L. Unger, E. J. W. List-Kratochvil, *Mater. Horizons* **2020**, *7*, 1773–1781.

[94]   T. Wu, J. Li, Y. Zou, H. Xu, K. Wen, S. Wan, S. Bai, T. Song, J. A. McLeod, S. Duhm, et al., *Angew. Chemie Int. Ed.* **2020**, *59*, 4099–4105.

[95]   S. P. Senanayak, M. Abdi-Jalebi, V. S. Kamboj, R. Carey, R. Shivanna, T. Tian, G. Schweicher, J. Wang, N. Giesbrecht, D. Di Nuzzo, et al., *Sci. Adv.* **2020**, *6*, eaaz4948.

[96]   H. S. Gill, B. Elshahat, A. Kokil, L. Li, R. Mosurkal, P. Zygmanski, E. Sajo, J. Kumar, *Phys. Med.* **2018**, *5*, 20–23.

[97]   S. Albrecht, M. Saliba, J. P. Correa-Baena, K. Jäger, L. Korte, A. Hagfeldt, M. Grätzel, B. Rech, *J. Opt. (United Kingdom)* **2016**, *18*, DOI 10.1088/2040-8978/18/6/064012.

[98]   D. P. McMeekin, G. Sadoughi, W. Rehman, G. E. Eperon, M. Saliba, M. T. Hörantner, A. Haghighirad, N. Sakai, L. Korte, B. Rech, et al., *Science (80-.).* **2016**, *351*, 151–155.

[99]   C. D. Bailie, M. G. Christoforo, J. P. Mailoa, A. R. Bowring, E. L. Unger, W. H. Nguyen, J. Burschka, N. Pellet, J. Z. Lee, M. Grätzel, et al., *Energy Environ. Sci.* **2015**, *8*, 956–963.

[100] B. Saparov, D. B. Mitzi, *Chem. Rev.* **2016**, *116*, 4558–4596.

[101] M. G. Goesten, R. Hoffmann, *J. Am. Chem. Soc.* **2018**, *140*, 12996–13010.

[102] R. J. Elliott, *Phys. Rev.* **1957**, *108*, 1384–1389.

[103] A. M. Soufiani, F. Huang, P. Reece, R. Sheng, A. Ho-Baillie, M. A. Green, *Appl. Phys. Lett.* **2015**, *107*, 231902.

[104] (ICDD; 2018) PDF 01-084-7607, **2020**.

[105] (ICDD; 1957) PDF 00-007-0235, **2020**.

[106] P. W. (Peter W. Atkins, J. De Paula, *Atkins' Physical Chemistry*, Oxford University Press, **2010**.

[107] Y. Liu, S. Akin, A. Hinderhofer, F. T. Eickemeyer, H. Zhu, J. Seo, J. Zhang, F. Schreiber, H. Zhang, S. M. Zakeeruddin, et al., *Angew. Chemie Int. Ed.* **2020**, *59*, 15688–15694.

[108] R. Hu, Y. Zhang, S. Paek, X. X. Gao, X. Li, M. K. Nazeeruddin, *J. Mater. Chem. A* **2020**, *8*, 8058–8064.

[109] A. Le Bail, H. Duroy, J. L. Fourquet, *Mater. Res. Bull.* **1988**, *23*, 447–452.

[110] M. Baranowski, P. Plochocka, *Adv. Energy Mater.* **2020**, *10*, 1903659.

[111] T. J. Coutts, J. S. Ward, D. L. Young, K. A. Emery, T. A. Gessert, R. Noufi, *Prog. Photovoltaics Res. Appl.* **2003**, *11*, 359–375.

[112] K. Jäger, L. Korte, B. Rech, S. Albrecht, *Opt. Express* **2017**, *25*, A473.

[113] E. L. Unger, L. Kegelmann, K. Suchan, D. Sörell, L. Korte, S. Albrecht, *J. Mater. Chem. A* **2017**, *5*, 11401–11409.

[114] G. F. Samu, C. Janáky, P. V. Kamat, *ACS Energy Lett.* **2017**, *2*, 1860–1861.

[115] R. G. Balakrishna, S. M. Kobosko, P. V. Kamat, *ACS Energy Lett.* **2018**, *3*, 2267–2272.

[116] S. Mahesh, J. M. Ball, R. D. J. Oliver, D. P. McMeekin, P. K. Nayak, M. B. Johnston, H. J. Snaith, *Energy Environ. Sci.* **2020**, DOI 10.1039/c9ee02162k.

[117] A. Sadhanala, F. Deschler, T. H. Thomas, S. E. Dutton, K. C. Goedel, F. C. Hanusch, M. L. Lai, U. Steiner, T. Bein, P. Docampo, et al., *J. Phys. Chem. Lett.* **2014**, *5*, 2501–2505.

[118] C. M. Sutter-Fella, Y. Li, M. Amani, J. W. Ager, F. M. Toma, E. Yablonovitch, I. D. Sharp, A. Javey, *Nano Lett.* **2016**, *16*, 800–806.

[119] A. J. Barker, A. Sadhanala, F. Deschler, M. Gandini, S. P. Senanayak, P. M. Pearce, E. Mosconi, A. J. Pearson, Y. Wu, A. R. Srimath Kandada, et al., *ACS Energy Lett.* **2017**, *2*, DOI 10.1021/acsenergylett.7b00282.

[120] M. Hu, C. Bi, Y. Yuan, Y. Bai, J. Huang, *Adv. Sci.* **2016**, *3*, 1500301.

[121] K. Suchan, A. Merdasa, C. Reherman, E. Unger, I. G. Scheblykin, *J. Lumin.* **2020**, 117073.

[122] B. W. Park, B. Philippe, S. M. Jain, X. Zhang, T. Edvinsson, H. Rensmo, B. Zietz, G. Boschloo, *J. Mater. Chem. A* **2015**, *3*, 21760–21771.

[123] S. J. Yoon, S. Draguta, J. S. Manser, O. Sharia, W. F. Schneider, M. Kuno, P. V. Kamat, *ACS Energy Lett.* **2016**, *1*, 290–296.

[124] T. Leijtens, G. E. Eperon, A. J. Barker, G. Grancini, W. Zhang, J. M. Ball, A. R. S. Kandada, H. J. Snaith, A. Petrozza, *Energy Environ. Sci.* **2016**, *9*, 3472–3481.

[125] T. Jesper Jacobsson, J.-P. Correa-Baena, M. Pazoki, M. Saliba, K. Schenk, M. Grätzel, A. Hagfeldt, *Energy Environ. Sci.* **2016**, *9*, 1706–1724.

[126] P. Pistor, T. Burwig, C. Brzuska, B. Weber, W. Fränzel, *J. Mater. Chem. A* **2018**, *6*, 11496–11506.

[127] F. Lehmann, A. Franz, D. M. Többens, S. Levcenco, T. Unold, A. Taubert, S. Schorr, *RSC Adv.* **2019**, *9*, 11151–11159.

[128] Y. Tidhar, E. Edri, H. Weissman, D. Zohar, G. Hodes, D. Cahen, B. Rybtchinski, S. Kirmayer, *J. Am. Chem. Soc.* **2014**, *136*, 13249–13256.

[129] I. Wharf, T. Gramstad, R. Makhija, M. Onyszchuk, *Can. J. Chem.* **1976**, *54*, 3430–3438.

[130] J. S. Manser, B. Reid, P. V. Kamat, *J. Phys. Chem. C* **2015**, *119*, 17065–17073.

[131] S. J. Yoon, K. G. Stamplecoskie, P. V. Kamat, *J. Phys. Chem. Lett.* **2016**, *7*, 1368–1373.

[132] D. Burkitt, J. Searle, T. Watson, *R. Soc. Open Sci.* **2018**, *5*, 172158.

[133] F. Di Giacomo, S. Shanmugam, H. Fledderus, B. J. Bruijnaers, W. J. H. Verhees, M. S. Dorenkamper, S. C. Veenstra, W. Qiu, R. Gehlhaar, T. Merckx, et al., *Sol. Energy Mater. Sol. Cells* **2018**, *181*, 53–59.

[134] "Solaronix Achieves Major Breakthrough Toward Perovskite Solar Cell Industrialization – Solaronix," can be found under https://www.solaronix.com/news/solaronix-achieves-major-breakthrough-toward-perovskite-solar-cell-industrialization/, **n.d.**

[135] C. Gong, S. Tong, K. Huang, H. Li, H. Huang, J. Zhang, J. Yang, *Sol. RRL* **2020**, *4*, 1900204.

[136] J. Zhang, T. Bu, J. Li, H. Li, Y. Mo, Z. Wu, Y. Liu, X. L. Zhang, Y. B. Cheng, F. Huang, *J. Mater. Chem. A* **2020**, *8*, 8447–8454.

[137] C. Schultz, M. Fenske, J. Dagar, A. Zeiser, A. Bartelt, R. Schlatmann, E. Unger, B. Stegemann, *Sol. Energy* **2020**, *198*, 410–418.

[138] M. Jošt, B. Lipovšek, B. Glažar, A. Al-Ashouri, K. Brecl, G. Matič, A. Magomedov, V. Getautis, M. Topič, S. Albrecht, *Adv. Energy Mater.* **2020**, *10*, 2000454.

[139] C. Liu, Y. B. Cheng, Z. Ge, *Chem. Soc. Rev.* **2020**, *49*, 1653–1687.

[140] M. Saliba, K. W. Tan, H. Sai, D. T. Moore, T. Scott, W. Zhang, L. A. Estroff, U. Wiesner, H. J. Snaith, *J. Phys. Chem. C* **2014**, *118*, 17171–17177.

[141] S. R. Raga, M. C. Jung, M. V. Lee, M. R. Leyden, Y. Kato, Y. Qi, *Chem. Mater.* **2015**, *27*, 1597–1603.

[142] G. E. Eperon, S. N. Habisreutinger, T. Leijtens, B. J. Bruijnaers, J. J. Van Franeker, D. W. Dequilettes, S. Pathak, R. J. Sutton, G. Grancini, D. S. Ginger, et al., *ACS Nano* **2015**, *9*, 9380–9393.

[143] S. Pathak, A. Sepe, A. Sadhanala, F. Deschler, A. Haghighirad, N. Sakai, K. C. Goedel, S. D. Stranks, N. Noel, M. Price, et al., *ACS Nano* **2015**, *9*, 2311–2320.

[144] J. Li, A. Dobrovolsky, A. Merdasa, E. L. Unger, I. G. Scheblykin, *ACS Omega* **2018**, *3*, 14494–14502.

[145] M. Buchhorn, S. Wedler, F. Panzer, *J. Phys. Chem. A* **2018**, *122*, 9115–9122.

[146] T.-B. Song, Z. Yuan, F. Babbe, D. P. Nenon, E. Aydin, S. De Wolf, C. M. Sutter-Fella, *ACS Appl. Energy Mater.* **2020**, acsaem.9b02052.

[147] S. Pratap, N. Tamura, C. Stan, Z. Yuan, H. Goudey, A. MacDowell, T.-B. Song, N. Barchi, P. Müller-Buschbaum, C. Sutter-Fella, et al., *Acta Crystallogr. Sect. A Found. Adv.* **2019**, *75*, a155–a156.

[148] Thorlabs, *SLS201L (/ M) SLS202L (/ M) Stabilized Tungsten Light Sources User Guide*, Thorlabs, **2020**.

[149] "M415F3_EmissionSpectrum," can be found under https://www.thorlabs.com/newgrouppage9.cfm?objectgroup_id=5206&pn=M415F3, **2020**.

[150] M. C. Brennan, A. Ruth, P. V. Kamat, M. Kuno, *Trends Chem.* **2020**, *2*, 282–301.

[151] A. Merdasa, C. Rehermann, K. Hirselandt, J. Li, O. Maus, J. Dagar, R. Munir, E. L. Unger, *submitted* **n.d.**

[152] R. Munir, A. D. Sheikh, M. Abdelsamie, H. Hu, L. Yu, K. Zhao, T. Kim, O. El Tall, R. Li, D.-M. Smilgies, et al., *Adv. Mater.* **2017**, *29*, 1604113.

[153] A. Jaffe, Y. Lin, C. M. Beavers, J. Voss, W. L. Mao, H. I. Karunadasa, *ACS Cent. Sci.* **2016**, *2*, 201–209.

[154] B. Brunetti, C. Cavallo, A. Ciccioli, G. Gigli, A. Latini, *Sci. Rep.* **2016**, *6*, DOI 10.1038/srep31896.

[155] G. P. Nagabhushana, R. Shivaramaiah, A. Navrotsky, *Proc. Natl. Acad. Sci. U. S. A.* **2016**, *113*, 7717–7721.

[156] K. Suchan, J. Just, P. Becker, E. L. Unger, T. Unold, *J. Mater. Chem. A* **2020**, *8*, 10439–10449.

[157] J. C. Hamill, J. Schwartz, Y.-L. Loo, *ACS Energy Lett.* **2018**, *3*, 92–97.

[158] Y. Deng, C. H. van Brackle, X. Dai, J. Zhao, B. Chen, J. Huang, *Sci. Adv.* **2019**, *5*, eaax7537.

[159] X. Liu, Y. Cheng, C. Liu, T. Zhang, N. Zhang, S. Zhang, J. Chen, Q. Xu, J. Ouyang, H. Gong, *Energy Environ. Sci.* **2019**, *12*, 1622–1633.

[160] Y. Zhang, S. Seo, S. Y. Lim, Y. Kim, S. G. Kim, D. K. Lee, S. H. Lee, H. Shin, H. Cheong, N. G. Park, *ACS Energy Lett.* **2020**, 360–366.

[161] M. M. Elsenety, M. Antoniadou, N. Balis, A. Kaltzoglou, L. Sygellou, A. Stergiou, N. Tagmatarchis, P. Falaras, *ACS Appl. Energy Mater.* **2020**, *3*, 2465–2477.

[162] T. Song, Z. Yuan, M. Mori, F. Motiwala, G. Segev, E. Masquelier, C. V. Stan, J. L. Slack, N. Tamura, C. M. Sutter-Fella, *Adv. Funct. Mater.* **2020**, *30*, 1908337.

[163] J. C. Hamill, J. Schwartz, Y. L. Loo, *ACS Energy Lett.* **2018**, *3*, 92–97.

[164] A. A. Petrov, S. A. Fateev, V. N. Khrustalev, Y. Li, P. V. Dorovatovskii, Y. V. Zubavichus, E. A. Goodilin, A. B. Tarasov, *Chem. Mater.* **2020**, DOI 10.1021/acs.chemmater.0c02156.

[165] O. Shargaieva, H. Näsström, J. A. Smith, D. Többens, R. Munir, E. Unger, *Mater. Adv.* **2020**, DOI 10.1039/D0MA00815J.

[166] M. Kulbak, I. Levine, E. Barak-Kulbak, S. Gupta, A. Zohar, I. Balberg, G. Hodes, D. Cahen, *Adv. Energy Mater.* **2018**, DOI 10.1002/aenm.201800398.

[167] J. Mooney, P. Kambhampati, *J. Phys. Chem. Lett.* **2013**, *4*, 3316–3318.

[168] J. Mooney, P. Kambhampati, *J. Phys. Chem. Lett.* **2014**, *5*, 3497.

[169] R. O. Ansell, T. Dickinson, A. F. Povey, P. M. . Sherwood, *J Electroanal. Chem.* **1979**, *96*, 79–89.

[170] M. Kojima, Isao; Kurahashi, *J. Electron Spectros. Relat. Phenomena* **1987**, *42*, 177–181.

[171] S. Braunger, L. E. Mundt, C. M. Wolff, M. Mews, C. Rehermann, M. Jošt, A. Tejada, D. Eisenhauer, C. Becker, J. A. Guerra, et al., *J. Phys. Chem. C* **2018**, *122*, 17123–17135.

[172] K. A. Bush, N. Rolston, A. Gold-Parker, S. Manzoor, J. Hausele, Z. J. Yu, J. A. Raiford, R. Cheacharoen, Z. C. Holman, M. F. Toney, et al., *ACS Energy Lett.* **2018**, *3*, 1225–1232.

[173] C. M. Sutter-Fella, D. W. Miller, Q. P. Ngo, E. T. Roe, F. M. Toma, I. D. Sharp, M. C. Lonergan, A. Javey, *ACS Energy Lett.* **2017**, *2*, 709–715.

[174] V. K. Lamer, R. H. Dinegar, *J. Am. Chem. Soc.* **1950**, *72*, 4847–4854.

[175] S. B. Naghadeh, S. Sarang, A. Brewer, A. Allen, Y. H. Chiu, Y. J. Hsu, J. Y. Wu, S. Ghosh, J. Z. Zhang, *J. Chem. Phys.* **2019**, *151*, 154705.

[176] D. Di, K. P. Musselman, G. Li, A. Sadhanala, Y. Ievskaya, Q. Song, Z. K. Tan, M. L. Lai, J. L. MacManus-Driscoll, N. C. Greenham, et al., *J. Phys. Chem. Lett.* **2015**, *6*, 446–450.

[177] J. A. Sichert, Y. Tong, N. Mutz, M. Vollmer, S. Fischer, K. Z. Milowska, R. García Cortadella, B. Nickel, C. Cardenas-Daw, J. K. Stolarczyk, et al., *Nano Lett.* **2015**, *15*, 6521–6527.

[178] P. Kumar, C. Muthu, V. C. Nair, K. S. Narayan, *J. Phys. Chem. C* **2016**, *120*, 18333–18339.

[179] P. Ijaz, M. Imran, M. M. Soares, H. C. N. Tolentino, B. Martín-García, C. Giannini, I. Moreels, L. Manna, R. Krahne, *J. Phys. Chem. Lett.* **2020**, *11*, 2079–2085.

[180] H. Diab, C. Arnold, F. Lédée, G. Trippé-Allard, G. Delport, C. Vilar, F. Bretenaker, J. Barjon, J. S. Lauret, E. Deleporte, et al., *J. Phys. Chem. Lett.* **2017**, *8*, 2977–2983.

[181] F. Staub, I. Anusca, D. C. Lupascu, U. Rau, T. Kirchartz, *J. Phys. Mater.* **2020**, *3*, 025003.

[182] N. J. Harrick, *Appl. Opt.* **1971**, *10*, 2344.

[183] A. G. Emslie, F. T. Bonner, L. G. Peck, *J. Appl. Phys.* **1958**, *29*, 858–862.

[184] S. Eickelmann, Experimental Study of Liquid Interfaces with Compositional Gradients: Distortion & Rupture of Ultra-Thin Films and Other Effects, Universität Potsdam Potsdam, **2018**.

[185] M. A. Flatken, A. Hoell, R. Wendt, E. Härk, A. Dallmann, J. Pascual, E. Unger, A. Abate, *submitted* **2020**.

[186] I. Breßler, J. Kohlbrecher, A. F. Thünemann, *J. Appl. Crystallogr.* **2015**, *48*, 1587–1598.

[187] V. S. Raghuwanshi, M. Ochmann, A. Hoell, F. Polzer, K. Rademann, *Langmuir* **2014**, *30*, 6038.

[188] K. Oldenburg, A. Vogler, *Electronic Spectra and Photochemistry of Tin(II), Lead(II), Antimony(III), and Bismuth(III) Bromide Complexes in Solution*, **1993**.

[189] M. I. Saidaminov, A. L. Abdelhady, B. Murali, E. Alarousu, V. M. Burlakov, W. Peng, I. Dursun, L. Wang, Y. He, G. MacUlan, et al., *Nat. Commun.* **2015**, *6*, 1–6.

[190] M. I. Saidaminov, A. L. Abdelhady, G. Maculan, O. M. Bakr, *Chem. Commun.* **2015**, *51*, 17658–17661.

[191] W. J. Moore, *Appl. Opt.* **1994**, *33*, 4164.

[192] N. Nickel, E. Unger, V. Blank, F. Mathies, C. Rehermann, J. Rappich, C. Kaspari, C. Camus, *37th Eur. Photovolt. Sol. Energy Conf. Exhib.* **2020**, 596–600.

[193] G. P. Nagabhushana, R. Shivaramaiah, A. Navrotsky, *Proc. Natl. Acad. Sci. U. S. A.* **2016**, *113*, 7717–21.

A. Appendix

A.1 Scientific Appendix Chapter 4
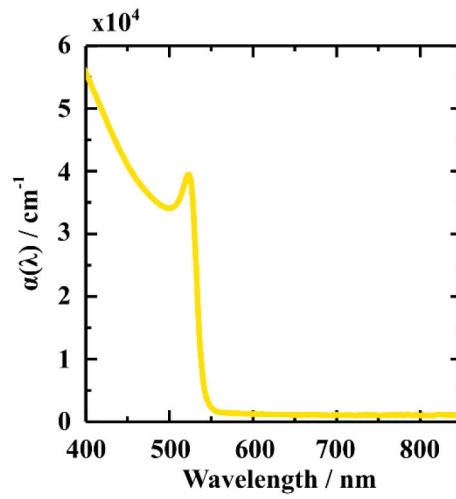
Figure A.1.1: Absorption coefficient α for high-quality 270 nm thick MAPbBr$_3$ thin-film.
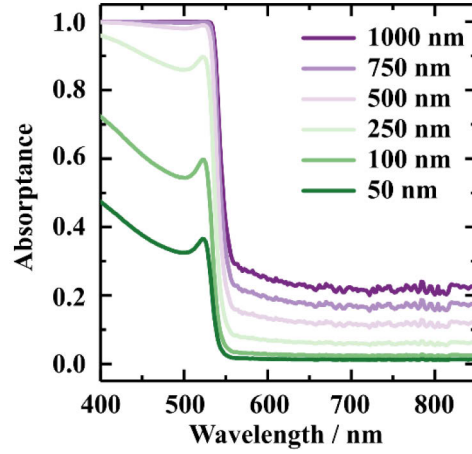
Figure A.1.2: Calculated absorptance spectra for MAPbBr₃ thin-films assuming no scattering ($\gamma = 0$) and a full coverage ($\beta = 1$) with varying film thickness *d*.
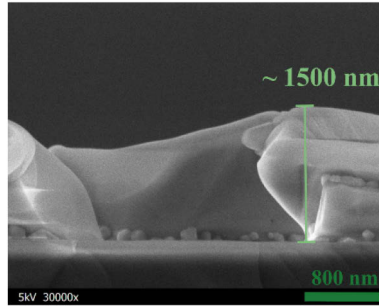
Figure A.1.3: SEM cross section image of a low-quality MAPbBr₃ film presenting a maximum thickness of around 1500 nm.

Table A.1.1: Calculated bandgap (E_g) and exciton binding energy (E_B) for perovskites compositions discussed in this chapter.

	MAPbI₃	**MAPbBr₃**	**MAPbI₃**	**FAPbI₃**	**FAPbBr₃**	**FAPbCl₃**
E_g /eV	1.63	2.37	3.17	1.57	2.35	3.15
E_B /meV	7.7	25.3	66.8	10.5	33.8	55.1

	CsPbBr₃	**3CatPbBr₃**
E_g /eV	2.44	2.34
E_B /meV	38.8	27.8

A.2 Scientific Appendix Chapter 5
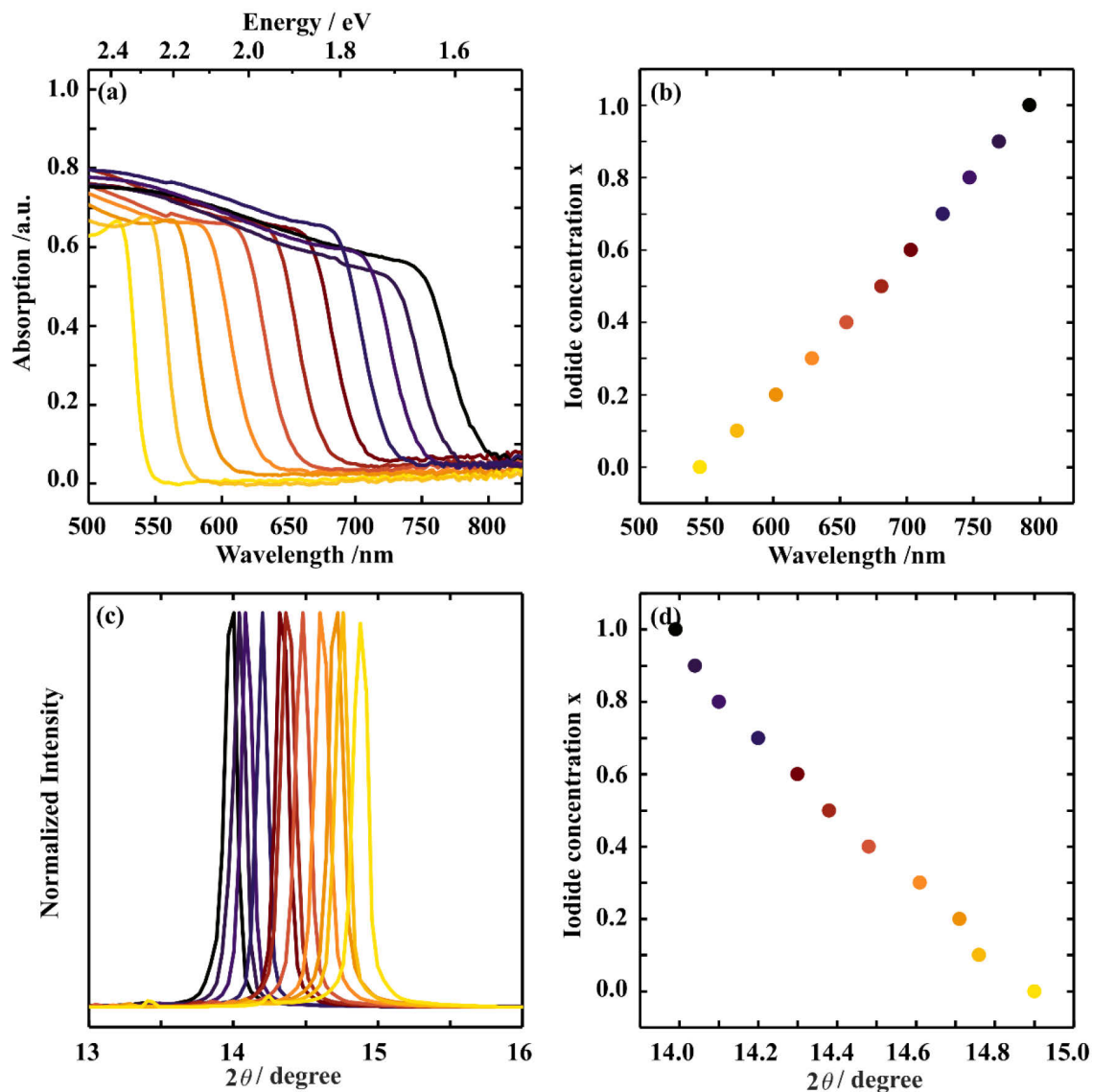
Figure A.2.1: UV-vis and XRD measurements on final films of the full MAPb(I$_x$Br$_{1-x}$)$_3$ series from X_{sol} = 0.0 to X_{sol} = 1.0 in 0.1 steps prepared from 4:1 DMF:DMSO. (a) Absorption measurements and (b) calibration curve for the absorption onset as a function of the mixed in iodide amount X_{sol}. (c) XRD measurements for 100/ 110 reflection and (b) calibration curve for the 100/ 110 reflection position as a function of the mixed in iodide amount X_{sol}.
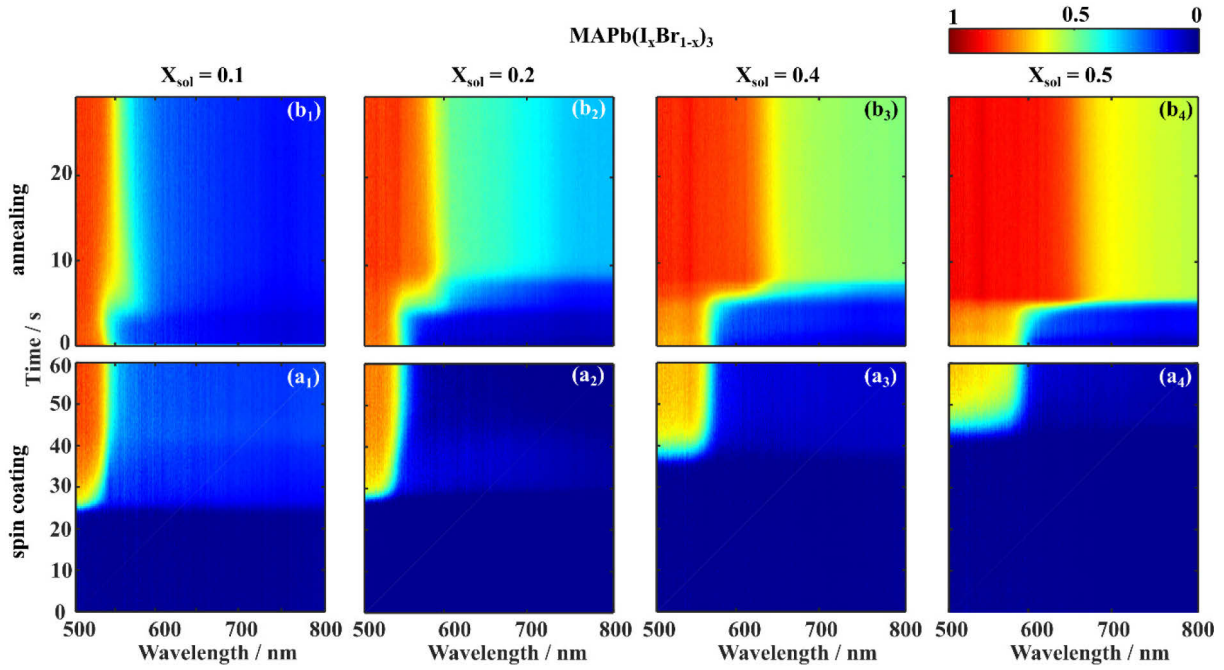
Figure A.2.2: In-situ UV-vis measurements for (a) spin-coating and (b) annealing process for (1) $X_{sol} = 0.1$, (2) $X_{sol} = 0.2$, (3) $X_{sol} = 0.4$, and (4) $X_{sol} = 0.5$.

Already, for $X_{sol} = 0.1$ the formation proceeds via two competing pathways, identified by in-situ UV-vis measurements. A bromide-rich perovskite phase with an absorption edge at 550 nm forms during spin-coating. While annealing, the iodide incorporation into the perovskite takes place, represented by the stepwise shift of the absorption edge to 570 nm. As well, all halide ratios $0.1 \leq X_{sol} \leq 0.6$ follow this trend of a bromide-rich perovskite formation during spin-coating and iodide incorporation during annealing.
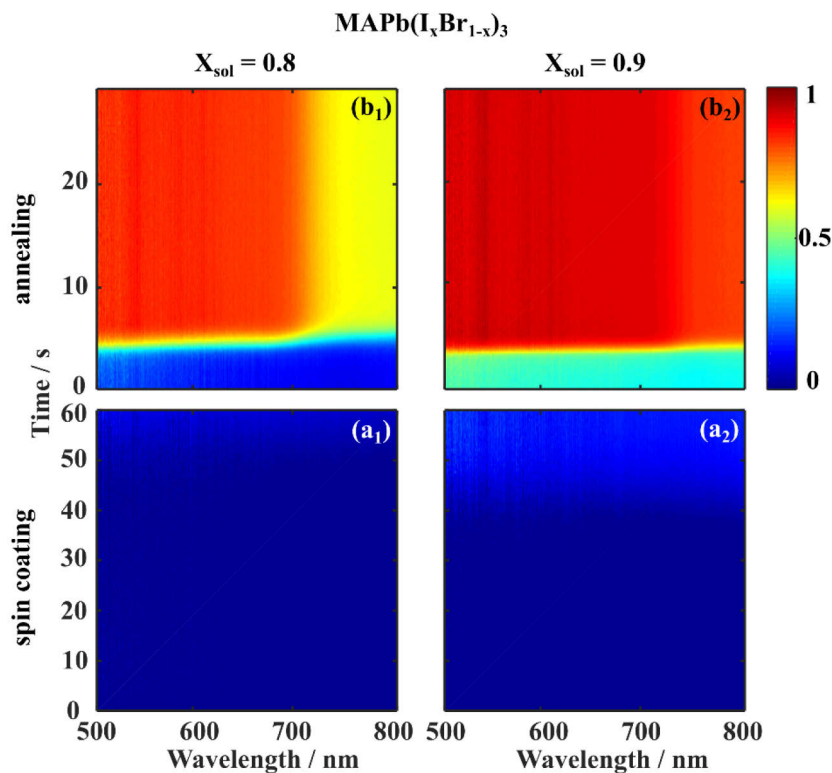
Figure A.2.3: In-situ UV-vis measurements for (a) spin-coating and (b) annealing process for (1) $X_{sol} = 0.8$ and (2) $X_{sol} = 0.9$.

Films from $X_{sol} = 0.8$ and 0.9 do not show an absorption onset during spin-coating, hence no perovskite phase crystallizes and an intermediate solvate phase dominates the formation while spin-coating as described for $X_{sol} = 0.7$ and 1.0.
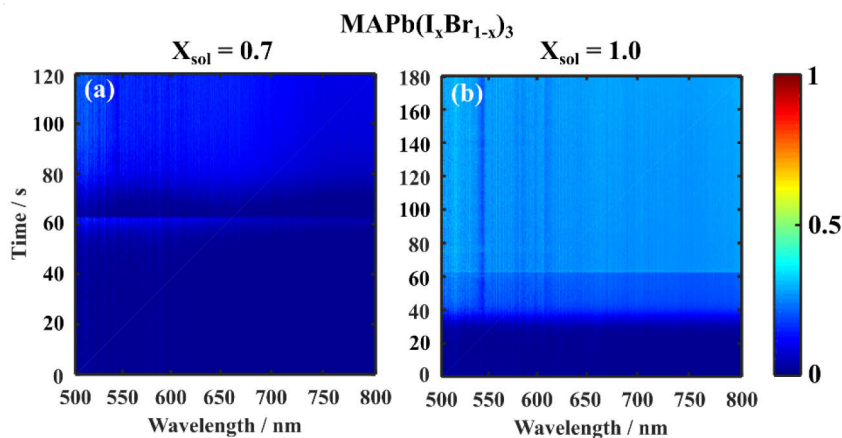
Figure A.2.4: In-situ UV-vis measurements for (a) $X_{sol} = 0.7$ and (b) $X_{sol} = 1.0$ during 60 s of spin-coating and subsequent drying for 60 s or 120 s.
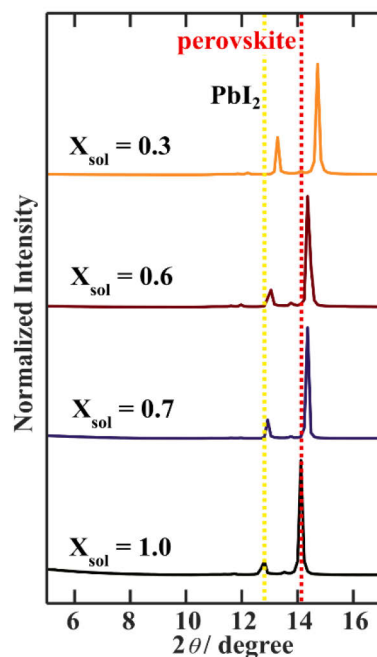
Figure A.2.5: XRD patterns for thin-films containing iodine, measured within 3 h after thermal annealing.

Table A.2.1: Overview of ΔHf for MAPbI₃, MAPbBr₃ and different iodide-based solvate phases.

Material	ΔH_f
$MAPbI_3$	-371.6 kJ/mol [77], -375.6 kJ/mol [154], -341.59 kJ/mol [193]
$MAPbBr_3$	-543.08 kJ/mol [77], -539.6 kJ/mol [154], -529.61 kJ/mol [193]
$(MA)_2(DMSO)_2Pb_3I_8$	-1633.4 kJ/mol (-390.4 kcal/mol) [76]
$(MA)_2(DMF)_2Pb_3I_8$	-753.5 kJ/mol (-180.1 kcal/mol).[76]
$(MA)_2(DMF)_2Pb_2I_6$	-743,1 kJ/mol (-177.6 kcal/mol) [76]
$(MA)_3(DMF)PbI_5$	-559,8 kJ/mol (-133.8 kcal/mol) [76]

Table A.2.2: Positions of first five reflections for the $(MA)_2(DMSO)_2Pb_3I_8$ solvate phase and the solvate phases formed from after spin-coating from solutions with $X_{sol} = 1.0$ and 0.7 with the respective shift in reflection position.

Phase	2θ Reflection Position ($\lambda = 1.5406$ Å)					
$(MA)_2(DMSO)_2Pb_3I_8$[75]	6.58	7.28	9.25	11.85	12.99	13.21
solvate phase from $X_{sol} = 1.0$	6.58	7.23	9.19	11.76	12.89	13.15
solvate phase from $X_{sol} = 0.7$	6.71	7.35	9.34	11.95	13.09	13.34
Shift in reflection position between $(MA)_2(DMSO)_2Pb_3I_8$[75] and $X_{sol} = 0.7$	0.13	0.13	0.11	0.10	0.10	0.13

A.3 Scientific Appendix Chapter 6
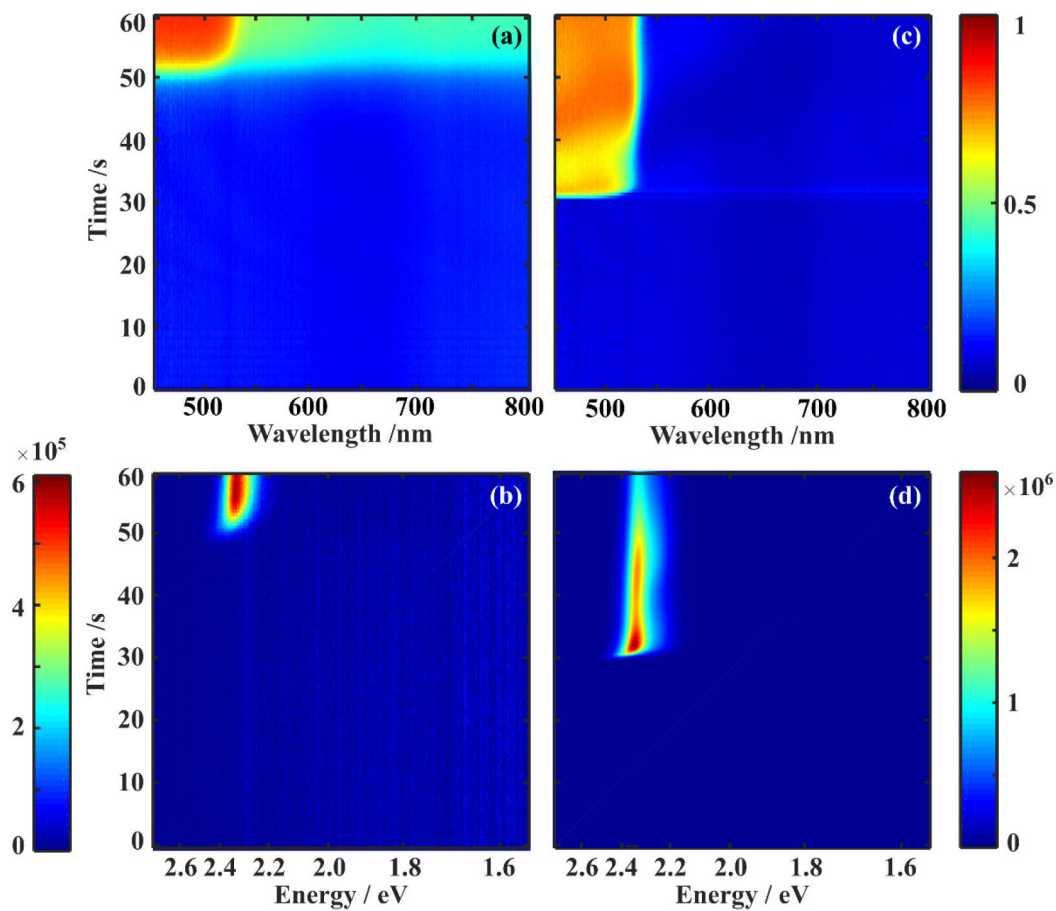
Figure A.3.1: 2D heat maps presenting the formation process of MAPbBr₃ without (left) and with (right) dropping an anti-solvent tracked over 60 s of spin-coating. (a) and (c) present the in-situ UV-vis measurements, while (b) and (d) show the in-situ PL measurements, respectively.
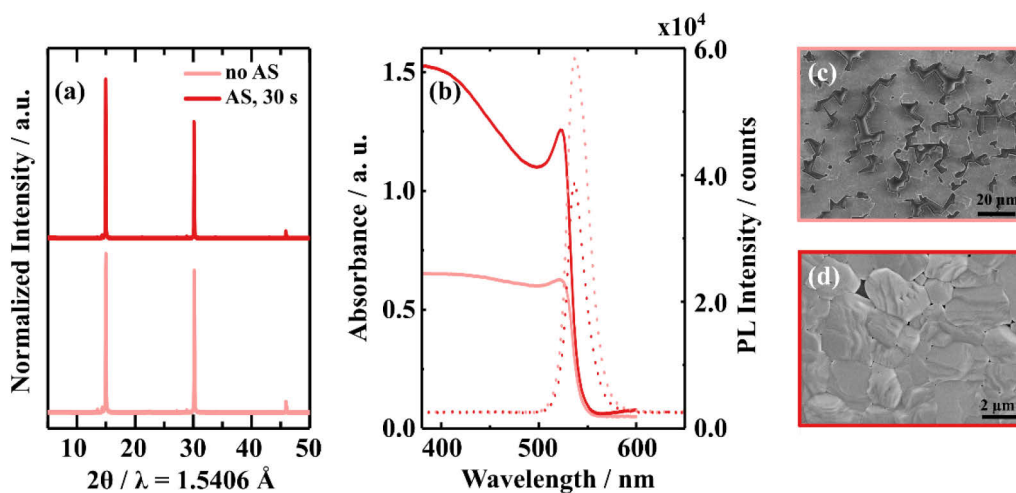
Figure A.3.2: Final MAPbBr₃ film properties based on setting an anti-solvent drop during spin-coating, (a) XRD pattern, (b) UV-vis and PL spectra, and (c) SEM top view images.
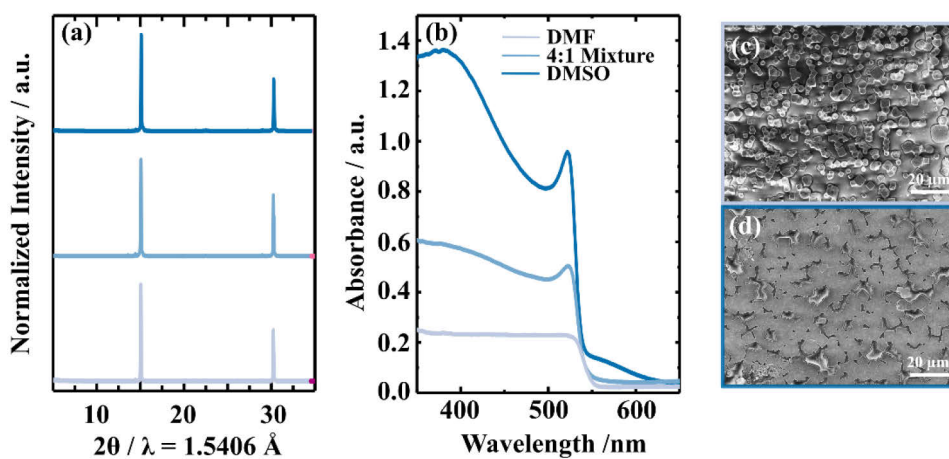
Figure A.3.3: Final MAPbBr₃ film properties based on solutions prepared utilizing DMF, 4:1 DMF:DMSO, and DMSO, (a) XRD pattern, (b) UV-vis and PL spectra, and (c) SEM top view images.
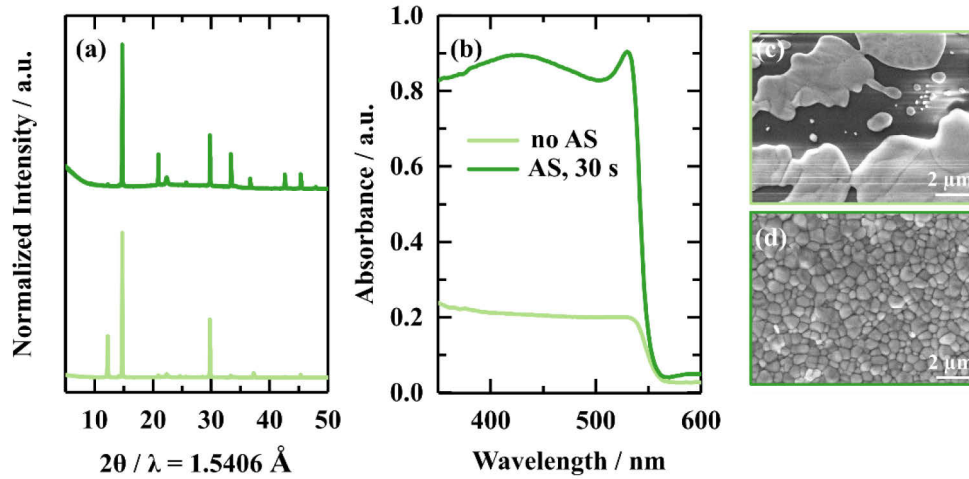
Figure A.3.4: Final FAPbBr₃ film properties based on setting an anti-solvent drop during spin-coating, (a) XRD pattern, (b) UV-vis and PL spectra, and (c) SEM top view images.
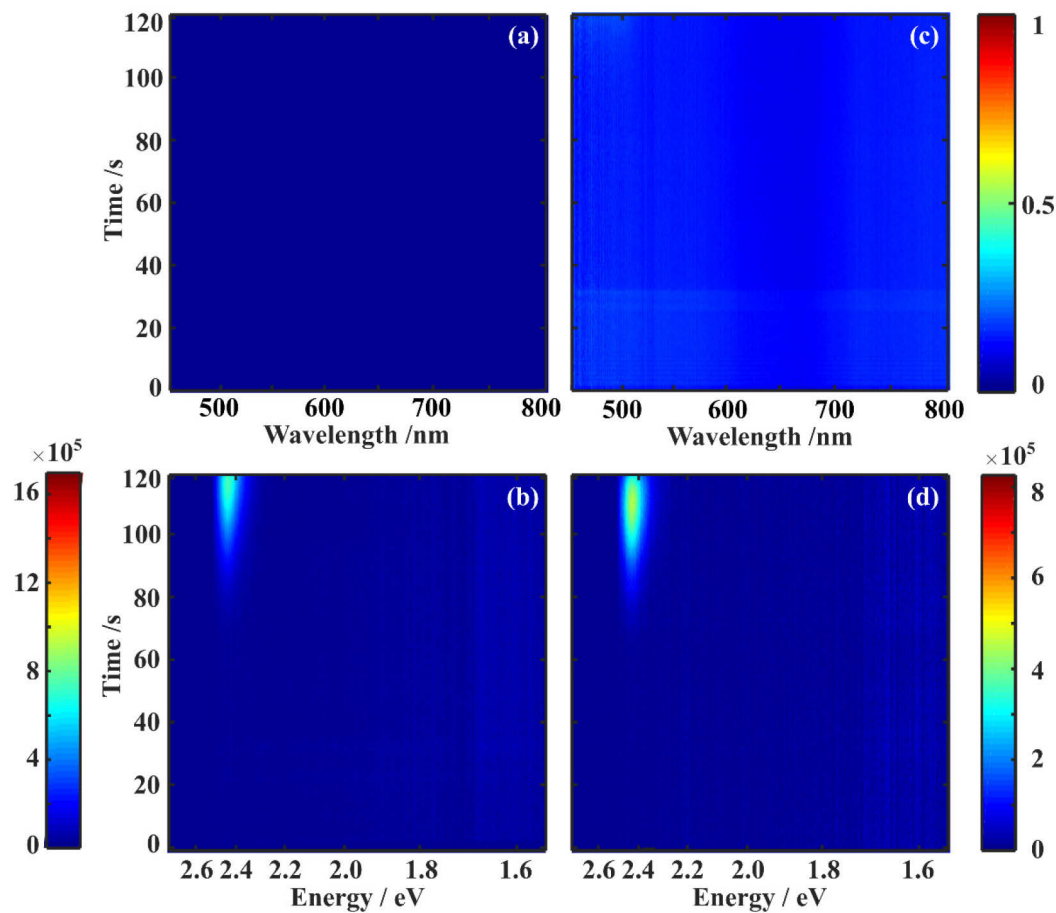
Figure A.3.5: 2D heat maps presenting the formation process of CsPbBr₃ without (left) and with (right) dropping an anti-solvent tracked over 120 s of spin-coating. (a) and (c) present the in-situ UV-vis measurements, while (b) and (d) show the in-situ PL measurements, respectively.
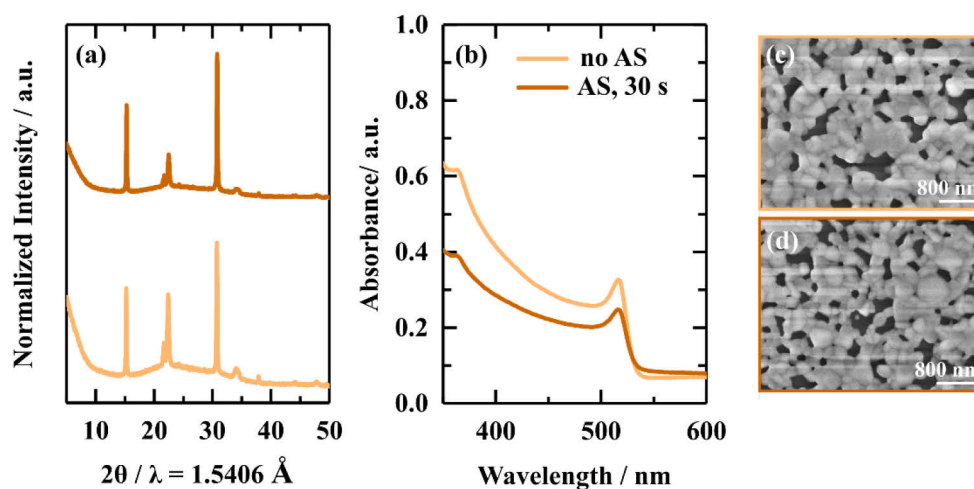
Figure A.3.6: Final CsPbBr₃ film properties based on setting an anti-solvent drop during spin-coating, (a) XRD pattern, (b) UV-vis and PL spectra, and (c) SEM top view images.
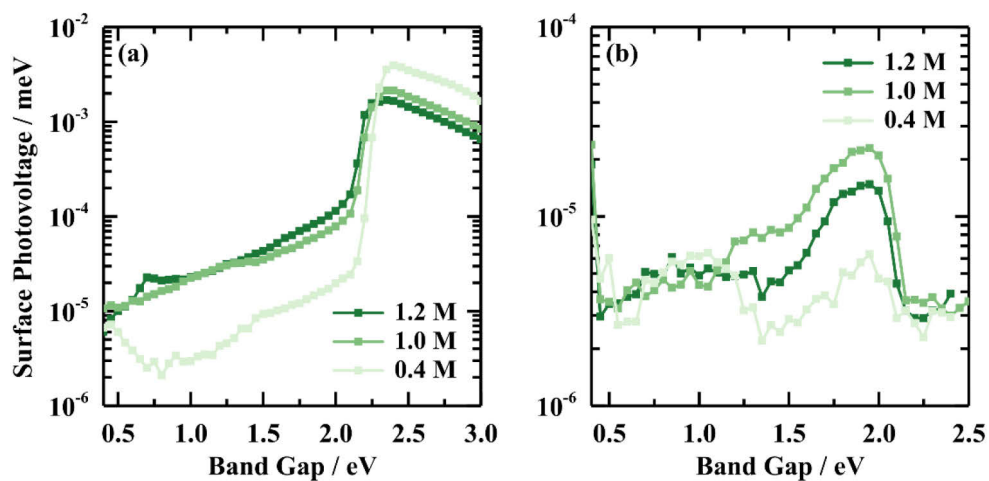
Figure A.3.7: Modulated SPV measurements on a MAPbBr₃ thin-film series, spin-coated from 1.2 M, 1.0 M, and 0.4 M solutions on ITO|PTAA as contact layers. The overview signal is presented in (a) and the defect sensitive measurement with a LP 610 nm filter in (b).
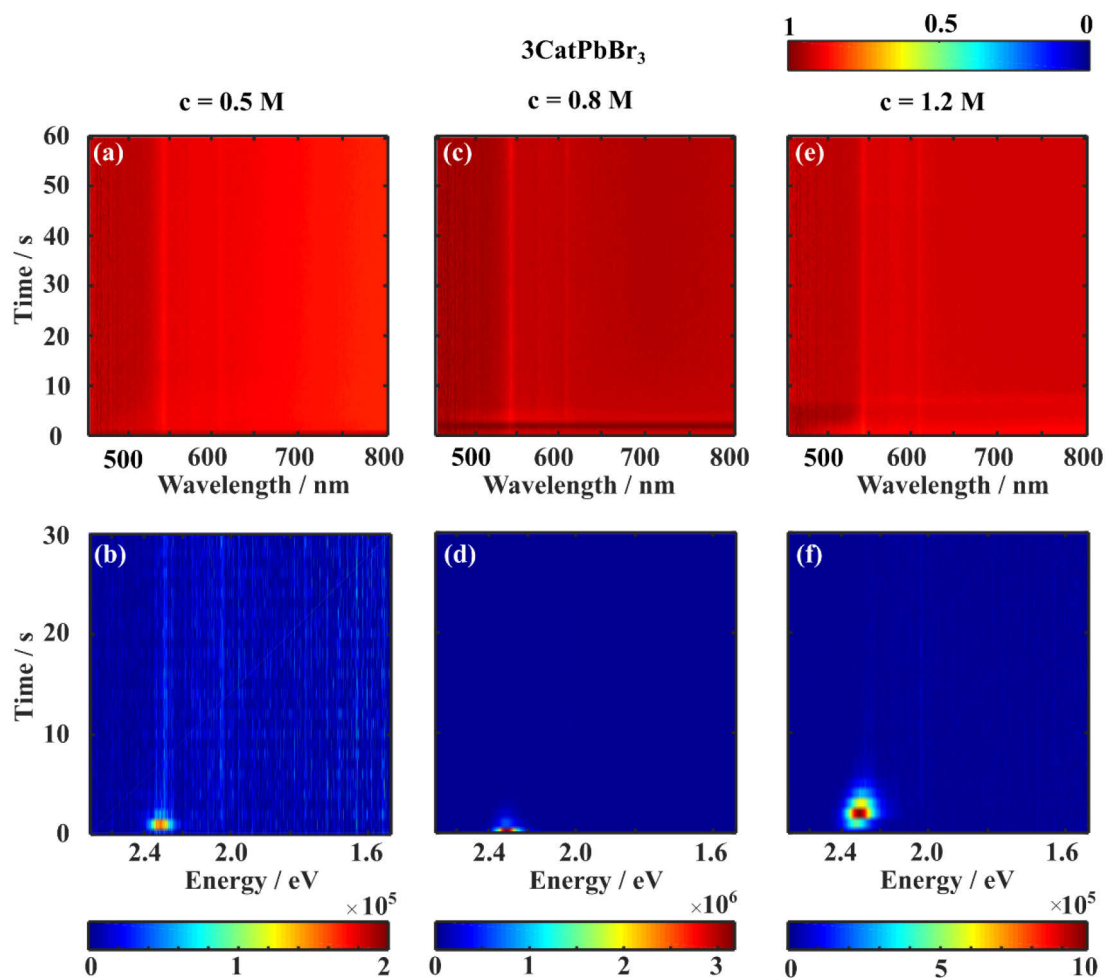
Figure A.3.8: 2D heat maps of in-situ UV-vis (a, c, e) and in-situ PL (b, d, f) measurements during annealing for the 3CatPbBr₃ concentration series, (a) and (b) for the 0.5 M solution, (c) and (d) for the 0.8 M solution, and (e) and (f) for the 1.2 M solution. The annealing process is tracked for the first 60 s for UV-vis and for 30 s for in-situ PL measurements.
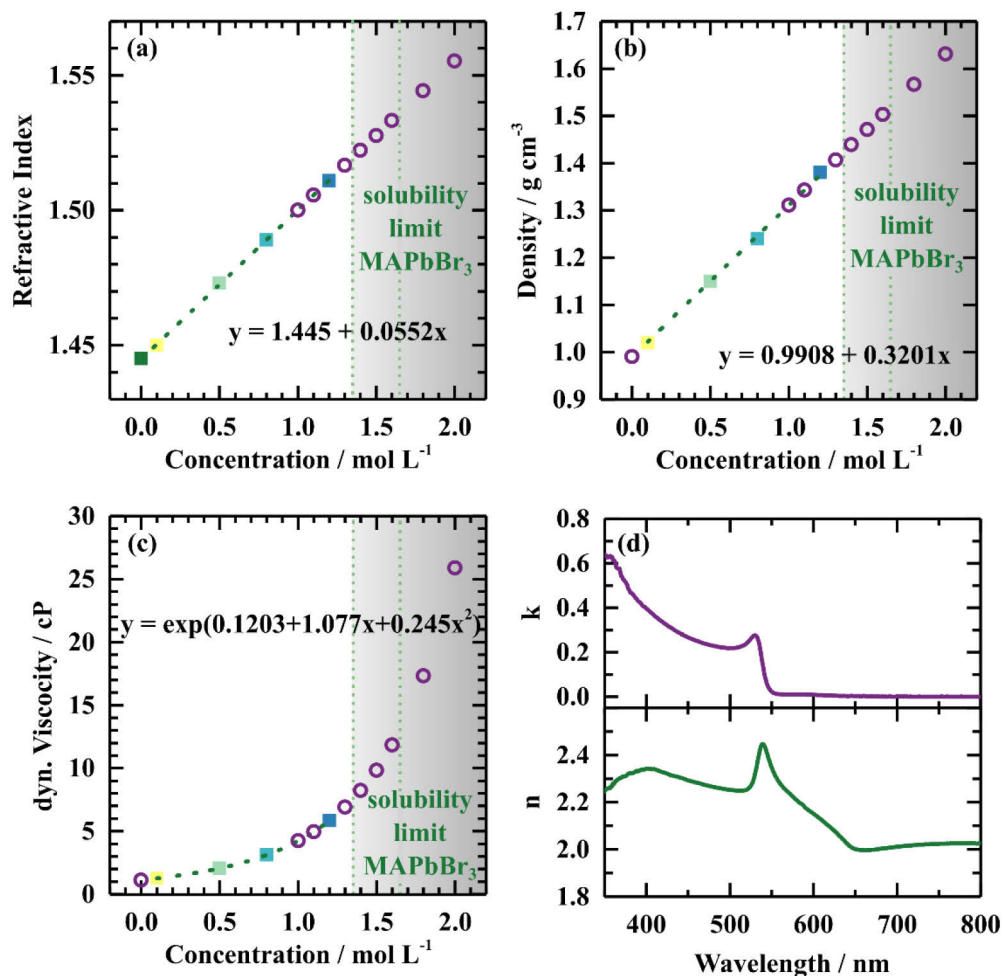
Figure A.3.9: Visualization of the solution characteristics of the 3CatPbBr₃ concentration series and the wavelength dependent optical characteristics of the final 3CatPbBr₃ thin-film. The concentration dependency of (a) the refractive index, (b) the density, and (c) the dynamic viscosity are demonstrated. The dashed green line, respectively, gives the fit of the individual data points measured (solid squares) and purple circles give values for additional concentrations extrapolated from the fit. In (d), the wavelength dependent *n* (green) and *k* (purple) of the final film are presented.
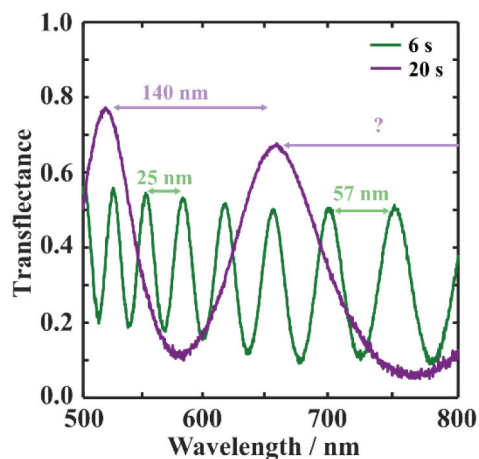
Figure A.3.10: Two exemplary interference pattern 6 s and 20 s within the spin-coating process of a 0.8 M 3CatPbBr₃ solution. The difference in spacing between two maxima causing an uncertainty in the thickness calculation are indicated.
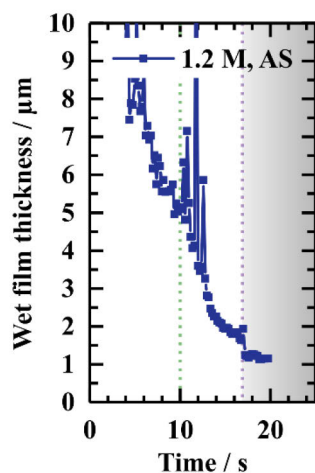
Figure A.3.11: Wet-film thinning for a 1.2 M 3CatPbBr₃ solution with dropping an anti-solvent 17 s within the spin-coating process. The dashed, green line marks the acceleration of the spin speed after 10 s and the dashed, purple line the dropping of the anti-solvent. The grey area marks the region in which the thickness calculation is questionable or rather not possible due to the multi-layer system created.

c = 1.2 M, with AS
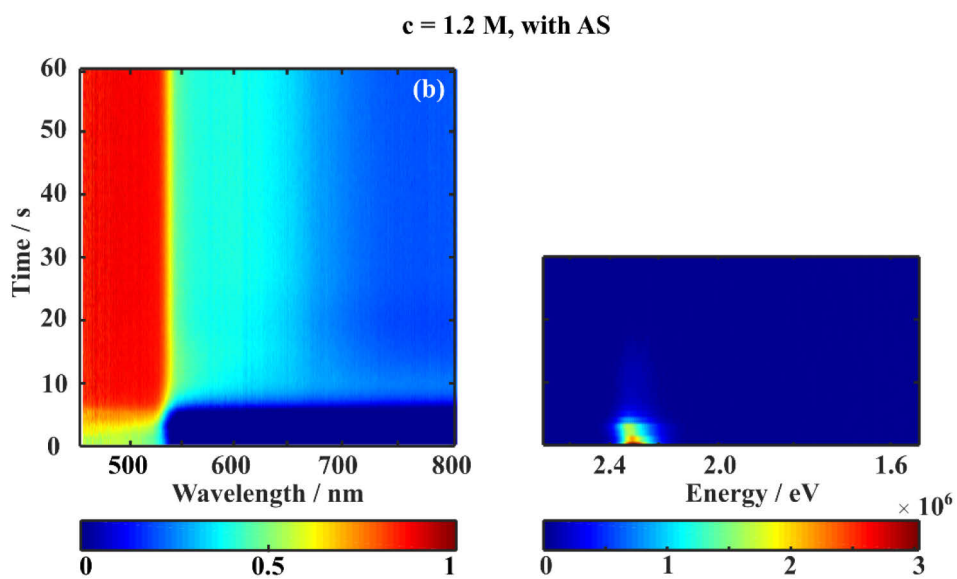
Figure A.3.12:2D heat maps for the annealing process of a 3CatPbBr$_3$ film prepared from a 1.2 M solution setting the anti-solvent drop 17 s within the spin-coating process, (a) in-situ UV-vis tracked for 60 s and (b) in-situ PL tracked for 30 s of the annealing.

A.4 List of Publications and Conference Contributions

Manuscripts in the framework of this thesis:

Origin of Ionic Inhomogeneity in $MAPb(I_xBr_{1-x})_3$ Perovskite Thin Films Revealed by In-Situ Spectroscopy during Spin-coating and Annealing
C. Rehermann, A. Merdasa, K. Suchan, V. Schröder, F. Mathies, E. L. Unger
ACS Appl. Mater. Interfaces **2020**, *12*, 30343–30352.

In-situ Monitoring of Perovskite Thin Film Formation by High-Speed Optical Reflectance Spectroscopy
C. Camus, C. Kaspari, J. Rappich, C. Rehermann, F. Mathies, V. Blank, E. L. Unger, N. Nickel
37th Eur. Photovolt. Sol. Energy Conf. Exhib. **2020**, 596–600.

Exposing the Formation Kinetics of Triple Cation Perovskite Thin Films during Spin-Coating and Annealing
A. Merdasa, C. Rehermann, K. Hirselandt, J. Li, O. Maus, F. Mathies, T. Unold, J. Dagar, R. Munir, E.L. Unger
https://www.researchsquare.com/article/rs-102041/v1

Finally, inkjet-printed metal halide perovskite LEDs – utilizing seed crystal templating of salty PEDOT:PSS
F. Hermerschmidt, F. Mathies, V. R. F. Schröder, C. Rehermann, N. Z. Morales, E. L. Unger, E. J. W. List-Kratochvil
Mater. Horizons **2020**, *7*, 1773–1781.

Perfluorinated Self-Assembled Monolayers Enhance the Stability and Efficiency of Inverted Perovskite Solar Cells
C. M. Wolff, L. Canil, C. Rehermann, N. Ngoc Linh, F. Zu, M. Ralaiarisoa, P. Caprioglio, L. Fiedler, M. Stolterfoht, S. Kogikoski, I. Bald, N. Koch, E. L. Unger, T. Dittrich, A. D. Neher
ACS Nano **2020**, *14*, 1445–1456.

Excitation wavelength dependence of photoluminescence flickering in degraded $MAPbI_3$ perovskite and its connection to lead iodide formation
A. Kiligaridis, A. Merdasa, C. Rehermann, E. L. Unger, I. G. Scheblykin
J. Lumin. **2020**, *222*, 117129.

Complex evolution of photoluminescence during phase segregation of $MAPb(I_{1-x}Br_x)_3$ mixed halide perovskite
K. Suchan, A. Merdasa, C. Rehermann, E. Unger, I. G. Scheblykin
J. Lumin. **2020**, 117073.

Photoinduced phase segregation and degradation of perovskites revealed by x-ray photoelectron spectroscopy.
R. Felix, C. Rehermann, D. Liu, E. Handick, C. Hartmann, R. G. Wilks, E. Unger, M. Bar
Conf. Rec. IEEE Photovolt. Spec. Conf., Institute Of Electrical And Electronics Engineers Inc., **2019**, pp. 2362–2367.

Impact of Excess Lead Iodide on the Recombination Kinetics in Metal Halide Perovskites
A. Merdasa, A. Kiligaridis, C. Rehermann, M. Abdi-Jalebi, J. Stöber, B. Louis, M. Gerhard, S. D. Stranks, E. L. Unger, I. G. Scheblykin
ACS Energy Lett. **2019**, *4*, 1370–1378.

Deep Defect States in Wide-Band-Gap ABX$_3$ Halide Perovskites
I. Levine, O. G. Vera, M. Kulbak, D. R. Ceratti, C. Rehermann, J. A. Márquez, S. Levcenko, T. Unold, G. Hodes, I. Balberg, D. Cahen, T. Dittrich
ACS Energy Lett. **2019**, *4*, 1150–1157.

Cs$_x$FA$_{1-x}$Pb(I$_{1-y}$Br$_y$)$_3$ Perovskite Compositions: The Appearance of Wrinkled Morphology and its Impact on Solar Cell Performance
S. Braunger, L. E. Mundt, C. M. Wolff, M. Mews, C. Rehermann, M. Jošt, A. Tejada, D. Eisenhauer, C. Becker, J. A. Guerra, E. Unger, L. Korte, D. Neher, M. C. Schubert, B. Rech, S. Albrecht
J. Phys. Chem. C **2018**, *122*, 17123–17135.

Oral conference contributions:

Understanding film formation of MAPb(I$_x$Br$_{1-x}$)$_3$ via optical in-situ methods
C. Rehermann, A. Merdasa, K. Suchan, E. L. Unger
Perovskite Solar Cells and Optoelectronics, Lausanne, Switzerland, 09/2019.

Clarification of impacts on halide perovskite film formation via optical in-situ methods
C. Rehermann, A. Merdasa, K. Suchan, E. L. Unger
EMRS Fall Meeting 2019, Warsaw, Poland, 09/2019.

Poster conference contributions:

Insights into Kinetics and Reaction Pathways of 2-Step conversion of MAPb($_{I1-x}$Br$_x$)$_3$ series via in-situ UV/vis measurements
C. Rehermann, K. Hirselandt, A. Merdasa, E. L. Unger
HEST-PV, Rehovot, Israel, 10/2017.

Insights into Kinetics and Reaction Pathways of 2-Step conversion of MAPb($_{I1-x}$Br$_x$)$_3$ series via in-situ UV/vis measurements
C. Rehermann, K. Hirselandt, A. Merdasa, E. L. Unger
21st Sede Boqer Symposium on Solar Electricity Production, Sede Boqer, Israel, 03/2018.

Insights into Kinetics and Reaction Pathways of 2-Step conversion of MAPb($_{I1-x}$Br$_x$)$_3$ series via in-situ UV/vis measurements
C. Rehermann, K. Hirselandt, A. Merdasa, E. L. Unger
DPG Frühjahrstagung 2018, Berlin, Germany, 03/2018.

Determination of the exciton binding energies in lead halide perovskites
C. Rehermann, A. M. Soufiani, E. L. Unger
HIOS Symposium 2018, Berlin, Germany, 09/2018.

Determination of the exciton binding energies in lead halide perovskites
C. Rehermann, A. M. Soufiani, E. L. Unger
Perovskite Solar Cells and Optoelectronics, Lausanne, Switzerland, 10/2018.

A.5 List of Abbreviations and Symbols

Abbreviations

Ag	Silver
CBM	Conduction Band Maximum
DMF	Dimethyl formamide
DMSO	Dimethyl sulfoxide
et al.	et alii
EQE	External Quantum Efficiency
FA$^+$	Formamidinium cation
FWHM	Full Width Half Maximum
ITO	Indium tin oxide
LED	Light emitting diode
LP	Long pass
MA$^+$	Methyl ammonium cation
ND	Neutral density
PCE	Power Conversion Efficiency
PL	Photoluminescence
PLE	Photoluminescence Emission
PLQY	Photoluminescence Quantum Yield
SEM	Scanning electron microscopy
SP	Short pass
SPV	Surface Photovoltage
TF	Transflectance
UV-vis	Ultraviolet and visible absorption spectroscopy
VBM	Valance Band Maximum
vs	versus
XRD	X-ray diffraction

Symbols

A	Absorptance
α(λ)	Wavelength dependent absorption coefficient
β	Coverage of thin-films
CuKα	Cupper K-alpha emission line with $\lambda = 1.5406$ Å
γ	Scattering of a thin-film
γ(λ)	Wavelength dependent scattering
d	Film thickness
E_B	Exciton Binding Energy
E_g	Bandgap
E_g^{IP}	Bandgap derived from Inflection Point
ΔH$_f$	Formation Enthalpy
I_0	Light intensity of incident light
I_R	Light intensity of reflected light
I_{sct}	Light intensity of scattered light
I_t	Light intensity of transmitted light
$I(\lambda)_B$	bright reference spectrum
$I(\lambda)_D$	dark reference spectrum
$I(\lambda)_S$	dynamic signal measured during the formation process
λ	wavelength
T_f	Goldschmidt´s tolerance factor
T	Transmittance
$t_{crystal}$	Time of crystallization onset
V_{OC}	Open circuit voltage
X_{UVvis}	Iodide amount x derived from absorption edge position
X_{sol}	Iodide amount x mixed into the precursor solution
X_{XRD}	Iodide amount x derived from XRD peak position
2θ	2 Theta angle

A.6 Acknowledgments

for administrative help, SEM measurements, ordering, maintaining the laboratory operation and the solution-oriented support.

What would life be without you? A huge "thank you" goes to dearest my **friends in Berlin, Munich, Brakel and all over the world**. It is impossible to list all the adventures and unforgettable moments with you here. Distraction clears the mind to return with new ideas, courage and strength.

Finally, but still important, I would like to express my deepest thanks to my **family**, who helped me to grow wings to fly. I am grateful to my **parents** who have supported me from the beginning, who never questioned a path I had chosen and who encouraged me to find my own way. I thank you, **little brother**, that you are a constant in my life and that I can rely on you in every situation.

A.7 Selbstständigkeitserklärung

Ich erkläre, dass ich die Dissertation selbständig und nur unter Verwendung der von mir gemäß § 7 Abs. 3 der Promotionsordnung der Mathematisch-Naturwissenschaftlichen Fakultät, veröffentlicht im Amtlichen Mitteilungsblatt der Humboldt-Universität zu Berlin Nr. 42/2018 am 11.07.2018 angegebenen Hilfsmittel angefertigt habe.

_____   _____
Datum, Ort   Unterschrift